2021

Experimental and numerical investigation of distribution patterns of diesel particulate matter and development of control strategies in an underground mine environment

Ramakrishna Morla

Experimental and numerical investigation of distribution patterns of diesel particulate matter and development of control strategies in an underground mine environment

Ramakrishna Morla

Supervisors:

A/Prof. Shivakumar Karekal and Dr Ajit Godbole

This thesis is presented as part of the requirement for the conferral of the degree:

Doctor of Philosophy

University of Wollongong

School of Civil, Mining and Environmental Engineering

January 2021

Abstract

Many nations use diesel-powered vehicles in underground mines despite their tendency to generate diesel particulate matter (DPM), a known Group-1 human carcinogen. Diesel-powered vehicles are more flexible and efficient than electric or battery-powered vehicles because of their ease of maintenance, consistency, durability, ability to travel between mine sections, power, robustness and cost-effectiveness. Moreover, if a mine already has a fleet of diesel-powered vehicles, changing to battery/electric-powered vehicles is challenging because of the expenditure and infrastructure requirements. The main concern with diesel-powered vehicles in underground mine environments is their exhaust contaminants, especially DPM.

Only a limited number of reported DPM monitoring investigations in the mining field and modelling studies are available in the literature. The main objectives of this research are to conduct extensive DPM field-monitoring investigations, develop and validate computational fluid dynamics (CFD) models, conduct modelling studies with different ventilation and operational conditions and develop DPM control strategies.

To accomplish the objectives of the thesis, eight stages of field-monitoring studies concerning DPM flow distributions were carried out in coal and metal mines and CFD with discrete phase modelling, species transport modelling and transient flow modelling studies were conducted. The simulated results were validated against field measurements and then comprehensive DPM modelling investigations were conducted.

The investigations from the field-monitoring studies indicated that at 10 m downstream of a stationary man-riding vehicle, the DPM particles spread over the entire cross-section of the roadway and occupants in the man-riding vehicle would be exposed to high DPM

concentrations, up to 226.8 μg/m^3. In a counter-flow the load haul dumper (LHD) operator would be exposed to a higher concentration of DPM than in a co-flow. The 10 m long dead-end crosscut experiment showed that after 5 minutes, DPM concentration reduced from 820 μg/m^3 to 232 μg/m^3. The shuttle car experiment indicates that personnel should not occupy the return side of the shuttle cars panel due to the high levels of DPM concentration. The results from monitoring a metal mine decline revealed that the DPM concentration depends mainly on the number of vehicles and the quantity of air available. The monitored time-weighted average exposure of different occupational personnel to DPM does not depend on their occupations.

The CFD modelling studies indicated that increasing the air velocity would decrease the DPM concentration. If the air velocity is reduced by 40% and 60%, the average concentration of DPM increase to 48% and 125%, respectively. The studies indicated that the exhaust pipe should be at the bottom of the vehicle. Furthermore, the temperature of diesel-powered vehicle exhausts has a slight influence on the concentration of DPM at the downstream side of the vehicle and increasing the temperature of the intake air increased the concentration of DPM at the downstream side of the vehicle. DPM concentration at the downstream side of the vehicle is influenced by the morphology of the vehicle. Studies show a high concentration of DPM on the downstream side of the truck loading bay and therefore personnel should not remain in this area for a long time.

The dead-end crosscut modelling studies indicated that an increasing air velocity in the adjacent gallery decreased the DPM concentration. The longer the dead-end, the longer it takes for DPM to dilute. The reduction of DPM as the angle of the dead-end crosscut increases is relatively low. The modelling investigations also demonstrated that a vortex airflow forms near the dead-end crosscut entrance and circulates in a curved form. The air velocity and pressure decrease towards the centre of the vortex, but DPM

concentration increases towards the centre of the vortex.

The DPM simulations enabled the virtually applicable novel DPM control strategies to be investigated. These investigations revealed that to control DPM concentration in a dead-end gallery with an auxiliary fan, the intake drive air quantity of an auxiliary fan must be greater than or equal to 150% of the gallery airflow and the auxiliary fan must be located at least 5 m from the dead-end crosscut entry. Studies found that the DPM concentration would decrease by increasing the efficiency of the diesel particle filters (DPFs). Investigations determined that reduction/removal of added resistance in a fresh air raise system reduced the DPM concentration in working areas and a pull–push ventilation system could reduce DPM concentration in underground declines. Finally, installing a rigid curtain to divert the airflow at the entrance to the 15 m long unventilated dead-end crosscut provided enough ventilation to dilute the DPM.

This thesis provided great insight into DPM flow patterns in an underground mine environment under different ventilation and operational conditions and provided DPM control strategies. This thesis also introduced DPM control strategies to proactively upgrade the underground mine environment to improve the health and safety of miners.

Acknowledgments

I wish to express my sincere thanks and gratitude to my primary supervisor A/Prof. Shivakumar Karekal for his guidance, encouragement and support throughout this study and research at the University of Wollongong. Without his kind help and support, I would not have gotten this far. In fact, his wisdom, kindness, conscientiousness, patience and selflessness have not only guided me through the difficult aspects of this study, they have also inspired me to set up further progress in life.

I am thankful to my co-supervisor Dr Ajit Godbole, for the insights he shared for CFD modelling strategies and editing skills. I am inspired by his technical knowledge, simplicity and generosity.

I would like to thank Mr Mandal, IIT Dhanbad, India, for his support during the underground coal mine field-measurements in India.

I sincerely thank Nasina Balasubrhamanyam and Satyanarana Inumula, Director General of Mine Safety, India and Prof. Ram Madhab Bhattacharjee, IIT Dhanbad, India, for providing the necessary resources, supervision and co-operation during the field experiments in India.

I would finally like to express my gratitude to my wife Purna Devi and son Bhavinesh for their support.

Certification

I, Ramakrishna Morla, declare that this thesis submitted in fulfilment of the requirements for the conferral of the degree of Doctor of Philosophy in the School of Civil, Mining and Environmental Engineering, University of Wollongong, is wholly my own work unless otherwise referenced or acknowledged. This document has not been submitted for qualifications at any other academic institution.

Ramakrishna Morla

Date: 7th January 2021

Awards and Publications

Award:

I received the third-best research paper award at the 18th North American Mine Ventilation Symposium for the manuscript titled "Optimising the location of secondary fans and quantity of air to control DPM recirculation in underground workings using discrete phase modelling".

Published book chapters:

1. MORLA, R., KAREKAL, S. & GODBOLE, A. 2021. Transient flow modelling of DPM dispersion in unventilated dead-end crosscuts and control strategy using curtain. Mine Ventilation. CRC Press.
2. MORLA, R., KAREKAL, S., GODBOLE, A., SRIWAS, M., JACOBS, J., TUKKARAJA, P. & CHAPULA, B. 2021. Optimizing secondary fan location and air quantity to control DPM recirculation in underground workings using discrete phase modelling. Mine Ventilation. CRC Press.
3. MORLA, R., KAREKAL, S. & GODBOLE, A. 2019. Analysis of Diesel Particulate Matter Flow Patterns in Different Ventilation and Operational Conditions of Underground Mines. Diesel Emissions. IntechOpen.

Published papers:

1. MORLA, R., KAREKAL, S. & GODBOLE, A. 2021. Investigation of optimum secondary fan location and air quantity to control DPM recirculation in underground

dead-end workings. International Journal of Mining and Mineral Engineering, IJMME, 310888.

2. MORLA, R., KAREKAL, S. & GODBOLE, A. 2021. Modelling of DPM dispersion in unventilated dead-end crosscuts using different crosscut lengths and adjacent gallery air velocity. Proceedings of MVSSA 2021 virtual conference, Mine Ventilation Society of South Africa.
3. MORLA, R., KAREKAL, S. & GODBOLE, A. 2020. CFD simulations of DPM flow patterns generated by vehicles in underground mines for different air flow and exhaust pipe directions. International Journal of Mining and Mineral Engineering, 11, 51-65.
4. MORLA, R., KAREKAL, S. & GODBOLE, A. 2020. Investigation of DPM dispersion in unventilated dead-ends using transient flow modelling. International Journal of Mining and Mineral Engineering, 11, 121-133.
5. MORLA, R., KAREKAL, S., GODBOLE, A., BHATTACHARJEE, R. M., NASINA, B. & INUMULA, S. 2019. Effect of ventilation air velocities on diesel particulate matter dispersion in underground coal mines. International Journal of Mining and Geo-Engineering, 53, 117-121.
6. MORLA, R., KAREKAL, S. & GODBOLE, A. 2019. Diesel-operated man-riding vehicle and load haul dumper DPM dispersion. International Conference on Recent Advances in Mining Technology. Bengaluru, India.
7. MORLA, R., KAREKAL, S. & GODBOLE, A. 2019. DPM flow pattern of LHD in underground mines with different ventilation conditions. Journal of Mining and Environment, 10(2), 315-326.

8. MORLA, R. & KAREKAL, S. 2018. Selection of fan(s) to dilute DPM for multi-seam board and pillar coal mines using Hardy Cross and CPM methods. International Journal of Engineering Technology Research and Management, 4(6), 36-47.
9. MORLA, R., GODBOLE, A., KAREKAL, S., BHATTACHARJEE, R. M. & BALASUBRAHMANYAM, N. 2018. Fundamental understanding of diesel-operated man-riding vehicle DPM dispersion – a case study. Journal of Sustainable Mining, 17, 105-110.
10. MORLA, R. & KAREKAL, S. 2017. Diesel particulate matter investigations in underground coal mines. International Journal of Engineering and Technology, 9(3), 1873-1876.

Papers under review:

1. MORLA, R., KAREKAL, S. & GODBOLE, A. 2021. Investigation of DPM modelling in underground mines using discrete phase and species transport modelling. Arabian Journal of Geosciences.
2. MORLA, R., KAREKAL, S. & GODBOLE, A. 2021. Investigation of collapsed rock in fresh air rise system on deep mine secondary fans. Journal of Sustainable Mining.
3. MORLA, R., KAREKAL, S. & GODBOLE, A. 2021. The effect of vortex flow on DPM concentration at the dead-end tunnel entrance. Particulate Science and Technology.

List of Symbols

A	Area (m^2)
b_{ki}	Fundamental matrix element of the loop
$c_{3\epsilon}$	The buoyancy extended coefficient
C_B	Concentration of pollutant in the dilution air ($\mu g/m^3$)
C_E	Concentration of pollutant in the exhaust ($\mu g/m^3$)
C_p	Specific heat (J/K/kg)
C_T	Target concentration of pollutant ($\mu g/m^3$)
C_{vm}	Virtual mass factor
C_p	Specific heat (J/K/kg)
D_h	Hydraulic diameter (m)
d_p	Particle diameter (m)
E	Total energy (J)
$\vec{F}$	Virtual mass force (kg)
F_D	Acceleration due to drag (ms^{-2})
$\vec{F}$	Virtual mass force (kg)
G_b	Generation of turbulent kinetic energy due to buoyancy (J)
g_i	Component of the gravitational vector in the i-direction
G_k	Production of turbulence kinetic energy due to the mean velocity gradient (J)
Gr	Grashof number
H	Height of the roadway (m)
h	Sensible heat (kW)
k	Turbulent kinetic energy ($J.kg^{-1}$)
ke	Thermal conductivity (W/m.K)

p	Perimeter (m)
P_{ni}	Increasing pressure due to natural ventilation in the branch (Pa)
P_{Fi}	Increasing pressure because of an installed fan (Pa)
Pr_t	Turbulent Prandtl number
Q	Quantity of air (m^3/s)
Q_a	Assumed quantity (m^3/s)
Q_E	Exhaust flow rate (m^3/s)
Q_V	Air quantity to dilute a pollutant emitted by a diesel engine (m^3/s)
R	Branch resistance (Ns^2/m^8)
Ra	Rayleigh number
Re	Reynolds number
R_i	Rate of production of species i by chemical reaction
S_h	Volumetric heat capacity ($J \cdot K^{-1} \cdot m^{-3}$)
S_i	Rate of creation by addition from the dispersed phase plus any user-defined sources
Y_M	Fluctuating dilution incompressible turbulence to the overall dissipation rate (m^2/s^3)
V	Velocity (m/s)
W	Width of the roadway (m)

List of Greek Symbols

ΔT_{DB}	Change in dry bulb temperature (°C)
ΔT_{WB}	Change in wet bulb temperature (°C)
ρ_p	Density of the particle material (kg/m^3)
ρ	Density of the fluid (kg/m^3)
$(\tau_{ij})_{eff}$	Deviatoric stress tensor (N/m^2)
ε	Dissipation rate (m^2/s^3)
μ	Dynamic viscosity (N.s/m^2)
η	Efficiency
$u_{i'}$	Fluctuating velocity (m/s)
$\vec{u}$	Fluid phase velocity (m/s)
$\triangle$	Flow intensity error (m^3/s)
ν	Kinematic viscosity (m^2/s)
$\bar{u}_i$	Mean velocity (m/s)
$\overrightarrow{u_p}$	Particle velocity (m/s)
$-\rho\,\overline{u_{i'}\,u_{j'}}$	Reynold's stress (N/m^2)
α	Thermal diffusivity (m^2/s)
β	Thermal expansion coefficient
μ_t	Turbulent viscosity (m^2/s)

List of Names or Abbreviations

ACARP	Australian Coal Industry Research Program
ACGIH	American Conference of Governmental Industrial Hygienists
CANMET	Canada Centre for Mineral and Energy Technology
CFD	Computational Fluid Dynamics
CO	Carbon monoxide
CO_2	Carbon dioxide
DBR	Drop Board Regulator
DEEP	Diesel Emissions Evolution Program
DP	Diesel particulate
DPF	Diesel particulate filter
DPM	Diesel particulate matter
EC	Elemental carbon
ER	Experimental results
FAR	Fresh air raise
FID	Flame ionisation detector
H_2	Hydrogen
H_2O	Water
HC	Hydrocarbons
HEI	Health Effects Institute
IARC	International Agency for Research on Cancer
LHD	Load haul dumper
MDG	Mining Design Guideline
MSHA	Mines Safety and Health Administration
MVSSA	Mine Ventilation Society of South Africa

N_2	Nitrogen
N_2O	Nitrous oxide
NCI	National Cancer Institute
NIOSH	National Institute of Occupational Safety and Health
nm	Nano meter
NMA	National Mining Association
NMHC	Non-methane hydrocarbons
NOx	Nitrogen oxides
NSSGA	National Stone, Sand and Gravel Association
OC	Organic carbon
OEL	Occupational exposure limit
PAHs	Polycyclic aromatic hydrocarbons
RANS	Reynolds-averaged Navier-Strokes
RAR	Return air raise
RCD	Respirable combustible dust
REC	Respirable elemental carbon
Sponcom	Spontaneous combustion of coal
STEL	Short-term exposure limit
TC	Total carbon
THC	Total hydrocarbons
TWA	Time-weighted average
USEPA	United States Environmental Protection Agency
USWA	United Steel Workers of America
WHS	Work health and safety

Table of Contents

List of Figures

List of Tables

Chapter 1

Introduction

1.1 Background

Although the diesel engine was invented by Dr Rudolf Diesel in 1892, the first diesel-powered locomotive was introduced into the Ruhr Coal mine in Germany in 1927 (Harrington and East, 1947). Later, in 1928, a diesel locomotive began to operate in the Witwatersrand gold mines in South Africa and in 1939 they began operations in French, Belgian and British coal mines. In 1946, American coal mines introduced diesel-powered vehicles into underground mines (Nundlall, 2014, Belle, 2010). Nowadays, most mines around the world use diesel-powered vehicles to transport men, material, ore, waste rock and coal and for various other mining operations (Rawlins, 2006). The commonly used diesel-powered vehicles in underground coal and/or metal mines are trucks (485 kW and 567 kW), load haul dumpers (LHDs) (150 kW and 306 kW), drill machines (115 kW), cable bolters (110 kW), long-hole drilling rigs (115 kW), man-riding vehicles (150 kW), telehandlers (75 kW), graders (101 kW), water trucks (164 kW), forklifts (25 kW), articulated wheel loaders (120 kW), agitators (170 kW) and shotcrete sprayers (110 kW) etc. (Matsui, 2009, Bugarski et al. 2012b, Rawlins, 2006, Davies, 2002).

Diesel-powered vehicles are more flexible than battery-powered or electric vehicles because they can travel longer distances and between working sections (Matsui, 2009, Bugarski et al., 2012b). Moreover, diesel vehicles are efficient, as evidenced by their ease of maintenance, consistency and durability, which is why many nations depend on them (Daniel, 1984, Morla et al., 2019).

The main concern with diesel-powered vehicles in underground mine environments is their exhaust pollutants (MDG, 2008). Since underground environments are necessarily confined and have restricted ventilation and enclosed areas, the contaminants generated by diesel engines cannot readily escape (MDG, 2008). The exhaust fumes from diesel-powered equipment are generally a mixture of diesel particulate matter (DPM) and other pollutant gases such as nitrogen oxides (NOx) and hydrocarbons (HC) as either total hydrocarbons (THC) or non-methane hydrocarbons (NMHC) and carbon monoxide (CO) (MDG, 2008).

DPM is a by-product of the incomplete combustion of diesel fuel in a diesel engine. DPM particles have a solid core and are made up of elemental carbon (EC). The EC adsorbs many toxic substances (MSHA, 2001). More than 1,800 different organic compounds have been identified as adsorbed on the EC core, some of which are organic chemicals (polycyclic aromatic hydrocarbons or PAHs), condensed liquid hydrocarbons, inorganic compounds (sulphates), nitrous oxide (N_2O), dioxins and metal oxides (Bugarski et al., 2012b, Liang et al., 2005, Robert et al., 2007, Sharma et al., 2005, Jin et al., 2014).

Recent health research studies concluded that exposure of miners to high concentrations of DPM in mine environments increases the risk of lung cancer (Ris, 2007, Ristovski et al., 2012, Patel et al., 2011, Noll et al., 2014, Watts Jr, 1987, NIOSH, 1988, Nauss, 1995, MSHA, 2001a, USEPA, 2002, Silverman et al., 2012). In 2012, the International Agency for Research on Cancer (IARC) included DPM as a Group-1 human carcinogenic agent (Benbrahim-Tallaa et al., 2012).

As per mining regulations, adequate airflow (0.06 $m^3/s/kW$) is required to dilute DPM concentration to within the statutory limits in all underground places with diesel-powered equipment (CMHSR, 2006, MDG, 2008, WHSA, 2013, WHSR, 2014). However,

sometimes diesel-powered vehicles need to be operated with insufficient ventilation. It takes a long time to dilute DPM without adequate ventilation, which means that mine operators are exposed to high DPM levels.

1.2 Problem statement

Diesel particulate matter is a complex mixture of solid and liquid material (Ristovski et al., 2012). Since 90% of DPM particles range from 3 nm to 30 nm in size (Bugarski et al., 2012a, Bugarski et al., 2004, Virtanen et al., 2006), they tend not to settle quickly under their own weight and remain suspended. A very long time is therefore needed to dilute DPM to acceptable levels in the breathing zone if no other measures are in place. If mine personnel are exposed to DPM, the smaller particles may be deposited in the gas exchange regions in the human lungs. Prolonged exposure to high concentrations of DPM may lead to adverse health effects, including cancer. In 2012, the IARC recognised DPM as a Group-1 human carcinogen (Benbrahim-Tallaa et al., 2012).

As underground mines go deeper and spread over larger areas in an attempt to meet ever-increasing production targets, there is a corresponding increase in the use of diesel-powered vehicles in coal, metal and non-metal mining operations (Daniel, 1984). Underground workspaces are narrow and have controlled ventilation systems. In some areas like declines or inclines, gate roads, etc. ventilation air must travel over longer distances to ventilate working sections. If DPM is released into those areas by diesel-powered vehicles, these particles will become airborne over the entire airway. Since diesel-powered vehicles need to be operated in isolated/unventilated areas such as parking cuddies, footwall drives, cut-throughs and other regions with restricted airflows and/or no ventilation, it takes a long time before DPM can be diluted to acceptable levels. Regrettably, in some of these areas, underground personnel have no option but to breathe

this polluted air.

To eliminate/minimise exposure to high concentrations of DPM, accurate mappings of DPM concentration contours at different ventilation and operational conditions are required to develop control strategies. To validate the modelling, effective field-monitoring DPM data with distinct underground mine vehicles, airflows and working conditions are required. Efficient mine ventilation systems must also be developed to mitigate the high DPM concentrations that accumulate in regions where these vehicles operate.

Limited reported DPM field-monitoring data is available for different diesel-powered vehicles. In previous field studies such as the NIOSH (Bugarski et al., 2004) and DEEP (McGinn et al., 2004) field studies, DPM was monitored at a few sampling stations for a long period of time. Also, in a Missouri University of Science and Technology (S&T) study, an experiment was conducted with a 30-kW skid-steer loader (Zheng, 2011); the DPM measurements were taken within 5 m downstream of the vehicle where the flow is highly turbulent. The available field-monitoring data was not enough to accurately map DPM. Also, only a limited number of reported DPM modelling investigations have been carried out in an underground mine environment to model DPM contours. A limited number of research studies have also been carried out to control DPM emissions from vehicle exhausts using different filters and different fuel combinations (Bugarski et al., 2004, Davies, 2004, McGinn et al., 2004), etc. A limited number of investigations have also been carried out to control DPM in a mine air environment.

To date, limited research has been conducted on the flow behaviour of DPM particles in the underground mine environment in order to understand basic DPM flow distribution. Therefore, there is a need for precise field-monitoring data, advanced DPM simulation

strategies under different ventilation and mining conditions and innovative DPM control strategies in an underground mine environment. DPM flow behaviour also needs to be investigated in different underground coal and metal mine environments where diesel-powered vehicles operate under different ventilation systems. The present research addresses this research gap.

This proposed research will monitor DPM flow concentrations in the field with different diesel-powered vehicles and in coal and metal/non-metal mines, by modelling DPM flow patterns and concentrations with varying velocities of air, temperatures and exhaust pipe directions. Investigations of DPM dispersion in unventilated isolated workings with different geometrical and ventilation conditions are also needed. Effective DPM control strategies are required to minimise personnel exposure.

1.3 Research aims and objectives

This research aims to investigate the flow patterns and concentrations of DPM under different ventilation and operating conditions in underground mines and to develop strategies that would optimise the ventilation networks to dilute DPM concentration. This was achieved by carrying out field experiments and CFD simulations. The results of these CFD simulations were validated against field experiments. The main objectives are:

a) To conduct extensive field-monitoring of DPM concentrations in underground coal and metal mines with different diesel-powered vehicles and ventilation conditions.
b) To develop 3D underground CFD models with different diesel-powered vehicles by considering all the features of the vehicles.
c) To conduct CFD simulations with different ventilation and operational conditions and validate the models with field experimental data using discrete phase and

species transport DPM modelling.

d) To evaluate the behaviour of DPM dispersion in unventilated dead-ends using transient flow modelling.

e) To develop DPM control strategies based on the DPM distribution under various ventilation scenarios and vehicle movements.

f) To develop DPM control strategies with different filter efficiencies, optimum locations of auxiliary fans, curtains, reducing airway resistance and pull–push ventilation systems on DPM dispersion.

1.4 Scope of work

A detailed literature review of DPM, field experiments and modelling investigations was carried out to identify the existing problems and meet the objectives of this thesis. Since there are a lack of detailed DPM field data, useful DPM mapping in airflow-restricted zones and proper DPM control strategies, extensive field experiments were carried out in eight stages in an Indian coal mine and some staged experiments in an Australian metal mine. The field results were used to validate the CFD models and to analyse DPM distribution. The scope of work includes the following aspects:

- Field experiments: Extensive field experiments on different diesel-powered vehicles and under different mining conditions were carried out in six stages in a coal mine and two stages in metal mines.
- Model construction: Development of 3D models in CAD and imported into Ansys. The models meshed with finer elements near the diesel vehicles.
- Selection of simulation tool: The CFD simulations were carried out using discrete phase modelling, treating DPM particles and mine air as two different phases. Dead-end modelling studies were carried out in transient flow modelling. Since

DPM particles are small (nanometres), species transport modelling was also used and it was assumed that DPM was a dense gas. Since discrete and species transport models would deliver similar results, discrete phase models were used in most cases, but in some instances species transport modelling was used because the simulation time is faster. Transient flow modelling was used to investigate DPM dispersion variation with time in dead-end workings. In a few cases, Ventsim modelling was also used where CFD modelling could not be used for simulation due to meshing issues encountered with a large underground mining model of over 24 km decline length and over 50 level galleries.

- Assumptions and Exclusions: The walls of the underground roadway were considered to be uniform over the entire cross-section. The diameter of the auxiliary fan is the same as the ventilation bag.
- Model validation: The CFD models were validated against field data and then the CFD models were used for extensive parametric studies.
- Modelling and analysis: The flow patterns of DPM were investigated under different ventilation and operating conditions. Studies were carried out to understand DPM dispersion in unventilated dead-ends. Innovative DPM control strategies were also developed.

1.5 Outline of the thesis

This thesis is divided into eight chapters to present the information related to this research. The organisation of the chapters is as follows:

Chapter 1: Introduction

This chapter provides a background on the research, problem statement, aim and objectives of the research, scope of work and the thesis outline.

Chapter 2: Literature review

A comprehensive review of research into DPM, including its characteristics, ventilation standards, health effects and available DPM monitoring systems, is conducted. Previous DPM field investigations, gap analysis and research questions are also presented.

Chapter 3: Experimental investigations

In this chapter, field experiments carried out in coal and metal mines in eight stages using various diesel-powered vehicles and mining conditions to determine DPM dispersion are presented. The results and discussions of the field experiments are also provided.

Chapter 4: DPM modelling methodology

In this chapter, the basic governing equations needed to model DPM, CFD formulation, DPM modelling and how CFD modelling is used in the underground mining industry to model different issues are provided. This chapter also describes the development of base case CFD models for field experiments, meshing and modelling and also presents model validation with experimental data.

Chapter 5: Parametric studies with different ventilation and operational conditions

This chapter describes DPM modelling with different ventilation and operational conditions. In this chapter, studies were undertaken with different air velocities and

diesel-powered vehicle exhaust directions, including the effects of temperatures of the exhaust fumes and the intake air. Simulation studies were also conducted with vehicle morphology and truck loading bay.

Chapter 6: Transient flow parametric studies: Effect of dead-end crosscut geometry and air velocity

This chapter describes how DPM is dispersed in unventilated dead-end crosscuts. DPM concentration with different dead-end crosscut lengths, velocities of air in the main galleries and different dead-end crosscut angles using transient flow modelling is provided.

Chapter 7: DPM control strategies in an underground environment

This chapter proposes strategies for controlling DPM using the optimum location of secondary fans, different filter efficiencies, controlling DPM by removing collapsed rock in the fresh air drives, pull–push decline ventilation system and dead-end DPM control strategies using curtains.

Chapter 8: Conclusions and recommendations

This chapter summarises the significant findings of the research and then makes some recommendations for potential areas of future research.

Chapter 2

Review of Literature Relevant to Diesel Particulate Matter

2.1 Introduction to DPM

Since 1927, the use of diesel-powered vehicles in underground mines has increased to cope with deeper mines and increased production targets (Xu et al., 2018, Nundlall, 2014, Davies, 2004). Despite their utility, diesel-powered vehicles generate diesel particulate matter (DPM), which is a known carcinogenic agent (Benbrahim-Tallaa et al., 2012). This chapter discusses the properties of DPM, such as its chemistry, particle size distribution and density. It also discusses the health effects of DPM, workplace exposure standards in underground mines and DPM monitoring strategies. This chapter also reviews previous field investigations involving DPM.

The molecular structure of diesel consists of hydrogen (H_2) and carbon (C) atoms. In an ideal diesel engine, oxygen (O_2) from the air converts all the hydrogen in the fuel to H_2O and the carbon to carbon dioxide (CO_2), while the nitrogen (N_2) in the air remains unaffected (2-1) (Bugarski et al., 2012a).

$$Diesel\ fuel + nO_2 \rightleftharpoons pH_2O + mCO_2 + \text{energy} \qquad \textbf{(2-1)}$$

In reality the combustion process is not perfect because diesel engines are always operated with more air than is needed, with the result that a large fraction of the oxygen and nitrogen supplied by combustible air is not consumed in this process. Moreover, the incomplete combustion of fuel, the reactions between mixture components under high temperature and pressure, the combustion of engine lubrication oil and oil additives and the combustion of nonhydrocarbon components of diesel fuel, also occur. All these

processes are responsible for generating the pollutants emitted from engines, including DPM (Bugarski et al., 2012a).

The high concentration of DPM is challenging in underground mining environments, where heavy machinery can work for many hours in confined spaces and with long distances between the workplace and open air.

2.1.1 Properties of DPM

The chemical composition of DPM depends on the composition of the diesel, lubricating oil, engine technology, operating conditions and the technology used to treat the exhaust (Jin et al., 2016, Liang et al., 2005, Yergey et al., 1982). The major constituents of the total particle mass emitted by diesel engines include elemental carbon (EC), organic carbon (OC) and inorganic ions such as sulphates, nitrates, ammonia, sodium, chloride ions and trace metallic compounds (Bugarski et al., 2004, Bugarski et al., 2011, Wichmann, 2007).

Elemental carbon (EC) and organic carbon (OC) emissions, cumulatively known as total carbon (TC), make up the largest fraction of aerosols emitted by diesel engines (Noll et al., 2007, Gray et al., 1984, Feng et al., 2009). Total carbon is generally considered to make up about 70% to 90% of DPM. On average, EC comprises 50%–70% of total carbon and more than 45% of total DPM emissions. OC makes up between 10% and 80% of total carbon (Bugarski et al., 2004, McGinn et al., 2004).

Fig. 2.1 shows the details of EC, OC and TC in a DPM cluster. The EC fraction of DPM is a product of the fuel's pyrolysis and the lubricating oil in the combustion chamber. The OC fraction is a complex mixture of burned and unburned lubricating oil and fuel compounds (MSHA, 2001b).

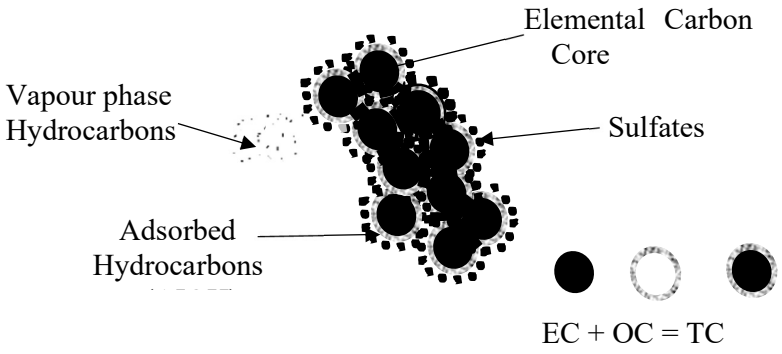

Fig. 2.1 DPM components (MSHA, 2001b)

2.1.2 Particle size distribution

The particles comprising DPM are very small and are divided into three categories based on their size: nanoparticles less than 50 nm in diameter, ultrafine particles between 50 nm and 100 nm in diameter and fine particles that are between 100 nm and 2.5 μm in diameter (Kittelson, 2001). **Fig. 2.2** shows a typical DPM size distribution weighted by number, surface area and mass (MSHA, 2001b).

The DPM particle distribution can be characterised in three different ways: 'Nucleation mode', 'Accumulation mode' and 'Coarse mode'. 'Nucleation mode': In this mode, the particles are between 3 to 30 nm in diameter. They mainly consist of volatile organic and sulphur compounds in varying proportions, as well as a small amount of solid material that is likely to consist of carbon and metallic compounds. The nucleation mode typically contains 0.1–10% of the particle mass and up to 90% of the number of particles. 'Accumulation mode': In this mode, the particles are between 30-500 nm in diameter. Most of the DPM mass is composed primarily of carbonaceous agglomerates and adsorbed materials and is found in the accumulation mode. 'Coarse mode': This consists of particles larger than 1,000 nm and contains 5–20% of the diesel aerosol mass. Hence, DPM contains numerous small particles with very little mass that are mixed with some

larger particles which contain most of the total mass.

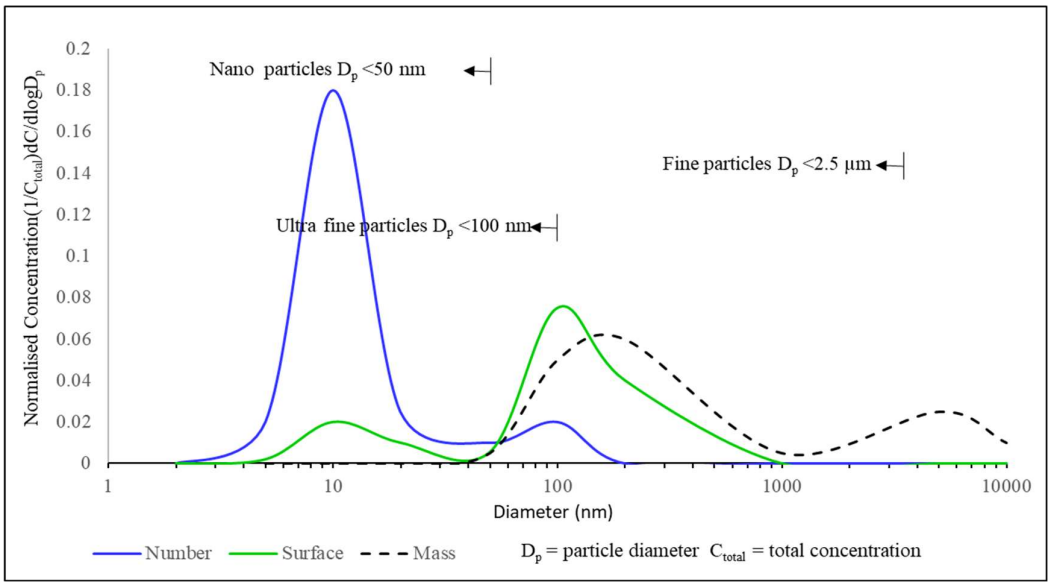

Fig. 2.2 DPM particles size distribution (MSHA, 2001a)

2.1.3 Density

The density of DPM depends mainly on particle size, so the 'effective density' decreases as the particles increase in size. This is because the particles are more agglomerated as their size increases. The 'effective' density (mass per unit volume) of agglomerated 30 nm diesel particles varies from 1.1 to 1.2 g/cm^3 (Ristim, 2006), but decreases sharply to 0.3 g/cm^3 for 300 nm particles (Bugarski et al., 2012a). The average density of the semi-volatile liquid on the DPM is approximately 0.8 g/cm^3. The density of diesel particles preheated to remove the volatile components is 1.77 ± 0.07 g/cm^3. In comparison, the approximate densities of diesel fuel, lubricating oil, sulphuric acid (H_2SO_4) and elemental carbon are 0.82 g/cm^3, 0.9 g/cm^3, 1.83 g/cm^3 and 2.2 g/cm^3, respectively (Bugarski et al., 2012a, Bugarski et al., 2004, Virtanen et al., 2006). The average density of particle-bound organic material is 0.8 g/cm^3. In summary, the density of DPM is between 0.9 and 1.2 g/cm^3 (Shi et al., 1999).

2.2 Influence of DPM on miners' health

Underground mines are going ever deeper and the use of diesel-powered vehicles is increasing. The result is an increased risk of operators being exposed to DPM for longer periods of time. Due to their small size, DPM particles may be deposited in the gas exchange regions in human lungs, which inevitably means that prolonged exposure to high concentrations of DPM may have adverse health effects.

2.2.1 DPM deposition in the human respiratory tract

DPM particle deposition in the human respiratory tract depends mainly on the size of the particles. 'Course mode' aerosols are mainly deposited in the anterior nose and extra-thoracic regions, while very small diesel aerosols are mainly deposited in the bronchial, bronchiolar and alveolar regions of the human respiratory tract. Nucleation-mode and accumulation-mode diesel aerosols can readily penetrate the alveolar regions where gas exchange occurs. The removal of solid diesel aerosols from unciliated alveolar regions is much slower than aerosols deposited in the ciliated upper-lung region (MSHA, 2001b).

On average, 30% ± 9% of the total number of diesel aerosols with a median diameter of 125 nm and a geometric standard deviation of 1.7 are deposited in the human respiratory tract (Bugarski et al. 2011); 56% of inhalable particles emitted by a heavy-duty diesel engine equipped with a diesel oxidation catalyst and 51% of inhalable particles emitted by an engine equipped with a partial diesel particulate filter (DPF) are deposited in the respiratory tract (Davies, 2004, MSHA, 2001b, Zheng, 2011).

2.2.2 Health issues and investigations

DPM-related health issues have been investigated for a number of years. Experimental studies were carried out on rats and mice in 1988 by the National Institute of Occupational Safety and Health (NIOSH, 1988). This study found that prolonged exposure to diesel exhaust gases increased cancer occurrence in rats and mice. Since then, far more scientific studies have been carried out on this topic.

In 1995, the Health Effects Institute (HEI) published their research report after reviewing over 30 epidemiologic studies of workers exposed to DPM in occupational settings from 1950 through to the early 1980s (Nauss, 1995). It was concluded that a direct correlation exists between exposure to diesel exhaust and human lung cancer. Long-term exposure to DPM in various occupational circumstances is associated with a 1.2 to 1.5fold increase in the relative risk of lung cancer compared with workers classified as unexposed.

The Mines Safety and Health Administration (MSHA) reviewed 47 epidemiological studies and determined that in 41 of those studies there was some degree of association between occupational exposure to DPM and the prevalence of lung cancer. However, some of these studies had limited statistical value because they either included relatively few workers or had an inadequate allowance for the latency or follow-up period. The MSHA then concluded that exposure at a mean DP concentration of 0.64 mg/m^3 for 45 years would result in relative risk of 2.0 for lung cancer (MSHA, 2001a).

The United States Environmental Protection Agency (USEPA) conducted a health assessment for humans exposed to diesel engine exhaust (USEPA, 2002). They found acute adverse effects on eyes and throat, bronchial irritation, light-headedness, nausea and cough. With respect to chronic non-cancerous respiratory effects, the results of studies on animals suggested the potential for chronic respiratory diseases in humans. USEPA also

concluded that lung cancer was evident in occupationally exposed groups but did not define sufficient dose-response data to produce a quantitative risk assessment.

The National Cancer Institute (NCI) conducted a nested case-control study on a cohort of 12,315 workers in eight non-metal mining facilities (Silverman et al., 2012). For each case subject, the researchers selected up to four control subjects individually matched with mining facility, sex, race/ethnicity and birth year from all the workers who were alive before the day the case subject died. For each subject, they estimated the exposure to diesel exhaust, as represented by respirable elemental carbon (REC) and by job and year, based on an extensive retrospective exposure assessment at each mining facility. The researchers observed an increasing trend in the risk of lung cancer with increasing cumulative REC and average REC intensity. The risk of lung cancer among workers heavily exposed to REC (between 640 and 1280 $\mu g/m^3$) was five times that observed among workers in the lowest exposure category (<20 $\mu g/m^3$) (Silverman et al., 2012).

It can be concluded from these research studies that exposure to diesel exhaust causes cancer in humans. Since the 1980s, hundreds of studies have documented links between DPM and cancer in humans (Ris, 2007, Ristovski et al., 2012, Patel et al., 2011, Noll et al., 2014, Watts Jr, 1987, NIOSH, 1988, Nauss, 1995, MSHA, 2001a, USEPA, 2002, Silverman et al., 2012, AIOH, 2013). Recently, Australian mine regulations have recognised DPM as a Category-1 carcinogenic agent (SWA, 2019) and the IARC incorporated DPM as a Group-1 human carcinogen (Benbrahim-Tallaa et al., 2012).

2.3 Workplace exposure limits and ventilation standards

To regulate personal exposure to a Group-1 carcinogenic agent in the form of DPM in underground working environments, mine management follows strict rules and

regulations. Different countries specify different DPM workplace exposure limits and mine ventilation standards. A summary of DPM exposure limits and ventilation requirements (Mahe, 2012, Niekerk et al., 2002) is shown in **Table 2.1.** The DPM-related mine regulations for various countries are outlined in the following sections.

Table 2.1 International DPM exposure limits and ventilation standards (Niekerk et al., 2002, Mahe, 2012, Nundlall, 2014)

Country	Exposure guideline/limit		Ventilation Standards
	($\mu g/m^3$)	Substance	
Australia	100	EC	Minimum air quantity of 0.06 $m^3/s/kW$ or 3.5 m^3/s, whichever is greater
	160	TC	
	200	DP	
Canada (Ontario)	400	TC	0.06 $m^3/s/kW$
USA	160	TC	As per MSHA certificate
India	100	EC	Minimum air quantity of 0.06 $m^3/s/kW$
Germany	100	EC	Minimum air quantity of 0.06 $m^3/s/kW$
China	–	–	Minimum air quantity of 0.067 $m^3/s/kW$
South Africa	100	EC	Minimum air quantity of 0.1 $m^3/s/kW$
Switzerland	100	EC	–
Germany (Tunnelling)	300	EC	Minimum air quantity of 0.06 $m^3/s/kW$
Germany (Other)	100	EC	Minimum air quantity of 0.06 $m^3/s/kW$

2.3.1 Australia

As per the Australian mine regulations (CMHSR, 2006, MDG, 2008, WHSA, 2013, WHSR, 2014), the maximum allowable limit for an eight-hour time-weighted average exposure (mine atmosphere) for elemental carbon (EC) is 100 $\mu g/m^3$. This is approximately equivalent to 160 $\mu g/m^3$ of TC or 200 $\mu g/m^3$ diesel particulate (MDG, 2008).

As per MDG-29 (MDG, 2008), if a miner's time-weighted average exposure is more than 8 hours in multiple shifts over a month, the average allowable workplace exposure values of EC, TC and DP will decrease. This reduction is quantified in terms of a 'reduction factor'. The reduction factor for multi-shift exposure for one shift rosters is less than 170 hours per month and 170/x if the shift roster is more than 170 hours per month. Here 'x' is the average number of hours worked in the month and 170 is the typical number of hours worked in a month for a normal 8 hours/day, five days/week work cycle (MDG, 2008).

For example, if a mine were to operate a shift change-out on a 12-hour shift basis, then the exposure factor x is 170 / (12 hours per day * 15 days per month) = 0.94. Thus, the EC workplace exposure limit would be 100 $\mu g/m^3$ * 0.94 = 94 $\mu g/m^3$.

To dilute DPM to within the regulatory limits, Australian mines follow strict regulations. As per the NSW Coal Mines Health and Safety Regulation 2006 (CMHSR, 2006) and the guidelines for the management of diesel engine pollutants in underground environments (MDG, 2008), the ventilation air volume flow rate in each location where a diesel engine operates must be at least either 0.06 $m^3/s/kW$ of the maximum capacity of the diesel engine or 3.5 m^3/s, whichever is the greater quantity. This ventilation airflow must be directed along the airway in which the engine operates.

If more than one diesel engine is being operated in the same ventilating current, the engine kilowatts must be added and the minimum ventilation requirement is 0.06 $m^3/s/kW$ or 3.5 m^3/s, whichever is greater (MDG, 2008).

The ventilation air required to dilute any of the gases (CO, CO_2, SO_2, NO and NO_2) or DPM emitted by a diesel engine to the targeted concentration level (Q_v) can theoretically be calculated for any given movement using the following equation (Bugarski et al., 2012a)

$$Q_V\left[\frac{m^3}{s}\right] = \frac{Q_E\left[\frac{m^3}{s}\right] X \left(C_E\left[ppm\ or\ \frac{\mu g}{m^3}\right] - C_T\left[ppm\ or\ \frac{\mu g}{m^3}\right]\right)}{C_T\left[ppm\ or\ \frac{\mu g}{m^3}\right] - C_B\left[ppm\ or\ \frac{\mu g}{m^3}\right]} \quad \textbf{(2-2)}$$

Where Q_E is the exhaust flow rate, C_E is the concentration of the specific pollutant (gas or DPM) in the exhaust, C_T is the target concentration of the corresponding gas or DPM and C_B is the concentration of the specific pollutant (gas or DPM) in the dilution air.

2.3.2 USA

As recommended by the United States Mine Safety and Health Administration (MSHA, 2008), a miner's exposure to DPM in an underground mine must not exceed an average eight-hour equivalent full shift airborne concentration of 160 $\mu g/m^3$ of total carbon per cubic metre of air (Zhou et al., 2015a).

As per the MSHA, the minimum ventilation air quantity (MSHA, 2001b) requirement is based on the 'nameplate' airflow for the equipment engines. These nameplate airflows are determined by laboratory testing using the MSHA test procedure designed to approximate the engines' duty cycles. The air quantity rates are based on the exhaust contaminants measured at different engine speeds and loading factors. The projected

time-weighted average (TWA) is calculated as (MSHA, 2001b):

$$TWA_{projected} = \frac{Q_{measured}}{Q_{requested}} TWA_{measured} \quad \textbf{(2-3)}$$

2.3.3 South Africa

In South Africa, the Mine Ventilation Society of South Africa (MVSSA) recommended a minimum of 0.1 m^3/s of air per rated kW power of the diesel engine(s) to dilute diesel engine emissions (Belle, 2010, Nundlall, 2014). There are no specific operational exposure limits (OELs) for DPM in the South African mining industry, but some mining companies have adopted DPM occupational exposure levels of 0.2 mg/m^3 of TC or 0.1 mg/m^3 as EC (Stanton et al., 2007).

2.4 DPM monitoring systems

Various monitoring techniques are used globally to measure the DPM levels in underground mine environments. The most broadly accepted method is the NIOSH Analytical Method 5040, followed by the Canadian Respirable Combustible Dust (RCD) method and real-time monitoring method, as outlined in the following paragraphs.

2.4.1 NIOSH analytical method 5040 to estimate DPM

This method works on the principle of analysing the evolved gas using a thermal-optical analyser technique. This process has two stages. In the first stage, organic carbon and carbonate carbon are evolved in a helium atmosphere as the temperature is steadily increased to approximately 850°C. The evolved carbon is catalytically oxidised to CO_2 in a bed of granular MnO_2. In the second stage, the oven temperature is reduced, an oxygen–helium mixture is introduced and the temperature is then increased to 940°C. The point

at which the filter reaches its initial value is called the split between OC and EC; the carbon that evolved before the split is considered OC and after the split is EC (Birch, 2003).

2.4.2 NIOSH near real-time DPM monitor

In the standard NIOSH analytical method 5040, the DPM sample is collected at the mine and analysed in the laboratory. This process takes several days to report the results to the mine. Furthermore, this process provides an average EC concentration for a sampling period. The changes in DPM concentration during a vehicle's movements cannot be accounted for and a miner may travel to and from various working sections during the sampling period.

NIOSH developed a portable near real-time DPM monitoring instrument that can measure EC concentration in almost real-time. This instrument can provide EC and TC concentrations with respect to time (Janisko and Noll, 2008). This instrument is an efficient and highly portable real-time elemental carbon/DPM monitor (Airtec, 2019). This instrument works on the principle of real-time particle capture and the light transmission method to yield EC values that correlate closely with NIOSH 5040 measurements of EC (Khan, 2017).

2.4.3 Canadian respirable combustible dust (RCD) sampling method

In the Canadian respirable combustible dust method, a 10 mm nylon cyclone removes the non-respirable portion of airborne dust. This separation is possible when the dust and air are passed through the cyclone at a set flow rate of 1.7 l/m. The centrifugal force produced by the air vortex removes the larger, non-respirable particulates in the dust, while the smaller respirable dust particles are conveyed to the filtration stage by the air stream. The

filter used in this study is a 0.8 μm pore size slice-membrane filter. This system is based on the burning of the combustible principal, carbon-based components of the airborne respirable dust, which are collected on a silver membrane filter. Complete burning of the DPM takes place at a low temperature of 400°C with the catalysing effect of the silver membrane filter. Weighing the filter before and after burning yields the mass of dust burned off in the process. This value is used to estimate the mass of DPM collected (Grenier et al., 2001, Grenier et al., 1998).

2.5 Previous field investigations

NIOSH conducted a detailed DPM field study to quantify the effectiveness of diesel vehicle filters and biodiesel in an isolated underground environment at the Stillwater Mining Company's Nye Mine (Bugarski et al., 2004). Later, the Diesel Emissions Evolution Program (DEEP) carried out a field study at the Noranda Inc. Brunswick Mine to quantify the effectiveness of diesel particulate filters (McGinn et al., 2004). More recently, an experimental study has been carried out by the Missouri University of Science and Technology to understand how diesel particulate matter disperses in underground metal/non-metal mines (Zheng, 2011).

2.5.1 NIOSH field study

NIOSH carried out a field study to assess how effectively DP filter systems could control DPM. This study was carried out by a metal/non-metal diesel partnership formed by NIOSH, the National Mining Association (NMA), the National Stone, Sand and Gravel Association (NSSGA), the United Steel Workers of America (USWA) and the MARG Diesel Coalition (Bugarski et al., 2004). This study took place in a 533 m long-isolated gallery located at the 52E ramp of the Stillwater Mining Company's Nye Mine. The

average width and height of the experimental galleries were 3.6 m and 2.7 m, respectively and the ramp had a 9% rise towards the downstream end.

The experiment took place in two phases. The first phase was to determine the effectiveness of different DP filters and diesel oils in reducing diesel emissions by using an 'isolated zone' methodology. The second phase was to assess the diesel particulate filter's ability to control underground miners' exposure in actual production scenarios.

For this experiment, two trucks and three load haul dumpers (LHDs) were used. The major alterations to the vehicles consisted of removing the oxidation catalytic converters to establish engine baseline emissions and installing diesel particulate filter (DPF) systems. In this study, the DPF systems tested were Engelhard DPX, DCL MineX, Clean Air System, DCL Blue Sky, Mac's Mining Repair/Donaldson P604516 and ECS Cattrap and Biodiesel (Bugarski et al., 2004).

The vehicles tested were operated over the simulated duty cycles between the upstream and downstream points. Three sampling stations were selected 91 m upstream of the load/dump point, 137 m downstream of the load/dump point and on the vehicle itself, as shown in **Fig. 2.3**. The duty cycle for trucks simulated the loading and tramming of a full load of ore. The cycle starts at the upstream dumping point by hauling a full box of ore up the ramp to the loading point and then the operator simulated a loading cycle by repositioning the trucks for loading by an imaginary LHD and then tramming down the ramp towards the dumping point to complete the loading cycle. At the dumping point, the operator simulated unloading the box by engaging the hydraulics and loading the engine. The duty cycle for the LHDs simulated collecting ore from a stope and loading it onto trucks, as shown in **Fig. 2.3**. The cycle starts at the upstream load/dump point with a full bucket of ore. The operator unloads the bucket and retreats for the length of the vehicle

and then advances and loads the bucket again. The next step is to reverse the vehicle out of the stope and advance two vehicle lengths up to the ramp. The operator then engages the hydraulics to simulate the loading of an imaginary truck and then reverses the vehicle back to the starting point. These loading operations are repeated three times. After the third execution, the loaded LHD trams up to the ramp at the downstream load/dump point. The LHDs then execute three load/dump tasks, similar to those performed at the upstream location. At the end of the load/dump session at the downstream point, the vehicle trams a load down the ramp to the upstream starting point to complete the cycle.

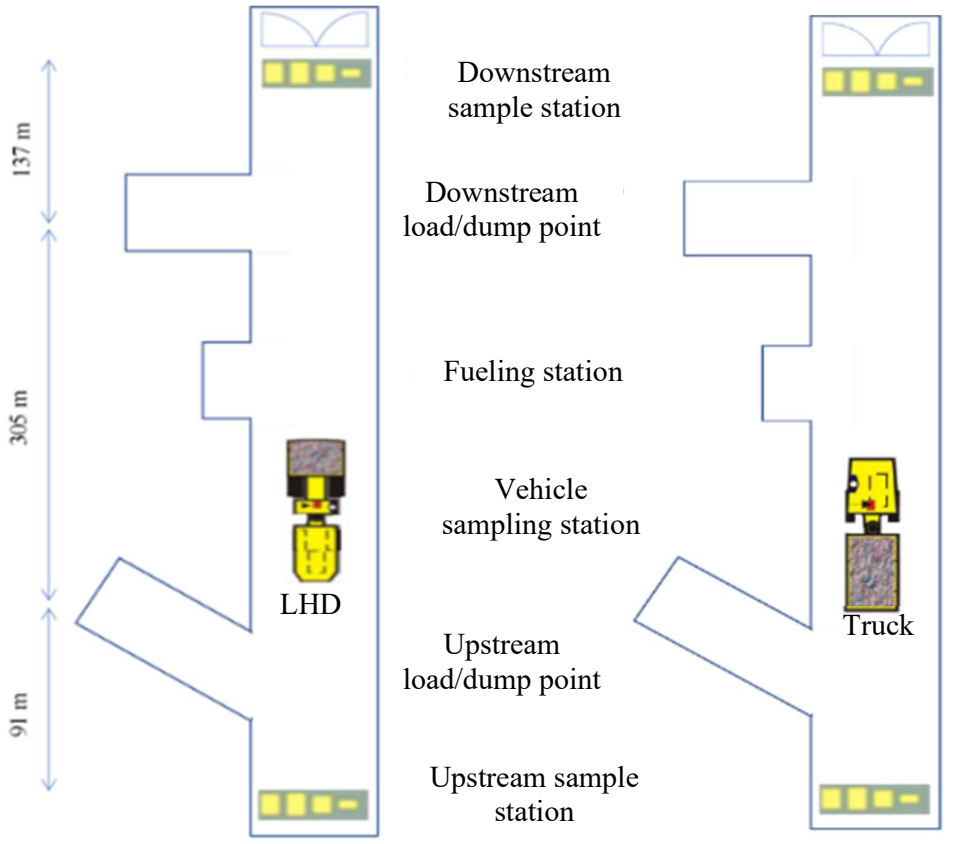

a. Duty cycle for LHD

b. Duty cycle for Truck

Fig. 2.3 NIOSH test duty cycle for the LHD and truck (Bugarski et al., 2004)

The results of the NIOSH field experiment are shown in **Table 2.2.** The experiment shows that the concentration of elemental carbon rapidly decreased with the use of diesel particulate filters and the concentration of DPM also decreased when biodiesel was used.

Table 2.2 Elemental Carbon results normalised with respect to ventilation rates (Bugarski et al., 2004)

DPF System	Truck/LHD Number	MSHA vent rate (m^3/s)	Elemental Carbon ($\mu g/m^3$)	
			Base Line	After DPF
Engelhard DPX	Truck-92128	5.66	1182	51
Clean Air system/CDT	Truck-92133	5.66	1038	15
Bio-Diesel B20	LHD-92526	4.71	1328	1015
Biodiesel B50/ PTX	LHD-92526	4.71	1328	703
DCL MineX	LHD-99942	7.07	1112	149

2.5.2 The DEEP field study

The Diesel Emissions Evolution Program (DEEP) was conducted to assess the effectiveness of the DPF systems to control DPM and gases (McGinn et al., 2004). This study was conducted at Narannda's Brunswick Mine in Bathurst, Canada. The participants in this study were the Brunswick mine, Natural Resources Canada, Canada Centre for Mineral and Energy Technology (CANMET), National Institute of Occupational Safety and Health (NIOSH), Andreas Mayer of VERT and diesel particulate filter (DPF) system suppliers (McGinn et al., 2004).

Four LHDs of 242 kW capacity and two haulage trucks of 278 kW capacity were used for this study. The tested DPF systems were ECS Catalysed Filter, ECS Octel Filter, DCL

Catalysed/Electric Filter and Ober Land Mangold Octel Filter (McGinn et al., 2004).

The vehicles operated inside the 400 m isolated tested zone as shown in **Fig. 2.4**. The LHD operating cycle started from the intake side. The engine was run for 15 seconds at full torque and with the hydraulics stalled. Later the engine ran at full throttle in neutral and with no load for 15 seconds. These two steps were repeated four times. Later, the vehicle trammed for 400 m to the return side. The return air dump cycle was 30 seconds, run at full throttle with the transmission in neutral and no load on the engine. Finally, the vehicle returned to the intake side. Each vehicle was operated over four hours and for at least eight cycles.

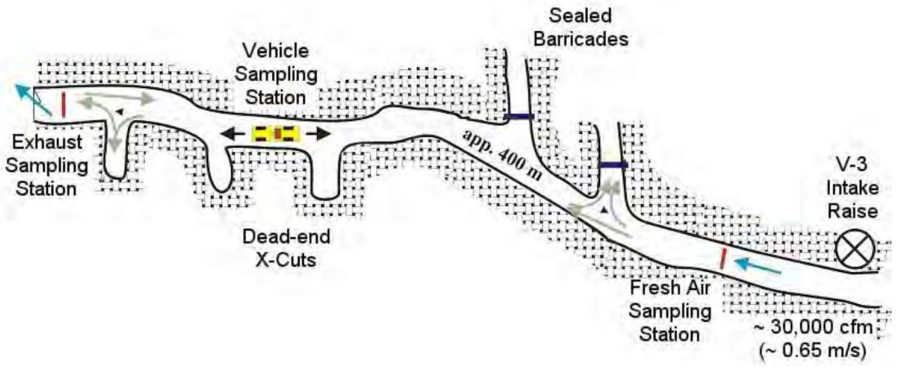

Fig. 2.4 Isolated zone of DEEP field study (McGinn et al., 2004)

A ventilation airflow of 14.15 m^3/s was used for this study. Three sample stations were established to monitor DPM: (1) at the intake side, (2) at the operator cabin and (3) at the return air side. Five samples of DPM were collected from each station. The researchers concluded that the concentration of DPM in the fresh air sample station was very low. There was a slightly higher concentration of TC recorded at the exhaust sampling station than near the vehicle. **Fig. 2.5** shows the results of TC and EC at the return side of the sampling station.

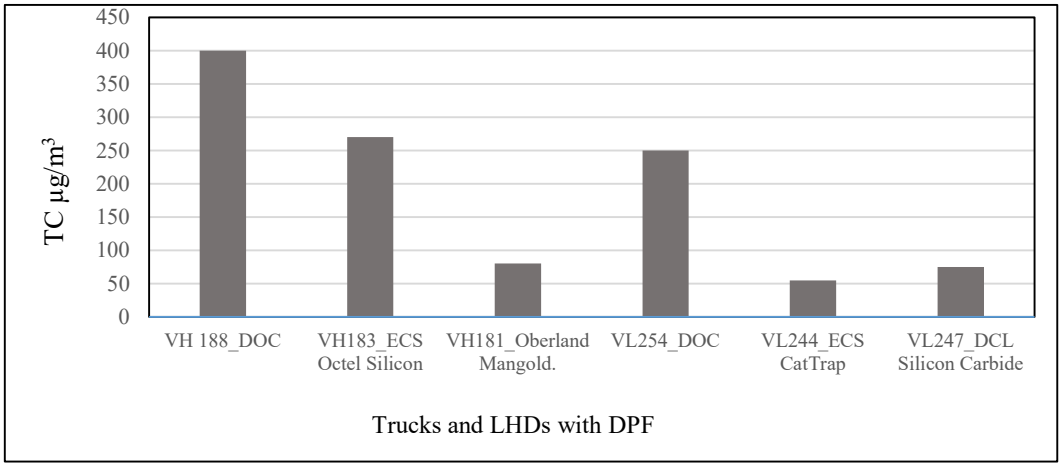

a. Total Carbon

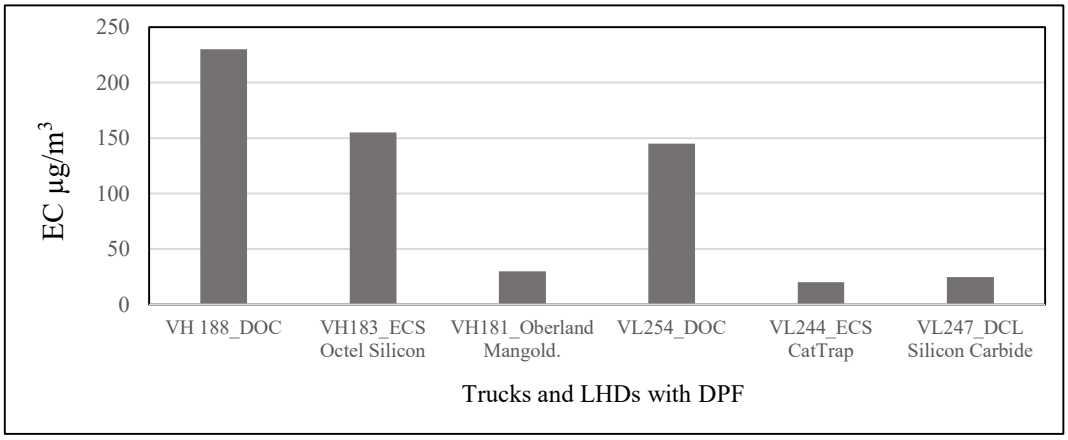

b. Elemental Carbon

Fig. 2.5 TC and EC concentrations for different DPFs (McGinn et al., 2004)

2.5.3 Missouri University of Science and Technology field study

This study was conducted as part of a PhD research at the Missouri University of Science and Technology. This study took place in an experimental mine gallery, utilising a skid-steer loader with a 30 kW engine (Zheng, 2011). The site was ventilated by a Joy axial-flow fan delivering 17.93 m^3/s of airflow. This field study was conducted in two stages: stage-I and stage-II**. Fig. 2.6** shows the location of the experiment in the S&T experimental mine.

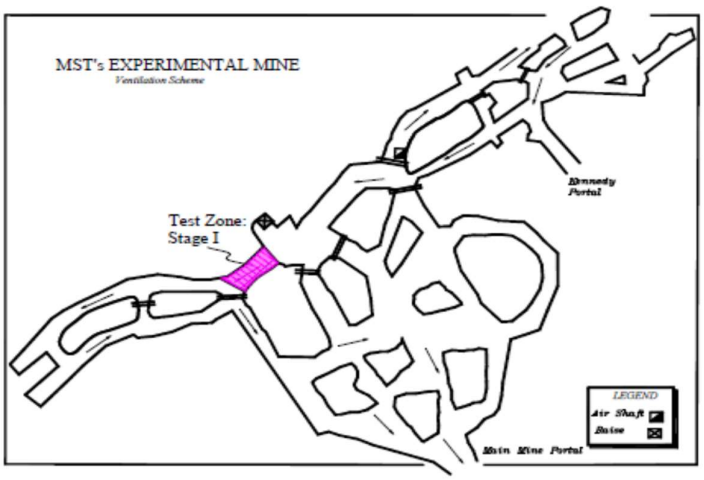

Fig. 2.6 Location of the test zone for stage-I at S&T mine (Zheng 2011)

In stage-I, four sampling stations P1, P2, P3 and P4 were selected at a distance of 0.33 m, 1.14 m, 3.05 m and 4.52 m from the exhaust pipe. The height of sampling stations P1, P2, P3 and P4 were 1.8 m, 1.98 m, 1.66 m and 1.75 m, respectively, from the floor (**Fig. 2.7**). The duration of the sample was 2 hours and five samples were collected from each sample station. For this study, the sample pump rate was increased from 1.7 L/min to 3.4 L/min.

The air velocities for each of the five tests were 0.73 m/s, 0.76 m/s, 0.72 m/s, 0.84 m/s and 0.78 m/s, respectively. The temperature of the tailpipe was 350ºC and the velocity of the exhaust was 14.4 m/s.

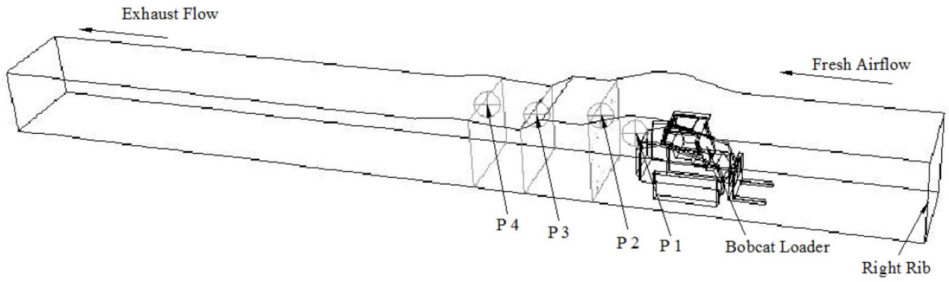

a. Stage-1 Experiment

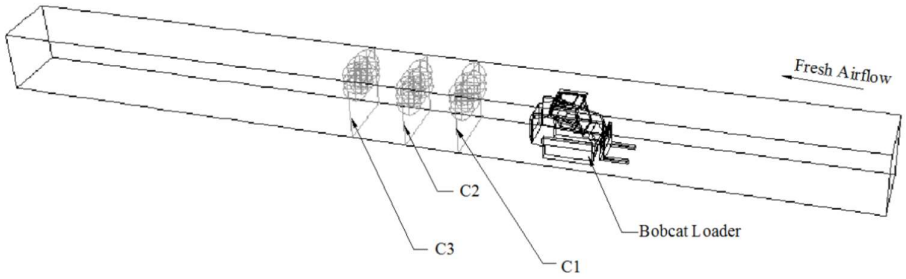

b. Stage-II Experiment

Fig. 2.7 Location of stage-I and stage-II sample stations (Zheng, 2011)

The results of stage-I are shown in **Table 2.3**. The DPM concentration at P1 is high because of the proximity to the exhaust pipe (0.33 m). Due to an instrument error, the concentrations of DPM at station P2 and at Test 2 are not included in this table.

Table 2.3 Stage-I experiment results (Zheng, 2011)

	Test 1 (μg/m^3)	Test 3 (μg/m^3)	Test 4 (μg/m^3)	Test 5 (μg/m^3)
P1	2818.6	2161.8	2436.3	2116.8
P3	500.0	460.8	449.5	451.5
P4	323.0	222.1	216.2	223.5
P5	247.5	204.9	209.8	200.0

In the second stage, DPM was monitored at three sampling groups and each group had nine sampling points. **Table 2.4** shows the results of stage-II experiments. Group-I, Group-II and Group-III samples were collected 0.28 m, 0.47 m and 0.67 m from the exhaust pipe. **Fig. 2.8** shows the DPM modelling results of stage-I and stage-II.

Table 2.4 Stage-II experimental results (Zheng, 2011)

	Group 1 (μg/m^3)			Group 2 (μg/m^3)			Group 3 (μg/m^3)		
	Left	Middle	Right	Left	Middle	Right	Left	Middle	Right
C1top	389.4	562.2	680.3	458.1	554.6	411.5	404.7	630.6	461.9
C1medium	107.5	306.5	232.9	92.4	243.6	217.6	136.1	247.8	171.8
C1bottom	109.9	94.1	127.4	92.1	90.7	87.8	79.7	100.8	74.9
C2top	537.5	264.7	311.5	377.9	183.2	487.9	394.7	244.3	288.6
C2medium	336.7	150.8	240.5	350.5	103.1	208.4	295.5	82.1	235.2
C2bottom	117.6	76.4	109.6	152.3	80.2	133.6	128.3	85.9	120.3
C3top	366.5	208.4	256.5	412.3	223.3	372.6	236.7	233.3	305.4
C3medium	335.9	282.6	366.5	374.1	217.6	236.7	297.8	167.7	290.1
C3bottom	305.4	111.3	274.9	268.8	136.1	268.8	268.8	111.3	226.0

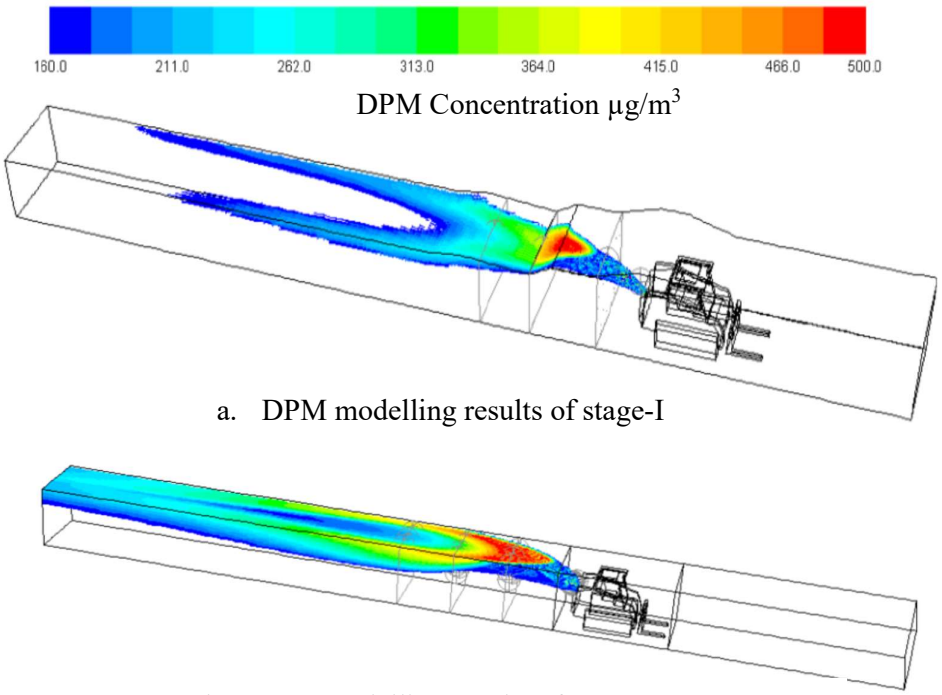

a. DPM modelling results of stage-I

b. DPM modelling results of stage-II

Fig. 2.8 DPM modelling results of stage-I and stage-II (Zheng, 2011)

2.5.4 Recent DPM investigations

The Australian Coal Industry Research Program (ACARP) carried out various investigations to control the DPM concentrations in diesel-powered vehicles. Researchers examined the feasibility of controlling DPM using alternative diesel fuels (Greenwood et al., 2011), ultrasonic transducers with electrostatic perspiration filters (Glynn et al., 2009) and exhaust cooling and scrubbers (Greenwood et al., 2013). Research programs have also investigated underground coal mine usage vehicle standards, statutory implications (O'Beirne et al., 1997, O'Beirne et al., 1996) and vehicle management strategies (Greenwood et al., 2009).

Chang et al. (2019b) carried out research to find the minimum distance required for a ventilation duct from the working face. They concluded that the secondary ventilation

ducts need to extend 10.2 m from the face for better DPM dilution. Chang et al. (2020) carried out research investigations to find high-concentration DPM regions in an LHD face and developed control strategies with optimising auxiliary ventilation design. Tan et al. (2020) conducted research studies to control DPM through the extended filtration model based on the DPM morphology for the DPF.

2.6 Rationale for PhD research

Adequate field experimental data is not available to model DPM in the underground mine environment. During NIOSH and DEEP DPM field-monitoring studies, DPM was monitored at a single sampling station for a period of time. This data was not enough to validate CFD models. The Missouri University of Science and Technology field experiments were conducted with a 30 kW diesel-powered vehicle and measurements were taken within the vehicle's 5 m downstream side. At this location, the flow was very turbulent and the measured data was not enough to validate the models. Also, all the DPM field studies took place in metal/non-metal mines; none of the field trials were carried out in coal mines. This calls for investigations in coal and metal mines because coal mines' geological and operating conditions are completely different from metal/non-metal mines.

Limited DPM modelling investigations are available. Though the basic DPM distribution modelling studies have been carried out in S&T metal and non-metal mines (Zheng, 2011), DPM particles had accumulated in the upper part of the roadway, whereas in reality DPM accumulates over the entire roadway due to the turbulent airflow.

Limited DPM control strategies are available. ACARP and all other investigations focused mainly on controlling DPM within the vehicles. A limited number of research

investigations were carried out to control DPM in the underground environment. None of these research investigations took place to extensively monitor the DPM in underground mines to map realistic DPM flow patterns to control DPM in mines.

2.7 Summary

DPM is one of the components of diesel engine exhausts which are primarily made up of carbon and other metallic abrasive particles, sulphates and silicates. DPM particles vary from 1 nm to 100 nm in size, with a mean size of 10 nm. The density of diesel particulate depends on particle size, which varies from 0.3 g/cm^3 to 1.2 g/cm^3. DPM is a fine carbon particle that can penetrate deep into human lungs, causing serious health risks. Mining authorities in Australia have identified DPM as a Category-1 human carcinogen and the International Agency for Research on Cancer (IARC) has listed DPM as a Group-1 human carcinogen. Nations follow different exposure levels and ventilation rates to dilute DPM. An exposure standard of 100 µg/m^3 of elemental carbon is acceptable for an 8-hour time-weighted average level in Australia.

Limited DPM monitoring data is available in the open literature. In the NIOSH and DEEP field studies, measured data was collected from a single sampling station. This is not sufficient to validate CFD models; sampling data was also collected 500 m downstream from a working engine, but it was still not enough to deduce the particle flow pattern and develop DPM control strategies near a diesel engine.

In the S&T experimental minefield study, the data collected was within 5 m from the diesel engine, where the airflow was very turbulent. The vehicle used for this experiment was a low-capacity (30 kW) engine skid-steer loader. Underground mines use very high capacity diesel-powered vehicles such as 567 kW trucks and 306 kW loaders, etc. This

data may not be enough to validate CFD models and deduce the effect of the vehicles on the particle flow pattern downstream. Furthermore, in both stages, samples were collected from approximately 1.5 m above ground level. DPM concentrations near floor level were not considered.

Limited DPM modelling data is available in the literature. Basic DPM distribution modelling studies in S&T metal and non-metal mines (Zheng, 2011) showed that DPM particles had accumulated in the upper part of the roadway, as shown in **Fig. 2.8**. However, in reality, DPM had accumulated over the entire roadway due to the turbulent airflow**.**

Limited DPM control investigations are available in the literature. The reported DPM control studies focused mainly on controlling DPM within vehicles. None of the research investigations had been carried out to control DPM in an underground environment.

To control DPM concentration in the underground mine environment and to improve personnel health and safety, accurate DPM concentration contours are required. To model DPM flow concentration contours at different ventilation and operational conditions, extensive field-monitoring data is needed. The following chapters will address this research gap.

Chapter 3

Experimental Investigations

This chapter describes the DPM field-monitoring investigations carried out in coal and metal mines. To fulfil the research objective, six stages of DPM monitoring investigations took place in a coal mine and two-staged studies took place in a metal mine. For the field studies, diesel-powered vehicles such as man-riding vehicles, LHDs, trucks and shuttle cars were used. For DPM monitoring, a gravimetric sampler to analyse DPM through the NIOSH 5040 method and Airtec real-time DPM monitor were used.

Geological and operational conditions in coal mines differ from metal mines; roadways in metal mines are wider and higher than coal mines (Woodruff, 2016). Since the conditions in coal and metal mines are different, field experiments were carried out in coal mines and metal mines. Coal mine experiments took place in the Jhanjra coal mine, India, where diesel-powered LHD, shuttle cars and man-riding vehicles are used. The metal mine experiments took place at a copper mine in Australia. Underground mining and operations conditions of Indian and Australian mines are the same. This chapter describes the field experiments in both mines. **Table 3.1** shows the commonly used diesel-powered vehicles in underground coal and metal/nonmetal mines (Matsui, 2009, Bugarski et al., 2012b, Rawlins, 2006, Davies, 2002).

Table 3.1 Commonly used diesel-powered vehicles in underground mines

Sr. No.	Commonly used diesel-powered vehicles in underground mines	Engine capacity
1	LHD	150 kW and 306 kW
2	Man-riding vehicle	150 kW
3	Shuttle car	200 kW
4	Diesel locomotives	76 kW and 225 kW
5	Trucks	485 kW and 567 kW
6	Drill machines	115 kW
7	Cable bolters	110 kW
8	Long hole drill	115 kW
9	Agitator	170 kW
10	Integrated telehandler	75 kW
11	Store truck	140 kW
12	Light vehicle	100 kW and 150 kW
13	Forklift	25 kW

3.1 Field experiments in a coal mine

The Jhanjra mine is one of India's biggest underground coal mines and is owned by the Coal India Company limited (Khera and Prasad, 1991). **Fig. 3.1** shows the location of the experimental area in the mine layout. The mine has eight working seams with two board and pillar depillaring panels, one longwall panel and a few development sections. The gradient of the experimental seam varies from 1 in 16 to 1 in 22 and the 'gassiness' of the seam was 'degree one'. The working sections were from 150 m to 400 m deep. Overall production at this mine is 3.5 million tonnes per annum, with a 3,100-person workforce. To eliminate the noxious effects of diesel fumes in the intake air, field experiments were

carried out in an isolated gallery close to the intake airshaft, as shown in **Fig. 3.1**. The mine has five intakes and two return air shafts and the ventilation system is operated by two axial-flow surface fans. Fan A operates at an airflow of 150 m^3/s at 510 Pa pressure and Fan B operates at an airflow of 140 m^3/s at 400 Pa pressure.

The mine has a man transport intake shaft from the surface that is 5 m in diameter and 150 m deep. The distance from the bottom of the winding shaft to the working section is about 4 km. The mine operators use diesel-powered man-riding vehicles to travel this distance. The mine also uses five diesel-powered load haul dumpers (LHD) and two diesel-powered shuttle cars. **Fig. 3.2** shows the vehicles used in the coal mine. **Fig. 3.2a** shows a typical 150 kW diesel-powered man-riding vehicle that can carry up to 16 passengers at a maximum speed of 25 km/h. **Fig. 3.2b** shows a typical 150 kW diesel-powered LHD; they are used to carry materials and loads of coal and rock (Ridley and Corke, 2003). **Fig. 3.2c** shows a typical 200 kW diesel-powered shuttle car; it has a 15-tonne capacity bucket with a 10 m^3 payload capacity. It also has a 55 kW traction motor and a 25 kW conveyor motor. These shuttle cars are used to transport coal from the face to the belt conveyor. In this coal mine, field experiments were carried out in the five stages described in the following paragraphs.

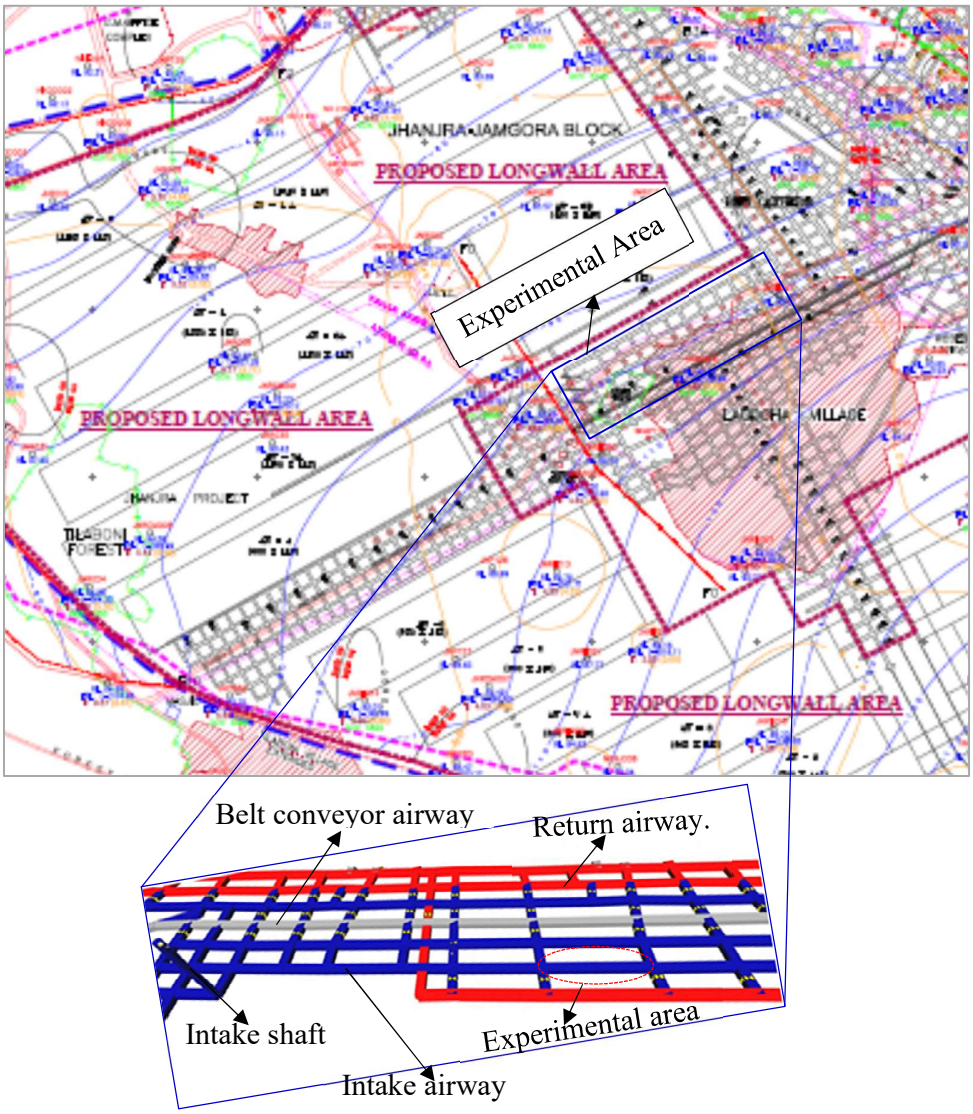

Fig. 3.1 Layout of the mine and location of the experimental area

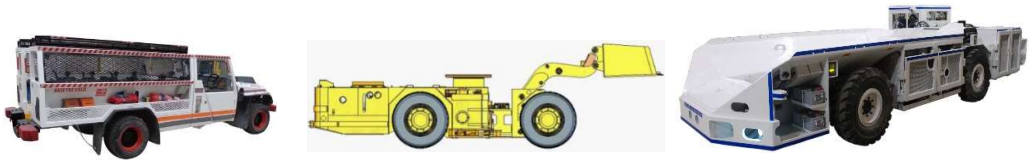

a. Man-riding vehicle b. LHD c. Shuttle car

Fig. 3.2 Diesel-powered vehicles used in the experimental coal mine

3.1.1 Details of instruments

Fig. 3.3 shows the list of instruments used for the field experiments. In the field experiments the air velocity was monitored with a vane anemometer (Howell and Sauer, 1990, Kellerman et al., 2002, KHERA and PRASAD, 1991, Rudow and Klawans, 1974) and then cross-checked against spot measurements with Kestrel. A real-time DPM monitoring instrument (Airtec, 2019) was used to monitor the DPM. **Fig. 3.3** shows the Airtec real-time DPM monitoring instrument. A gravimetric DPM sampler was also used to find the DPM concentration with the NIOSH 5040 method. The width and height of the roadway were measured with a laser distance-measuring tool (Hoshino and Sato, 1987, Ridley and Corke, 2003).

a. DPM Monitor

b. Prefilter cartridge

c. Filter cassette

d. Anemometer

e. Kestrel

f. Laser Measurer

Fig. 3.3 Instruments used for field experiments

3.1.2 Stage-I field experiments with man-riding vehicle

A stage-I field experiment with a man-riding vehicle was carried out near the intake air shaft shown in **Fig. 3.1**. During this stage, three sampling stations located 1 m, 5 m and 10 m downstream of the vehicle were selected. Each station had three sampling points located 1.2 m from the floor. These sampling stations covered the cross-section of the gallery at the downstream side of the roadway. During this experiment, the flow rate of the DPM monitoring instrument was set at 2.83 x 10^{-5} m^3/s (1.7 litres per minute). The average air velocity in the experimental drive was 1.26 m/s. **Fig. 3.4** shows the locations and arrangements of the sampling stations and sampling points (a, b and c) at the rear of the man-riding vehicle.

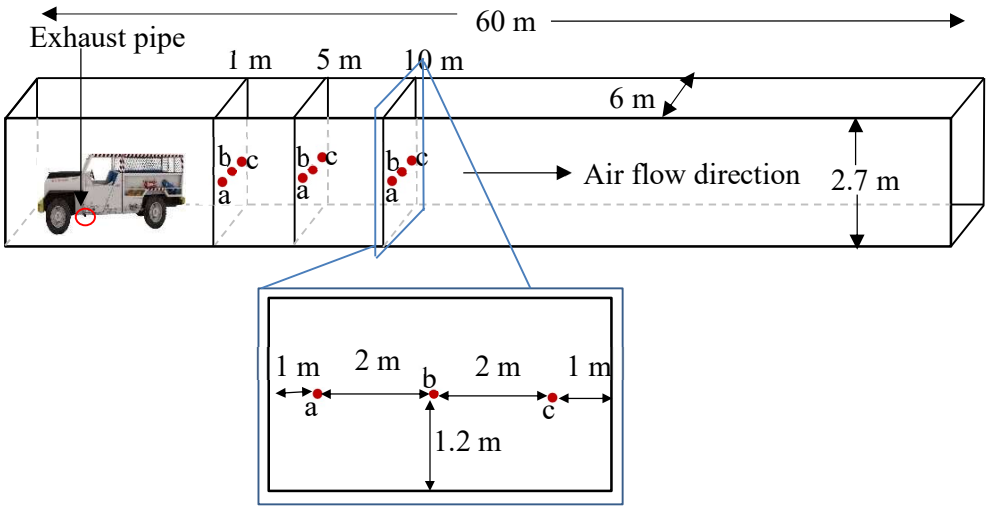

Fig. 3.4 Locations of sampling stations and points from DPM source (vehicle)

Table 3.2 shows the concentration of DPM measured at the three sampling stations. Note that 1 m downstream of the vehicle, the high concentration of DPM was at point 'a' and at sample point 'b' the DPM concentration gradually increased from 1 m to 10 m on the downstream side of the vehicle.

Table 3.2 Results of stage-I field experiment

At 1 m behind the vehicle		At 5 m behind the vehicle		At 10 m behind the vehicle	
Sampling point	DPM concentration ($\mu g/m^3$)	Sampling point	DPM concentration ($\mu g/m^3$)	Sampling point	DPM concentration ($\mu g/m^3$)
a	185.8	a	149.0	a	127.4
b	50	b	117	b	116.6
c	0	c	16	c	50.0

3.1.3 Stage-II field experiments with man-riding vehicle

The stage-II experiment was carried out on a man-riding vehicle with open sides so that the air and diesel fumes could flow through the passenger side area (**Fig. 3.2**a). The DPM concentration was measured in the passenger area with the vehicle in motion. The vehicle travelled up and down the dips from the bottom of the shaft to the working area (4 km). When the vehicle travelled up the dip, the engine ran at full capacity and emitted a maximum amount of fumes. The DPM was measured as the vehicle, carrying ten passengers, travelled from the bottom of the shaft to the continuous miner working area, a distance of 4 km. On level ground, the vehicle could travel at a maximum speed of 25 km/h and at a maximum speed of 18 km/h on a 1 in 7 gradient. During this experiment, the vehicle travelled at an average speed of 10 km/h (2.7 m/s). The velocity of air on the road varied from 1 m/s to 2.5 m/s.

Fig. 3.5 shows the concentration of DPM as a function of time over the 25-minute trip (4 km travel distance). This concentration changed as the relative velocity between the vehicle and the air changed. The vehicle continuously accelerated or decelerated as it travelled, going uphill or downhill depending on the gradients in the roadway. The air

velocities also changed due to the addition of intake airflow from the mains and/or when the airflow was directed towards development, depillaring and old workings.

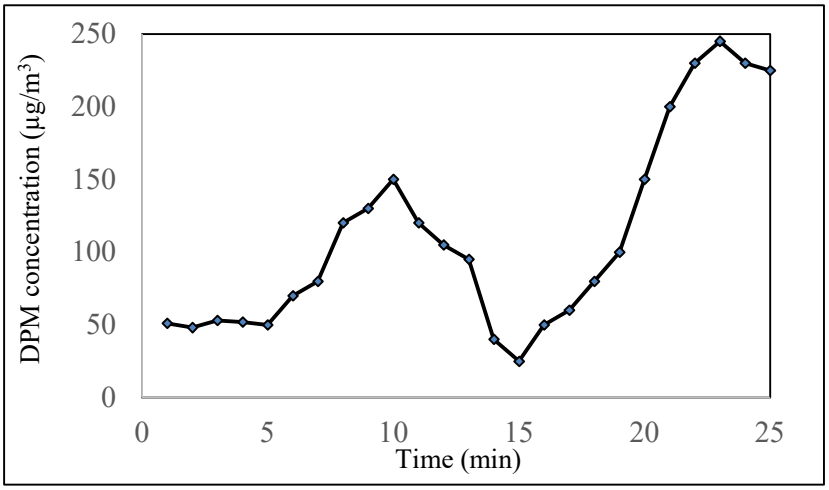

Fig. 3.5 DPM concentration at passenger seat (moving vehicle)

3.1.4 Stage-III field experiments with LHD

The stage-III experiment was carried out with samples of DPM collected from behind the LHD. In this stage the LHD exhaust fumes flowing from the exhaust pipe and intake air travelled in the same direction (co-flow). **Fig. 3.6** shows the LHD and sampling stations. Each station had nine sampling points placed in three rows (top, centre and bottom) and three columns (left, middle and right). **Fig. 3.7** shows the sampling points in the mine gallery. During this experiment, the flow rate of the DPM instrument was set at 2.83 x 10-5 m^3/s (1.7 litres per minute). The air velocity during this experiment was 2.0 m/s. **Table 3.3** shows the results of stage-III field experiments. In this table, DPM concentration at some of the sampling points was not included due to the instrument error.

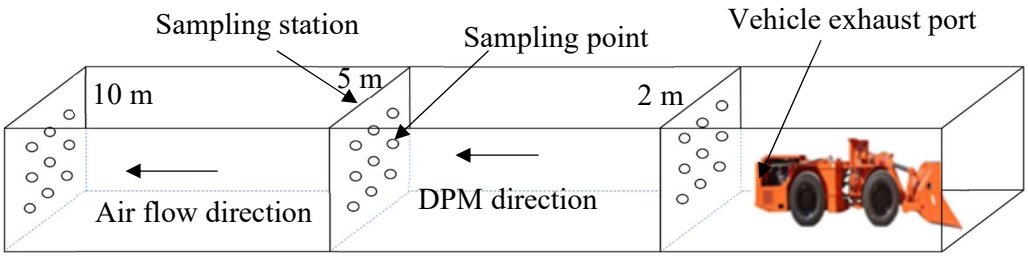

Fig. 3.6 Location of sampling stations and points in the experimental gallery

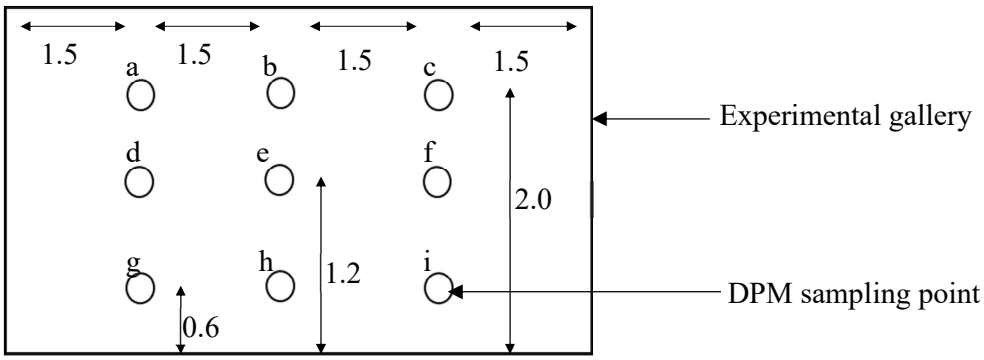

Fig. 3.7 Sampling point arrangement at a sampling station

Table 3.3 Results of stage-III field experiment

Sampling point	DPM	Sampling point	DPM	Sampling point	DPM
DPM concentration at 2 m sample station (μg/m^3)					
a	–	d	62	g	–
b	–	e	127	h	97
c	–	f	64	i	32
DPM concentration at 5 m sample station (μg/m^3)					
a	–	d	64	g	32
b	33	e	95	h	64
c	31	f	68	i	32
DPM concentration at 10 m sample station (μg/m^3)					
a	–	d	64	g	–
b	61	e	95	h	29
c	–	f	–	i	41

3.1.5 Stage-IV field experiments with LHD

The stage-IV field experiments also took place with the fume source located on an LHD. In this stage, samples of DPM were collected on the downstream side of the LHD. In this instance, the direction of the exhaust pipe was opposite to the airflow (counter-flow). DPM samples were collected around the LHD and 6 m, 10 m and 20 m downstream from it, at a height of 1.2 m from the floor. Three samples were collected at the 6 m station and one sample from the middle of the roadway at every 10 m and 20 m station. The air velocity during this experiment was 2.0 m/s. **Fig. 3.8** and **Table 3.4** show the location of the sampling points and the results, respectively.

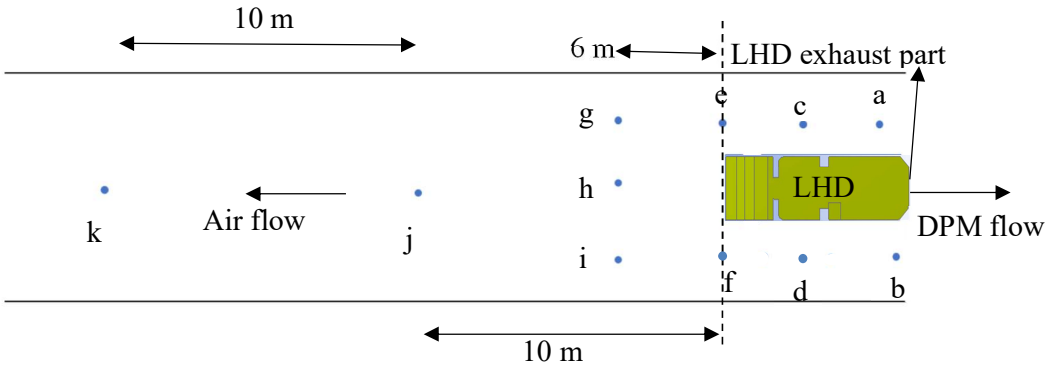

Fig. 3.8 Sampling stations and sampling points in the experimental gallery

Table 3.4 Results of stage-IV field experiment

Sampling point	DPM concentration ($\mu g/m^3$)	Sampling point	DPM concentration ($\mu g/m^3$)
a	281.4	g	14.2
b	70.0	h	42.7
c	56.5	i	28.5
d	55.8	j	42.8
e	42.5	k	37.3
f	27.8		

3.1.6 Stage-V field experiments with LHD

In stage-V experiment, the DPM particles in the dead-end gallery were analysed. This experiment took place in one of the longwall cut-throughs, as shown in **Fig. 3.9**. This cut-through is located between the belt drive and the intake drive and is separated by a ventilation wall. In this case, the DPM particles (exhaust) filled the dead-end gallery/cut-through where the LHD was located. After removing the LHD from that gallery, the concentration of DPM was measured for five minutes and was repeated three times. **Fig. 3.10** shows the location of sample point 10 m from the main ventilation gallery in the plan view. The initial DPM reading was 820 $\mu g/m^3$ and the dispersion of DPM was measured by the real-time monitoring instruments for 5 minutes. During this experiment, the air velocity in the gallery adjacent to the dead-end gallery was 2.52 m/s.

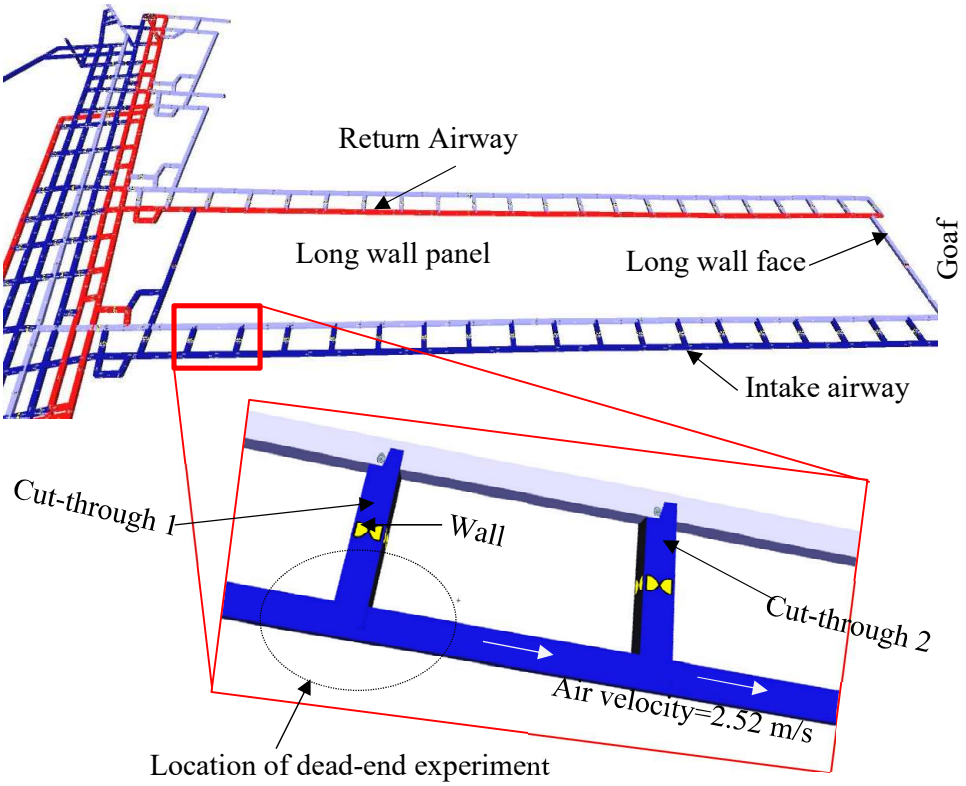

Fig. 3.9 Longwall working dead-end cut-through, experimental location

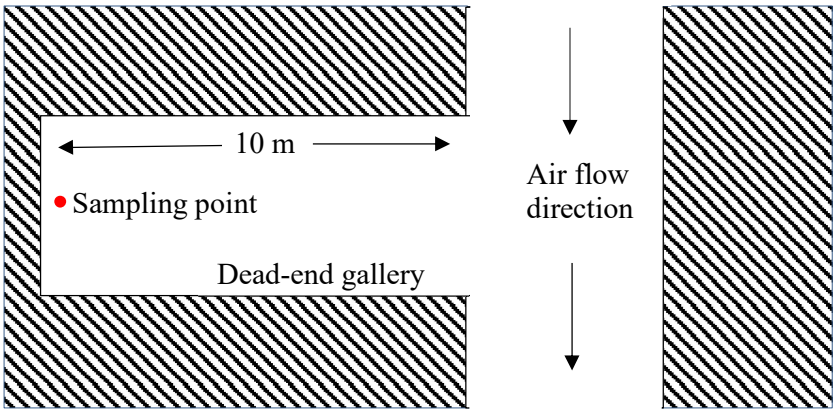

Fig. 3.10 Details of stage-V dead-end gallery experiment

Table 3.5 shows the results of the 10 m long dead-end crosscut experiment; it took 5 min for the DPM concentration to decrease from 820 µg/m^3 to 232 µg/m^3.

Table 3.5 Results of stage-V dead-end gallery field experiments

Time (min)	Measured DPM concentration (µg/m^3)			
	Experiment-1	Experiment-2	Experiment-3	Average
0	817	825	819	820
1	550	560	551	554
2	417	425	422	421
3	350	358	352	353
4	284	287	280	284
5	230	235	231	232

3.1.7 Stage-VI field experiments with a shuttle car

The stage-VI experiment was carried out with a diesel-powered shuttle car. Shuttle cars are generally used to haul coal from a continuous miner to the belt conveyor (Burgess-Limerick et al., 2012). They are 9 m long by 3.5 m wide and they operate in narrow underground roadways (4.5–6.2 m). Shuttle cars travel at approximately 10 km/h (maximum), carrying up to 8 tonnes of coal over often very rough roads. The cars have four-wheel steering to provide the manoeuvrability required to turn 90° corners. As the name suggests, these cars 'shuttle' back and forth between the continuous miner machine and the conveyor belt (Burgess–Limerick et al., 2013).

The dispersion of DPM particles in the operating panel of the shuttle car was investigated by collecting an average sample of DPM for two complete cycles of a shuttle car where it is loaded at the depillaring district, unloads the coal at the belt conveyor feeder and returns to the loading point. **Fig. 3.11** shows the location and operation conditions of the shuttle car experiment. In cycle-I, the average concentration of DPM at sample point A is 254.66 µg/m^3 and 206.67 µg/m^3 at sample point B. During Cycle-II, the concentration of

DPM at sample point A is 202.85 µg/m^3 and 187.27 µg/m^3 at sample point B. During these field measurements, the average air velocity in the return airway was 2.63 m/s and the width and height of the main return were 6.37 m and 3.36 m, respectively. DPM concentration at sample point A is higher than sample point B due to lower airflow at sample A than sample B.

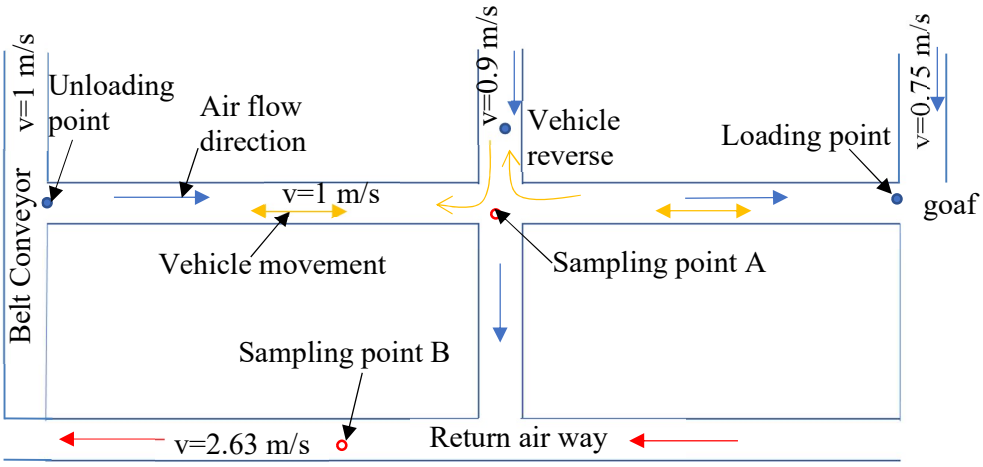

Fig. 3.11 Details of stage-VI shuttle car experiment

3.2 Stage-VII field experiments and DPM monitoring in a metal mine

To monitor the dispersion of DPM in metal mines, experiments were carried out at a copper mine in Australia. This mine is worked by the long hole and bench stoping methods in conjunction with mullock and cemented paste & hydraulic backfill (CPB/CHF) (Sivakugan et al., 2006). These non-entry production methods rely on self-supporting excavations, which means that personnel do not enter any production excavation (Brill, 1989, McQueen, 2006). Reinforcing the production spans is intended to control dilution and local stability prior to a timely placement of backfill, not to support excavations to a standard suitable for personnel entry. This mine does have a shaft and decline for access.

The ventilation system of a mine consists of four 1.35 MW centrifugal fans, which produce 700 m^3/s of air at 4 kPa pressure as an operating condition. About 50 auxiliary fans are used to ventilate the various working sections of the mine. This mine has five discrete ore systems: West, East, Central, South and North. Mineralisation of the mine is hosted in the variably cleaved siltstone, a moderate-to-steep West dipping basal unit of the amphitheatre group. **Fig. 3.12** shows the section of a mine from 1250 m below the surface to a depth of 1800 m. This decline was 1,200 m long with a vertical height of 500 m. This mine has different levels, some of which are active and some inactive.

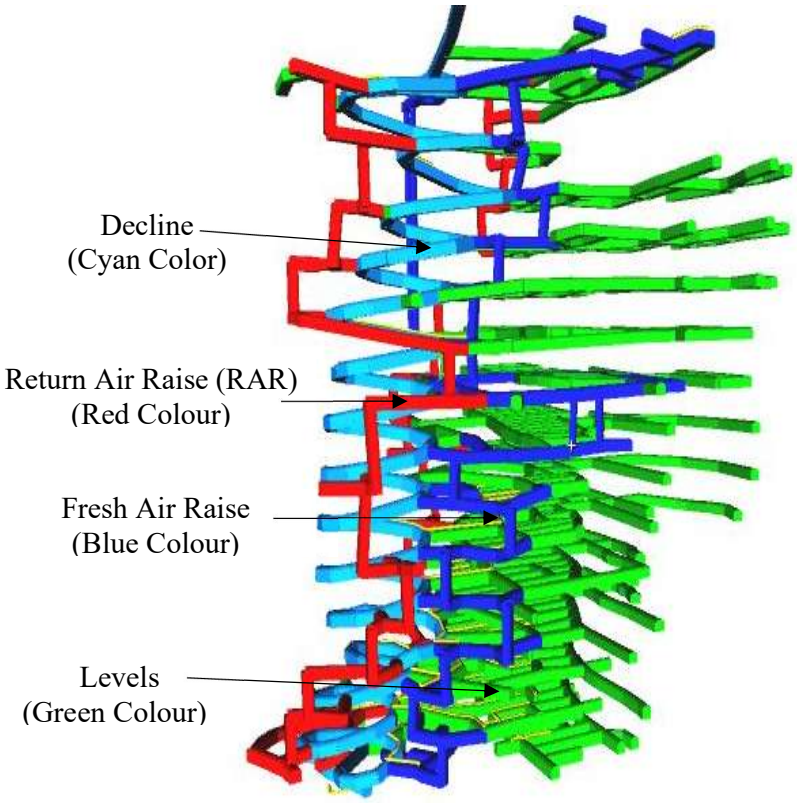

Fig. 3.12 Working sections of the mine

Fig. 3.13 shows a typical level layout of a mine. The figure shows that the level is connected with the decline through the level access and the footwall drive is also connected with the level access. Different crosscuts developed from the footwall drive

and footwall are also connected to the return air raise (RAR) system. The level is also connected with the fresh air raise (FAR) system, which supplies fresh air to the underground levels (McPherson, 1993). Air from the fresh air raise system to different crosscuts of the level are supplied through ventilation bags that are connected to a secondary fan (Hartman et al., 2012). The FAR connection with the level is closed by the wall and at the secondary fans. The return air raise connected to the decline is closed by a wall fitted with a drop board regulator (DBR) to draw some of the decline air. Some of the fresh air comes to decline from the levels.(Baer, 1997, Georgaras, 1999).

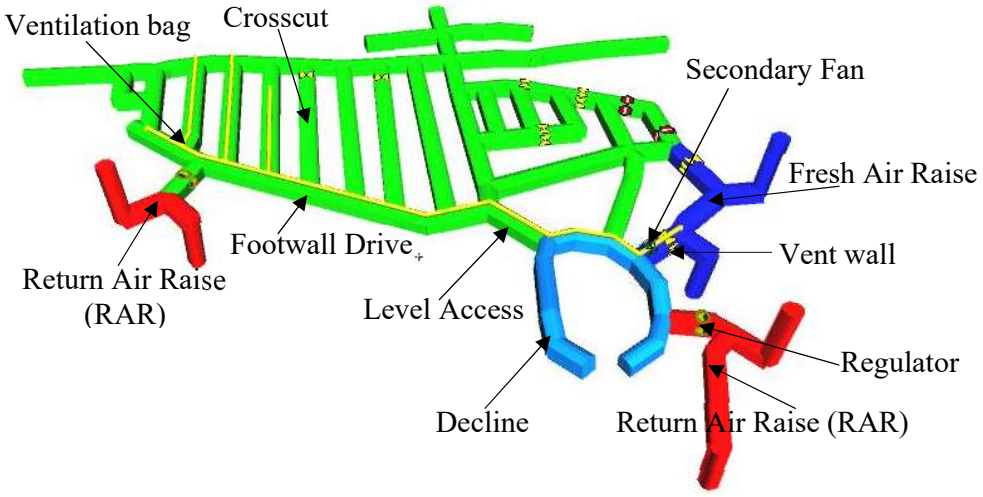

Fig. 3.13 A typical metal mine level layout

The hybrid ventilation method (McPherson, 1993, McPherson, 2012) is commonly used for secondary ventilation at this mine; this is where the forced ventilation system is connected in a tight circuit with a fresh air raise, as shown in **Fig. 3.14**. Ventsim models in **Fig. 3.12**, **Fig. 3.13** and **Fig. 3.14** were developed as a part of this research.

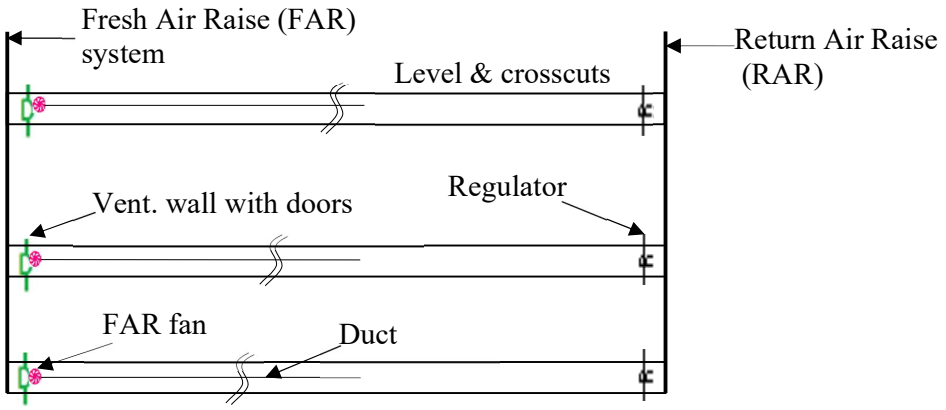

Fig. 3.14 Fresh air raise secondary fan ventilation system (McPherson, 2012)

3.2.1 Field experiment in metal mine decline

DPM measurements were taken at various locations along with the decline, at vertical height intervals of 50 m after collecting each sample over 15 minutes. During the measurements, an average of eight trucks were moving in the decline, some were moving upwards and some were moving down the decline. At the same time, other diesel-powered vehicles such as loaders, light vehicles and agitators and graders were also moving in the decline. **Fig. 3.15** shows the DPM monitoring stations in the decline. The average airflow in decline changed with the locations shown in the figure due to fresh air coming from the levels and return air moving through the decline RAR system. **Table 3.6** shows the DPM monitoring readings over the decline.

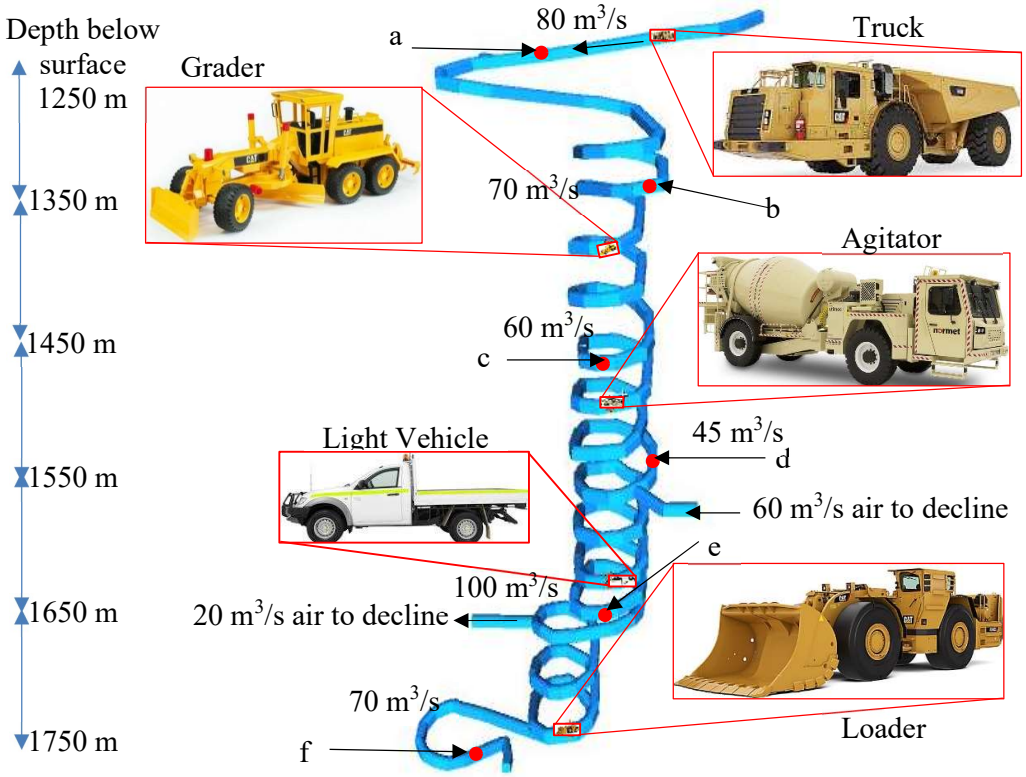

Fig. 3.15 DPM measured locations in decline

Table 3.6 Results of stage-VII decline DPM measurements

Sample station	Depth of the sample below surface (m)	Air quantity near sample station (m^3/s)	DPM concentration ($\mu g/m^3$)
a	1250	80	51
b	1350	70	58
c	1450	60	65
d	1550	45	85
e	1650	100	45
f	1750	70	32
Average		70	56

3.2.2 Stage-VIII personnel DPM monitoring

In this stage the time-weighted average concentration exposure of different occupational personnel to DPM was measured over a 12-hour shift. The DPM was collected in filters and then sent for analysis. During analysis DPM was measured through the NIOSH analytical method 5040. The standard limit for occupational exposure for a 12-hour shift is 94 $\mu g/m^3$ (section 2.3.1 of Chapter 2) and the flow rate of the diesel particulate filter is 2.51 l/min. The DPM monitoring instrument was fixed on each operator, and the air inlet section of the instrument was attached near the shirt pocket.

Table 3.7 shows the level of exposure to DPM for underground personnel over a 12-hour shift; the table shows that these levels of exposure are within the statutory limit. The 12-hour time-weighted average concentration of DPM is different from the average value over a short time because it includes travel time, working time, crib time and rest time. All the vehicles in the mine have closed cabins fitted with air conditioning. The table shows that the DPM exposure levels of operators are very low (within the statutory limit).

Table 3.7 Measured DPM exposure levels of different underground personnel

Sample No.	Sample Exposure Group	Sample Duration (min)	Air Volume (m^3)	DPM as EC (µg/filter)	DPM as EC (µg/m^3)	DPM as TC (µg/filter)	DPM as TC (µg/m^3)
1	Electrical maintenance	730	1.8	66	3.6	160	90
2	Shotcrete operator	722	1.8	3	1.7	47	27
3	Cable bolter operator	759	1.9	14	7.1	95	50
4	Truck operator	740	1.9	21	11	110	61
5	Crusher operator	699	1.8	3	1.9	47	27
6	Boiler maker	713	1.8	16	9.0	76	43
7	Loader operator	719	1.8	7	3.8	68	38
8	Service crew	603	1.5	35	2.3	140	89
9	Production driller	703	1.8	15	8.2	74	42

3.3 Summary

Field experiments were carried out in coal and metal mines. The field experiments in the coal mine were carried out in six stages using a man-riding vehicle (150 kW), LHD (150 kW) and shuttle car (200 kW). The metal mine DPM monitoring experiments were carried out in a decline and with various occupational groups.

The stage-I DPM field-monitoring experiment was carried out with a stationary man-riding vehicle (150 kW) with an air velocity in the roadway of 1.26 m/s. The field results concluded a high concentration of DPM at the exhaust pipe side of the roadway. At 10 m downstream of the vehicle, DPM particles had spread over the entire cross-section of the

roadway.

The stage-II DPM field-monitoring experiment was carried out with a man-riding vehicle (150 kW), during which the DPM concentration was measured while the vehicle travelled 4 kilometres for 30 minutes. During this measurement, vehicle speed was between 5 km/h to 18 km/h and the air velocity in the gallery was between 1 m/s to 2.5 m/s. The results indicated that while travelling in the man-riding vehicle, miners might also be exposed to high concentrations of DPM of up to 226.8 $\mu g/m^3$.

Stage-III and stage-IV field experiments were carried out with a 150 kW capacity LHD, during which the air velocity in the gallery was 2 m/s. In stage-III, the airflow in the gallery and exhaust fumes flow from the LHD were in the same direction (co-flow). In stage-IV, the airflow in the gallery and exhaust fumes flow from the LHD were in opposite directions (counter-flow). These results indicated that the LHD operator would be exposed to a higher concentration of DPM in counter-flow than co-flow. In co-flow, most of the DPM particles flow in the middle of the roadway, whereas in counter-flow the particles spread right across the roadway section.

The stage-V field experiment was conducted in an unventilated dead-end cut-through of a longwall panel. The air velocity in the gallery adjacent to the dead-end cut-through was 2.52 m/s. Initially, a DPM concentration of 820 $\mu g/m^3$ filled the 10 m long cut-through using LHD. This experiment showed that it took a long time for the DPM particles to dilute in the airflow-restricted zones: in the 10 m long dead-end crosscut it took 5 min for the DPM concentration to decrease from 820 $\mu g/m^3$ to 232 $\mu g/m^3$.

The stage-VI field investigation was carried out with a shuttle car (200 kW) where the air velocity in the panel return airway was 2.63 m/s. DPM concentration was monitored in two complete shuttle car cycles. In each cycle, the shuttle car was loaded with coal at the

loading point, unloaded at the belt conveyor feeder and then returned to the loading point. The results indicated that the average DPM concentration of two shuttle car cycles in the panel's return airway was 254.66 $\mu g/m^3$. It was recommended that personnel should not be exposed to the shuttle car panel's return sides due to the high levels of DPM concentration.

In stage-VII the DPM concentration was monitored in a metal mine decline at five sampling points spaced 100 m apart in the decline. During these measurements, trucks (567 kW), graders (101 kW), agitators (170 kW), light vehicles (110 kW) and LHDs (306 kW) were moving in the decline so the volume of air in the decline varied from 45 m^3/s to 100 m^3/s. At each sample station the DPM was measured for 15 min. The monitoring results concluded that the DPM concentration in the decline depended mainly on the number of vehicle movements and volume of air. The maximum 15 min time-weighted average of DPM in the decline was 85 $\mu g/m^3$ and the average concentration of DPM in the decline was 56 $\mu g/m^3$.

In stage-VIII the time-weighted average exposure of different occupational personnel to DPM concentration was measured over a 12-hour shift. The results indicated that the exposure levels of DPM concentration do not depend on personnel occupations; in fact, the levels of exposure to DPM for underground personnel over a 12-hour shift are within the statutory limits.

Field experiments provided a great deal of information about the distribution of DPM with different vehicles and different operational conditions; these results were used to validate the CFD models in Chapter 4.

Chapter 4

DPM Modelling Methodology and Validation

After completing the extensive DPM field-monitoring investigations described in Chapter 3, a literature review was carried out to find an optimum modelling tool to simulate DPM in an underground environment. This chapter describes different underground environment modelling packages, CFD modelling, previous underground CFD modelling studies and governing equations. It also describes the development of base case CFD and Ventsim models and the related topics of meshing, model setup and model validation using experimental data.

4.1 Existing underground mine environment modelling

Underground mines commonly use Ventsim software (Ventsim, 2019) to simulate underground mine ventilation networks (Widzyk–Capehart and Fawcett, 2001, Maleki et al., 2018, Widzyk–Capehart and Watson, 2001). This software simulates ventilation, heat, fires and other contaminants such as DPM, dust and gas, etc. For example, Habibi et al. (2015) and Smoorenburg et al. (2021) used Ventsim to model heat flow in underground coal mines. Brake (2013) used it to model fire in underground mines and Moreby (2019) used it to model low-pressure gas drainage and high-pressure nitrogen reticulation systems. Ventsim can be used to simulate a complete underground mine ventilation system. In this thesis it was used to simulate DPM in a 5 km long decline.

Ventsim works on the principle of the Hardy–Cross numerical model (Cross, 1936), where a combination of nodes and branches represents the airways of a mine. The main inputs for the numerical model are branch resistance and fan characteristics, which are calculated in terms of airflow quantity and pressure drop between nodes using Atkinson's

equations (Cross, 1936). The Hardy–Cross method aims to find air quality in the ventilation circuit and estimate the flow intensity error in the ventilation circuit (Cross, 1936). This model was further modified by Wang (Sereshki et al., 2016). The following equations are used in Ventsim:

$$Q = Q_a + \Delta \quad \textbf{(4-1)}$$

$$\Delta = -\frac{\sum \pm R_i {Q_i}^2}{2\sum R_i Q_i} = -\frac{\sum_{i=1}^{i=n} b_{ki}(R_i |Q_i| Q_i - P_{ni} - P_{Fi})}{2\sum_{i=1}^{i=n} {b_{ki}}^2 R_i |Qi|} \quad \textbf{(4-2)}$$

Where: Δ is the flow intensity error in the loop (m^3/s), Q_a is an assumed quantity, b_{ki} is the fundamental matrix element of the loop, P_{ni} is the increasing pressure due to natural ventilation in the branch, P_{Fi} is the increasing pressure because of an installed fan (forced ventilation) in the branch, R is the branch resistance and Q is the quantity of air. Output from the Hardy–Cross simulator was verified and the results are within ± 5% of the actual measurement, thus validating the simulation. After validating the data, various alternatives were simulated to optimise the ventilation system (Sereshki et al., 2016).

There are many other commercially available ventilation simulation software packages, e.g. VentPC in the USA (Taatjes et al., 2007), VUMA in South Africa (Bluhm et al., 2001), Mivena in Japan (Sasaki and Dindiwe, 2002), etc.

These ventilation network simulators are better at simulating the overall airflow in a whole mine. However, it is difficult to demonstrate the details of 3D DPM mapping/contours in localised areas of an underground mine. In this scenario computational fluid dynamics (CFD) techniques can provide better and more detailed mapping of contaminants in underground mines. CFD modelling and Ventsim simulations are not integrated in this research.

4.2 Previous underground mine CFD modelling studies

Computational fluid dynamics (CFD) is one of the developments of advanced computer-based numerical codes (Anderson and Wendt, 1995), which can scientifically address many typical underground mining problems such as ventilation, gas, dust, spontaneous combustion of coal, mine fires and DPM, etc. These 3D modelling studies will improve our understanding of DPM-related problems at various coal and metal/non-metal mining operating conditions and also help us to design ventilation systems that will improve the safety and productivity of underground mines. Several CFD studies of underground mines are discussed below.

4.2.1 CFD modelling for underground air velocity pattern mapping

CFD techniques have been used to model the airflow patterns in underground mines. Wang et al. (2018) used CFD simulations to model the flow patterns of air, gas and respirable dust particles at a longwall face. They concluded that the air velocity is highest between the face and cable tray and lowest between the shield supports' front and back legs. Ndenguma et al. (2014) used CFD to model the airflow patterns in underground mines to determine the optimum location of the jet fan responsible for diluting contaminant gas at different stages of mining. Hwang and Edwards (2005) used CFD modelling to investigate variances between simulated and measured air velocity patterns. They concluded that the CFD simulations agreed with the experimental data taken from horizontal and inclined tunnels. Toraño et al. (2011) used CFD modelling to design an axial ventilation system in road header workings to dilute dust particles. Yuan (2010) used CFD simulations to map the velocity contours in a longwall face; he mapped the higher and lower air velocity regions of the longwall and concluded that high airflow is close to the cable tray region. Cheng et al., (2016) used CFD modelling to optimise

ventilation to improve mine safety in longwall faces. They modelled ventilation parameters such as the volume of air supplied to the mine working face, the negative ventilation pressure in the roof roadway for gas drainage and the distributed airflow in tailgate. Toraño et al. (2006) used CFD modelling to ventilate dead-end tunnels and galleries. Ramos et al. (2013) used CFD modelling to simulate natural ventilation of underground substations; they analysed the airflow patterns and the air temperature inside the substation, as well as the heat transfer coefficients on the surfaces of the transformer and the walls of the enclosure.

4.2.2 CFD modelling for underground 'sponcom' and fire

CFD modelling was used to simulate spontaneous combustion of coal (sponcom) and/or fire control strategies. Morla (2013), Morla et al. (2013) and Morla et al. (2015) used CFD simulations to investigate blasting gallery panel goaf airflow patterns and options to control spontaneous combustion of coal. They concluded that in a descentional ventilation system, methane moves in the opposite direction to the airflow so that less air flows into the goaf and offers better inertisation. Inertisation from in-bye locations of the goaf region is more effective than inertisation from out-bye locations. Multiple inert gas injection points cover more goaf areas and provide more efficient inertisation than single-point inertisation. Sealing the bottom-most room provides the most effective inertisation. Ren and Balusu (2005) and Tanguturi and Balusu (2018) used CFD modelling to investigate the mitigation of goaf gas and control spontaneous combustion in longwalls. Jojo (2004) used CFD modelling to model fire flow patterns and intensity in tunnels. Khattri et al. (2019) used CFD modelling to investigate the effect that the oxygen in ventilation air had on tunnel fires.

4.2.3 Gas modelling with CFD

CFD modelling was used to model gas flow in underground coal and metal mines. Yuan (2010) used CFD modelling to investigate the ventilation airflow paths in longwall goaf areas to control methane air and the spontaneous combustion of coal. He simulated the velocity flow patterns in the goaf with one-entry, two-entry and three-entry bleeder systems. This modelling considered the airflow in the goaf as laminar and in the gate roads as turbulent. He concluded that there are slightly higher air velocities near the second return entry in a two-entry ventilation system. Similarly, Tanguturi and Balusu (2014) used CFD modelling investigations to control the flow of methane in the rear side of the supports near the tailgate. They concluded that in a longwall top coal caving, curtains near the tailgate rear conveyor motor side of the face supports would control gas flow at the face and behind the conveyor motor region. Guo et al. (2012) investigated the flow of methane from adjacent coal seams of a longwall panel into the goaf using CFD modelling studies. The released methane migrates first through the perimeter of each level of the goaf and then gradually expands to the central area. The goaf area near the perimeter has higher velocities of gas and methane than other parts of the goaf. Zhou et al. (2015a) used CFD modelling to investigate methane flow at a continuous miner face where curtains had been set back at different distances to regulate the concentration of gas near the face. Kiša and Jelemenský (2009) used CFD modelling for emergency-preparedness by mapping the strength of pressurised liquefied ammonia.

4.2.4 DPM modelling using CFD

In recent years CFD modelling has been used to model DPM flow patterns. Chang et al. (2019b) used CFD modelling to investigate the minimum length of ventilation duct from the working face needed to reduce DPM concentration and concluded that at least 10.2 m

would be needed. Zheng (2011) carried out DPM modelling using CFD for his PhD thesis. Zheng et al. (2015b) used CFD modelling with buoyancy effects to model DPM. Zheng et al. (2015a) and Zheng et al. (2015c) used CFD to model DPM in longer headings using an axillary ventilation system and concluded that a push–pull system would dilute DPM in longer headings. Zheng et al. (2017) used CFD modelling to study the effect of roadway inclination on changes in DPM dispersion and concluded that there is less DPM with down-dip workings than up-dip workings. Thiruvengadam et al. (2016b) used CFD to model the dispersion of DPM using both continuous species transport and discrete element transport models and found that, since DPM particles are small, discrete phase modelling and species transport modelling yield very similar results. Thiruvengadam et al. (2016a) used CFD to model DPM dispersion in a single dead-end entry using a dynamic mesh model and concluded that their results would help to develop control strategies.

Xu et al. (2018) used CFD to model the distributions of DPM in isolated workings and found that the simulated outcomes agreed with the experimental data when the DPM was represented as a discrete phase. Locations with a high concentration of DPM were identified.

Chang et al. (2019a) used CFD to model DPM using three modelling methods: (1) the Eulerian–Lagrangian method, (2) the Eulerian–Eulerian method that treats DPM as discrete-phase particles and (3) the species transport method that treats DPM as a continuous phase gas. They concluded that the general concentration of DPM for the three numerical methods was similar in simple geometry but there were large discrepancies in the flow features in a development heading with complex geometry. They suggested that when simulating DPM, although the species transport method can provide relatively accurate results with much less computational time, the modelled gas parameters need to

be carefully calibrated to get a better simulation result. For key areas where diesel machinery and miners are usually located, the Eulerian–Lagrangian method provided more accurate results.

4.2.5 Modelling sub-surface dust with CFD

CFD modelling has been used to examine the spread of dust particles in an underground environment. Liu et al. (2019) used CFD to study the effectiveness of a dust extraction system in tunnel boring machine (TBM) construction tunnels and found that if the dust is extracted at 8 m^3/s, the dust diffuses over the entire working area. If the flow rate is ≤ 8 m^3/s, the dust particles spread over the whole face region and if the flow rate is > 8 m^3/s the full-face dust can be controlled.

Arya and Novak (2020) used CFD modelling to design a novel wet scrubber for an underground coal mine to capture respirable dust particles and found that the innovative wet Vortecone scrubber was more efficient to filter respirable dust particles with little maintenance.

Zhou et al. (2017) used CFD to model respirable diffusion of ducts in a mechanised caving face and found that the respirable dust generated by a back drum rushes into the sidewalk space with turbulence, while the respirable dust from coal caving moves quickly into the sidewalk and pollutes this area. Geng et al. (2017) used CFD to investigate dust dispersion in an underground roadway with a hybrid ventilation system and found that dust particles of varying sizes exhibit different tendencies during dispersion.

From all these research investigations, I concluded that CFD is the perfect tool for modelling the dispersion of DPM in an underground environment.

4.3 Governing equations used for DPM modelling

The following governing equations – mass conservation equation (4-6), momentum equation (4-7), energy equation (4-10) and other auxiliary/supporting equations, were used for DPM modelling studies: (4-3) to (4-26). Ventilation air in an underground mine was considered as a Newtonian and viscous fluid. Diesel exhaust fumes were considered as non-reacting and the temperature of the exhaust fumes was assumed to differ from mine ventilation air and vary with the working conditions.

To determine the nature of ventilated airflow, the Reynolds number (Re) was used:

$$\mathrm{Re} = \frac{\text{Inertial force}}{\text{viscous force}} \text{ or } \frac{\rho\, V\, D}{\mu} \text{ or } \frac{VD}{\nu} \qquad \textbf{(4-3)}$$

Where

V is the velocity of the fluid (m/s)

μ is the dynamic viscosity (N s/m^2) = $\nu\, \rho$

ν is kinematic viscosity (m^2/s)

ρ is density of the fluid (kg/m^3)

D_h is the hydraulic diameter and

If Re is below 2000, then the fluid flow is considered as laminar flow and if Re is more than 4000, its flow is treated as a turbulent flow.

For rectangular underground roadways, the hydraulic diameter is defined as:

$$D_h = 4\,\frac{A}{P} = \frac{4[\mathrm{HW}]}{2[\mathrm{H+W}]} = \frac{2WH}{W+H} \qquad \textbf{(4-4)}$$

Where H is the height of the roadway and W is the width of the roadway, A is the area and P is the perimeter of the roadway.

Example: At 27°C underground temperature, the kinematic viscosity of air is 15.11 x 10^{-6} m^2/s width and height of the mine gallery are 6 m and 2.7 m respectively and air velocity is 0.5 m/s (the minimum statutory air velocity in the mine gallery should be ≥ 0.5 m/s) then Re is 1,230,973. Therefore, the underground airflow was treated as a turbulent flow (Aminossadati and Hooman, 2008, Widiatmojo et al., 2013, Sasmito et al., 2013).

The Reynolds–averaged Navier–Strokes (RANS) equations were used to model the turbulent flow of mine air. In Reynolds averaging, the solution variables in the Navier–Stokes equations are made up of time-averaged and fluctuating components. For example, for the x-velocity component u (ANSYS, 2013),

$$u_i = \bar{u}_i + u_i' \tag{4-5}$$

Where $\bar{u}_i$ and u_i' are the mean and fluctuating velocity components (i= 1,2,3).

The RANS equations are obtained by substituting time and average velocity in the mass conservation equation:

$$\frac{\partial \rho}{\partial t} + \frac{\partial}{\partial x_i}(\rho u_i) = 0 \tag{4-6}$$

$$\frac{\partial}{\partial x}(\rho u_i) + \frac{\partial}{\partial x_j}(\rho u_i u_j) = -\frac{\partial p}{\partial x_i} + \frac{\partial}{\partial x_j}\left[\mu\left(\frac{\partial u_i}{\partial x_j} + \frac{\partial u_j}{\partial x_i} - \frac{2}{3}\delta_{ij}\frac{\partial u_l}{\partial x_l}\right)\right] + \frac{\partial}{\partial x_j}\left(-\rho\,\overline{u_{i'}\,u_{j'}}\right) \tag{4-7}$$

Where the term $-\rho\,\overline{u_{i'}\,u_{j'}}$ represents the Reynolds stress and can be solved with the Boussinesq hypothesis and Reynolds stress models (RSM). In the Boussinesq Hypothesis, the Reynolds stress is related to the average velocity gradient (ANSYS, 2013).

$$-\rho\,\overline{u_{i'}\,u_{j'}} = \mu_t\left(\frac{\partial u_i}{\partial x_j} + \frac{\partial u_j}{\partial x_i}\right) - \frac{2}{3}\left(\rho k + \mu_t\frac{\partial u_k}{\partial x_k}\right)\delta_{ij} \tag{4-8}$$

To determine the turbulent viscosity μ_t, the k– ε model was used.

$$\mu_t = \rho C_\mu \frac{k^2}{\varepsilon} \quad \textbf{(4-9)}$$

Where C_μ is a constant, k is the turbulent kinetic energy and ε is the dissipation rate of k. The turbulent heat transport is modelled using the Reynolds analogy to turbulent momentum transfer. The modelled energy equations are as follows:

$$\frac{\partial}{\partial t}(\rho E) + \frac{\partial}{\partial x_i}[u_i(\rho E + p)] = \frac{\partial}{\partial x_j}\left[\left(ke + \frac{c_p \mu_t}{\sigma_k}\right)\frac{\partial T}{\partial x_j} + u_i(\tau_{ij})_{eff}\right] + S_h \quad \textbf{(4-10)}$$

Where ke is the thermal conductivity, E is the total energy and $(\tau_{ij})_{eff}$ is the deviatoric stress tensor defined as

$$(\tau_{ij})_{eff} = \mu_{eff}\left(\frac{\partial u_j}{\partial x_i} + \frac{\partial u_i}{\partial x_j}\right) - \frac{2}{3}\mu_{eff}\frac{\partial u_k}{\partial x_k}\delta_{ij} \quad \textbf{(4-11)}$$

4.3.1 Standard k– ε model

The standard k– ε model is based on the model transport equations for turbulent kinetic energy (k) and its dispersion rate (ε). The model transport equation for k is derived from the exact equation, while the model transport equation for ε was obtained using physical reasoning and bears little resemblance to its mathematical counterpart.

In the derivation of the k– ε model, the assumption is that the flow is fully turbulent and the effect of molecular viscosity is negligible. Since mine airflow can be considered as fully turbulent, the k– ε model is valid for mine air. The k– ε model is the most common model used in CFD to simulate mean flow characteristics for turbulent flow conditions. The original impetus for the k– ε model was to improve the mixing-length

model, as well as to find an alternative to algebraically prescribing turbulent length scales in moderate to high complexity flows.

The turbulent kinetic energy k and its rate of dissipation ε are obtained from the governing equations (ANSYS, 2013)

$$\frac{\partial}{\partial t}(\rho k) + \frac{\partial}{\partial x_i}(\rho k u_i) = \frac{\partial}{\partial x_j}\left[\left(\mu + \frac{\mu_t}{\sigma_k}\right)\frac{\partial k}{\partial x_j}\right] + G_k + G_b - \rho\varepsilon - Y_M + S_k \qquad \textbf{(4-12)}$$

and

$$\frac{\partial}{\partial t}(\rho \varepsilon) + \frac{\partial}{\partial x_i}(\rho \varepsilon u_i) = \frac{\partial}{\partial x_j}\left[\left(\mu + \frac{\mu_t}{\sigma_\varepsilon}\right)\frac{\partial \varepsilon}{\partial x_j}\right] + C_{1\varepsilon}\frac{\varepsilon}{K}(G_k + C_{3\varepsilon}G_b) - C_{2\varepsilon}\rho\frac{\varepsilon^2}{K} + S_\varepsilon \qquad \textbf{(4-13)}$$

Where G_b is the generation of turbulent kinetic energy due to buoyancy, G_k is the production of turbulence kinetic energy due to the mean velocity gradient, Y_M is the contribution of the fluctuating dilution incompressible turbulence to the overall dissipation rate, and $C_{1\varepsilon}$, $C_{2\varepsilon}$ and $C_{3\varepsilon}$ are constants. S_k and S_ε are user-defined source terms.

4.3.2 Effect of buoyancy

DPM in a mine atmosphere would be influenced by gravity. This calls for the buoyancy effect to be included in this research (Zheng et al., 2015b). The effect of buoyancy forces in a mixed convection flow can be measured in terms of the ratio of the Grashof and Reynolds numbers:

$$\frac{Gr}{Re^2} = \frac{g\beta\Delta\mathrm{TL}}{v^2} \qquad \textbf{(4-14)}$$

When this number approaches or exceeds unity, strong buoyancy would be added to the flow, but if the number is very small, the buoyancy forces may be ignored. In pure natural (buoyancy-driven) convection, the strength of the flow induced by buoyancy is measured

by the Rayleigh number:

$$Ra = \frac{g\beta\Delta T L^3 \rho}{\mu\alpha} \quad \textbf{(4-15)}$$

Where

β = Thermal expansion coefficient = $\frac{1}{\rho}\left(\frac{\partial\rho}{\partial T}\right)_p$ **(4-16)**

□ = Thermal diffusivity = $\frac{k}{\rho c_p}$ **(4-17)**

Rayleigh numbers less than 10^8 indicate a laminar flow induced by buoyancy where the transition to turbulence occurs over the range of $10^8 < Ra < 10^{10}$.

4.3.3 Effect of buoyancy on turbulence in the k– ε models

When a non-zero gravity field and temperature gradient are present instantaneously, the k– ε models account for the generation of k due to buoyancy and its corresponding contribution to the production of ε. The generation of turbulence due to buoyancy is given by

$$G_b = \beta g_i \frac{\mu_t}{Pr_t}\frac{\partial T}{\partial x_i} \quad \textbf{(4-18)}$$

Where Pr_t is the turbulent Prandtl number for energy and g_i is the component of the gravitational vector in the i-direction. For the standard and realisable k– ε models, the default value of Pr_t is taken as 0.85. In the case of the Re-Normalisation Group (RNG) k– ε model, $Pr_t = 1/\alpha$, then $\alpha_0 = 1/Pr = k/\mu c_p$, then the coefficient of thermal expansion β is defined as

$$\beta = \frac{1}{\rho}\left(\frac{\partial\rho}{\partial T}\right)_p \quad \textbf{(4-19)}$$

For ideal gases, G_b reduces to

$$G_b = -g_i \frac{\mu_t}{\rho Pr_t} \frac{\partial \rho}{\partial x_i} \quad \textbf{(4-20)}$$

The degree to which ε is affected by buoyancy as, determined by the constant $C_{3\varepsilon}$, is calculated as:

$$C_{3\varepsilon} = tanh \left|\frac{v}{u}\right| \quad \textbf{(4-21)}$$

Where v is the component of the flow velocity parallel to the gravitational vector and u is the component of the flow velocity perpendicular to the gravitational vector.

4.3.4 Species transport model

To conduct DPM investigations in an underground mine environment, conservation equations for chemical species are considered in some cases for faster results. ANSYS Fluent predicts the local mass fraction of each species Y_i through the solution of a convection-diffusion equation for the i^{th} species. The conversation equation takes the following general form:

$$\frac{\partial}{\partial t}(\rho Y_i) + \Delta.(\rho \vec{v} Y_i) = -\Delta \vec{J_i} + R_i + S_i \quad \textbf{(4-22)}$$

Where R_i is the net rate of production of species i by a chemical reaction and S_i is the rate of creation by addition from the dispersed phase plus any source defined by the user. An equation of this form will be solved for (N-1) species, where N is the total number of fluid-phase chemical species present in the system. Since the mass fraction of the species sums to unity, the N^{th} mass fraction is determined as one minus the sum of the remaining (N-1) mass fractions. To minimise numerical error, the N^{th} species should be selected as the species with the overall largest mass fraction such as nitrogen (N_2) when the oxidiser is air.

4.3.5 Discrete phase models

The particle flow is modelled using the Euler–Lagrange approach, where particle properties are studied along the path of particle flow (Chang et al., 2019a). These models are used to define particle flow by considering the various forces that act on the particle (Thiruvengadam et al., 2016b). The forces commonly encountered are the drag force between the fluid and the particle, the lift force, the virtual mass force and the Brownian force, etc.

The fluid phase is treated as a continuum by solving the Navier–Strokes equations, while the dispersed phase is solved by tracking a large number of particles, bubbles, or droplets dispersed through the calculated flow field. The dispersed phase can exchange momentum, mass and energy with the fluid phase. DPM particles are tracked using the Lagrangian method in the discrete phase and the particle or droplet trajectories are computed individually at specified intervals during the fluid phase calculation. The force balance equation relates the particle inertia with the forces acting on the particle and can be written as

$$\frac{d\overrightarrow{u_p}}{dt} = F_D\left(\vec{u} - \overrightarrow{u_p}\right) + \frac{\vec{g}(\rho_p - \rho)}{\rho_p} + \vec{F} \qquad \textbf{(4-23)}$$

Where $\vec{F}$ is an additional acceleration (force / unit particle mass), $F_D(\vec{u} - \overrightarrow{u_p})$ is the drag force per unit particle mass and

$$F_D = \frac{18\mu}{\rho_p {d_p}^2} \frac{C_D\, Re}{24} \qquad \textbf{(4-24)}$$

Here $\vec{u}$ is the fluid phase velocity, $\overrightarrow{u_p}$ is the particle velocity, μ is the dynamic viscosity of the fluid, ρ is the fluid density, ρ_p is the density of the particle material and d_p is the particle diameter. Re is the relative Reynolds number, which is defined as

$$\mathrm{Re} = \frac{\rho d_p \left|\overrightarrow{u_p} - \vec{u}\right|}{\mu} \quad \textbf{(4-25)}$$

The additional forces induced on the particle due to the fluid surrounding the particle due to growth in the boundary layer is called the virtual mass force and is given by

$$\vec{F} = C_{vm} \frac{\rho}{\rho_p} \left(\overrightarrow{u_p} \nabla \vec{u} - \frac{d\overrightarrow{u_p}}{dt} \right) \quad \textbf{(4-26)}$$

Where C_{vm} is the virtual mass factor with a default value of 0.5, the fluid and the particle are coupled together mathematically in the form of slip velocity.

4.4 Basic Ventsim modelling using the NIOSH field study

Initially, to simulate the NIOSH field experiment, Ventsim modelling studies were conducted. For this Ventsim modelling the gallery was 533 m long by 3.6 m high by 2.7 m wide. The intake air temperature was 300 K and the quantity of intake airflow was 24 m^3/s. In this modelling the diesel-powered vehicles were fitted with DPF. **Fig. 4.1** shows the DPM concentration in a mine gallery. Ventsim software can simulate larger working areas and mining sections, but it does have limited applications; it cannot show the mapping/flow pattern of the contaminant in the localised area. In this scenario, CFD modelling will provide accurate results.

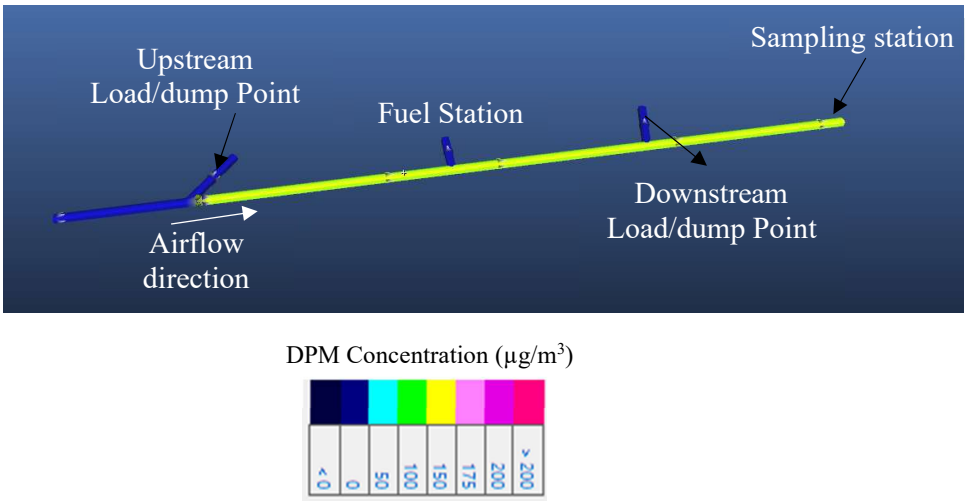

Fig. 4.1 Ventsim results of NIOSH experimental gallery DPM particles flow pattern

4.5 Basic CFD modelling using NIOSH field study

To simulate the NIOSH DPM field experiment, the density of DPM particles was considered to vary from 0.3 to 1.2 g/cm^3 (Virtanen et al., 2006), the size of the DPM particles was considered to range from 0.05 to 0.1 µm and the mean size of particles was considered as 10 nm. The intake air temperature was 300 K and the quantity of intake airflow was 24 m^3/s. The temperature and velocity of diesel engine exhaust gases were 327 K and 25 m/s, respectively.

Fig. 4.2a shows the geometric model of the NIOSH experimental gallery; the gallery is 533 m long, 3.6 m wide and 2.7 m in height; it also has a 9% rise towards the downstream end.

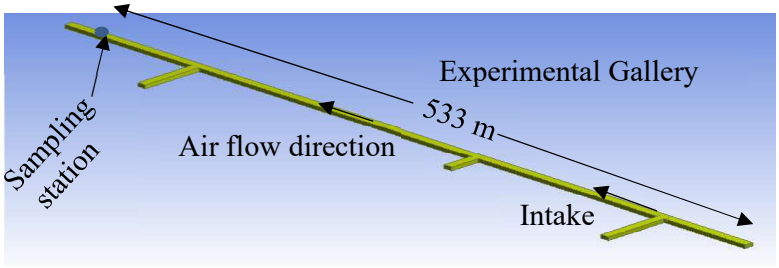

a. Experimental gallery geometry

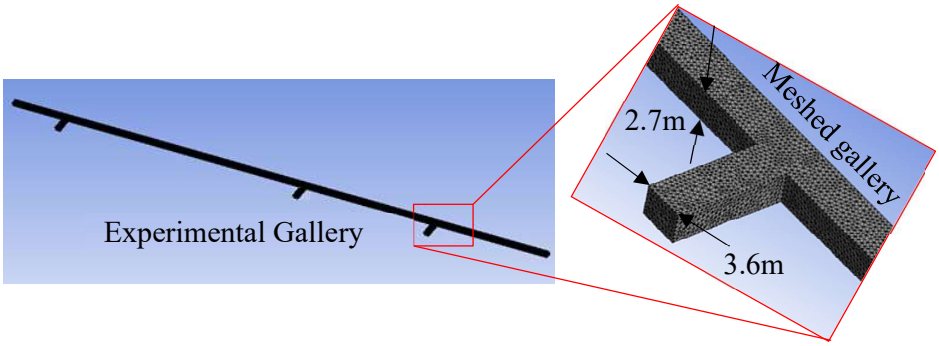

b. Experimental gallery meshed model

Fig. 4.2 NIOSH experimental gallery geometry and mesh

Fig. 4.2b shows the 'computational mesh' representing the NIOSH experimental gallery used in the CFD simulation. The computational mesh contains 1 million tetrahedral cells. The airflow in the gallery was treated as turbulent and modelled with the standard k– ε turbulence model. The effect of buoyancy was also included in the steady-state simulations.

The model was validated against the NIOSH field experimental results. As per the field measurement results, the DPM concentration at the downstream sampling station with diesel particulate filter, DCL MineX, was 149 µg/m^3 and the baseline concentration without the filter was 1112 µg/m^3. **Fig. 4.3** shows the simulated results of the NIOSH experimental gallery.

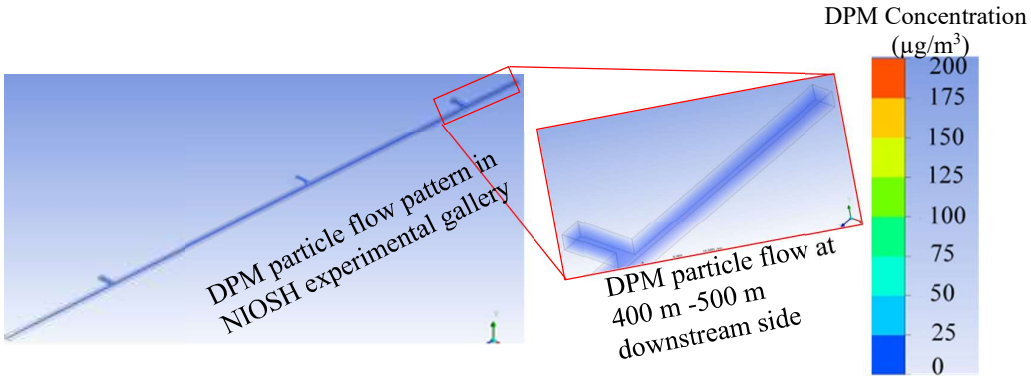

Fig. 4.3 NIOSH experimental gallery DPM particles flow pattern with DPF

4.5.1 Simulation results with and without DPF

Fig. 4.4 shows the NIOSH field experimental simulation results with and without DPF at 500 m on the downstream side. At 500 m downstream of the LHD loading point, the concentration of DPM without DPF covered the entire roadway with 130 µg/m^3 **Fig. 4.4**a and **Fig. 4.4**b show the concentration of DPM 500 m downstream of the LHD loading point; LHD was not used as DPF. The results show that the concentration of DPM was almost equally distributed over the entire roadway with about 35 µg/m^3 concentration of DPM.

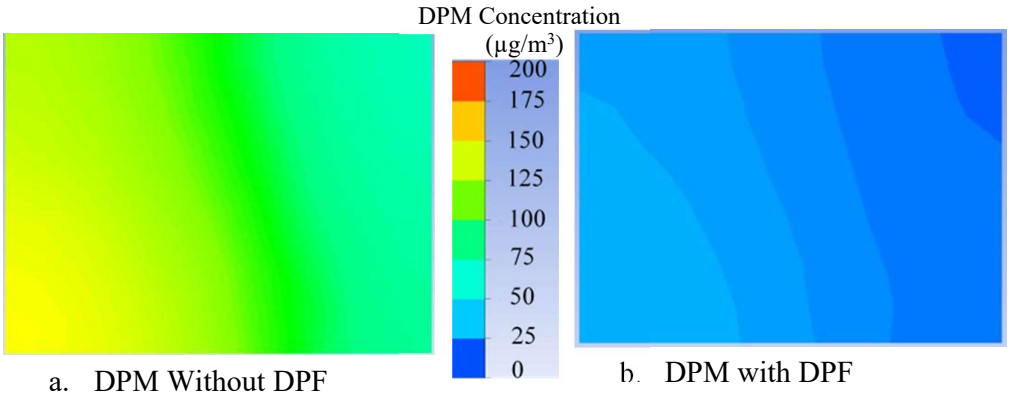

Fig. 4.4 DPM concentration 500 m downstream of the truck without and with DPF

4.6 Development and validation of CFD models for field investigations

To develop confidence in DPM patterns simulated using CFD techniques, the models had to be validated against experimental field data. The following sections explain the development of a CFD model, meshing, simulations under boundary conditions and validating the field data model.

4.7 Development of man-riding vehicle model, CFD simulations and validation

4.7.1 Construction of computational domain

To validate the stage-I field experiment with a man-riding vehicle, the flow in a 50 m long, 6 m wide and 2.7 m high ventilation gallery was simulated. The man-riding vehicle was designed and modelled in 3D CAD and imported to ANSYS Fluent. The length, width and height of the man-riding vehicle were 6.25 m, 2 m and 1.95 m, respectively. The exhaust pipe is located behind the left front wheel and on the opposite side to the operator, as shown in **Fig. 4.5**a. The engine has a diesel particulate filter, so the exhaust flow is a mixture of DPM and air. The dip of the airway was considered as 1 in 22 **Fig. 4.5** shows the details of this computational domain.

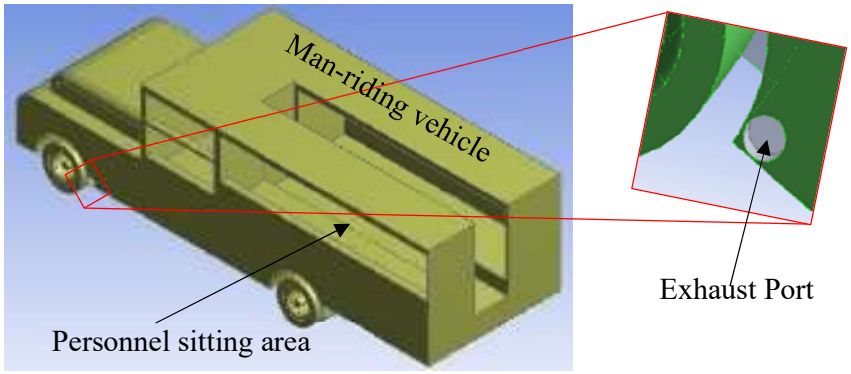

a. CAD model of man-riding vehicle with detail showing location of exhaust port

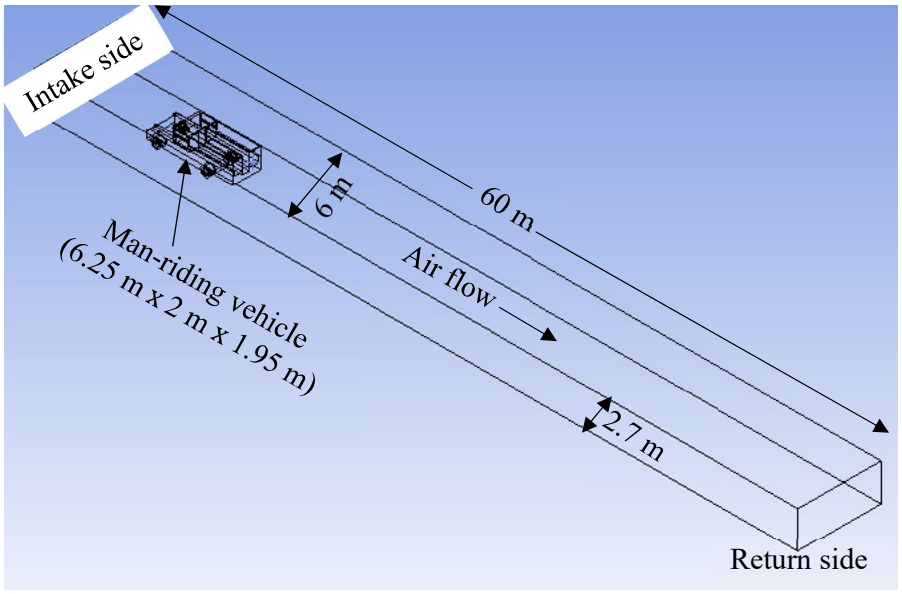

b. CFD model of man-riding vehicle with gallery – computational domain

Fig. 4.5 CFD model of a man-riding vehicle and experimental gallery

4.7.2 Construction of computational mesh

Fig. 4.6 shows the man-riding vehicle's surface mesh and meshed airway with man-riding vehicle. For accurate results, finer mesh was used for the man-riding vehicle. The finer mesh cells were also used adjacent to gallery walls, with seven layers of cells accommodated in the boundary layers. The overall mesh contained half a million

tetrahedron shaped computational cells with a minimum cell size of $7.3(10^{-3})$ m, minimum edge length of 0.025 m and 'size function'. The residual RMS error value is 10^{-4} and the domain has imbalances of less than 0.01.

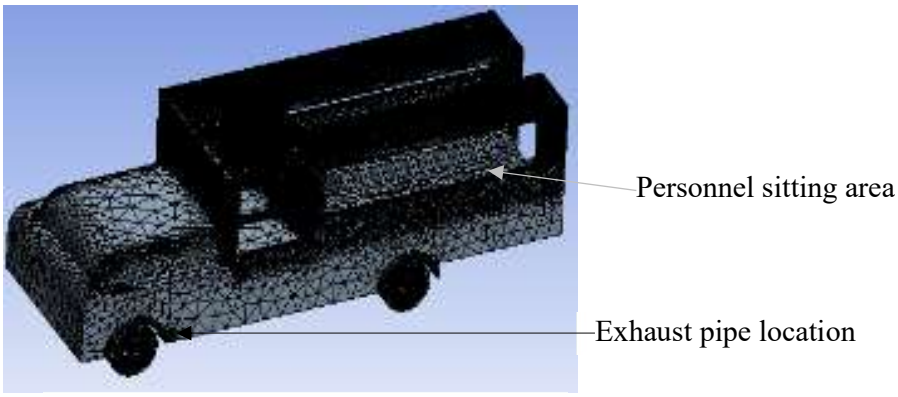

a. Surface mesh for man-riding vehicle

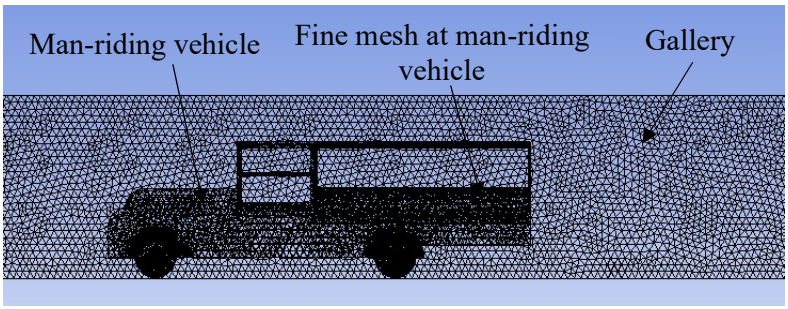

b. Cross-section of airway mesh

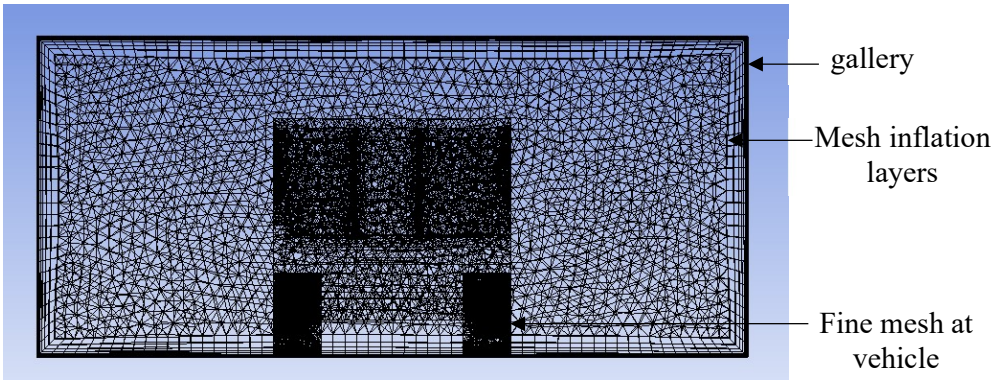

c. Surface mesh of man-riding vehicle & gallery

Fig. 4.6 Meshed model of man-riding vehicle and experimental gallery

4.7.3 Setting up the flow and boundary conditions

Discrete-phase modelling was used to model the DPM flow patterns of a man-riding vehicle. For this modelling, DPM particle injection is from the exhaust pipe. The diameters of the DPM particles ranged between $1e^{-9}$ m to $1e^{-7}$ m with a mean diameter of $1e^{-8}$ m. DPM particles were treated as inert materials and the Rosin–Rammler diameter distribution was used. For physical models, the spherical drag law was used as a drag parameter. For stochastic tracking, a discrete random walk model with 10 number of tries and a 0.15-time scale was used. The intake air and DPM are considered as two different phases. The Eulerian–Lagrangian approach is used whereby the gas phase (air) was solved using the Eulerian approach and the particle-phase (DPM) was tracked using the Lagrangian approach. Particle-to-particle interactions in the DPM were not considered because the particulate volume fraction was 0.5% (dilute).

The intake air velocity was set as 1.26 m/s (volume flow rate 20.6 m^3/s) at 300 K, the outlet pressure was 0 Pa and the 'walls' were considered as 'no-slip' surfaces. DPM was injected from the exhaust pipe at 24 m/s velocity and 335 K temperature. Buoyancy effects and turbulence (standard k– ε model) were activated. The location of the operator was on the opposite side of the exhaust pipe.

Fig. 4.7 and **Fig. 4.8** show the discrete flow modelling results of man-riding vehicle DPM particles tracking lines. **Fig. 4.9** and **Fig. 4.10** show the results of the base case CFD simulations. In **Fig. 4.9**, DPM concentration at the upwind side is high due to velocity of exhaust fumes being greater (24 m/s) than the air velocity (1.26 m/s). This means the high-velocity exhaust fumes hit the wall and some of the DPM particles travel towards the upwind side. **Fig. 4.10**a shows the concentration of DPM near the operator, with maximum concentration at the gallery's exhaust pipe side. At 1 m (**Fig. 4.10**b) and 5 m

(**Fig. 4.10**c) downstream of the vehicle, the maximum concentration of DPM is at the top and exhaust pipe side of the wall. At 10 m (**Fig. 4.10**d) downstream of the vehicle, the DPM had dispersed over the entire roadway.

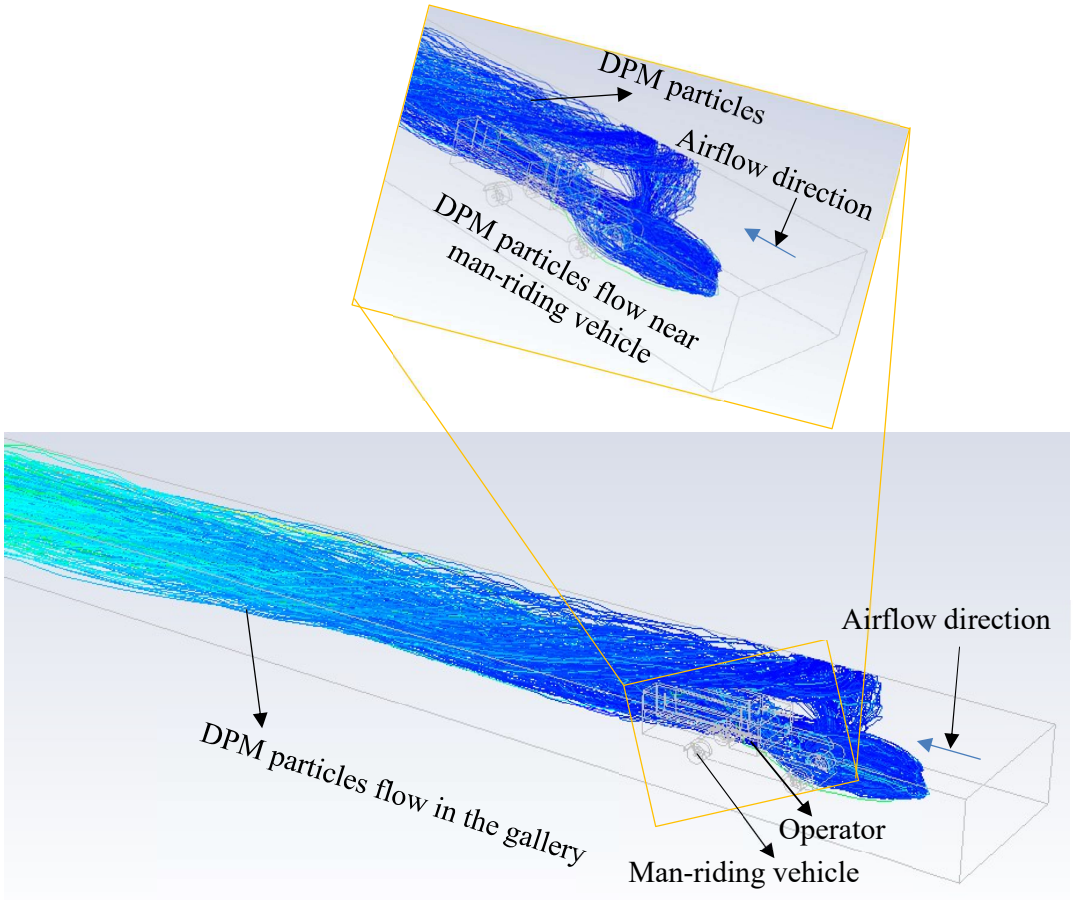

Fig. 4.7 Results of base case DPM modelling; DPM particles tracking lines

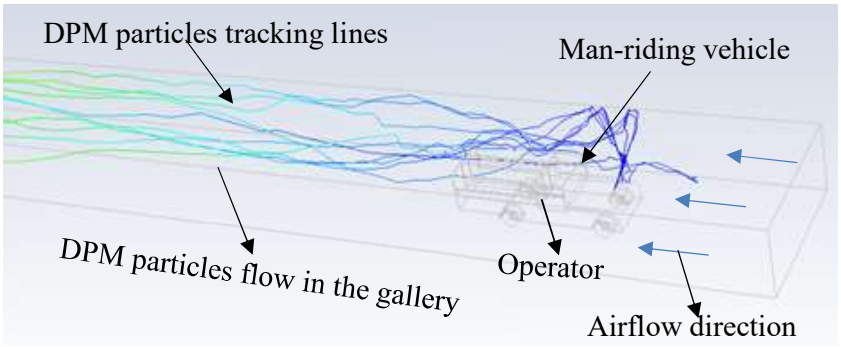

Fig. 4.8 DPM particles tracking lines from man-riding vehicle's exhaust pipe

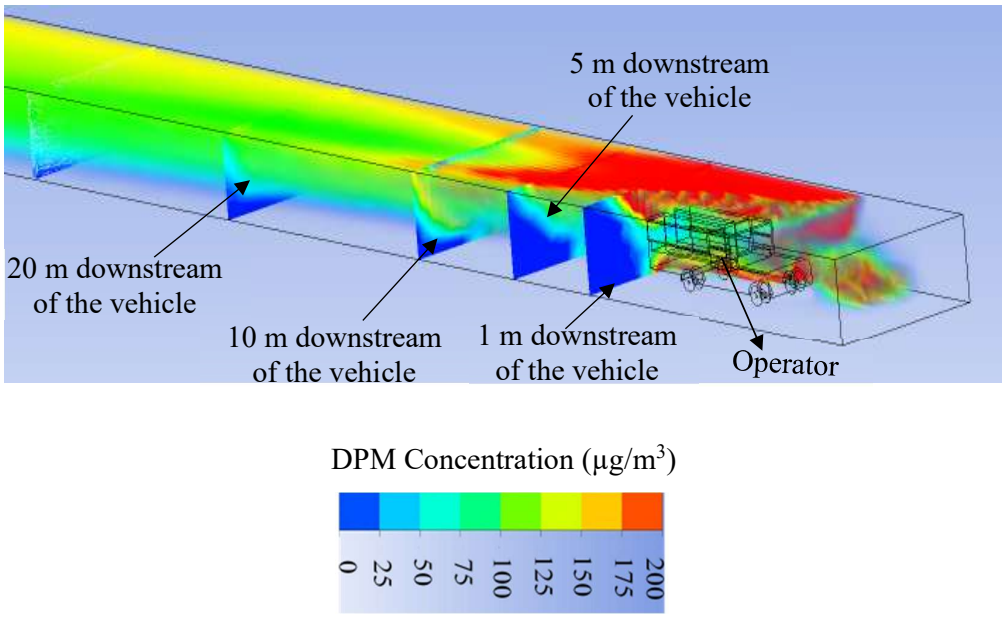

Fig. 4.9 Base case model DPM flow concentration contours, isometric view from the man-riding side

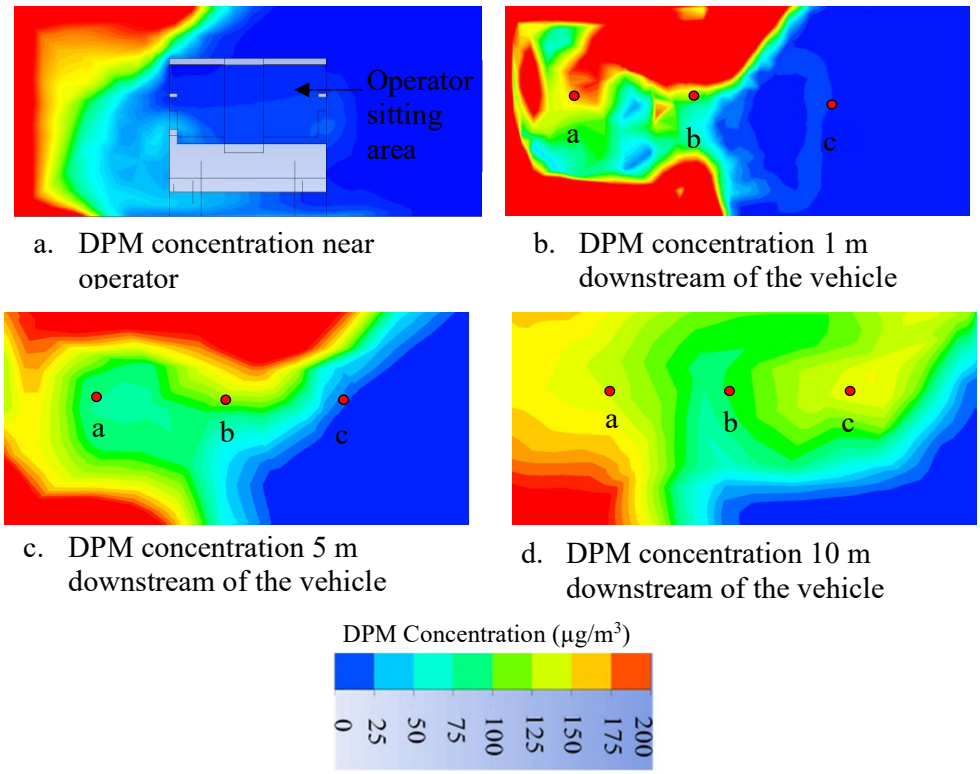

a. DPM concentration near operator

b. DPM concentration 1 m downstream of the vehicle

c. DPM concentration 5 m downstream of the vehicle

d. DPM concentration 10 m downstream of the vehicle

Fig. 4.10 DPM concentration contours at different locations of downstream of the vehicle

4.7.4 Model validation

Table 4.1 shows the base case simulations and field experiments at 1 m, 5 m and 10 m downstream of the vehicle and at sample points a, b and c. These simulated results were in fair agreement with the data measured at almost all locations; those results that deviated slightly from the measured data can be due to uneven gallery walls, which were not considered while modelling. The difference varies from –13% to +10%.

Table 4.1 Comparison of simulated results with experimental results: base case

Sampling point	Experimental value ($\mu g/m^3$)	Simulation value ($\mu g/m^3$)	Difference (%)
At 1 m sample station			
a	185.8	165	–11%
b	50	55	+10%
c	0	0	0%
At 5 m sample station			
a	149.0	141	–5%
b	117	110	–5%
c	16	16	0%
At 10 m sample station			
a	127.4	110	–13%
b	50	45	+2%
c	116.6	120	–10%

Note: Difference (%) is the difference between simulation results and test results and is calculated as (Simulation value – Experimental value)/ Experimental value) × 100 %.

4.7.5 Air velocity flow patterns

Fig. 4.11 shows the flow streamline pattern near the man-riding vehicle; there is uniform airflow in front of the vehicle and a highly turbulent flow near the vehicle. It also shows the total volume of air flowing through the gaps between the vehicle and the airway's sidewalls and over the top of the vehicle through the top gap.

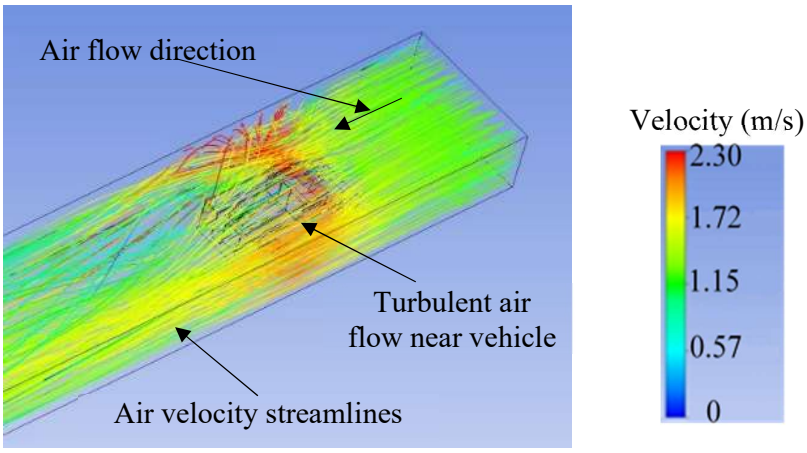

a. Base case model air velocity streamlines, isometric view

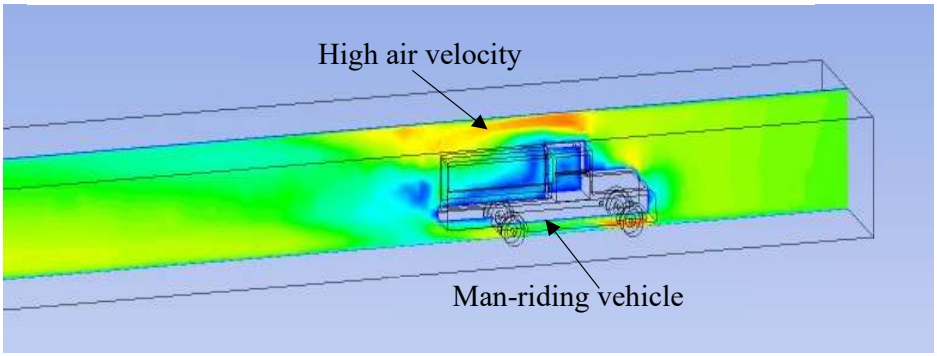

b. Base case model air velocity field at central vertical plane, isometric view

Fig. 4.11 Air velocity streamlines and contours

4.7.6 Man-riding vehicle DPM simulation with species transport modelling

Species transport modelling was used to simulate the concentration of DPM around the man-riding vehicle. n-octane vapour (C_8H_{18}) (Zheng, 2011) was used to simulate DPM. Chemical reactions between the species were not considered. The Boussinesq approximation was considered valid and the k– ε model was used to model the turbulent flow. The intake air velocity in the gallery was set as 1.26 m/s. **Fig. 4.12** shows the top view of the simulated DPM concentration field, showing high DPM concentration between the exhaust pipe side of the vehicle and the gallery wall. Downstream of the vehicle, the DPM is seen to spread over the whole gallery.

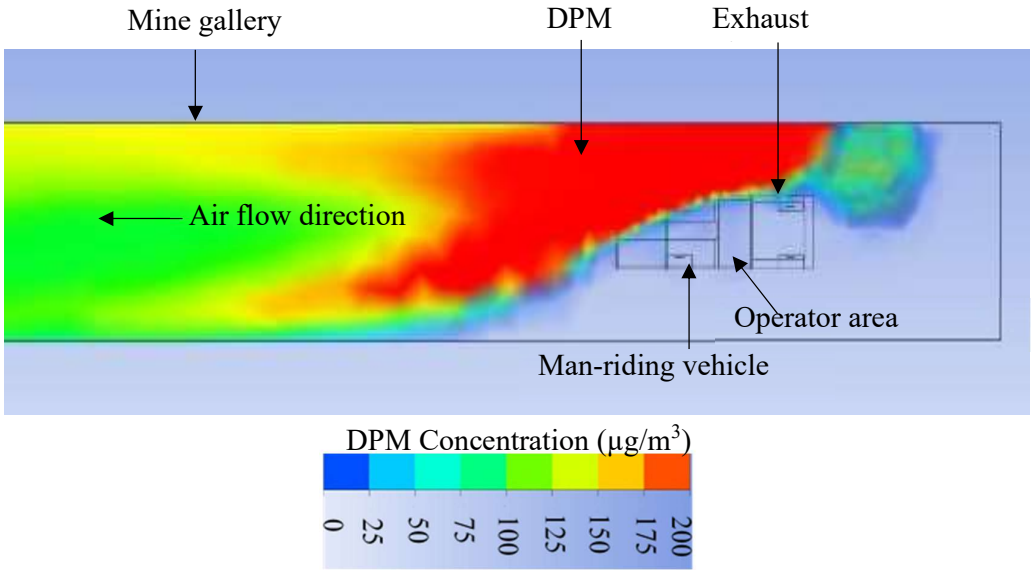

Fig. 4.12 DPM concentration field near man-riding vehicle – top view

Fig. 4.13a shows the concentration of DPM near the operator area; the concentration is high near the wall, but there is no DPM near the operator. At 1 m downstream of the vehicle (**Fig. 4.13**b), the maximum concentration is near the left side of the roof. There are traces of DPM on the roadway and very little on the right side of the roadway. At 5 m downstream of the vehicle (**Fig. 4.13**c) the DPM flow has moved towards the right side of the roadway with a maximum concentration close to the roof in the middle of the roadway. At 10 m downstream of the vehicle (**Fig. 4.13**c) the amount of DPM at Sample point 'c' on the roadway is 150 µg/m^3, but the concentration on the right side of the roadway is low.

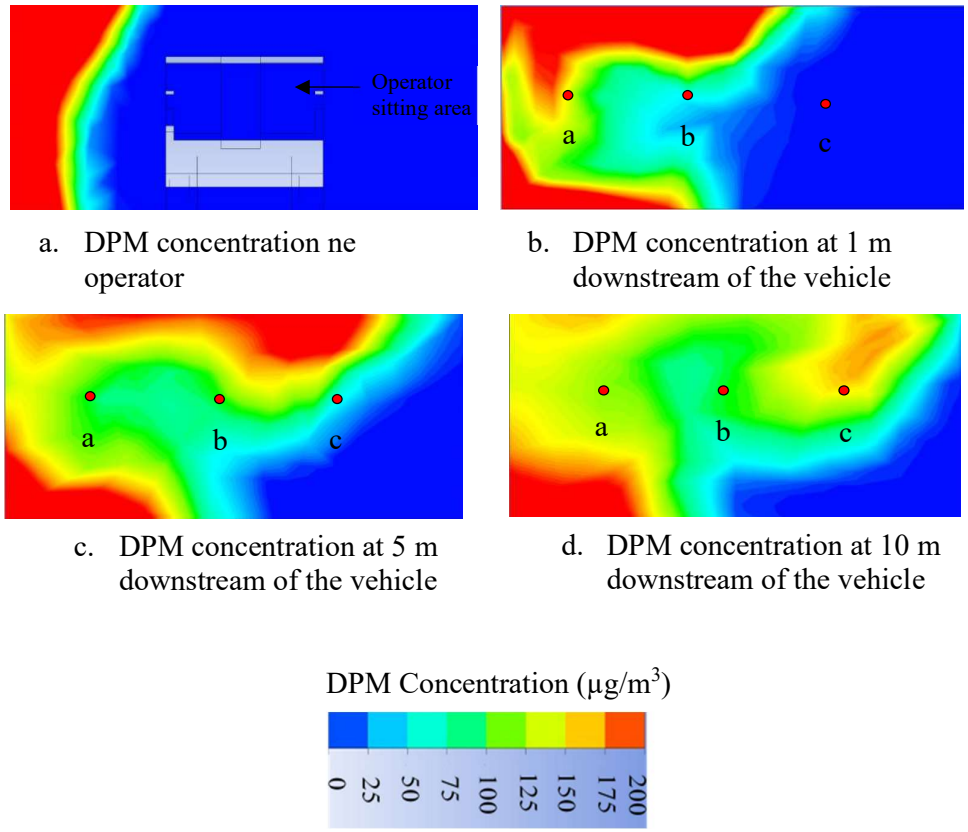

a. DPM concentration ne operator

b. DPM concentration at 1 m downstream of the vehicle

c. DPM concentration at 5 m downstream of the vehicle

d. DPM concentration at 10 m downstream of the vehicle

Fig. 4.13 DPM concentration field using species transport modelling (a) near the operator, (b) 1 m, (c) 5 m and (d) 10 m downstream of the vehicle

4.7.7 Discrete phase vs species transport DPM modelling

Table 4.2 summarises the difference between the simulated DPM concentration fields using discrete-phase modelling and species transport modelling; the difference was between -9% to +11%. This shows that the DPM concentration fields can be almost equally well modelled by the discrete-phase and species transport modelling approaches.

Table 4.2 Comparison of discrete phase modelling results with species transport modelling results

DPM concentration ($\mu g/m^3$) at 1 m sample station			
Sampling point	Discrete phase modelling	Species transport modelling	Difference (%)
a	165	176	+6%
b	55	50	–9%
c	0	0	0%
DPM concentration ($\mu g/m^3$) at 5 m sample station			
a	141	130	–7%
b	110	108	–2%
c	16	16	0%
DPM concentration ($\mu g/m^3$) at 10 m sample station			
a	110	115	+4%
b	45	50	+11%
c	120	110	–8%

Note: Difference (%) is the difference between species transport modelling and discrete phase modelling, calculated as (species transport value – discrete phase value)/ discrete phase value) × 100%.

4.8 LHD model development, simulation and validation for co-flow

Diesel-powered LHD/utility vehicles are commonly used in underground mines to load and transport coal, ore, waste rock and other materials (Jakkula and SN, 2019, Balaraju et al., 2018). These machines are an efficient way to reduce manpower and improve productivity and safety. LHDs generally travel at 20 to 30 km/h; they are between 8 and 15 m long, 2.5 m to 3.5 m wide and weigh between 20 and 75 tons (Gustafson, 2013). Each LHD has front and rear parts that are connected by articulated points. Each section

of the unit has rubber wheels that are not steerable; a hydraulic system operates the brakes, bucket and steering. These machines can operate both manually or with an automatic system (Sakthi et al., 2019).

4.8.1 DPM and ventilation airflow in the same direction (co-flow)

In this instance, the LHD exhaust and intake airflow are in the same direction (co-flow), as shown in **Fig. 4.14**. The DPM samples were collected downstream of the LHD. Three sampling stations were located at 2 m, 5 m and 10 m from the vehicle. **Fig. 4.14** shows the location of the LHD and the sampling stations. To cover the roadway cross-section, each station had nine sampling points arranged in three rows (top, centre and bottom) and three columns (left, middle and right) **Fig. 3.6** and **Fig. 3.7** show the sampling points in the mine gallery.

4.8.2 Construction of computational domain and mesh

The computational domain is a 70 m long tunnel with a rectangular cross-section (6 m wide by 2.7 m high). A CAD model of an LHD vehicle was designed and imported into the computational domain. The DPM exhaust is emitted from the source located at the LHD's rear end and it is a mixture of DPM and air. **Fig. 4.14**a shows the CAD model representing the vehicle and **Fig. 4.14**b shows the experimental gallery with the LHD.

Fig. 4.15a shows the mesh generated for the vehicle's complex surfaces and **Fig. 4.15**b shows the details of the computational domain and the mesh made up of about half a million computational cells. Finer cells were used to capture the flow details in regions such as small gaps and adjacent to solid surfaces.

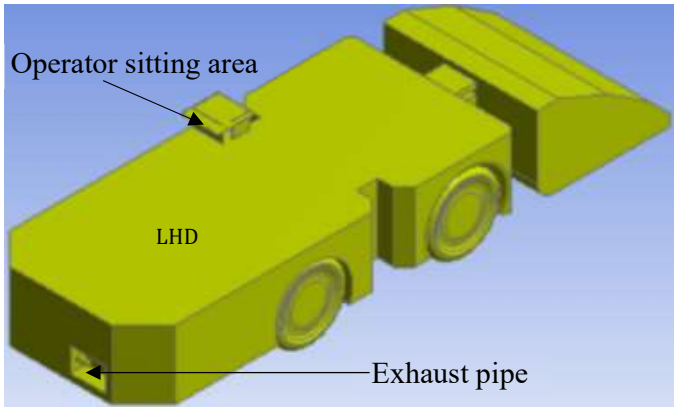

a. LHD–CAD model.

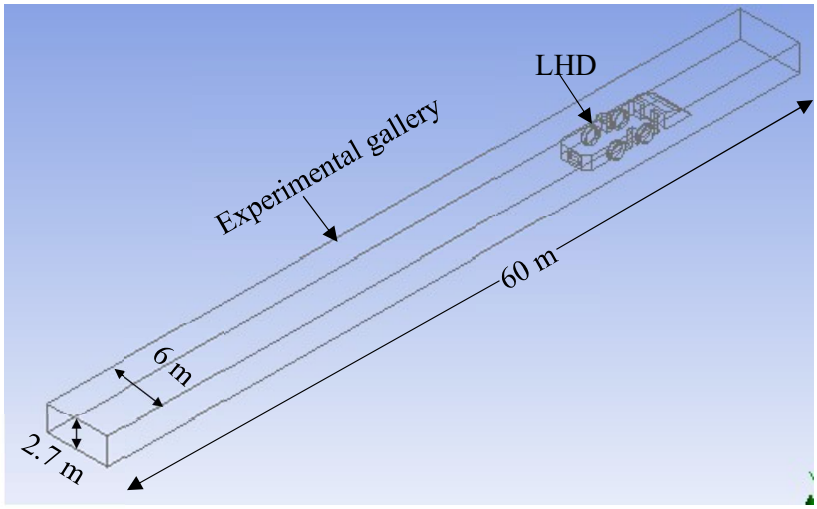

b. Experimental gallery with LHD.

Fig. 4.14 CFD model of LHD and experimental gallery

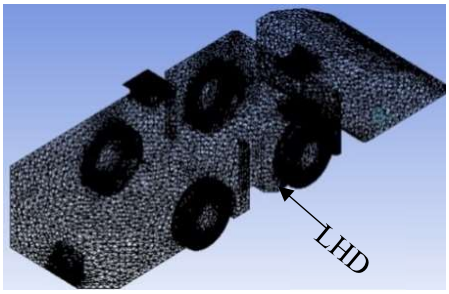

a. Surface mesh of LHD

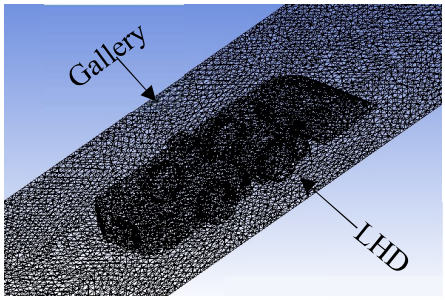

b. Surface mesh of LHD & gallery

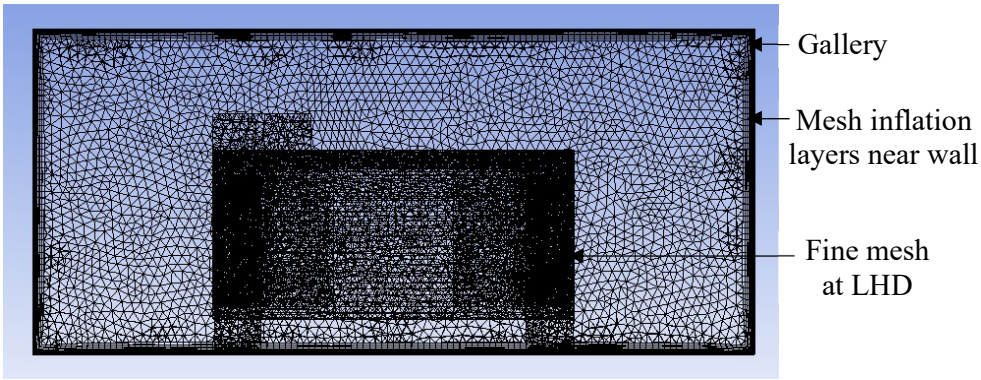

c. Surface mesh of LHD & gallery

Fig. 4.15 Computational mesh: LHD and gallery with LHD

4.8.3 Setting up flow conditions

The boundary conditions of this model were: intake air velocity 2 m/s and temperature 300 K; the velocity and temperature of the DPM-laden exhaust was specified as 24 m/s and 335 K. The discrete-phase modelling approach was used. In this approach, the gas phase was solved using the Eulerian approach and the particles were tracked by the Lagrangian approach. Inter-particle interactions among the DPM were not considered. The DPM material density was considered as 1.1 x 10^3 kg/m^3, and the diameter of the DPM particles was considered to vary from 1 nm to 100 nm, with a mean of 7.2 nm. The Boussinesq approximation was invoked to simulate the effect of buoyancy and the standard k-ε model to simulate turbulence. Convergence and mesh independent studies

were conducted in this modelling. The residual RMS error value is 10^{-4} and the domain has imbalances of less than 0.01. The minimum wall Y+ value for the model is 1. **Fig. 4.16** shows a 3D view of the DPM cloud with a number of gallery cross-sections when the DPM and airflow are in the same direction (co-flow). Near the vehicle, a high DPM concentration is seen in the middle of the gallery, but 50 m downstream of the vehicle, the DPM particles have spread over most of the gallery cross-section.

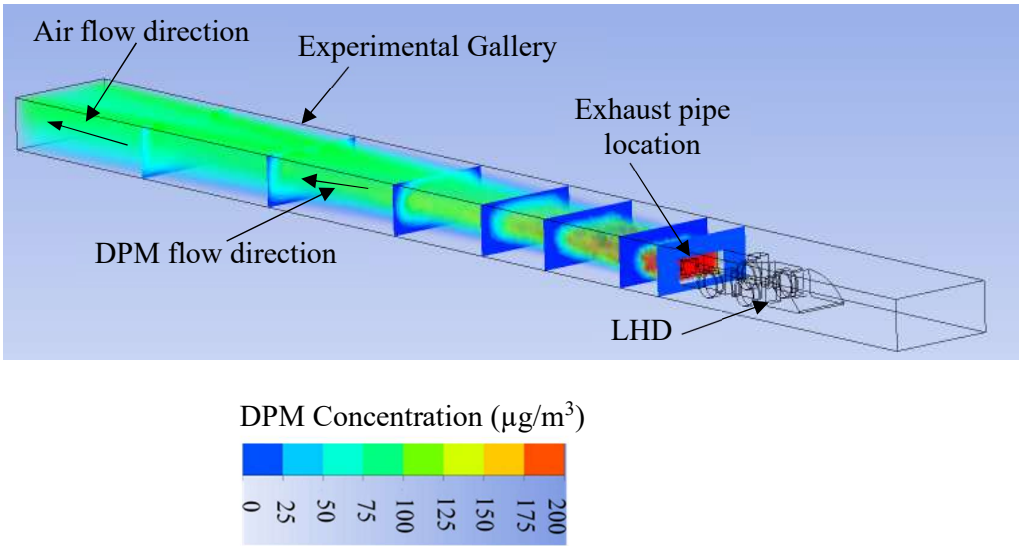

Fig. 4.16 3D view of DPM flow pattern for co-flow

Fig. 4.17 shows the contours of DPM concentration at 2 m, 5 m and 10 m downstream of the vehicle. In **Fig. 4.17**a, there is a higher concentration in the middle of the roadway. **Fig. 4.17**b shows the maximum concentration in the middle of the gallery and negligible concentration on the left and right sides of the roadway. **Fig. 4.17**c shows that the DPM flow moves towards the roof of the roadway; DPM concentration at the centre of the roadway is 70 µg/m^3 and low concentrations are at the left and right sides of the roadway.

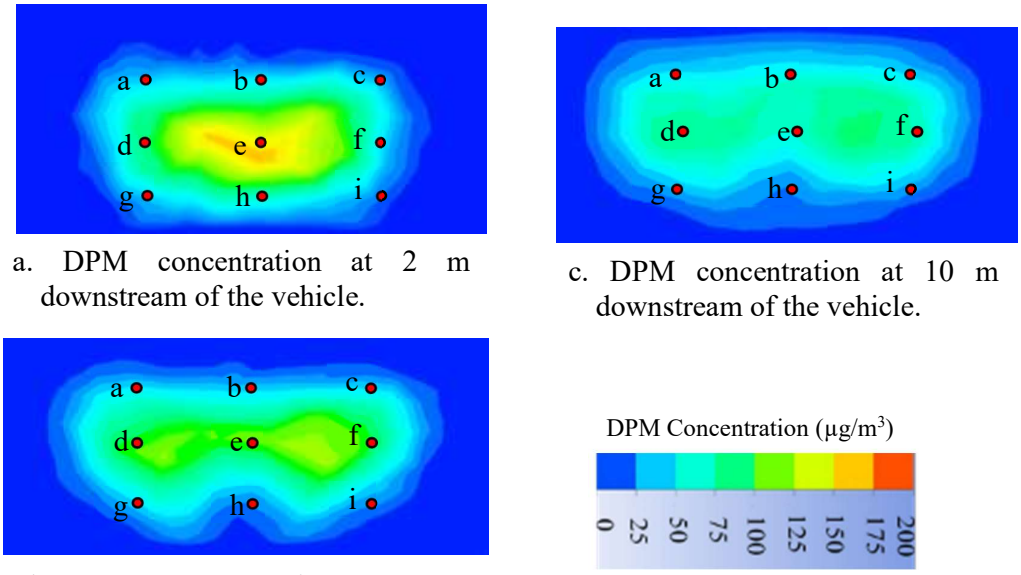

a. DPM concentration at 2 m downstream of the vehicle.

b. DPM concentration at 5 m downstream of the vehicle.

c. DPM concentration at 10 m downstream of the vehicle.

Fig. 4.17 DPM concentration at 2 m, 5 m and 10 m downstream of the vehicle

4.8.4 Model validation

Table 4.3 compares the field measurements with the CFD simulations of DPM at the three sampling stations downstream of the vehicle. Due to the instrument error, some of the experimental DPM results are not included in this table. Note that the simulated results agreed reasonably well with the measured data in most cases, even though some discrepancies were due to uneven surfaces in the gallery vehicle morphology that were not considered while modelling. Overall, these differences varied from –17% to +13%.

Table 4.3 Comparison between the simulated results (SR, µg/m^3) and the experimental results (ER, µg/m^3)

DPM concentration at 2 m sample station (µg/m^3)											
SP	ER	SR	DP	SP	ER	SR	DP	SP	ER	SR	DP
a	–	58	–	d	62	65	+4	g	–	34	–
b	–	69	–	e	127	125	–1%	h	97	110	+13%
c	–	61	–	f	64	65	+1%	i	32	30	–6%
DPM concentration at 5 m sample station (µg/m^3)											
a	–	37	–	d	64	70	+9%	g	32	35	9%
b	33	37	+10%	e	95	102	+7%	h	64	55	–14%
c	31	32	+3%	f	68	72	+5%	i	32	28	–12%
DPM concentration at 10 m sample station (µg/m^3)											
a	–	45	–	d	64	65	+1%	g	–	41	–
b	61	52	–17%	e	95	85	–10%	h	29	27	–7%
c	–	49	–	f	–	75	–	i	41	37	–10%

Where: SP is sample point and DP is difference percentage.

4.9 LHD model development, simulation and validation for counter-flow

Fig. 4.18 shows the CFD simulations in an isometric view when the DPM and airflow are in opposite directions (counter-flow). Near LHD, there is a high DPM concentration in the middle of the gallery and above the LHD, whereas at the downstream side of LHD, the DPM particles spread throughout the gallery with maximum concentration in the middle and sides of the gallery.

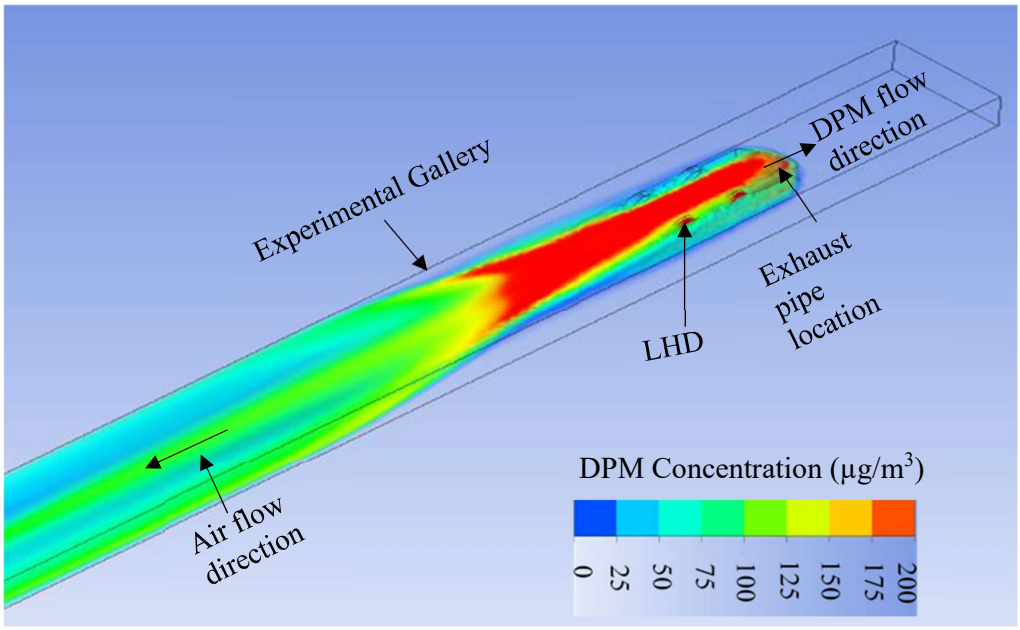

Fig. 4.18 3D view of the DPM flow pattern

Fig. 4.19 shows the DPM concentration at 2 m, 5 m and 8 m downstream of the vehicle's rear end. **Fig. 4.19**a shows a high concentration of DPM near the top and bottom portions of the vehicle. **Fig. 4.19**b shows the maximum concentration at the top and bottom portions of the vehicle; these concentrations also spread over the roadways' left and right sides. The DPM concentration near the LHD operator is 125 µg/m^3. **Fig. 4.19**c shows the DPM flow moving towards the roof and bottom of the roadway and then spreading towards the roadway's left and right sides.

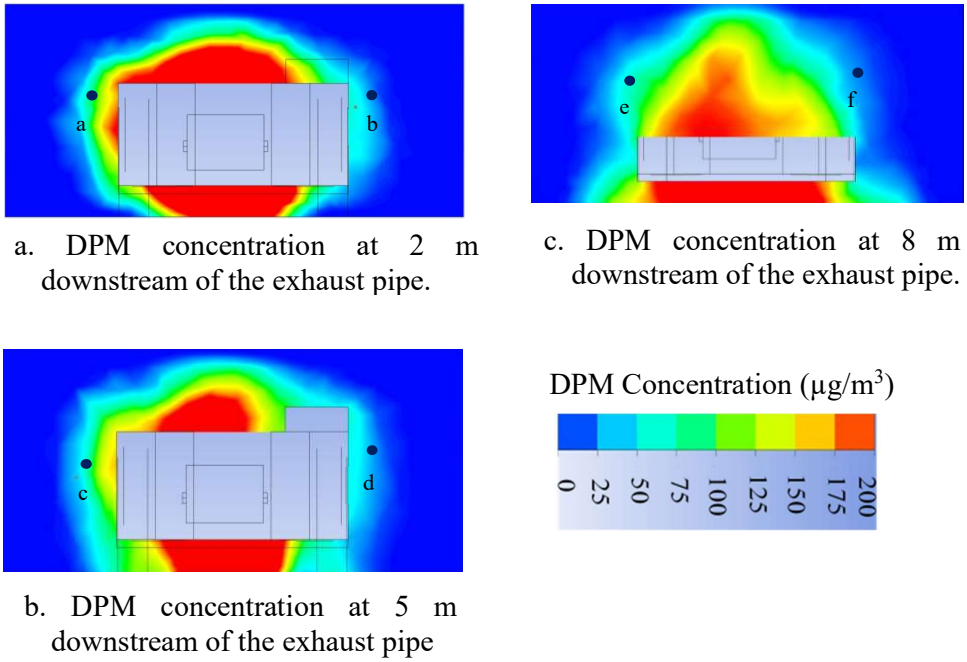

a. DPM concentration at 2 m downstream of the exhaust pipe.

c. DPM concentration at 8 m downstream of the exhaust pipe.

b. DPM concentration at 5 m downstream of the exhaust pipe

Fig. 4.19 DPM concentration at 2 m, 5 m and 8 m downstream of the exhaust pipe

Fig. 4.20 shows the DPM concentration at 6 m, 10 m and 20 m downstream of the vehicle. **Fig. 4.20**a shows the DPM 6 m downstream of the vehicle; there is a high concentration near the floor of the roadway, which gradually decreases towards the roof. **Fig. 4.20**b shows the DPM field at 10 m downstream of the vehicle, where the maximum concentration is at the middle of the gallery and the left and right sides of the roadway. **Fig. 4.20**c shows the DPM field 20 m downstream of the vehicle, where it has spread throughout the entire roadway. DPM concentration at the roadway centre was 34 µg/m^3 and similar concentrations were observed at the left and right sides of the roadway.

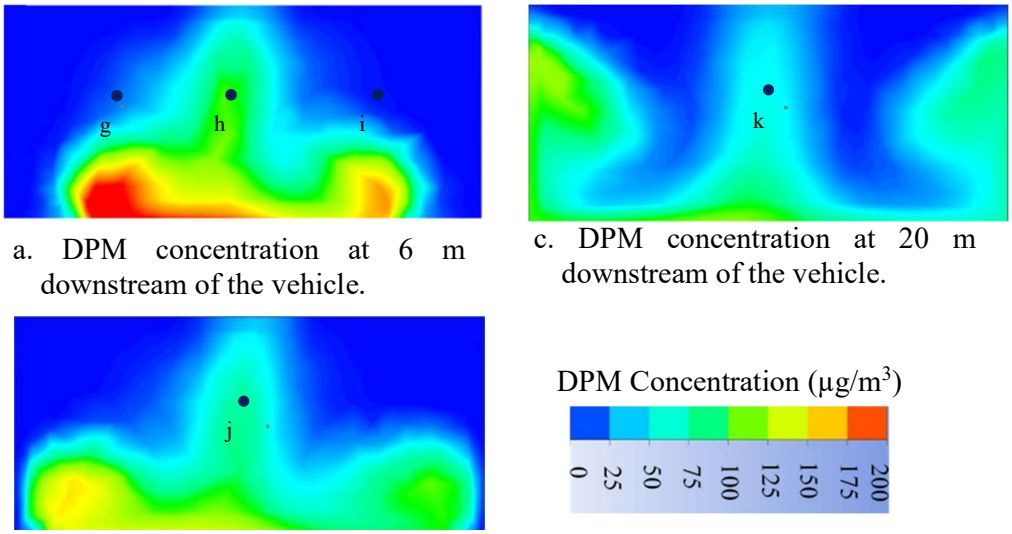

a. DPM concentration at 6 m downstream of the vehicle.

c. DPM concentration at 20 m downstream of the vehicle.

b. DPM concentration at 10 m downstream of the vehicle.

Fig. 4.20 DPM concentration at 6 m, 10 m and 20 m downstream of the vehicle

4.9.1 Model validation

Table 4.4 compares the measured and simulated DPM concentration values downstream of the vehicle at different sampling points. The table shows that the simulated results broadly agreed with the measured data, with differences that varied from –21% to +21%. Measured DPM data at sample point 'a' was not compared with the simulated data due to a very high concentration of 281.4 µg/m^3.

Table 4.4 Comparison between the simulated results (SR in µg/m^3) and the experimental results (ER in µg/m^3)

Sample point	DPM concentration [µg/m^3]		Difference
	Experimental results	Simulated results	
a	–	125	–
b	70	55	–21%
c	56	60	+7%
d	55	43	–21%
e	42	35	–16%
f	27	27	0%
g	14	17	+21%
h	42	48	+14%
i	26	25	–3%
j	42	48	+14%
k	28	34	+21%

4.10 Dead-end crosscut model development, simulation and validation

Dead-end workings are common in underground mining. As per mining regulations, diesel vehicles must be operated with enough airflow to dilute their emissions (section 2.3 of Chapter 2). However, sometimes, diesel vehicles must be operated in isolated areas or airflow-restricted zones such as parking cuddies, foot-wall drives, locations where ventilation bags are repaired, cut-throughs and other unventilated 'dead-end' areas with either restricted airflow or with no ventilation. Since 90% of DPM particles are from 3 nm to 30 nm in size and their density ranges from 0.3 gm/cm^3 to 1.2 gm/cm^3 (Bugarski et al., 2004), they do not tend to settle easily under their own weight. Consequently, it may take some time for the DPM to dilute to acceptable levels at such locations so that the operators may be exposed to high concentration of DPM for some time. This section presents transient CFD models of DPM dispersions in dead-ends. The models are

validated against experimental field data.

4.10.1 Construction of computational domain and mesh

The experimental site is a 100 m long tunnel with a rectangular cross-section (width 6 m, height 2.7 m), with a dead-end crosscut 10 m long and at 90° with the main gallery. **Fig. 4.21**a shows a CAD model representing the experimental gallery and the dead-end crosscut. **Fig. 4.21**b shows the mesh generated for the surfaces of the experimental gallery. **Fig. 4.21**a shows the sampling point at 0.5 m from the face, 1.2 m from the floor and 3 m from the sides. The finer mesh cells also used adjacent to gallery walls, with seven layers of cells accommodated in the boundary layers. The computational domain and mesh consist of almost half a million tetrahedron shaped computational cells. Convergence and mesh independent studies were conducted in this modelling. The residual RMS error value is 10^{-4} and the domain has imbalances of less than 0.01. The minimum wall Y+ value for the model is 1.

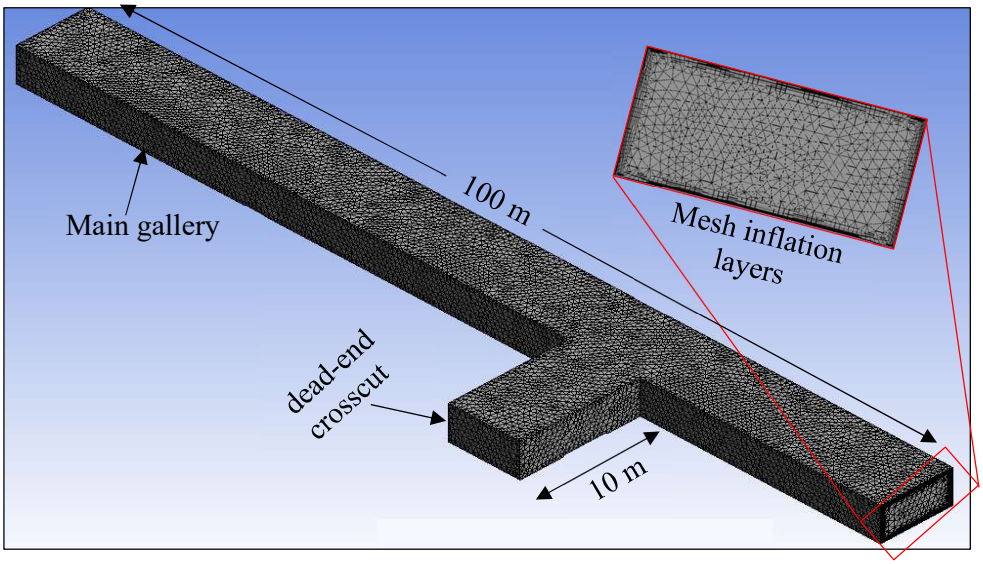

Fig. 4.21 Computational domain and mesh

4.10.2 Setting up flow conditions

The boundary conditions of the model were considered as having an intake air velocity of 2.52 m/s at 300 K and the initial DPM concentration in the dead-end crosscut was considered as 820 μg/m^3. The steady state transient flow modelling was used to model DPM concentration dispersion in a dead-end gallery. For this modelling, the diameters of the DPM particles were considered between $1e^{-9}$ m to $1e^{-7}$ m with a mean diameter of $1e^{-8}$ m. DPM particles were treated as inert materials and the Rosin–Rammler diameter distribution was used. For physical models, the spherical drag law was used as a drag parameter. As the air velocity is low (below 4 m/s), the standard k– ε turbulent model was used. For stochastic tracking, a discrete random walk model with 10 tries and a 0.15 time scale was used. The intake air and DPM are considered as two different phases. The Eulerian–Lagrangian approach is used whereby the gas phase (air) was solved using the Eulerian approach and the particle-phase (DPM) was tracked using the Lagrangian approach.

4.10.3 Model validation and discussion in dead-ends

Fig. 4.22 shows the results of the base case model. It shows how the concentration of the DPM trapped in the 10 m long dead-end crosscut changes over time. **Table 4.5** compares an average of three experimental measurements with the CFD simulation results of DPM concentration. Note that there is good agreement between the simulated results and experimental data, although there are some discrepancies between the simulated and measured results, which can be due to uneven surfaces in the gallery wall that were not considered while modelling; the overall difference varies from –7% to +7%.

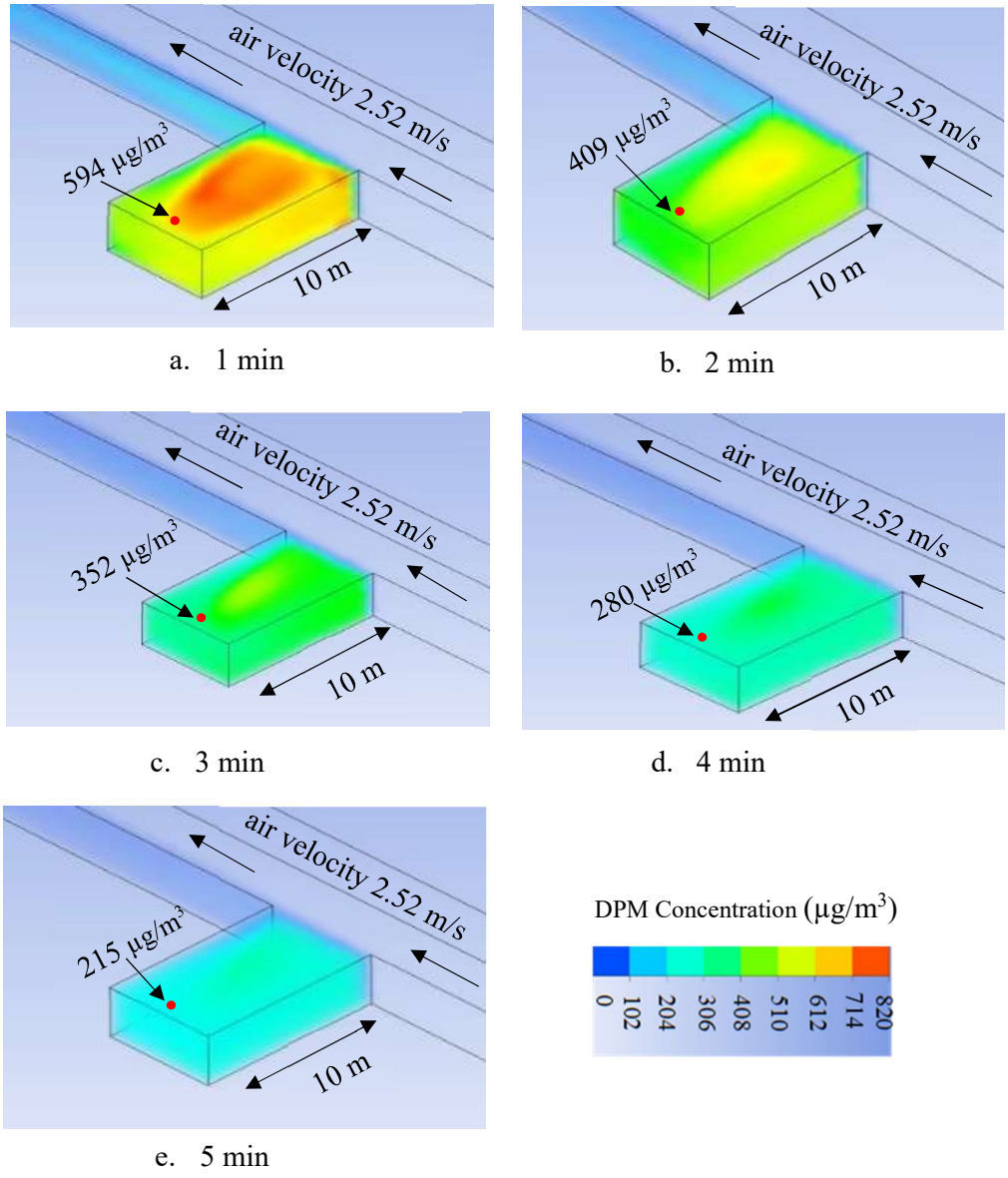

Fig. 4.22 Simulated results of 10 m crosscut DPM dispersion with time

Table 4.5 Comparison of simulated DPM results with experimental results

Time [sec]	Measured DPM concentration (μg/m^3)				Modelled DPM concentration (μg/m^3)	Difference (%)
	Experiment [1]	Experiment [2]	Experiment [3]	Average		
0	817	825	819	820	820	N/A
60	550	560	551	554	594	+7%
120	417	425	422	421	409	–3%
180	350	358	352	353	352	0%
240	284	287	280	284	280	–1%
300	230	235	231	232	215	–7%

Note: Difference (%) is the difference between simulation results and test results and is calculated as (Simulated value – Experimental value)/Experimental value) × 100.

4.10.4 Model validation using Reynolds stress transport model

In this section, the dead-end crosscut DPM dispersion investigations were conducted with the Reynolds stress transport model. **Fig. 4.23** shows the base case DPM dispersion results using the Reynolds stress transport model. **Fig. 4.24** and **Table 4.6** show the comparison of experimental results with simulated results using k– ε and Reynolds stress models. The results show that the average difference between the experimental results and simulated results with k– ε and Reynolds stress models is very low, –0.85 % and +1.93%. As the average difference between the experimental and simulated results with the k– ε model is lower than the Reynolds stress model, dead-end crosscut DPM dispersion studies were conducted with the k– ε model.

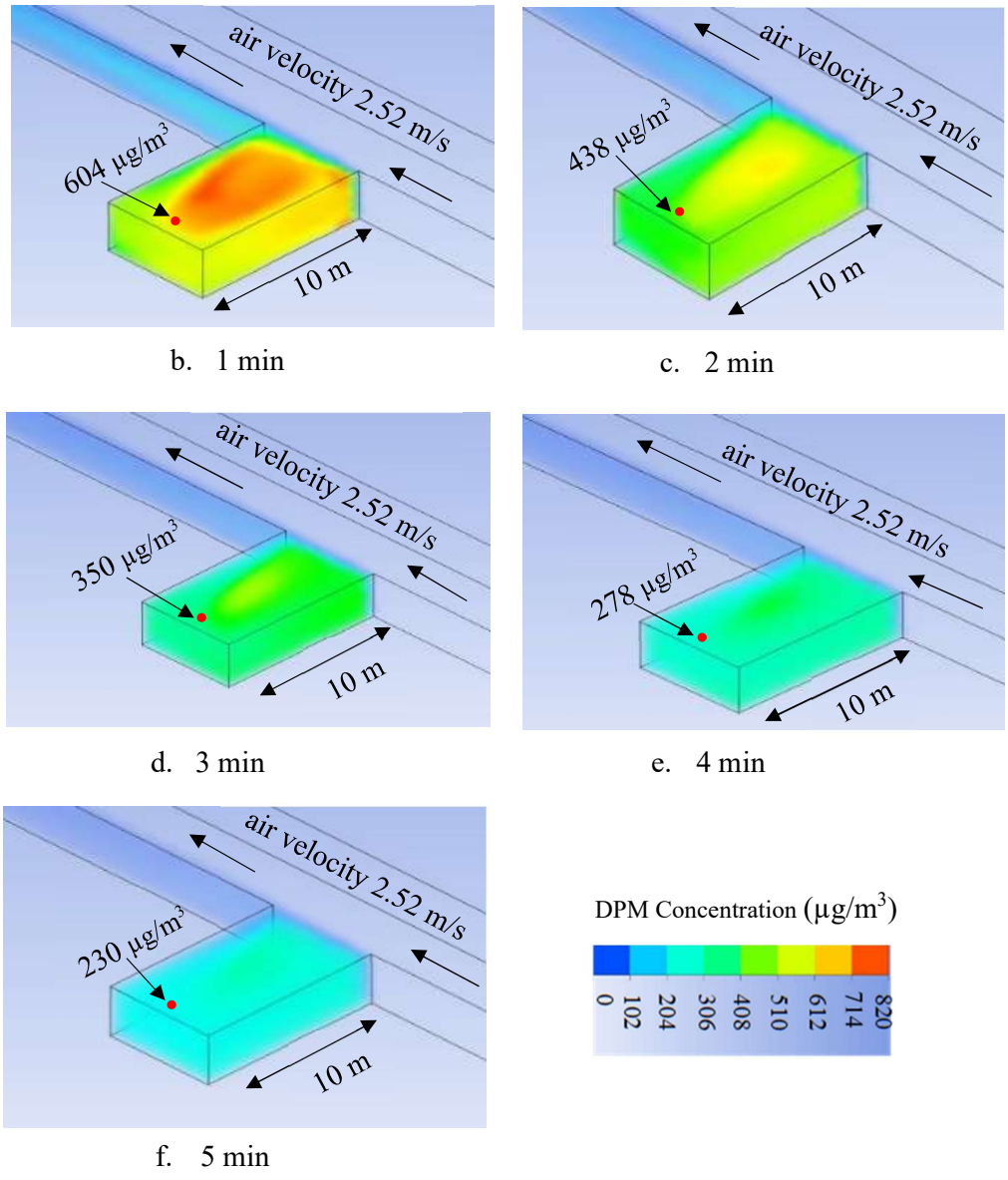

Fig. 4.23 Dead-end crosscut DPM simulated results using Reynolds stress model

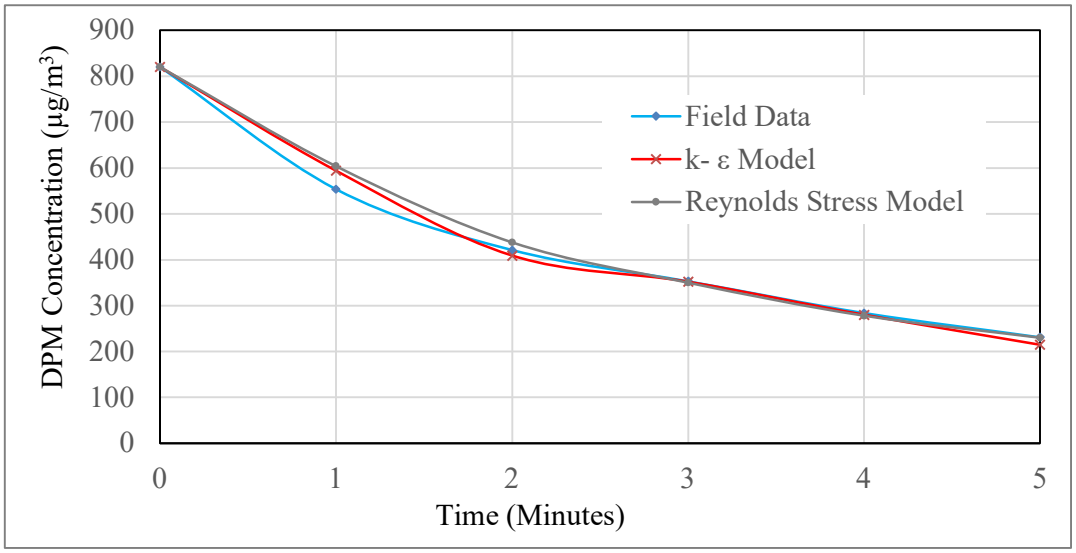

Fig. 4.24 CFD results of Field data, k-ε model and Reynolds Stress model

Table 4.6 Comparison of experimental results with CFD simulated results using k– ε model and Reynolds stress model

Time [sec]	DPM concentration (µg/m³)			Difference (%)	
	Field results	CFD modelling results		k– ε model	Reynolds Stress model
		k– ε model	Reynolds Stress model		
0	820	820	820	NA	NA
60	554	594	604	7	9
120	421	409	438	–3	4
180	353	352	350	0	–1
240	284	280	278	–1	–2
300	231	215	230	–7	0
Average difference %				–0.85	+1.93

Note: Difference (%) is the difference between simulation results and test results and is calculated as (Simulated value – Experimental value)/Experimental value) × 100.

4.11 Decline DPM modelling and validation

To model DPM concentrations in a mine decline, the Ventsim simulator was used. **Fig. 4.25** is the model validated against experimental field data between 9000L to 8500L (1250 m to 1750 m depth below surface). The quantity at 9000L is 80 m^3/s and the DPM in this region is 52 $\mu g/m^3$. Due to leakages in the ventilation wall, some of the decline air leaks to the return airways. In the Ventsim model, leakage was included by changing the ventilation wall resistance. In the model, due to the air leakages, air quantity decreased from 80 m^3/s to 45 m^3/s and from 1250 m to 1550 m, but the DPM concentration in the decline increased from 52 $\mu g/m^3$ to 85 $\mu g/m^3$. At 8750L, the DPM in decline decreased to 45 $\mu g/m^3$ due to the addition of 60 m^3/s of fresh air. At 8500L, the volume of air in decline was 70 m^3/s and the DPM concentration was 32 $\mu g/m^3$.

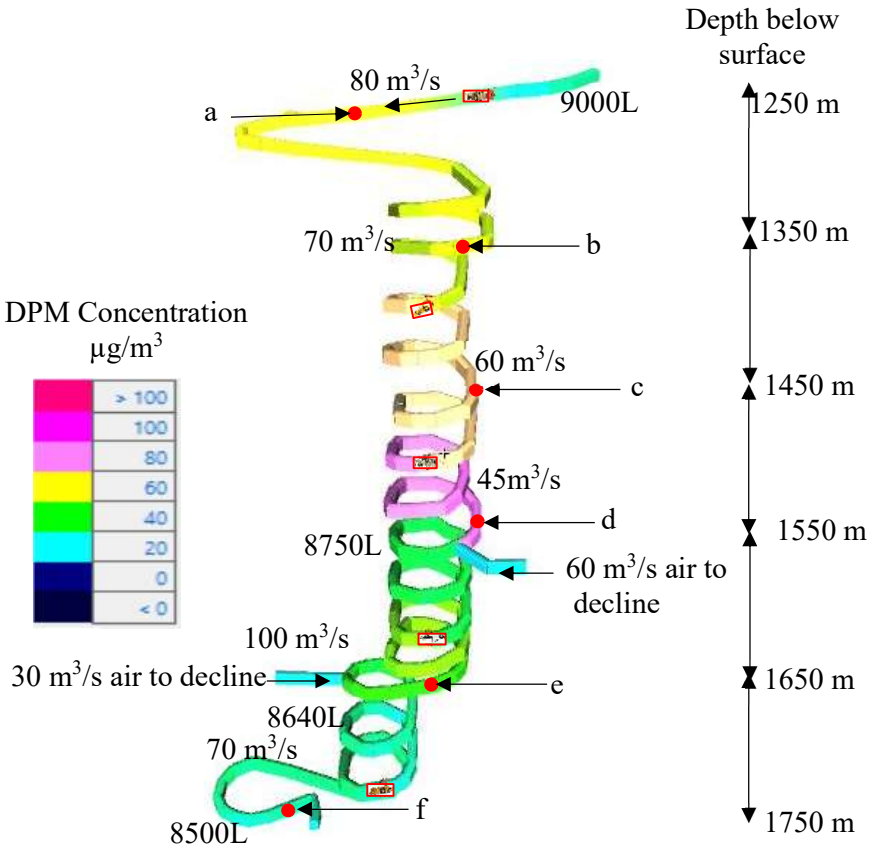

Fig. 4.25 Modelled DPM concentration in decline with field data

Table 4.7 Simulated DPM results vs experimental results in decline

Sample station	Depth of decline below surface (m)	Measured DPM concentration ($\mu g/m^3$)	Modelled DPM concentration ($\mu g/m^3$)	Difference (%)
a	1250	51	52	+2%
b	1350	58	60	+3%
c	1450	65	60	–7%
d	1550	85	85	+2%
e	1650	45	45	+2%
f	1750	35	32	–8%

Note: Difference (%) is the difference between simulation results and test results and is calculated as (Simulated value – Experimental value)/Experimental value) × 100.

Table 4.7 shows the comparison of experimental results with simulated results; note that the simulated results mostly agreed with the measured data; the overall difference varied from –8% to +2%.

4.12 Summary

Ventsim is a commonly used ventilation software for underground mines in Australia. While it can simulate an overall underground mine scenario, it is difficult to use Ventsim to generate contaminant maps in localised areas. Computational fluid dynamics (CFD) is one of the developments of advanced computer-based numerical codes. CFD has been used to address many typical underground mining problems such as ventilation, gases, dust and the spontaneous combustion of coal, mine fires and DPM.

This chapter described the governing equations of CFD models where CFD simulation studies were carried out with NIOSH filed data for an LHD. The DPM results were

compared with the field data, where the data was measured 500 m away from the LHD. The CFD simulations provided the air velocity and concentration of DPM 1 m and 500 m downstream of the exhaust pipe. The DPM concentrations were high near the exhaust pipe region and covered the entire roadway 500 m downstream of the diesel engine.

Base-case CFD models were developed and validated against experimental field data using discrete phase modelling. In a few dead-end DPM dispersion cases, species transport modelling studies were also used. These models used 3D CAD models of the vehicles and underground workings imported into ANSYS Fluent. The shape and dimensions of the computational domain are the same as those of the experimental underground galleries.

The man-riding vehicle model results show that a high DPM concentration exists between the exhaust pipe side of the vehicle and the wall. At the downstream vehicle side, DPM flow moves towards the centre of the gallery. At 20 m from the vehicle, DPM particles spread throughout the entire roadway.

DPM concentration simulation studies were conducted with both discrete-phase modelling and species transient flow modelling. Results show that the DPM concentration fields are almost equally well modelled by the discrete-phase and species transport modelling approaches. It is concluded that the difference of results between discrete phase modelling and species transport modelling is –9% to 11%.

The LHD modelling results show that if the DPM source flow and ventilation air co-flow (are in the same direction), the DPM is confined predominantly to the middle of the roadway. At 5 m downstream of the vehicle, the maximum concentration is in the middle of the gallery and negligible on the left and right sides of the roadway. At 1 m downstream of the vehicle, DPM concentration at the roadway centre is 70 $\mu g/m^3$ and low

concentrations at the left and right sides of the roadway.

If the DPM source flow and the ventilation airflow are in counter-flow (in opposite directions), the DPM spreads throughout the entire cross-section of the roadway. In this case, the vehicle operator will be more susceptible to exposure to high concentrations of DPM; the DPM concentration near the LHD operator is 125 $\mu g/m^3$. At 10 m downstream of the vehicle, the maximum concentration is at the middle of the gallery and the left and right sides of the roadway. At 20 m downstream of the vehicle, DPM spread throughout the entire roadway. DPM concentration at the centre of the roadway was 34 $\mu g/m^3$.

In every model validation, the simulated models were in reasonable agreement with the field experimental data, although there were some differences between the simulated and measured results due to uneven gallery walls and uneven machine surfaces that were not modelled in detail. The overall difference between the simulated DPM concentration values and the experimental values varied from –14.2% to +14% for the man-riding vehicle model, –17% to +21% for the LHD co-flow model, –21% to +21% for the LHD counter-flow model, –5% to +4% for the 10 m unventilated dead-end crosscut DPM dispersion model and –8% to +2% for the decline validation model.

These validated CFD models were used for progressive DPM modelling investigations from Chapter 5 to Chapter 7.

Chapter 5

Parametric Studies with Different Ventilation and Operating Conditions

This chapter describes DPM concentration distribution simulations under different operational and ventilation conditions. As the concentration of DPM in underground working areas depends on the underground environment and the conditions in which the vehicles operate (Bugarski, 1999, Kurnia et al., 2014), CFD simulations were carried out to understand the effect of different intake air velocities, different directions of diesel vehicle exhaust, different temperatures of the exhaust fumes and the intake air temperatures on DPM dispersion patterns in an underground environment. These parametric studies are useful to understand DPM particle flow in different mining conditions, provide DPM control strategies and minimise exposure to DPM. The validated CFD models presented in the previous chapter were used for this study.

5.1 Effect of intake air velocity on DPM dispersion

To understand the effect of intake air velocity on the dispersion and concentration of DPM emitted from diesel-powered vehicles, simulation studies were carried out with different air velocities: 0.5 m/s, 0.75 m/s, 1.26 m/s (base case), 2 m/s, 2.5 m/s and 3 m/s. For these simulations the computational domain, computational mesh, flow and boundary conditions were considered from the base case man-riding model of section 4.6 of Chapter 4.

5.1.1 Air velocity 0.5 m/s

The contours of DPM concentration in the mine gallery when the intake air velocity was 0.5 m/s are shown in **Fig. 5.1**. It shows a DPM concentration greater than 200 µg/m^3 in almost the entire cross-section of the roadway and on the passenger side of the vehicle.

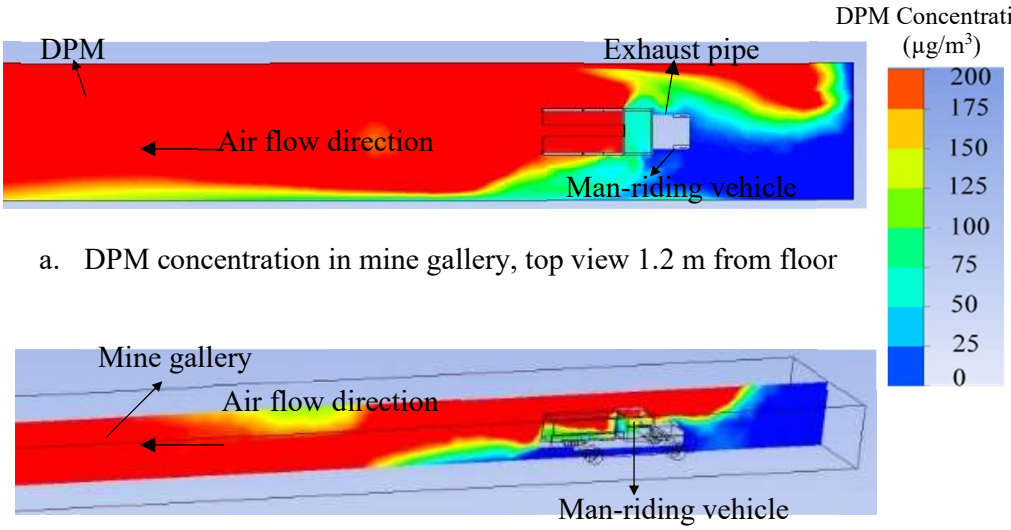

a. DPM concentration in mine gallery, top view 1.2 m from floor

b. DPM concentration in the vertical plane of symmetry of the gallery

Fig. 5.1 DPM distribution with 0.5 m/s air velocity

5.1.2 Air velocity 0.75 m/s

The concentration of DPM corresponding to an intake air velocity of 0.75 m/s is shown in **Fig. 5.2**. The DPM concentration near the vehicle is high at the gallery roof. DPM concentration of about 130 µg/m^3 is seen in the middle of the roadway and up to 20 m downstream of the vehicle. Beyond 20 m, the concentration is 100 µg/m^3 near the ceiling and negligible near the floor.

5.1.3 Air velocity 1 m/s

The concentration of DPM corresponding to an intake air velocity of 1 m/s is shown in

Fig. 4.3. The figure shows a high concentration near the gallery roof, a concentration of about 125 µg/m^3 in the middle of the roadway and up to 20 m downstream of the vehicle. Beyond 20 m downstream, the concentration was 60 µg/m^3 near the ceiling, reducing to nearly zero towards the floor.

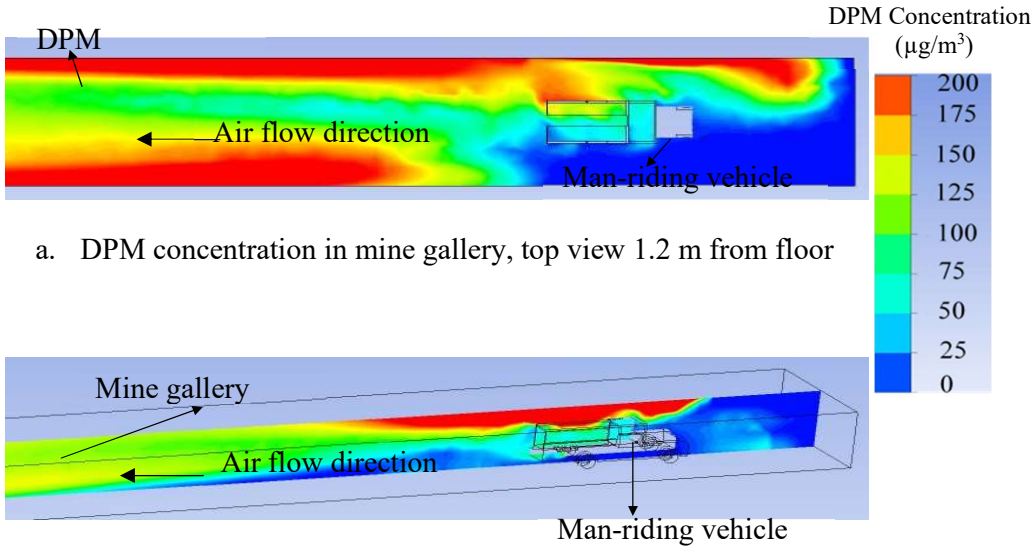

a. DPM concentration in mine gallery, top view 1.2 m from floor

b. DPM concentration in the vertical plane of symmetry of the gallery

Fig. 5.2 DPM distribution with 0.75 m/s air velocity

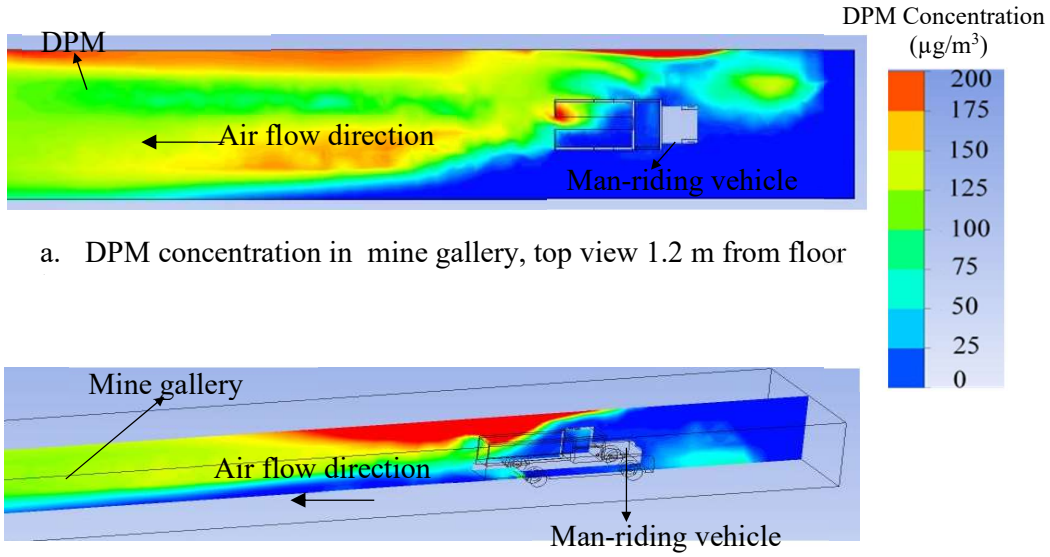

a. DPM concentration in mine gallery, top view 1.2 m from floor

b. DPM concentration in the vertical plane of symmetry of the gallery

Fig. 5.3 DPM distribution with 1 m/s air velocity

5.1.4 Air velocity 2 m/s

DPM concentration contours for an intake air velocity of 2 m/s are shown in **Fig. 5.4**. There is a high concentration of DPM near the exhaust pipe and most particles are dissipated towards the gallery ceiling due to the high air velocity. In the middle of the roadway, there was almost no DPM up to 5 m downstream of the side of the vehicle. From 5 m to 10 m, there was a high concentration near the roof and further downstream the DPM had spread throughout the entire roadway.

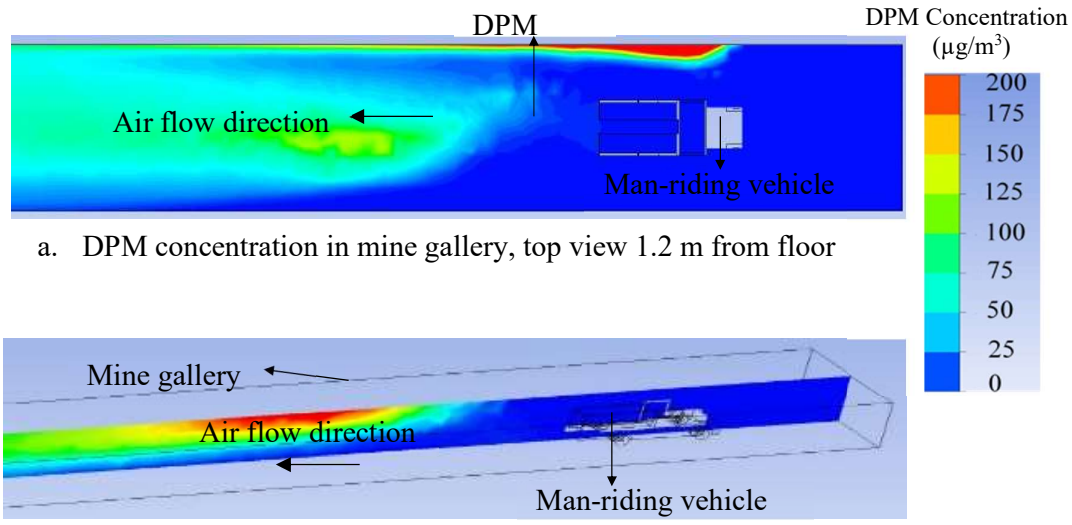

a. DPM concentration in mine gallery, top view 1.2 m from floor

b. DPM concentration at middle of the gallery

Fig. 5.4 DPM distribution with 2 m/s air velocity, top view and centre section of mine gallery

5.1.5 Air velocity 2.5 m/s

The DPM concentration corresponding to an intake air velocity of 2.5 m/s is shown in **Fig. 5.5**. Here the DPM concentration is high at the gallery roof, with 50 µg/m^3 of DPM in the middle of the roadway and up to 20 m downstream of the vehicle. Beyond 20 m downstream, a DPM concentration of about 30 µg/m^3 is near the ceiling and none close to the floor.

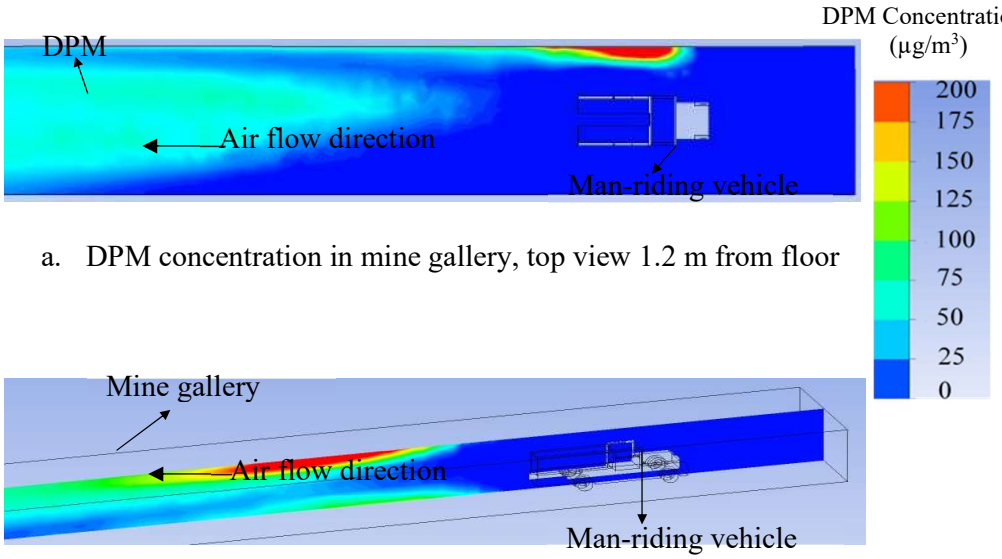

a. DPM concentration in mine gallery, top view 1.2 m from floor

b. DPM concentration in the vertical plane of symmetry of the gallery

Fig. 5.5 DPM distribution with 2.5 m/s air velocity, top view and centre section of a mine gallery

5.1.6 Air velocity 3 m/s

Fig. 5.6 shows the DPM concentration field when the intake air velocity was 3 m/s. The DPM concentration is high at the gallery roof and almost zero in the middle of the roadway up to 20 m downstream of the vehicle. Beyond 20 m, there was a concentration of about 25 µg/m^3 near the ceiling and almost zero near the floor.

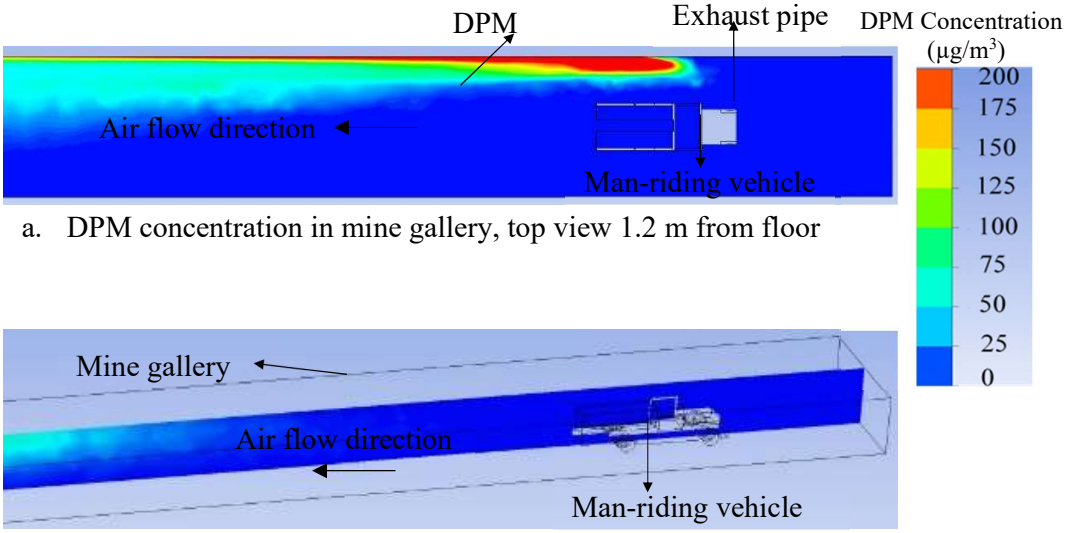

a. DPM concentration in mine gallery, top view 1.2 m from floor

b. DPM concentration at middle of the gallery

Fig. 5.6 DPM distribution with 3 m/s air velocity, top view and centre section view of mine gallery

Fig. 3.7 shows the concentration of DPM for different air velocities (0.5 m/s, 0.75 m/s, 1 m/s, 1.26 m/s, 2 m/s, 2.5 m/s and 3 m/s) and at various sampling points 'a' (**Fig. 3.4**) downstream of the vehicle. If the intake air velocity is 0.5 m/s, the concentration ranges from 250 µg/m^3 to 289 µg/m^3 over 15 m downstream of the vehicle, but up to 40 m from the vehicle the concentration spread is from about 220 µg/m^3 to 258 µg/m^3.

Beyond 15 m downstream of the vehicle, the concentrations of DPM is uniform across the passage due to turbulent mixing for all the different air velocities, but the concentration gradually decreases as the air velocity increases. With an air velocity of 0.5 m/s, the average concentration of DPM downstream of the vehicle was about 249 µg/m^3 and with an air velocity of 3 m/s the average concentration decreased to about 71 µg/m^3.

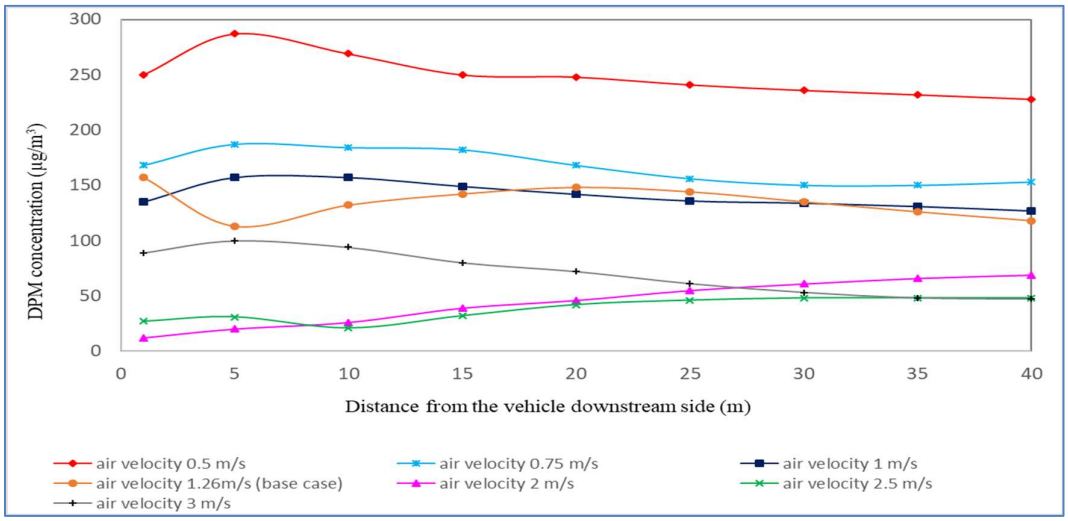

Fig. 5.7 Concentrations of DPM for different air velocities at different sampling stations at sampling point 'a'

Fig. 5.8 shows the concentrations of DPM for different air velocities (0.5 m/s, 0.75 m/s, 1 m/s, 1.26 m/s, 2 m/s, 2.5 m/s and 3 m/s) at different locations of sampling point 'b' (**Fig. 3.4**). If the air velocity was 0.5 m/s, from the source to 40 m, DPM was evenly distributed between 220 µg/m^3 to 234 µg/m^3 over about 40 m downstream of the source. If the air velocity was 3 m/s, there was almost no DPM in the middle of the airway up to about 15 m from the vehicle. Further downstream, the concentration of DPM gradually increased to about 43 µg/m^3 at 40 m; in the middle of the roadway, from 1 m to 40 m, the average concentration of DPM was 226 µg/m^3, 120 µg/m^3, 66 µg/m^3 and 19 µg/m^3 for air velocities of 0.5 m/s, 1 m/s, 2 m/s and 3 m/s, respectively.

Fig. 5.9 shows the concentrations of DPM as a function of downstream distance for different air velocities (0.5 m/s, 0.75 m/s, 1 m/s, 1.26 m/s, 2 m/s, 2.5 m/s and 3 m/s) at various locations of the sampling point 'c' (**Fig. 3.4**). If the air velocity was 3 m/s, there was no DPM at sample point 'c' up to about 30 m, but further downstream the DPM

gradually increased to 17 µg/m^3 at 40 m. From 1 m to 40 m, the average DPM concentration was about 213 µg/m^3, 109 µg/m^3, 28 µg/m^3 and 3 µg/m^3 for air velocities of 0.5 m/s, 1 m/s, 2 m/s and 3 m/s, respectively.

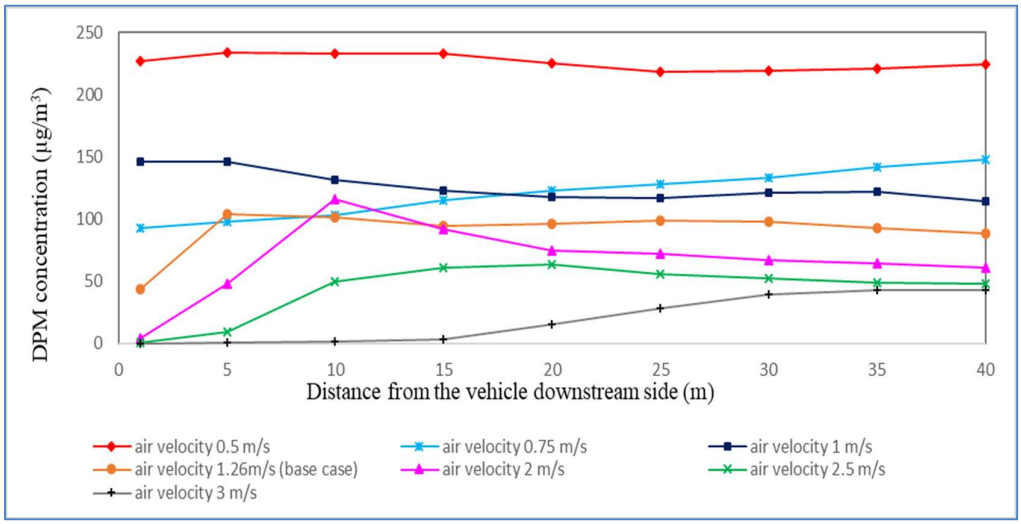

Fig. 5.8 Concentrations of DPM with different air velocities at different sampling stations at sampling point 'b'

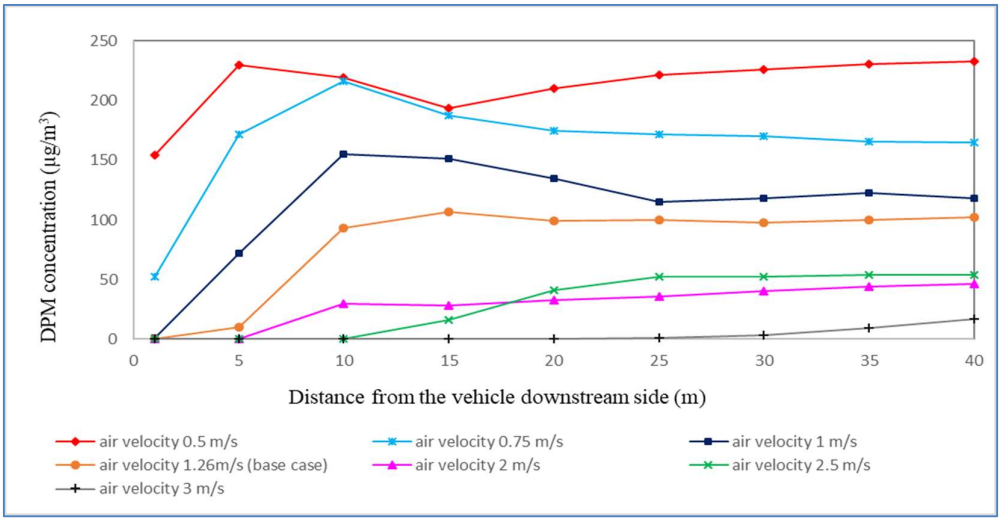

Fig. 5.9 Concentrations of DPM with different air velocities at different sampling stations at sampling point 'c' with respect to DPM source

Changes in the percentage of DPM with increasing intake air velocities were calculated for air velocities of 0.5 m/s, 0.75 m/s, 1 m/s, 1.26 m/s (Base case), 2 m/s, 2.5 m/s and 3 m/s at sampling points ‘a’, ‘b’ and ‘c’. **Fig. 5.10** shows the changes in DPM concentration at 10 m (a) and 40 m (b) downstream of the vehicle as functions of the intake air velocity.

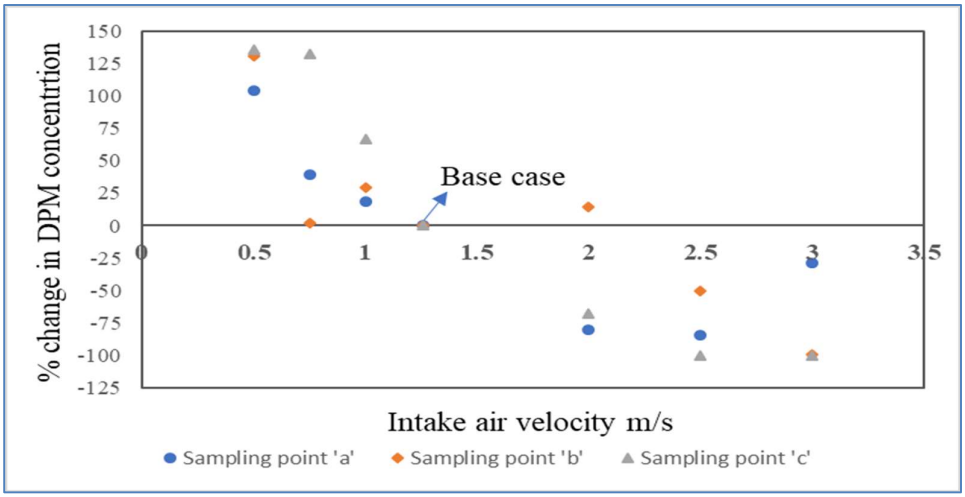

a. At 10 m downstream to the vehicle

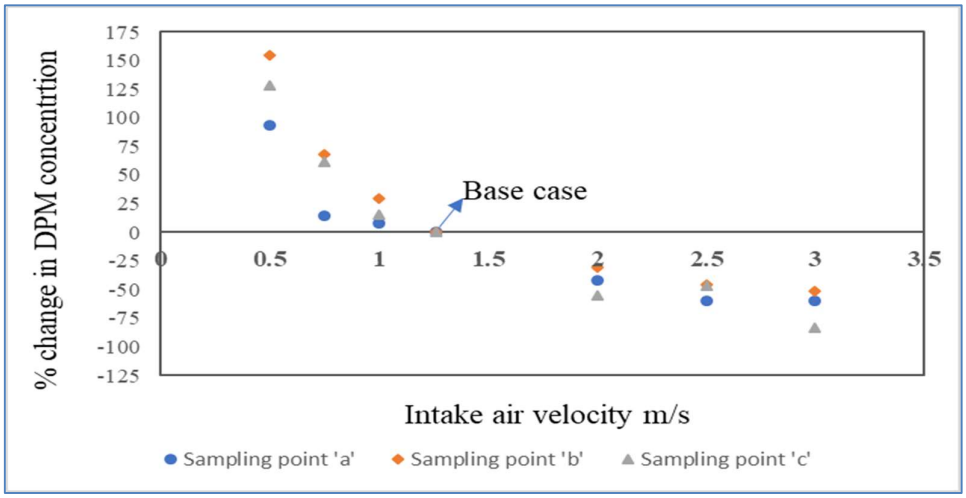

b. At 40 m downstream to the vehicle

Fig. 5.10 Changes in the percentage of intake air velocity causes changes in percentages of DPM at 10 m and 40 m downstream of the vehicle

At 10 m and 40 m downstream of the vehicle, the average variations of DPM concentration at sample points ‘a’, ‘b’ and ‘c’ were calculated with air velocities of 0.5 m/s, 0.75 m/s, 1 m/s, 1.26 m/s, 2 m/s, 2.5 m/s and 3 m/s. **Table 5.1** shows the average concentration of DPM 10 m and 40 m downstream of the vehicle with different intake air velocities. A 60% reduction in the air velocity caused a 125% increase in the DPM 40 m downstream of the vehicle and a 98% increase in air reduced the DPM by 50% at 40 m downstream of the side of the vehicle.

Table 5.1 Variations in the concentration of DPM with air velocities at 10 m and 40 m downstream side

Air velocity (m/s)	Air velocity Increased (+) / decreased (–)% from the base case	DPM concentration Increased (+) / decreased (–)% at 10 m downstream side	DPM concentration Increased (+) / decreased (–)% at 40 m downstream side
0.5	–60%	+12%	+125%
0.7	–40%	+57%	+48%
1	–20%	+38%	+17%
1.26 (Base case)	0	0	0
2	+58%	–44%	–42%
2.5	+98%	–78%	–50%
3	+138%	–75%	–64%

5.2 Effect of exhaust pipe location on DPM dispersion

The concentration of DPM near the vehicle on the operator’s side and the downstream side of the vehicle may depend on the direction of the exhaust pipe. To understand the variations in the DPM flow pattern due to the direction of the exhaust pipe, CFD modelling studies were carried out with the exhaust at the top, back and side of the

vehicle. For this study, the validated LHD model with the exhaust and airflow in opposite directions (counter-flow) was considered.

The locations and orientations of the exhaust pipes on diesel-powered vehicles are different for different manufacturing companies and types of vehicles, **Fig. 5.11** and **Fig. 5.12** show the most common locations of loader exhaust pipes. For this study, an intake air velocity of 2 m/s and exhaust fume temperature of 335 K were considered. For these simulations, computational domain, computational mesh, flow and boundary conditions are considered from the base case LHD counter-flow model of section 4.9 of Chapter 4.

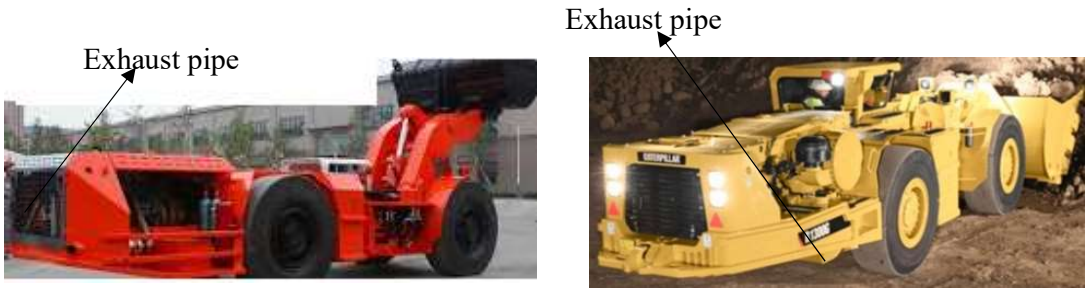

a. Exhaust pipe at back side

b. Exhaust pipe at bottom side

Fig. 5.11 Different exhaust pipe directions of loading vehicles

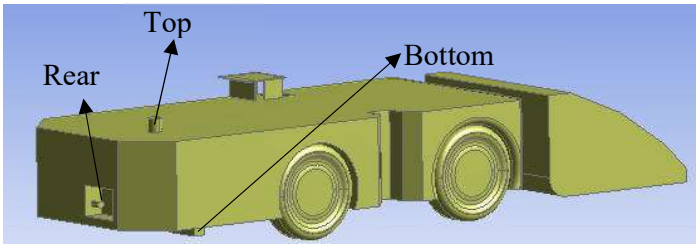

Fig. 5.12 Locations of exhaust pipes on an LHD model

Fig. 5.13 shows the patterns of DPM concentration for different exhaust pipe locations. If the exhaust pipe is at the bottom of the vehicle the DPM is concentrated at the bottom and side of the gallery near the vehicle, as shown in **Fig. 5.13**a. In this case the vehicle

operator is less likely to be exposed to high concentrations of DPM. If the exhaust pipe is at the rear of the vehicle the DPM is concentrated near the operator and on top of the gallery near the vehicle, as shown in **Fig. 5.13**b. In this case the operator is more likely to be exposed to high concentrations of DPM.

If the exhaust pipe is located at the top of the vehicle, the DPM is concentrated close to the roof of the gallery near the vehicle and then spreads throughout the entire roadway downstream of the vehicle, as shown in **Fig. 5.13**c. In this instance the operator may be exposed to high concentrations of DPM.

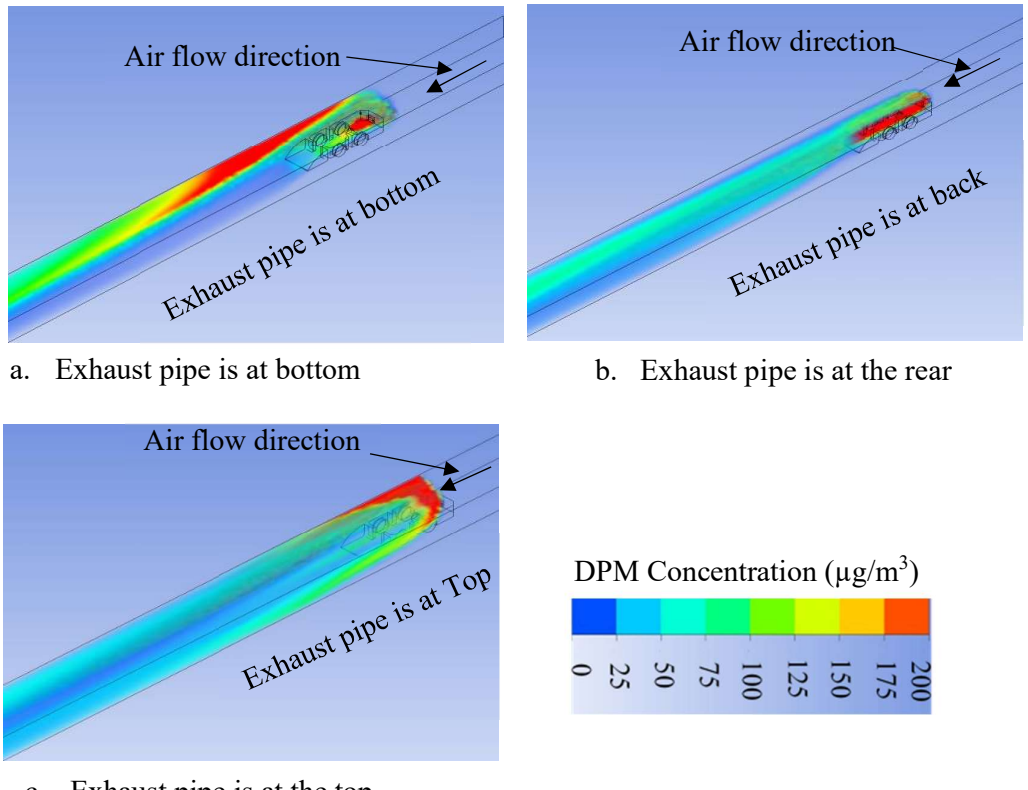

a. Exhaust pipe is at bottom

b. Exhaust pipe is at the rear

c. Exhaust pipe is at the top

Fig. 5.13 Concentration of DPM downstream of the vehicle when the exhaust pipe is at the back, bottom and top of the vehicle

Fig. 5.14 shows the concentration of DPM across the gallery at 10 m downstream of the vehicle when the exhaust pipe is at the back, bottom and top of the LHD. The figure

shows that if the exhaust pipe is at the back, bottom and top of the LHD, the concentration of DPM 10 m downstream and 1.2 m from the floor is 48 mg/m^3, 12 mg/m^3 and 10 mg/m^3, respectively, in the middle of the gallery.

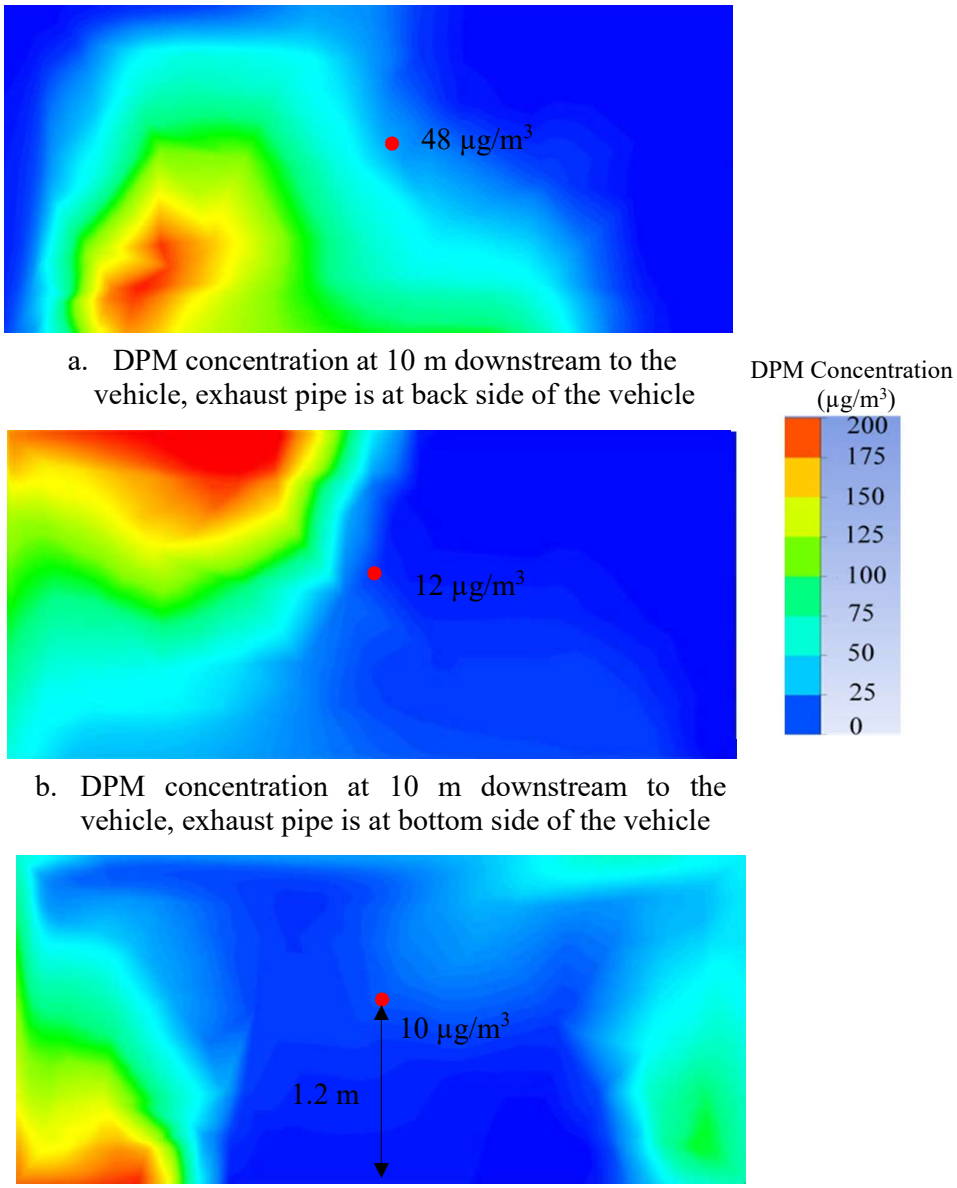

a. DPM concentration at 10 m downstream to the vehicle, exhaust pipe is at back side of the vehicle

b. DPM concentration at 10 m downstream to the vehicle, exhaust pipe is at bottom side of the vehicle

c. DPM concentration at 10 m downstream to the vehicle, exhaust pipe is at top side of the vehicle

Fig. 5.14 Concentrations of DPM 10 m downstream of the vehicle when the exhaust pipe is at the back, bottom and top of the vehicle

Fig. 5.15 shows the changes in the concentrations of DPM with LHD when the exhaust pipe is at the back, bottom and top. The figure shows the DPM concentration at the middle of the gallery and at 1.2 m from the floor; it also shows that if the exhaust pipe is at the back of the LHD, the concentration of DPM was about 50 mg/m^3 from 5 m to 50 m downstream of the vehicle. If the exhaust pipe is at the bottom of the LHD, the concentration of DPM sharply increased from 6 µg/m^3 at 5 m to 45 µg/m^3 at 20 m; further downstream, this concentration gradually increased to 52 µg/m^3 at 50 m. If the exhaust pipe is at the top of the LHD, the concentration gradually increased from 6 µg/m^3 at 5 m to 23 µg/m^3 at 50 m.

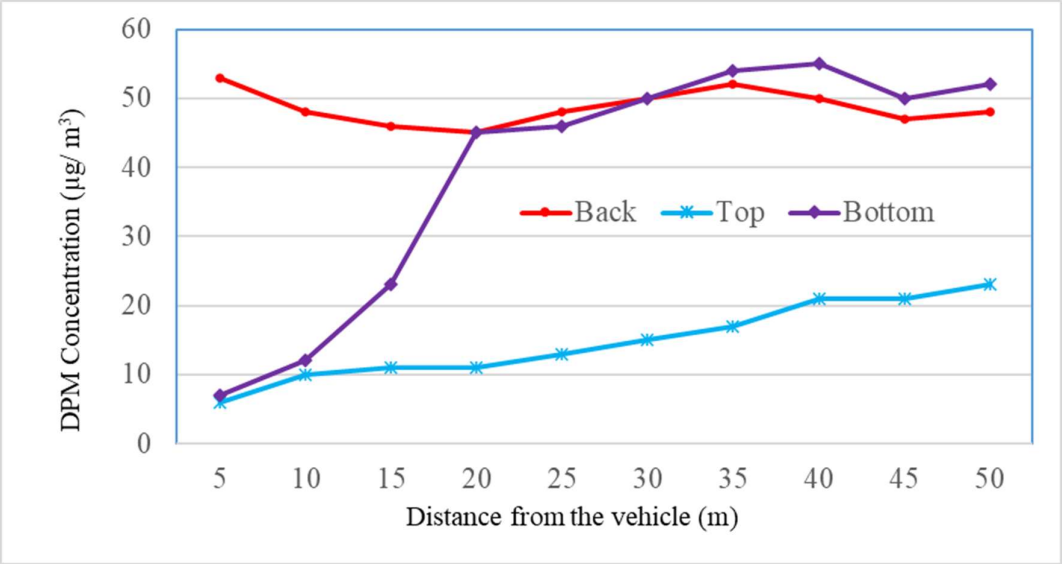

Fig. 5.15 Concentrations of DPM 10 m downstream of the vehicle and 1.2 m above the floor with the exhaust pipe at the back, bottom and top of the vehicle

Fig. 5.16 shows DPM concentrations at the LHD operator's cabin when the exhaust pipe is at the bottom, back and top sides of the LHD. In this investigation, the intake drive airflow was 2 m/s. The figure shows that if the exhaust pipe is at the back (**Fig. 5.16**a) and if the exhaust pipe is at the bottom **Fig. 5.16**b), there is no DPM where the operator sits, but if the exhaust pipe is on top of the LHD the operator is exposed to 9 µg/m^3 of

DPM (**Fig. 5.16**c). Therefore, from the operator's perspective, it is better to have the exhaust pipe at the bottom of the vehicle.

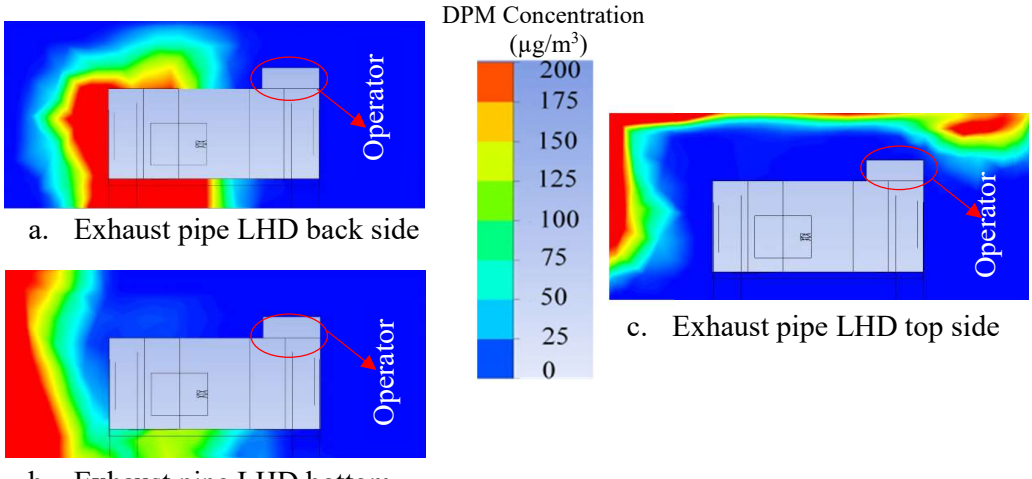

a. Exhaust pipe LHD back side

b. Exhaust pipe LHD bottom

c. Exhaust pipe LHD top side

Fig. 5.16 Concentrations of DPM when the LHD exhaust pipe is at the back, bottom and top of the vehicle

5.3 Effect of discharge temperature on DPM dispersion

The DPM temperature at the exhaust pipe discharge point varies with operating conditions because the temperature of a diesel-powered vehicle's exhaust fumes depends mainly on its oxidising catalyst particulate filter (Domesle et al., 1984) and the exhaust cooler and engine load (Gonzales, 2008). The concentration of DPM and the flow pattern downstream of the vehicle may depend on the temperature of DPM at the discharge point. To study the effect of temperature on the DPM flow patterns, CFD simulations were carried out by assuming DPM source temperatures of 50°C, 60°C, 70°C and 80°C, each case assuming co-flow (exhaust release and airflow in the same direction). For these simulations, computational domain, computational mesh, flow and boundary conditions are considered from the base case LHD co-flow model of section 4.8 of Chapter 4.

Fig. 5.17 and **Fig. 5.18** show DPM concentrations for different discharge temperatures at the source with the ventilation air and exhaust discharge in co-flow. If the temperature is high, the DPM is dispersed throughout the entire roadway. For DPM source temperatures of 50ºC, 60ºC, 70ºC and 80ºC, the concentration of DPM 50 m downstream to the source in the middle of the roadway at 1.2 m from the floor was 43 µg/m^3, 39 µg/m^3, 12 µg/m^3 and 9 µg/m^3, respectively.

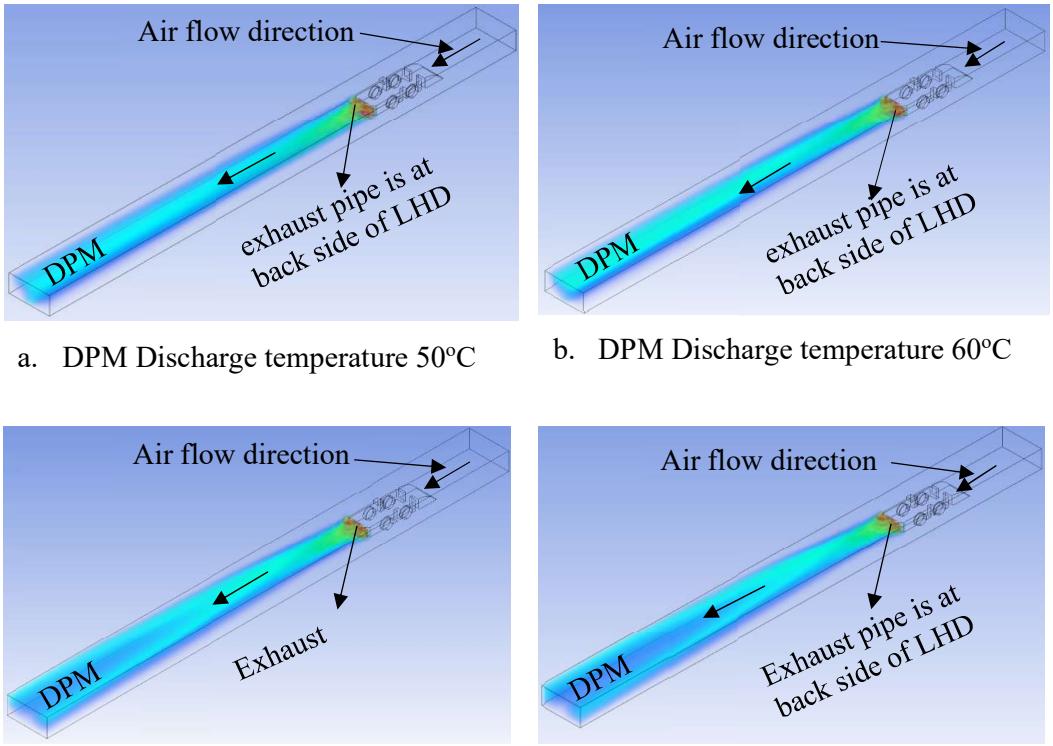

a. DPM Discharge temperature 50ºC

b. DPM Discharge temperature 60ºC

c. DPM Discharge temperature 70ºC

d. DPM Discharge temperature 80ºC

Fig. 5.17 Concentrations of DPM for different exhaust temperatures

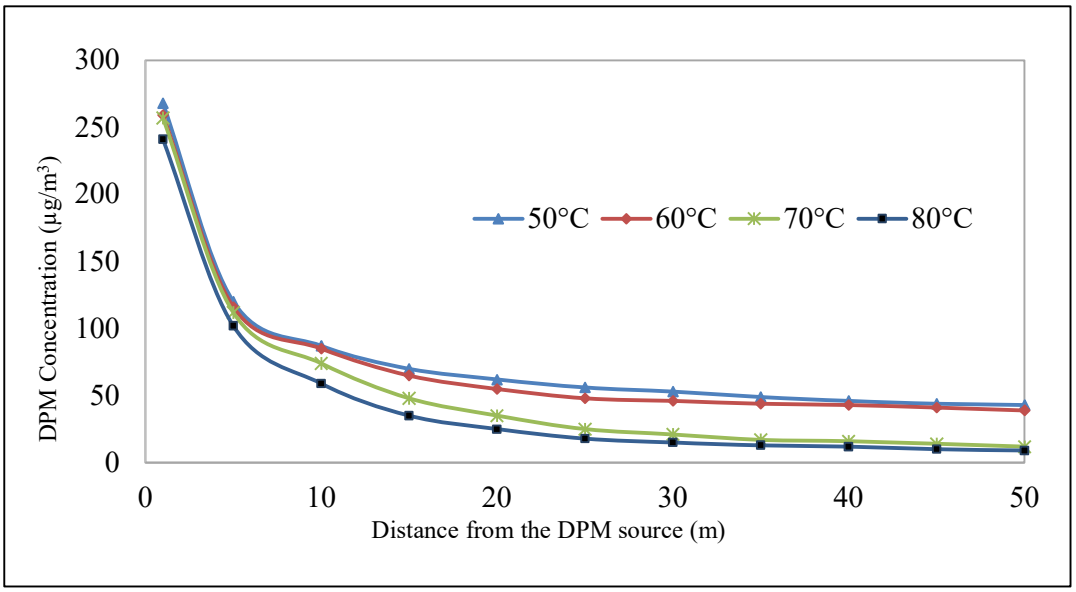

Fig. 5.18 Changes of DPM concentration at downstream of the LHD with different DPM temperatures at exhaust pipe for the co-flow case

5.4 Effect of intake air temperature on DPM dispersion

The effect of different intake air temperatures on the DPM concentration field was investigated. In these simulations, the source was assumed to be located on a man-riding vehicle. An intake air velocity of 1.5 m/s was assumed. Intake air dry bulb temperatures of 20ºC, 30ºC and 40ºC were considered. For these simulations, computational domain, computational mesh, flow and boundary conditions are considered from the base case man-riding model of section 4.6 of Chapter 4. **Fig. 5.19** shows the results of CFD modelling. It is seen that if the intake air temperature is lower, more DPM particles concentrate closer to the floor, but if the intake air temperature is high **(Fig. 5.19c)** the DPM particles disperse over the entire roadway and the concentration of DPM is higher in the middle of the roadway than when the intake air temperature is lower.

Fig. 5.20 shows the changes in DPM concentration with the intake air temperature in the

middle of the roadway and at 1.2 m from the floor. If the intake air temperature is high, more DPM concentrates in the middle of the gallery. DPM concentration at the middle of the gallery is increasing from 15 m downstream due to particles moving towards the centre of the roadway. From 35 m downstream of the vehicle, the concentration of DPM gradually reduced in every case due to particles spreading in the entire cross-section of the roadway (**Fig. 4.13**).

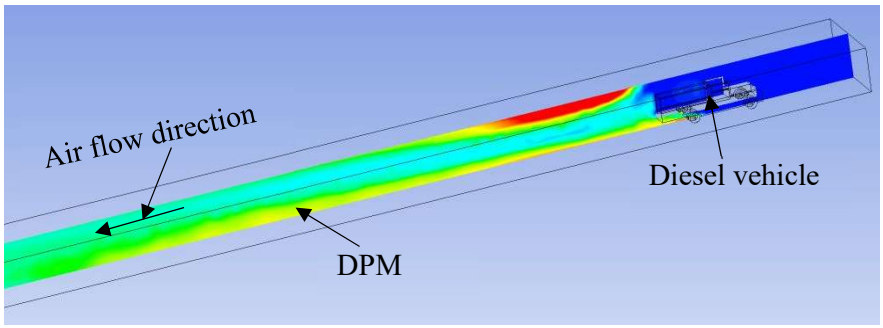

a. DPM Concentration, air temperature 20°C

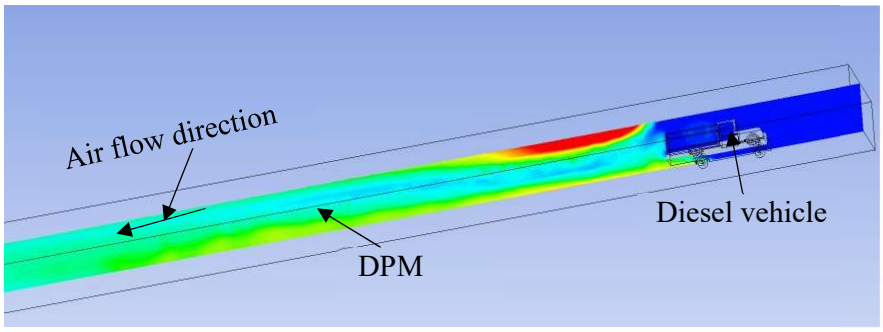

b. DPM Concentration, air temperature 30°C

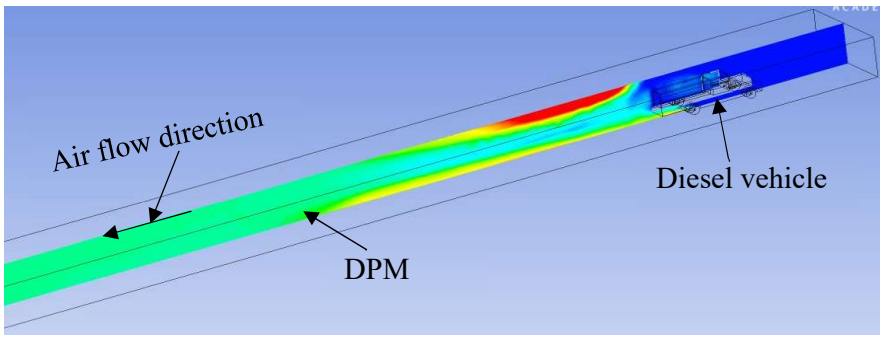

c. DPM Concentration, air temperature 40°C

Fig. 5.19 Concentration of DPM when the air temperature is 20°C, 30°C and 40°C

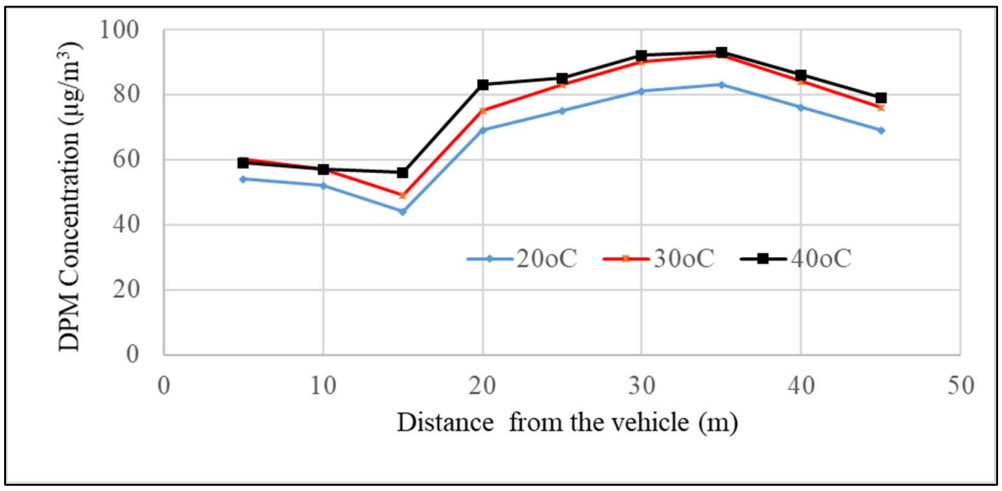

Fig. 5.20 Concentration of DPM at different locations on the downstream side of the vehicle when the air temperature is 20°C, 30°C and 40°C

5.5 Effect of vehicle morphology on DPM concentration

Different diesel-powered underground vehicles have different morphologies (shapes). To estimate the effect of vehicle morphology on DPM concentration patterns, simulation studies were conducted using a CAD model of a man-riding vehicle and an equivalent rectangular box of the same overall dimensions as the man-riding vehicle. Computational domain, computational mesh, flow and boundary conditions are considered from the base case man-riding model of section 4.7 of Chapter 4. The length, width and height of the box were 6.25 m, 2 m and 1.95 m, respectively. **Fig. 5.21** shows the CFD model and meshed model of the man-riding vehicle sized box. Simulation studies were conducted with a 1 m/s air velocity. **Fig. 5.22** shows comparisons between the CFD simulation results with the man-riding vehicle and man-riding vehicle sized box. The slight difference between the DPM concentration contours downstream of the vehicle is due to the morphology (shape) of the vehicle. The difference is more pronounced near the obstacle than at farther locations.

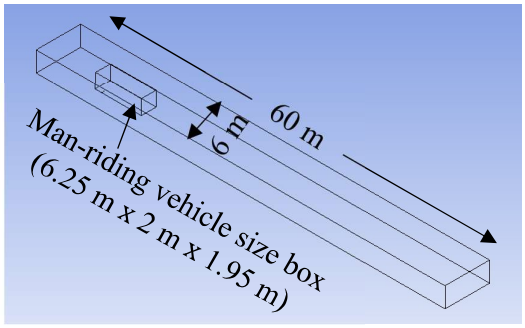

a. CFD model of man-riding vehicle sized box with gallery – computational domain

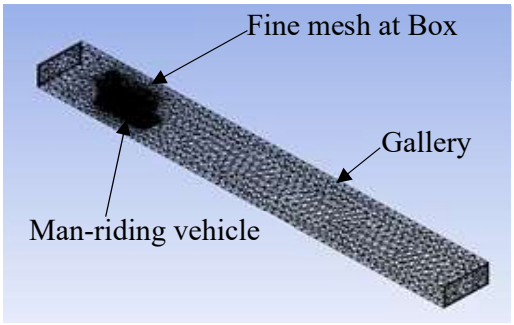

b. Meshed model of man-riding sized shaped box with gallery – computational domain

Fig. 5.21 CFD and meshed model of man-riding vehicle sized box and gallery

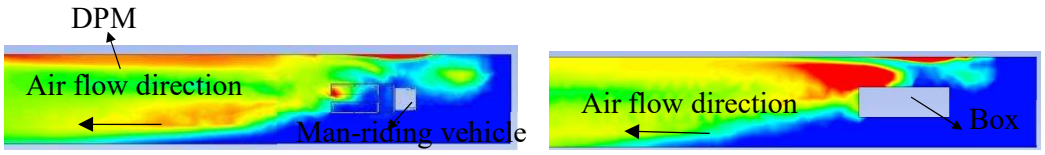

a. DPM concentration in mine gallery, top view 1.2 m from floor

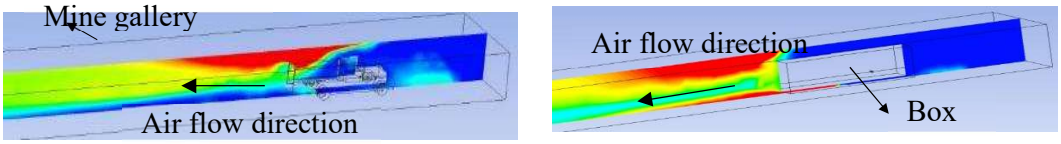

b. DPM concentration in the vertical plane of symmetry of the gallery

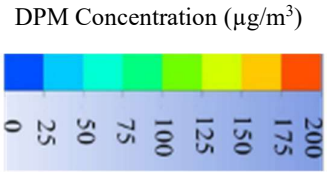

Fig. 5.22 DPM distribution with 1 m/s air velocity with man-riding vehicle and box-shaped vehicle

Fig. 5.23 shows the concentrations of DPM for the man-riding vehicle and the equivalent box at the middle of the roadway and 1.2 m height from the floor, of sampling point 'b' **Fig. 3.4**. If the air velocity is 1 m/s, the DPM concentration at 40 m from the man-riding

vehicle and the box are 123 µg/m^3 and 100 µg/m^3. Box-shaped obstacles show less DPM concentrations than the actual vehicles in the middle of the roadway.

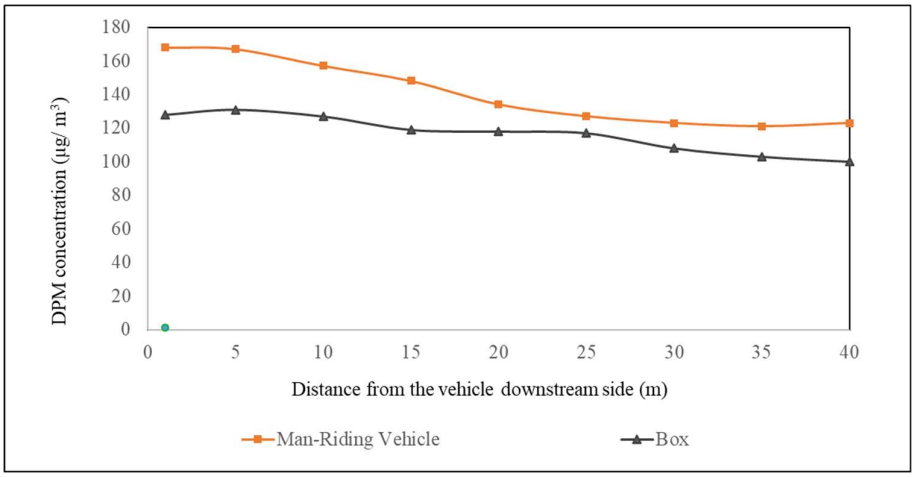

Fig. 5.23 Concentrations of DPM with different vehicle morphologies

5.6 DPM modelling at truck loading bay

The truck loading bay is one area of an underground mine with potentially high concentrations of DPM because high-engine capacity vehicles, e.g., the loader (up to 306 kW) and trucks (up to 567 kW) operate here simultaneously (Hamrin et al., 2001) and create large quantities of DPM. To simulate DPM flow at the truck and loader loading bays, 6 m high by 6 m wide by 50 m long roadway were considered on the upstream and downstream sides of the loading bay, as shown in **Fig. 5.24**a. The air velocities on the intake side were set at 1.5 m/s. For this simulation, the exhaust pipes are assumed to be located on the top of the vehicles and the vehicles are equipped with diesel particulate filters. Fine mesh with over half a million tetrahedron cells was used for the vehicles **Fig. 5.24**b. The flow and boundary conditions of these simulations are the same as in section 4.7.3 of Chapter 4.

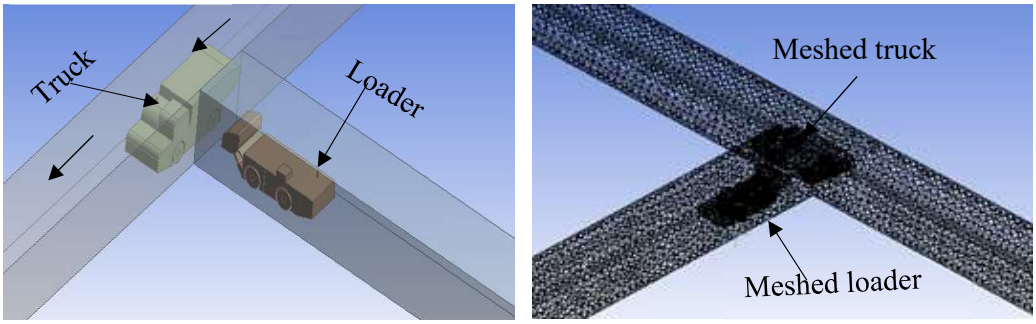

a. Loading bay model with loader and truck

b. Loading bay mesh with loader and truck

Fig. 5.24 Truck loading bay geometry and mesh with loader and truck

Fig. 5.25 shows the concentration of DPM downstream of the loading bay. 50 m downstream of the side of the vehicle there was a high concentration of DPM of more than 200 µg/m^3 spread over most of the roadway. It is therefore recommended to have the truck loading bay near the return air side to reduce operator exposure to the loading bay return air DPM.

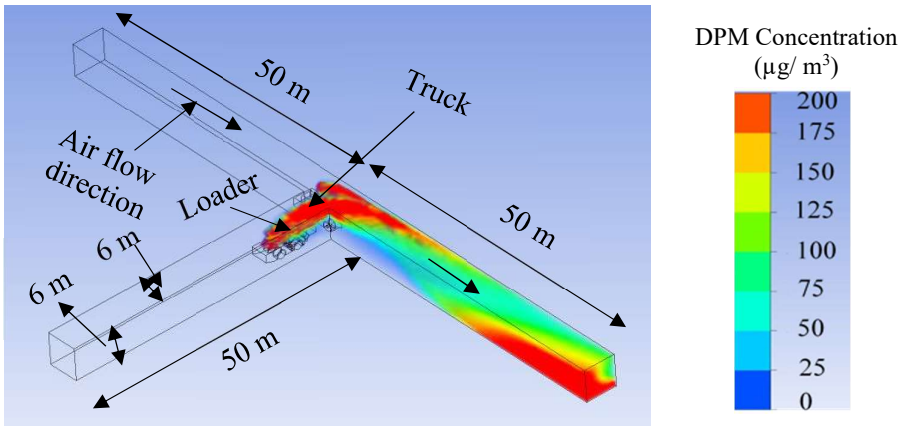

Fig. 5.25 DPM flow pattern of loading bay: Isometric view

To control the DPM concentration at the loading bay, it should be on the return side of the level if possible, but if this is not feasible, enough air must be supplied to the loading bay to reduce the DPM concentration to within the statutory limit (section 2.3 of Chapter

2). Since there was a high concentration of DPM at the downstream side of the truck loading bay, unnecessary exposure should be avoided.

5.7 Summary

This chapter reports the CFD investigations carried out to map the flow patterns of DPM generated by diesel-powered vehicles operating in an underground mine and influenced by different parameters. Simulations were conducted with different air velocities, air temperatures, location of DPM release sources, DPM release temperatures and loading bays.

DPM concentration depends mainly on air velocity in the roadway. For this modelling, a man-riding vehicle model with air velocities in the roadway of 0.5 m/s, 1 m/s, 2 m/s and 3 m/s were used. At 10 m downstream of the vehicle and in the middle of the roadway, for air velocities of 0.5 m/s, 1 m/s, 2 m/s and 3 m/s, the concentrations of DPM were 233 $\mu g/m^3$, 131 $\mu g/m^3$, 116 $\mu g/m^3$ and 1 $\mu g/m^3$, respectively. At 40 m downstream of the vehicle and with the velocity reduced by 40% and 60% of the base case value (1.26 m/s), the average concentration of DPM increased to 48% and 125%, respectively. On the other hand, if the intake air velocity increased by 58% and 98% of the base case value, the average concentration of DPM decreased to 42% and 50%, respectively.

DPM concentration near the vehicle depends mainly on the direction of the exhaust pipe. Simulation studies were carried out with different exhaust pipes at the back, bottom and top of the vehicles. In this study a 150 kW LHD model was used with an air velocity of 2 m/s. The concentration of DPM at 50 m downstream in the middle of the roadway and 1.2 m above the floor was measured. The results showed that DPM concentration for exhaust pipes located at the back, bottom and top was 48 $\mu g/m^3$, 52 $\mu g/m^3$ and 23 $\mu g/m^3$,

respectively. The operator should have the exhaust pipe at the bottom and backside of the vehicle because if the LHD exhaust pipe is on the top side the operators are exposed to high concentrations of DPM; in fact, it is better to have the exhaust pipe at the bottom side of the vehicle.

The temperature of the discharge fume slightly influences DPM concentration. For this modelling, a co-flow LHD (150 kW) model with an intake air velocity of 2 m/s, and DPM temperatures at the source of 50°C, 60°C, 70°C and 80°C, were used. The results showed that DPM concentration 50 m on the downstream side of the vehicle for 50°C, 60°C, 70°C and 80°C is 43 $\mu g/m^3$, 39 $\mu g/m^3$, 12 $\mu g/m^3$ and 9 $\mu g/m^3$, respectively.

The intake air temperature influences DPM concentration at the downstream side of the vehicle. For this modelling, a man-riding (150 kW) model with an intake air velocity of 1.5 m/s and intake air temperatures of 20°C, 30°C and 40°C were considered. The results showed that the temperatures of the intake air in the gallery influence the concentration of DPM on the downstream side of the vehicle, such that increasing intake air temperature increases the concentration of DPM on the downstream side of the vehicle.

DPM concentration at the downstream side of the vehicle is influenced by vehicle morphology. Simulation studies were conducted with a man-riding vehicle and a box of man-riding vehicle size. For this modelling, an air velocity of 1 m/s was considered. The results showed that box morphology has less DPM concentration than the downstream side of the vehicle.

The downstream side of the truck loading bay commonly contains a high concentration of DPM. Simulation studies were conducted with a truck (567 kW), a loader (306 kW) and an air velocity of 1.5 m/s. The results showed that at 50 m downstream of the loading bay, a high concentration of DPM of over 200 $\mu g/m^3$ was observed. It is recommended

that personnel should not remain in this area for a long time. To control the exposure of personnel to high concentrations of DPM at the truck loading bay, the loading bay should be located on the return side of the level if possible. An adequate quantity of air (0.06 $m^3/s/kW$) must be supplied to reduce the DPM to within the statutory limit.

Chapter 6

DPM Dispersion in Unventilated Dead-Ends Using Transient Flow Modelling

The validated unventilated dead-end crosscut model in Chapter 4 was used to investigate further DPM flow distribution in unventilated underground dead-end workings. In this chapter the DPM dispersion modelling studies were conducted with different unventilated dead-end crosscut lengths, velocities of air in the main galleries and different dead-end crosscut angles using transient (time-dependent) flow modelling.

6.1 Introduction

Dead-end operations are common in underground mines during development and/or when extracting coal or ore (Hartman and Mutmansky, 2002, Pivnyak et al., 2013, Sidorenko and Ivanov, 2016). Common dead-end workings are cut-throughs in longwalls, crosscuts, developing tunnels and gate roads, developing pillars in coal mines and parking cuddies, etc. (Hartman and Mutmansky, 2002). To dilute the concentration of DPM in dead-end workings, an auxiliary ventilation system is required (Drwięga et al., 2019, Hewage et al., 2014, Lowndes et al., 2004, Roghanchi and Kocsis, 2017). Diesel-powered vehicles sometimes need to operate in these isolated working areas for temporary maintenance or to fix problems and often the airflow is restricted or there is no auxiliary ventilation system.

Since 90% of DPM particles range from 3 nm to 30 nm (Section 2.1.2) in size and their density ranges from 0.3 gm/cm^3 to 1.2 gm/cm^3 (Bugarski et al., 2004) (Section 2.1.3), they do not settle easily under their own weight. It takes a long time for the DPM

concentration to fall to acceptable levels, so operators in these locations may be exposed to high concentrations of DPM. This chapter outlines a study into the dispersion of DPM in dead-ends. It also presents changes in DPM concentration depending on the length of the dead-end crosscut, air velocity in the main gallery and the crosscut angle. In general, underground mines have different dead-end crosscut lengths, angles and adjacent gallery air velocities. This chapter clearly illustrates the changes of DPM concentration in dead-end crosscuts with different dead-end crosscut lengths, dead-end crosscut angles, air velocities in the adjacent gallery and vortex flow, all of which are helpful to develop DPM control strategies to reduce underground miners' DPM exposure levels.

6.2 Effect of dead-end crosscut length on DPM dispersion

To better understand the characteristics of DPM accumulation and dispersion in dead-end zones, simulation studies were carried out for different lengths of dead-end crosscuts (10 m, 15 m, 20 m and 25 m from the airflow in the main gallery), as shown in **Fig. 6.1**. The crosscuts are at 90^{o} with the main gallery. The width and height of the crosscut and main gallery are 6 m and 2.7 m, respectively. The main gallery is 100 m long and the airflow velocity in the main gallery is 2 m/s. Initially, crosscuts were filled with 820 $\mu g/m^3$ of DPM. The effect on the concentration of DPM in the dead-end crosscut was monitored with respect to time. For this modelling, computational domain, computational mesh, flow and boundary conditions are considered from the base case dead-end crosscut model of sections 4.10.1 and 4.10.2 of Chapter 4.

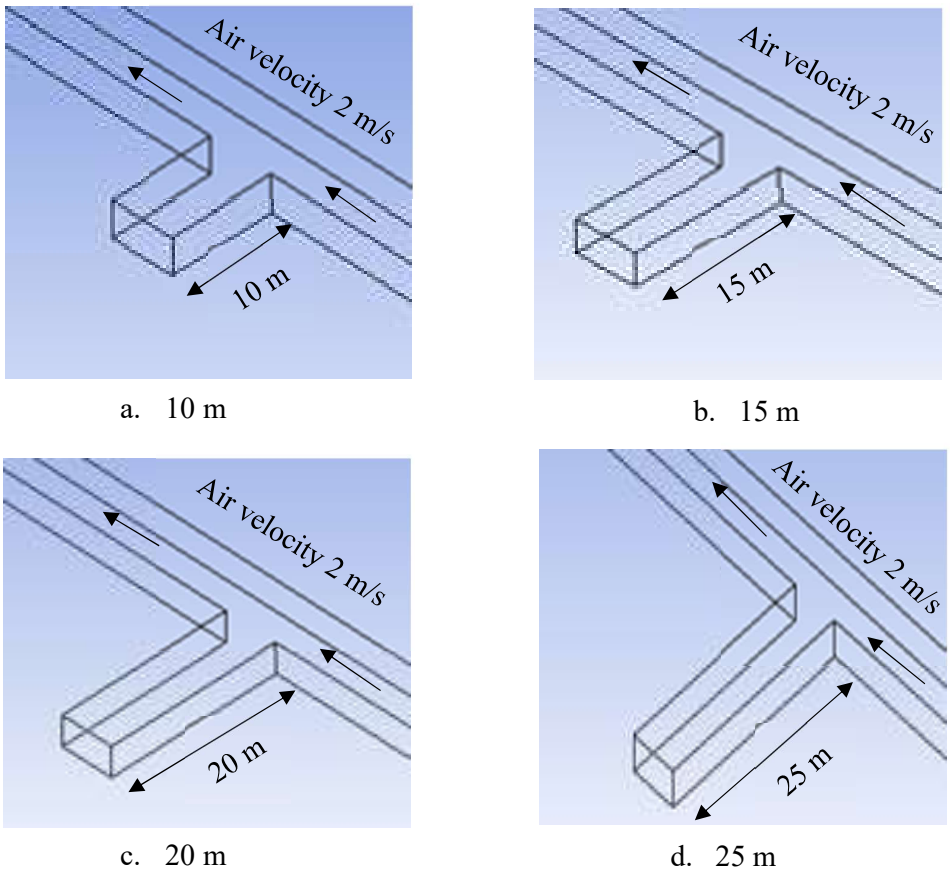

a. 10 m b. 15 m

c. 20 m d. 25 m

Fig. 6.1 Different lengths of crosscuts: 10 m, 15 m, 20 m and 25 m

Fig. 6.2 shows the DPM cloud at the different dead-end crosscuts. After 600 sec, the DPM concentration at 10 m, 15 m, 20 m and 25m from the airway was 147 µg/m^3, 267 µg/m^3, 340 µg/m^3 and 532 µg/m^3, respectively. Therefore, increasing the length of a dead-end crosscut reduced the airflow entering into the dead-end crosscut (**Fig. 6.2**), causing the DPM concentration to increase.

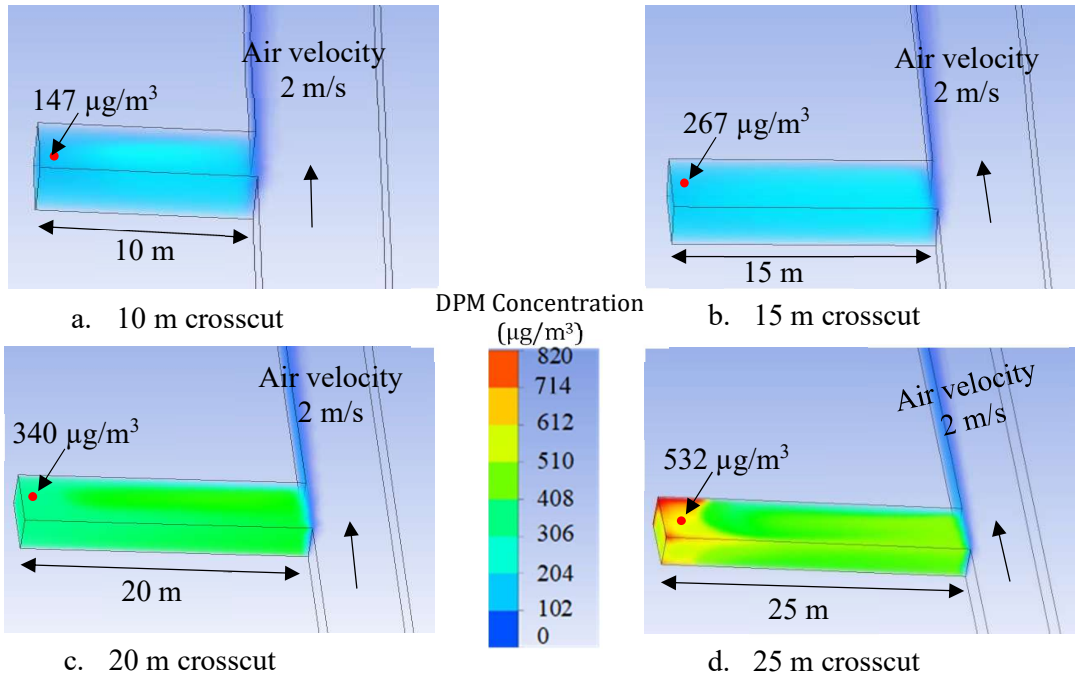

Fig. 6.2 DPM distribution after 10 minutes at 10 m, 15 m, 20 m and 25 m dead-end crosscuts

Table 6.1 and **Fig. 6.3** show the reduction in DPM concentration over 15 minutes at 10 m, 15 m, 20 m and 25 m from the airway. The air velocity in the main gallery is 2 m/s. If the crosscut is further away from the main gallery, the effectiveness of dilution of DPM decreases due to the lower influence of the main gallery airflow. The figure shows there is a nonlinear relationship between DPM dispersion and the length of the dead-end crosscut.

Table 6.1 DPM concentration with respect to time at 10 m, 15 m, 20 m and 25 m dead-end crosscuts

Time (minutes)	DPM concentration at different crosscut lengths (μg/m^3)			
	10 m	15 m	20 m	25 m
0	820	820	820	820
1	636	777	820	820
2	498	607	820	820
3	462	555	731	820
4	403	491	568	820
5	336	448	547	820
6	288	441	496	820
7	242	374	444	820
8	205	337	398	800
9	173	297	366	673
10	147	267	340	532
11	126	242	316	515
12	107	218	294	436
13	91	196	271	402
14	78	176	251	377
15	67	158	231	336

Fig. 6.4 shows the percentage reduction in spot DPM concentration after 15 min at 10 m, 15 m, 20 m and 25 m from the dead-end crosscuts. To reduce the DPM by 50% takes 4 min, 6.5 min, 9.5 min and 13 min for 10 m, 15 m, 20 m and 25 m from dead-end crosscuts, respectively. **Table 6.1** shows that if the dead-end crosscut is more than 20 m long, the ability of the air velocity in the main gallery to disperse DPM is very small.

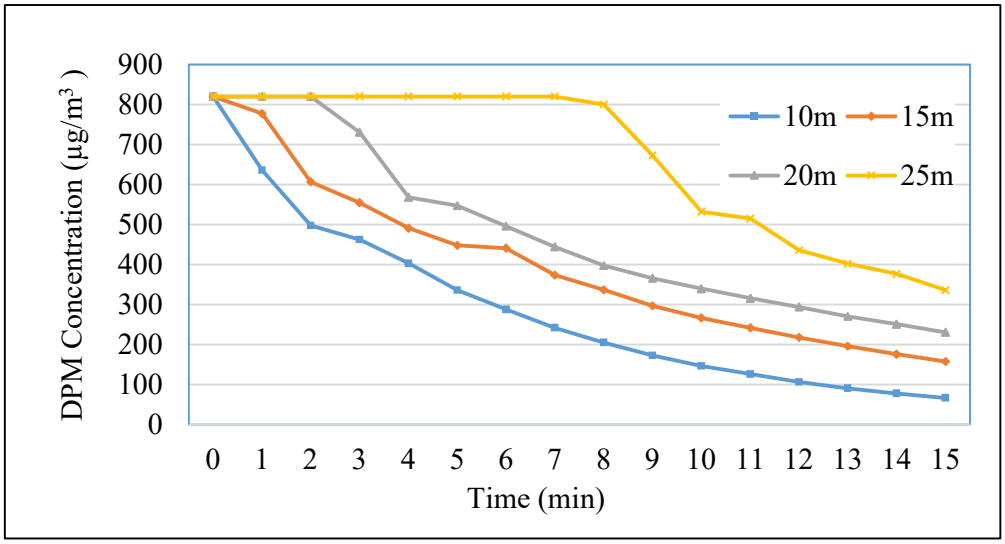

Fig. 6.3 DPM Concentration dispersion with time at 10 m, 15 m, 20 m and 25 m dead-end crosscuts

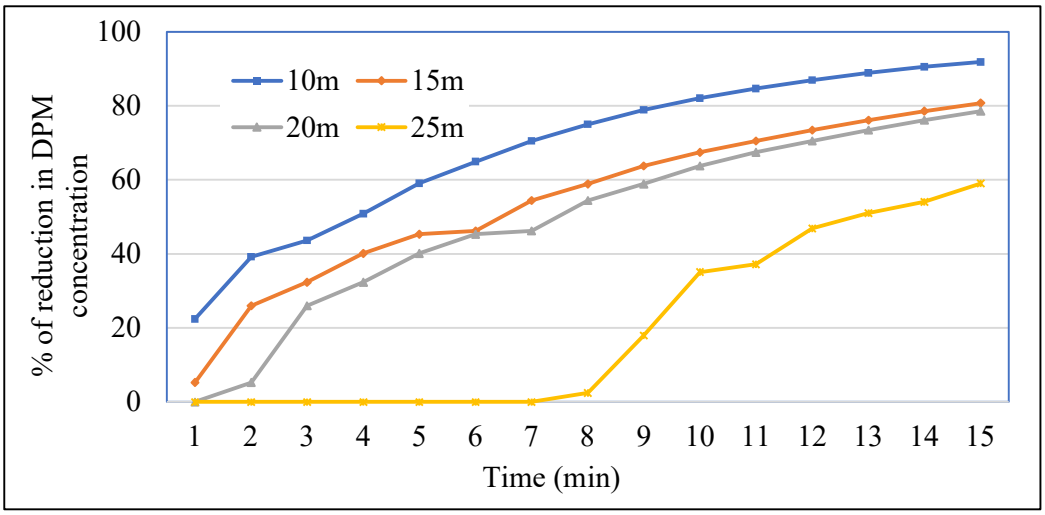

Fig. 6.4 DPM concentration percentage of reduction with time at 10 m, 15 m, 20 m and 25 m dead-end crosscuts

6.2.1 DPM dispersion in a 50 m dead-end crosscut

Simulation studies were also carried out with a 50 m long dead-end crosscut (**Fig. 6.5**). The figure shows that after 10 min, 1 hour and 5 hours, the spot concentrations of DPM were 820 µg/m^3, 540 µg/m^3 and 100 µg/m^3, respectively.

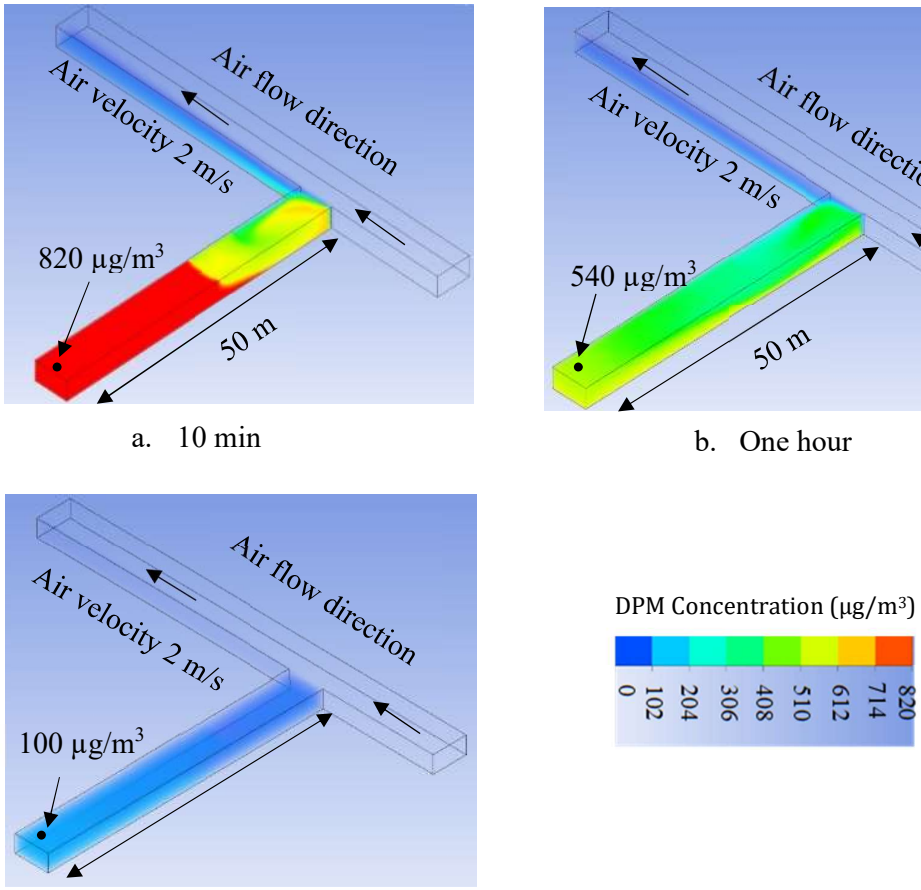

Fig. 6.5 DPM concentration after 10 minutes, 1 hour and 5 hours at 50 m dead-end crosscuts

6.3 Effect of main gallery air velocity on unventilated dead-end crosscut DPM dispersion

To investigate the influence of the main gallery air velocities on dispersing or diluting the DPM in dead-end crosscuts, CFD simulations were carried out for a 20 m long dead-end crosscut at 90^{o} to the main air gallery. The air velocities in the main gallery were 0.5 m/s, 1 m/s, 2 m/s, 3 m/s and 4 m/s. For this modelling, computational domain, computational mesh, flow and boundary conditions are considered from the base case dead-end crosscut model of sections 4.10.1 and 4.10.2 of Chapter 4.

Fig. 6.6 shows the concentration of DPM after 10 min with air velocities ranging from 0.5 m/s to 4 m/s. The figure shows that if the air velocity in the main gallery is 0.5 m/s, there is almost no change in the spot DPM concentration at the 20 m crosscut. However, if the air velocity was 4 m/s, the concentration decreased to 163 $\mu g/m^3$ in 10 minutes. If the air velocity in the adjacent gallery is high, more airflow is entering into the dead-end crosscut and will help reduction of DPM concentration.

Fig. 6.7 shows the concentration of DPM for different main gallery air velocities. With an air velocity of 0.5 m/s, there was virtually no change in DPM concentration over a 15-minute period and if the air velocity was 1 m/s, there was no DPM reduction for up to 8 minutes, but thereafter the concentration gradually decreased. As shown in **Fig. 6.7**, with higher airflow velocities in the main gallery, the reduction in DPM concentration is greater.

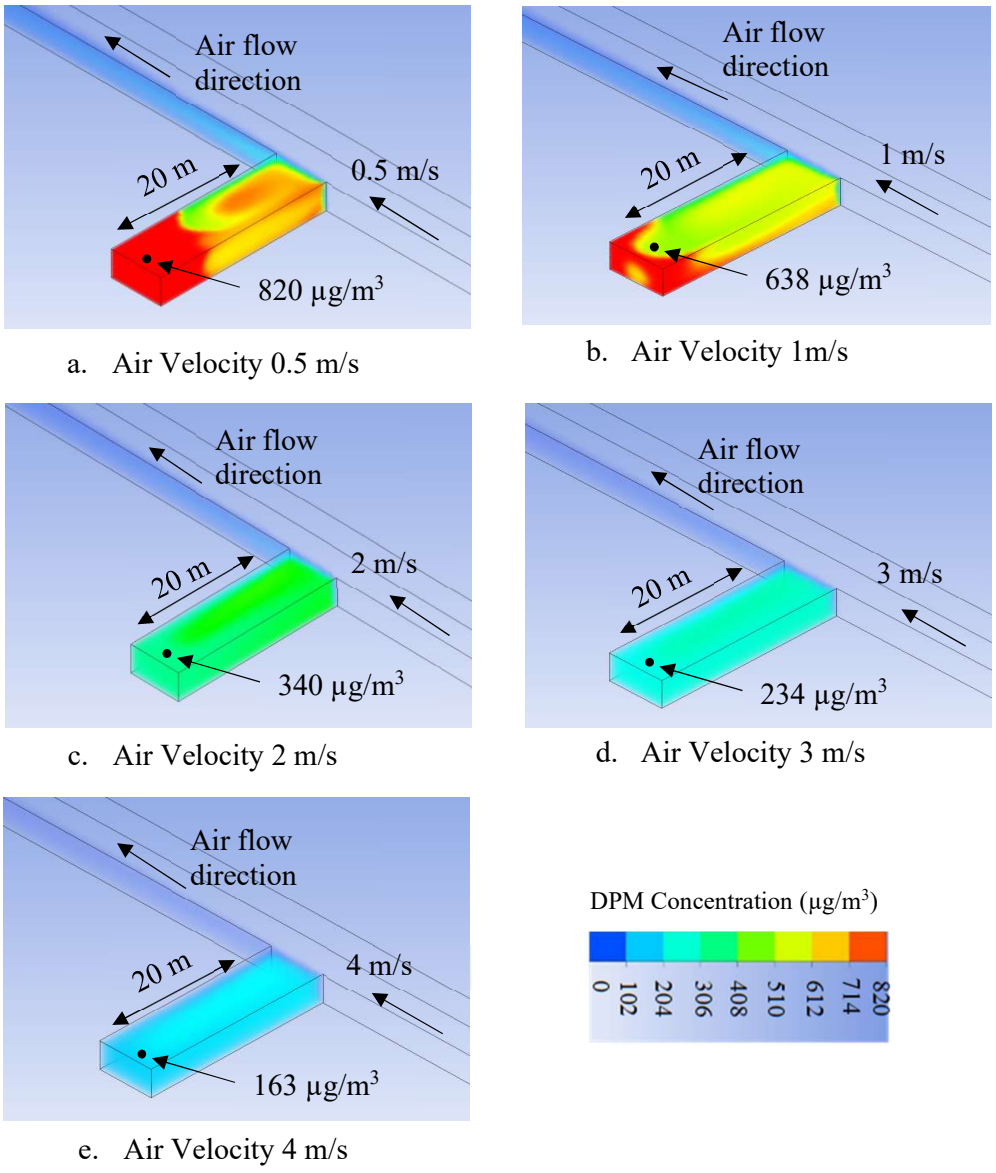

Fig. 6.6 Spot DPM concentration after 10 minutes: 20 m dead-end crosscut with 0.5 m/s, 1 m/s, 2 m/s, 3 m/s and 4 m/s air velocities in the main airway

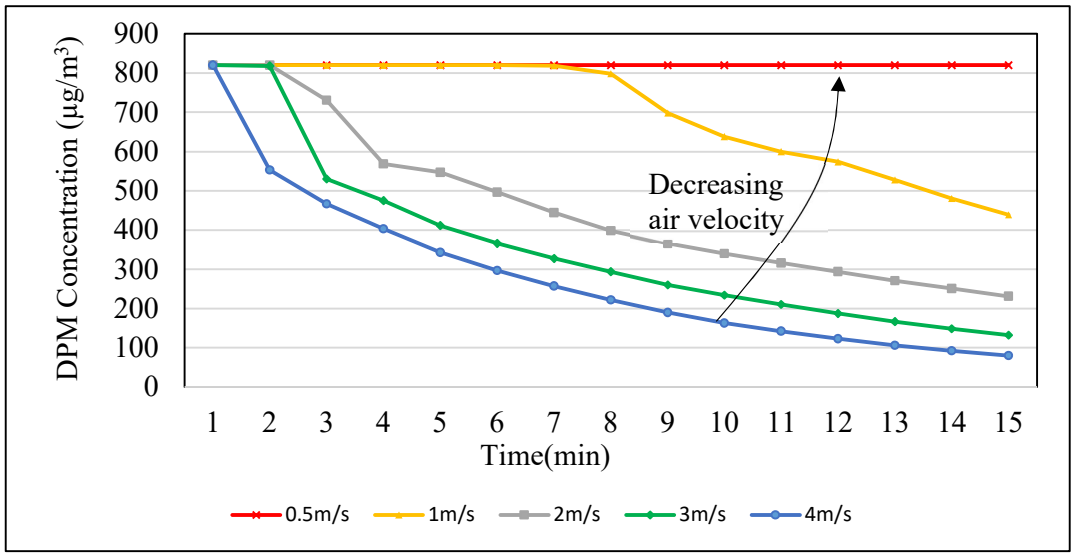

Fig. 6.7 DPM concentration in 20 m dead-end crosscut for different air velocities over a 15-minute duration

6.4 Effect of dead-end crosscut angle on unventilated dead-end crosscut DPM dispersion

To estimate DPM dispersion and dilution changes in dead-end crosscuts with dead-end crosscut angles, studies were carried out with dead-end crosscut angles of 45°, 90° and 135° to the footwall drive/main gallery (**Fig. 6.8** and **Fig. 6.9**). In these simulations, the length, width and height of the crosscuts were 20 m, 6 m and 2.7 m, respectively. The airflow velocity in the main gallery was considered as 2 m/s. Computational domain, computational mesh, flow and boundary conditions are considered from the base case dead-end crosscut model of sections 4.10.1 and 4.10.2 of Chapter 4.

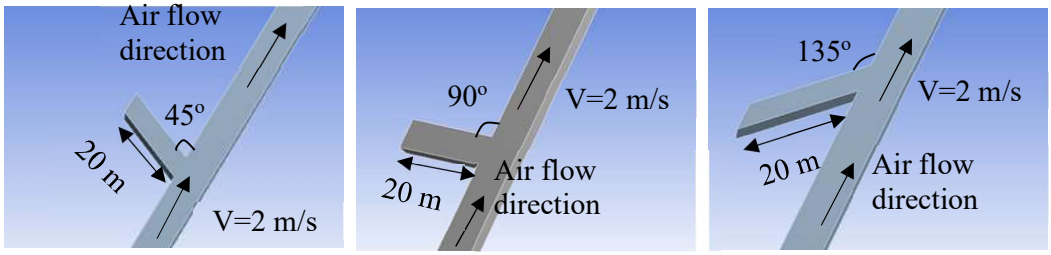

a. 45° b. 90° c. 135°

Fig. 6.8 Different angles of crosscut models: 45°, 90° and 135°

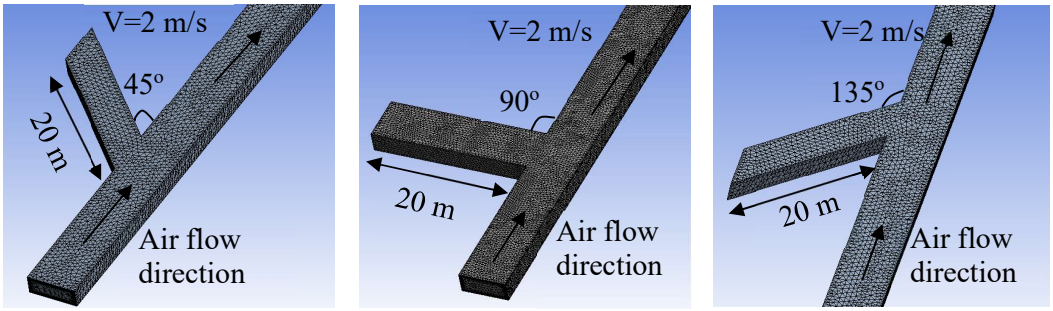

a. 45° b. 90° c. 135°

Fig. 6.9 Meshed models of crosscut with different angles: 45°, 90° and 135°

Fig. 6.10 shows the concentration of DPM after 10 min in the 45°, 90° and 135° angle dead-end crosscuts; after 10 mins, the DPM was 239 µg/m^3, 347 µg/m^3 and 508 µg/m^3, respectively. **Fig. 6.11** shows the reduction of DPM with time for the 45°, 90° and 135° crosscuts; the DPM concentration increased as the crosscut angle increased. For a 45° crosscut, it took 90 min to reduce DPM from 820 µg/m^3 to zero. If the dead-end crosscut angle is less, more airflow is entering into the dead-end crosscut and will help reduction of DPM concentration.

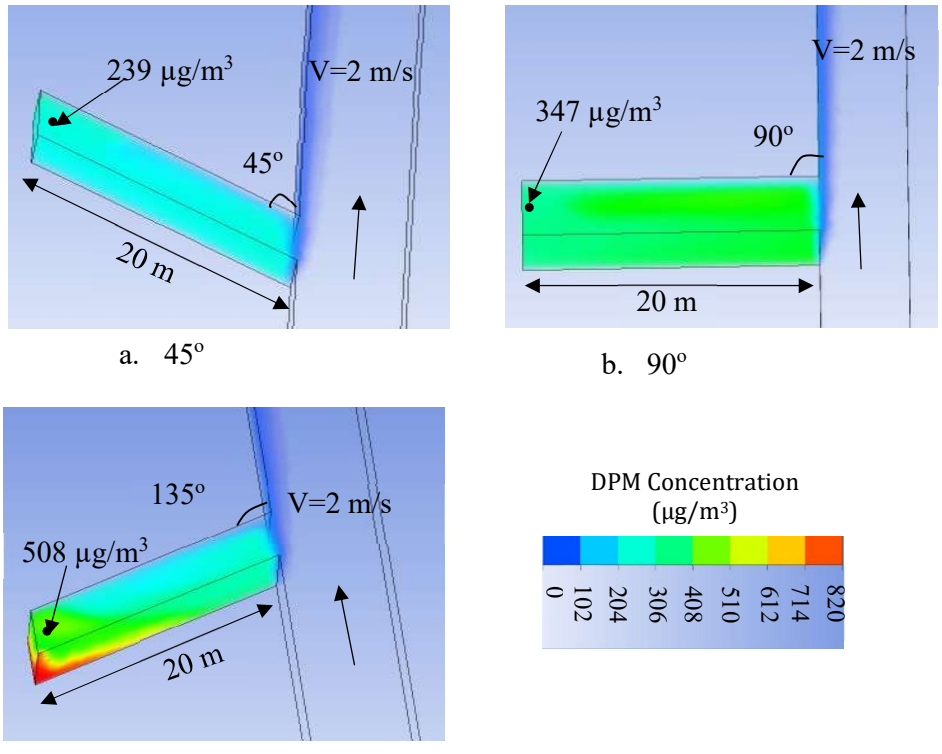

Fig. 6.10 Spot DPM concentration of dead-end crosscuts of 45°, 90° and 135° with the main gallery after 10 minutes

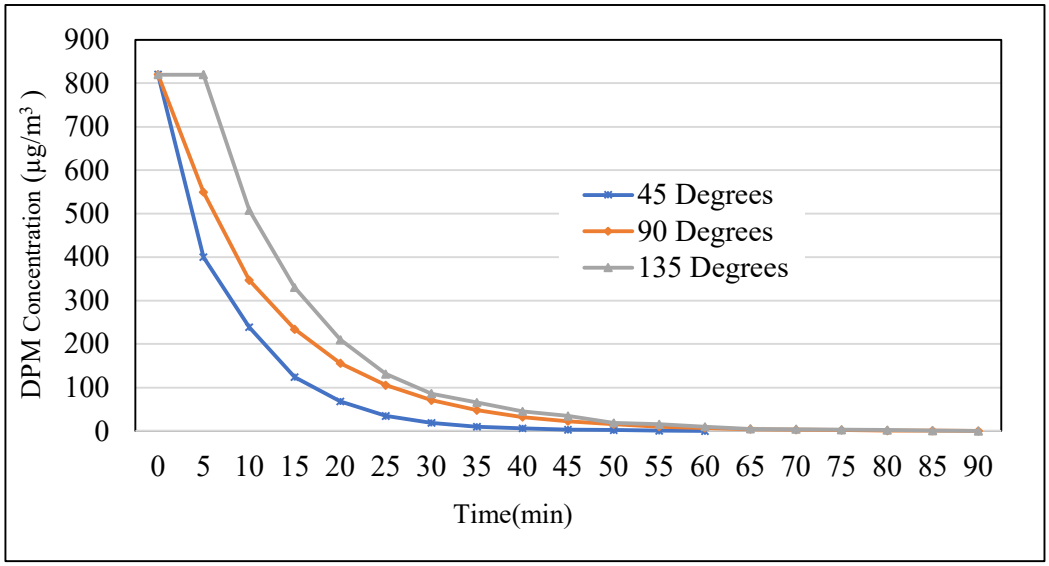

Fig. 6.11 DPM concentration of dead-end crosscuts of 45°, 90° and 135° to the main gallery

6.5 Vortex flow in unventilated dead-end crosscut

After the initial dead-end crosscut modelling studies, a detailed investigation was carried out on the airflow patterns in unventilated dead-end crosscuts. The simulation results showed a vortex-shaped flow in the dead-end crosscut. The airflow in this region is turbulent and decreases towards the centre of the vortex. For this modelling, computational domain, computational mesh, flow and boundary conditions are considered from the base case dead-end crosscut model of sections 4.10.1 and 4.10.2 of Chapter 4. The boundary conditions for this modelling are dead-end crosscut length of 10 m, 15 m, 20 m and 25 m dead-end crosscut angles of 45^{o}, 90^{o} and 135^{o} and air velocity in the adjacent gallery is 2 m/s.

Fig. 6.12 shows the CFD modelling results of air velocity distribution for 10 m, 15 m, 20 m, 25 m long dead-end cross cuts and 45^{o} and 135^{o} of 20 m long dead-end crosscuts. An intake air velocity of 2 m/s and air velocity contour plane of 1.2 m above the ground level were considered for this modelling. The figures show the vortex-shaped airflow in dead-end crosscuts. The air velocity in the crosscut is very low and is below 0.4 m/s. The air velocities at the centre of the vortex are lower but they increase towards the end of the vortex. The location of the centre of the vortex for 10 m, 15 m, 20 m, 25 m, 45^{o} and 135^{o} dead-end crosscuts are at 4.5 m, 8.5 m, 10 m, 10 m, 10 m and 6.5 m from the crosscut entrance. **Fig. 6.13** shows the changes in DPM concentration concerning air velocity inside the dead-end crosscut. Due to the centrifugal force, a high DPM concentration is at the centre of the vortex. DPM concentration increases with decreasing air velocity.

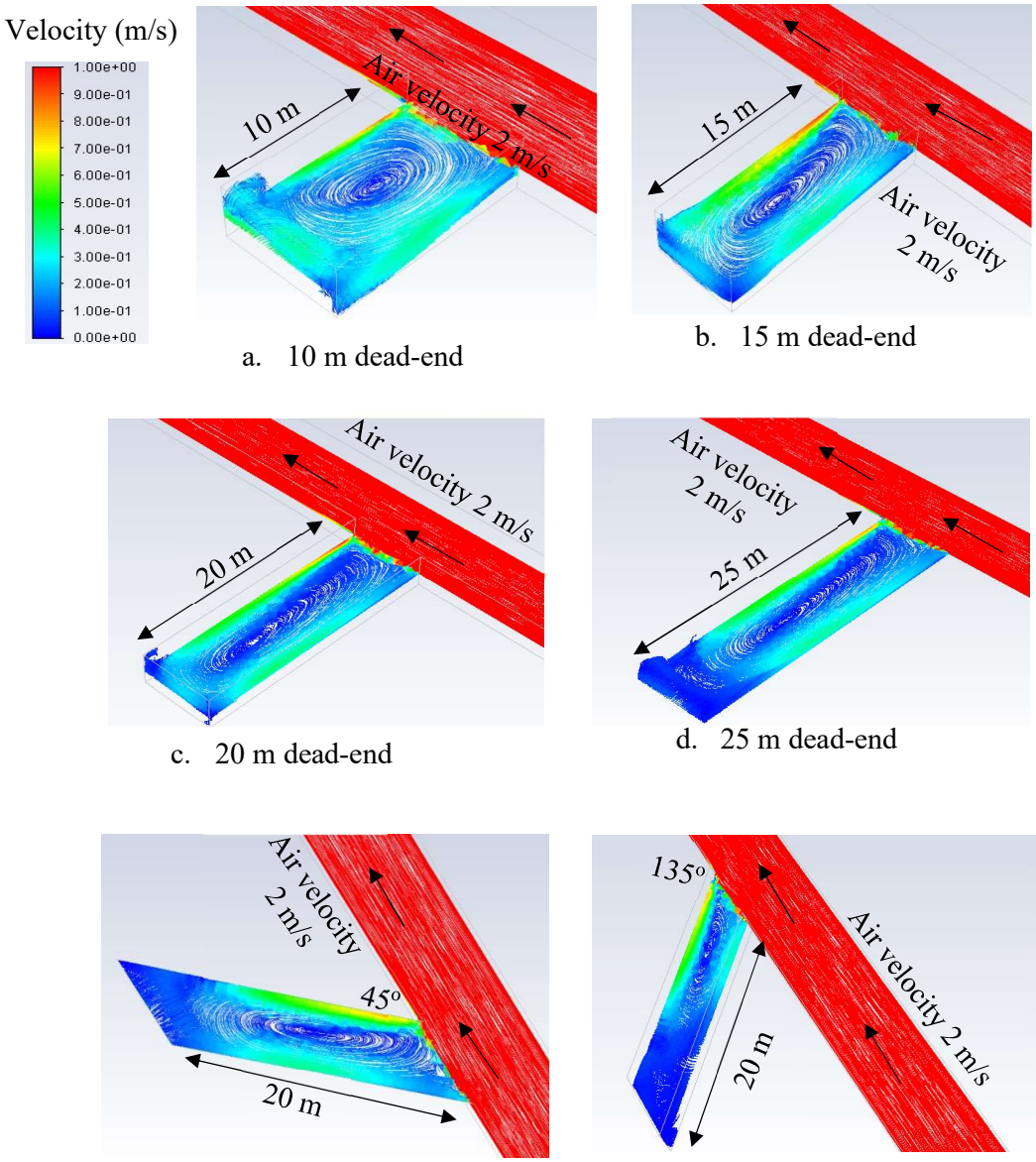

a. 10 m dead-end

b. 15 m dead-end

c. 20 m dead-end

d. 25 m dead-end

e. 45° & 20 m dead-end

f. 135° & 20 m dead-end

Fig. 6.12 Vortex air velocities in dead-end crosscut

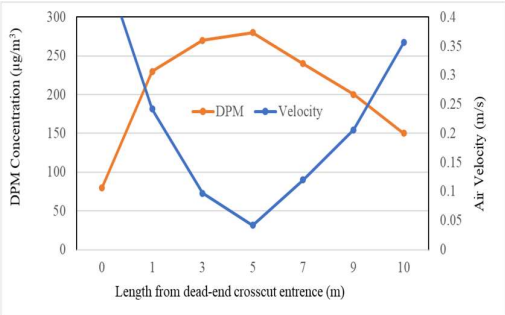

a. 10 m

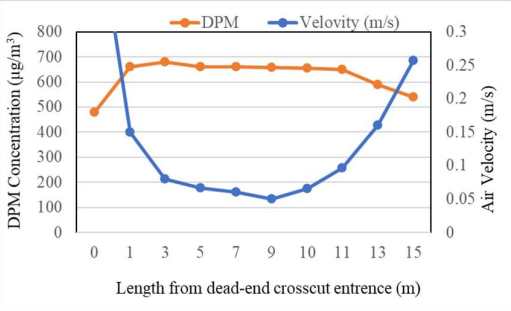

b. 15 m

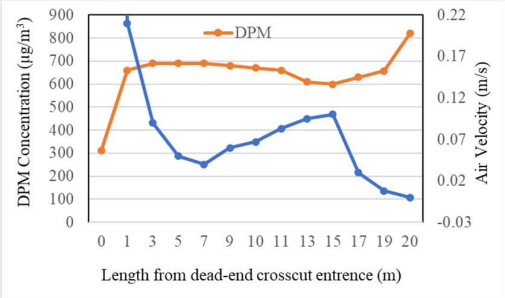

c. 20 m

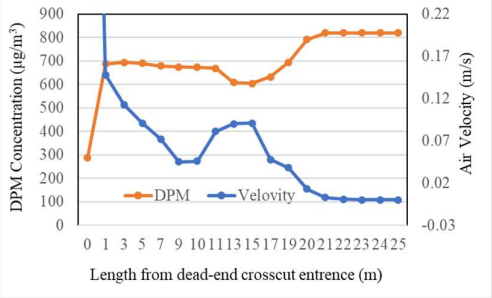

d. 25 m

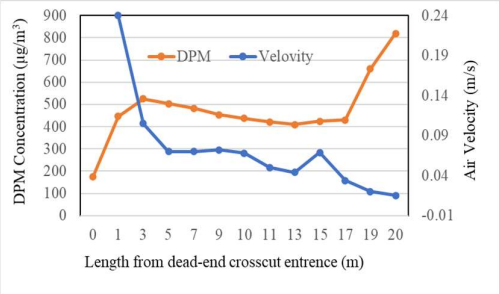

e. 45º and 20 m

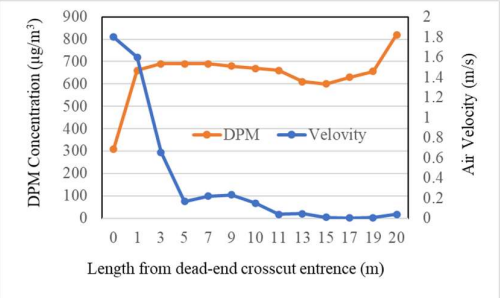

f. 135º and 20 m

Fig. 6.13 Changes of DPM concentration with air velocity for 10 m, 15 m, 20 m, 25 m, 45º and 135º dead-end crosscut vortex

Fig. 6.14 shows the distribution of vortex pressure in a dead-end crosscut. Dead-end crosscuts of 10 m, 15 m, 20 m, 25 m, 45º and 135º and an air velocity in the main gallery of 2 m/s were considered for this modelling. The results show that air pressure decreases towards the centre of the vortex. There is higher air pressure in the main gallery; the pressure difference between the main air gallery and the dead-end crosscut (ΔP) is very

low and is below 0.4 Pa. A higher air pressure exists in the main air gallery. **Fig. 6.16** shows changes in DPM concentration concerning pressure differences between the main gallery and dead-end gallery (ΔP). DPM concentration is increasing with decreasing air pressure. A high DPM concentration is at the centre of the vortex and the lower pressure drop is at the centre of the vortex.

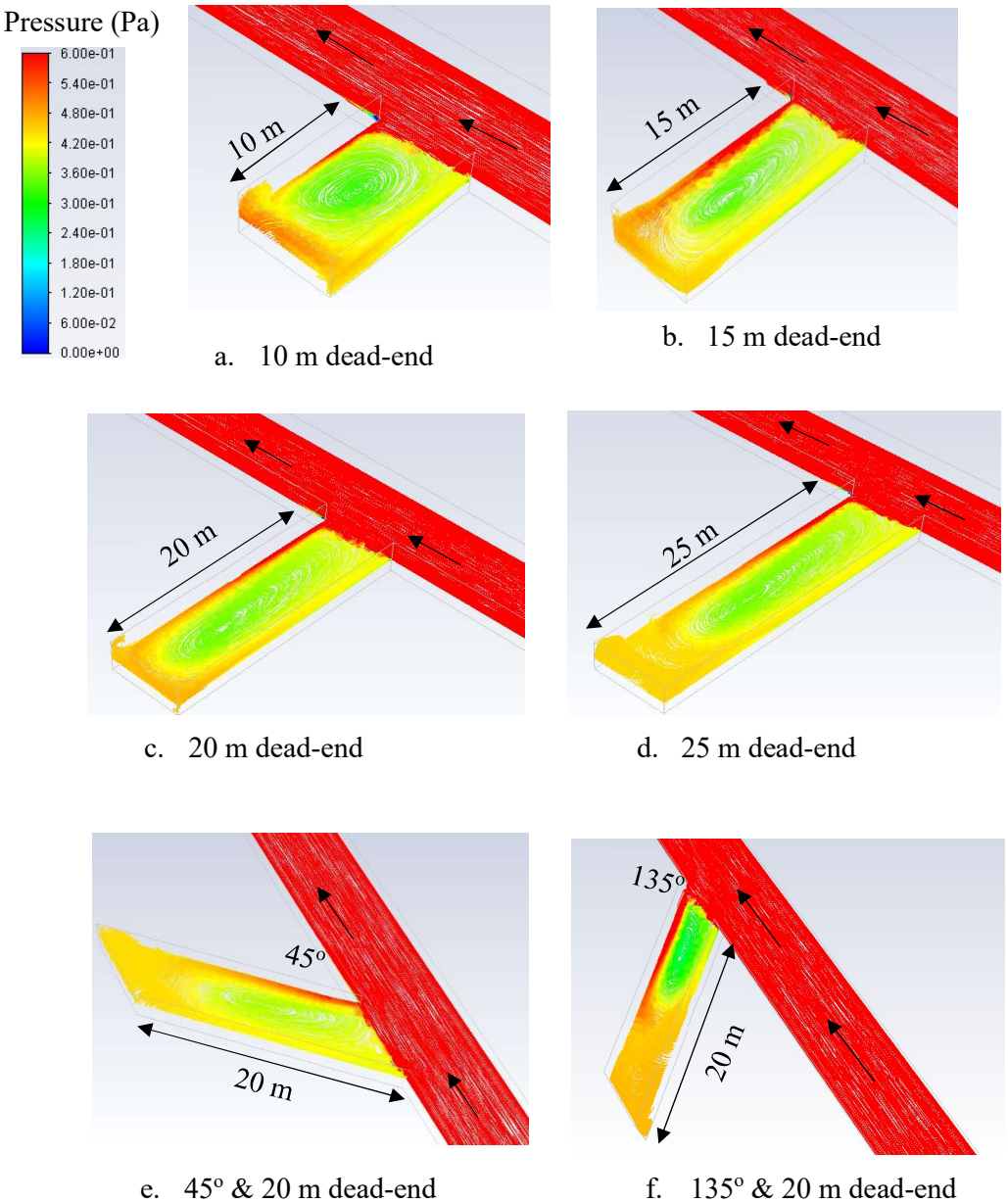

a. 10 m dead-end

b. 15 m dead-end

c. 20 m dead-end

d. 25 m dead-end

e. 45° & 20 m dead-end

f. 135° & 20 m dead-end

Fig. 6.14 Vortex-shaped pressure in dead-end crosscut

Fig. 6.15 shows vortex-shaped DPM distribution in different dead-end crosscuts. For this modelling, dead-end crosscuts of 10 m, 15 m, 20 m, 25 m, 45^{o} and 135^{o}, an air velocity of 2 m/s in the main gallery and an initial DPM concentration in the dead-end crosscut of 820 $\mu g/m^3$ were considered. Transient flow modelling studies were used for 180 sec for this modelling. There is a higher DPM concentration at the centre of the vortex but this concentration decreases towards the end of the vortex. The DPM concentration is higher in obtuse-angled crosscuts than acute-angled crosscuts.

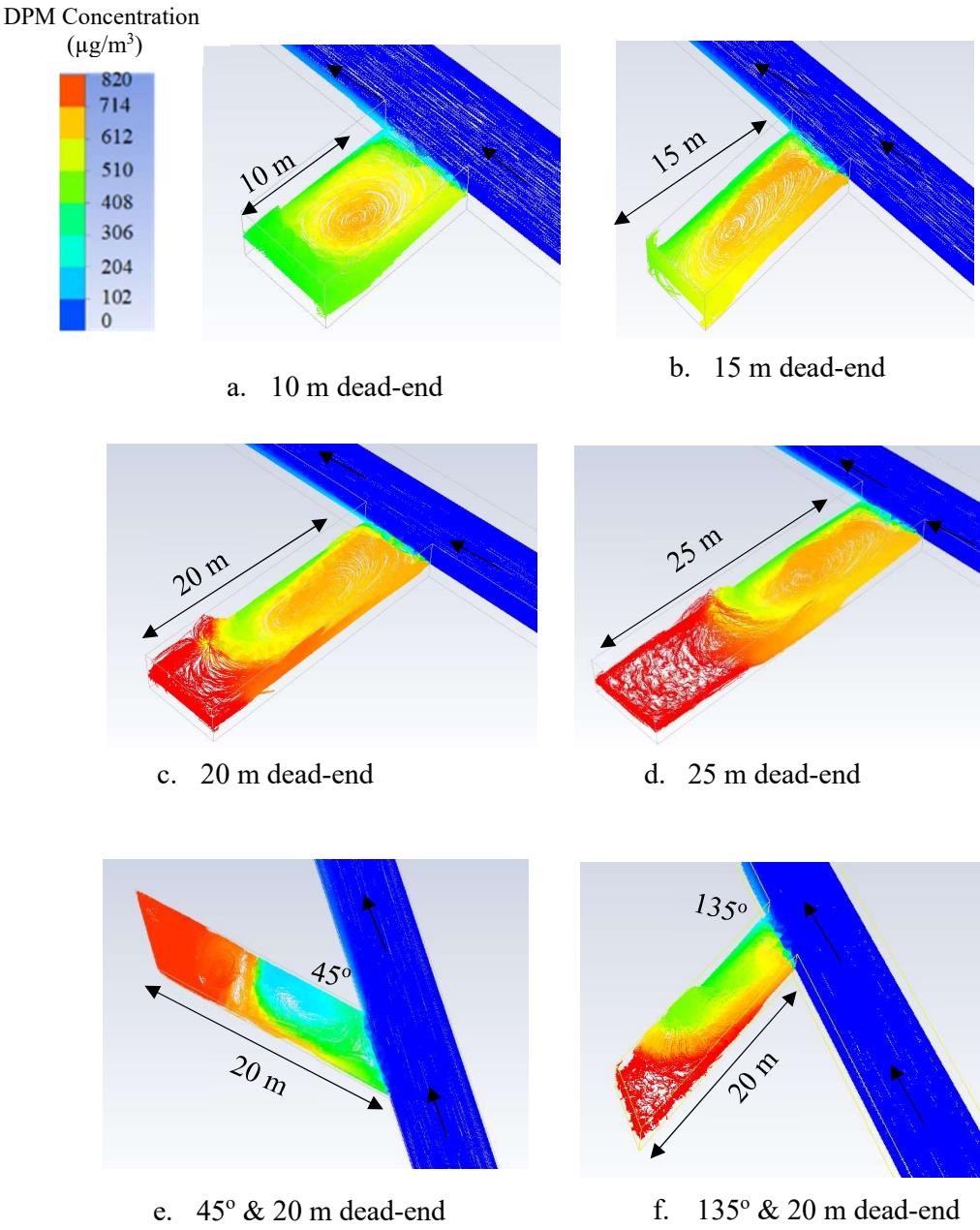

a. 10 m dead-end

b. 15 m dead-end

c. 20 m dead-end

d. 25 m dead-end

e. 45° & 20 m dead-end

f. 135° & 20 m dead-end

Fig. 6.15 DPM concentration in vortex shape in dead-end crosscut after 180 sec

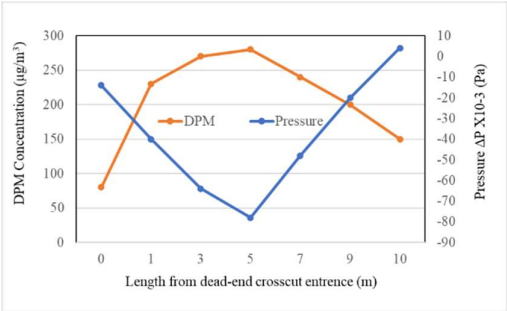

a. 10 m

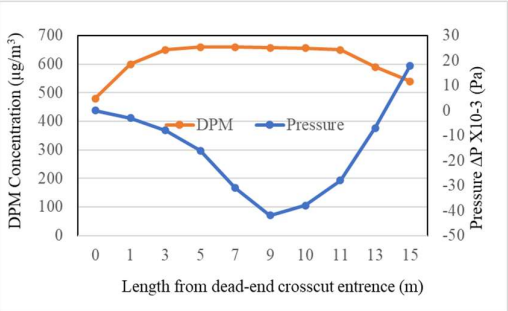

b. 15 m

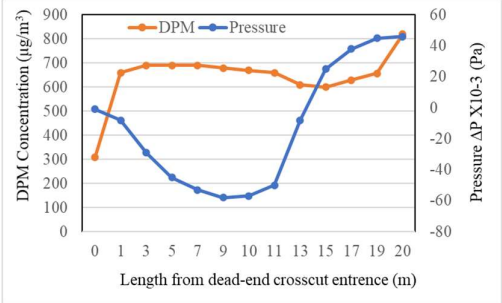

c. 20 m

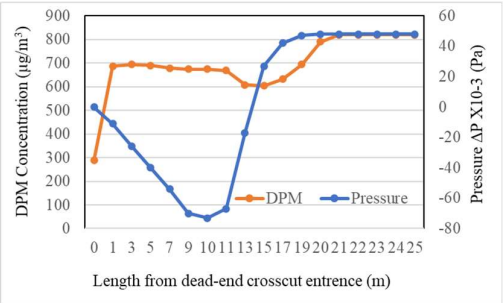

d. 25 m

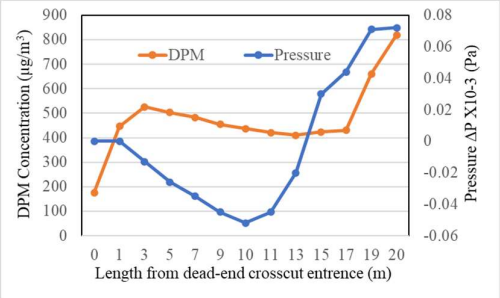

e. 45° and 20 m

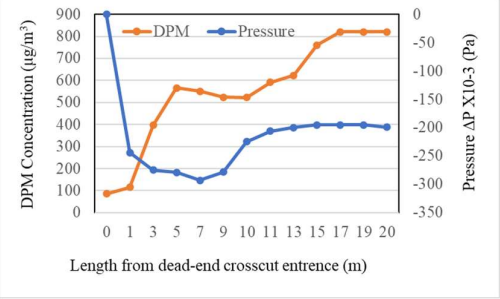

f. 135° and 20 m

Fig. 6.16 Changes of DPM concentration with pressure drop in 10 m, 15 m, 20 m, 25 m, 45° and 135° dead-end crosscut vortex

6.6 Summary

This chapter describes parametric studies on the dispersion of DPM in unventilated dead-end crosscuts. Studies were carried out for different dead-end crosscut lengths, crosscut angles and air velocities in the adjacent main gallery. The simulations assumed the initial DPM concentration in the dead-end crosscut to be 820 $\mu g/m^3$.

Increasing the air velocity in the adjacent gallery increased the dispersion/dilution of DPM in the dead-end crosscut. For this modelling, a 20 m long dead-end crosscut was considered with adjacent foot-wall drive air velocities of 0.5 m/s, 1 m/s, 2 m/s, 3 m/s and 4 m/s. Modelling results concluded that after 15 minutes, for 0.5 m/s, 1 m/s, 2 m/s, 3 m/s and 4 m/s air velocities, DPM concentration reduced to 820 $\mu g/m^3$ (no change), 425 $\mu g/m^3$, 220 $\mu g/m^3$, 115 $\mu g/m^3$ and 95 $\mu g/m^3$, respectively. Studies also showed that, if the air velocity is 0.5 m/s or less, the influence of the air velocity in an adjacent gallery on the dilution in a dead-end crosscut length of 20 m or longer is negligible.

DPM concentration in the dead-end crosscut is influenced by its length. For this modelling, the air velocity in the adjacent gallery was assumed to be 2 m/s. The dead-end crosscut lengths were assumed to be 10 m, 15 m, 20 m and 25 m. Results concluded that to reduce the DPM concentration by 50% for 10 m, 15 m, 20 m and 25 m length dead-end crosscuts, it took 4 min, 6.5 min, 7.5 min and 13.5 min, respectively. The results showed that for a 50 m long unventilated dead-end crosscut, it took 5 hours to reduce the DPM from 820 $\mu g/m^3$ to 100 $\mu g/m^3$; therefore, the longer the dead-end, the longer it takes for DPM to dilute.

Finally, DPM concentration in a dead-end crosscut is influenced by its angle with the

main gallery. A 20 m long dead-end crosscut with 45º, 90º and 135º angles to the adjacent footwall drive was considered for these simulations. It was assumed that the air velocity in the adjacent gallery is 2 m/s and that the initial DPM concentration in the crosscut is 820 µg/m^3. Results showed that after 10 min, the concentrations of DPM remaining in the crosscut at 45º, 90º and 135º were 239 µg/m^3, 347 µg/m^3 and 508 µg/m^3, respectively. Therefore, the DPM concentration increases as the angle between the cut-through and the main gallery increases.

A vortex airflow is formed near the dead-end crosscut entrance and circulates in a curved form, but the air velocity and pressure decrease towards the centre of the vortex. DPM concentration is increasing towards the centre of the vortex. The centre of the vortex depends on the length of the dead-end crosscut and the maximum length is 10 m from the entrance.

Chapter 7

DPM Control Strategies in an Underground Mine Environment

Controlling the concentration of DPM in underground mines means applying different DPM strategies (Mischler and Colinet, 2009). Different DPM control strategies were investigated. For example, using environmental cabs (Noll et al., 2008), passive particulate filters (Noll et al., 2010), diesel particulate filters (Bugarski et al., 2006), ventilation ducts extended to the face (Chang et al., 2019b), monitoring engine condition (Davies, 2003), using positive pressure environmental cabs, water sprays (Majewski, 2001), using biodiesel (Bugarski et al., 2010, Nuszkowski et al., 2011, Howell and Weber, 1997, Bickel et al., 1997) and using alcohol and diesel (Zhang and Balasubramanian, 2016), etc.

In this chapter, various DPM control strategies are discussed:

1. Optimising location(s) of secondary fan(s) to reduce DPM recirculation;
2. Efficient filters to reduce DPM concentration;
3. DPM controlling by removing airway resistance/blockages;
4. Pull–push ventilation system to minimise DPM concentrations in declines;
5. Using curtains to improve airflow in dead-ends.

7.1 Optimising secondary fan location and air quantity to control DPM

Ventilation is the most common method used to dilute DPM (Chang et al., 2019b, Grau et al., 2006, Halim, 2017). As per mining regulations, adequate ventilation is needed to dilute DPM within safe limits (MDG, 2008). However, miners sometimes have to work in unventilated dead-end headings. If DPM is detected in an unventilated dead-end

heading longer than 20 m (section 6.2 of Chapter 6), dilution with natural ventilation is difficult and therefore forced ventilation with auxiliary fans is often used (Chang et al., 2019b, Vutukuri and Lama, 1986). In this method, an auxiliary fan is placed on the upstream side of the development heading to force air to the face through ventilation ducting; the return air from the face flows back to the main flow through the primary ventilation system (Desouza, 2004).

The main drawback with a forced ventilation system from a decline is the possibility of uncontrolled recirculation in the dead-ends if the auxiliary fan is not in the correct location (Baines, 1988), in which case it may lead to potentially dangerous levels of DPM concentration. This re-circulation of air can be due to the auxiliary fan in the wrong location with respect to the development heading and a mismatch in the quantity of intake drive air with the capacity of the fan. In this section, an effort has been made to optimise the location of the auxiliary fan and minimum airflow requirement in the intake drive for an auxiliary fan by using CFD modelling.

7.1.1 Construction of computational domain

The computational domain geometry was modelled as shown in **Fig. 7.1**. It consists of a 100-m long ventilation drive and a 70-m long crosscut whose width and height are 6 m by 5 m. A 3D CAD model of a Load Haul Dump (LHD) vehicle or bogger, and a twin 75 kW fan with a 50 m long by 1.22 m diameter ventilation duct, were designed and imported into the computational domain. The loader engine was equipped with a DPM filter and the exhaust flow was a mixture of DPM and air.

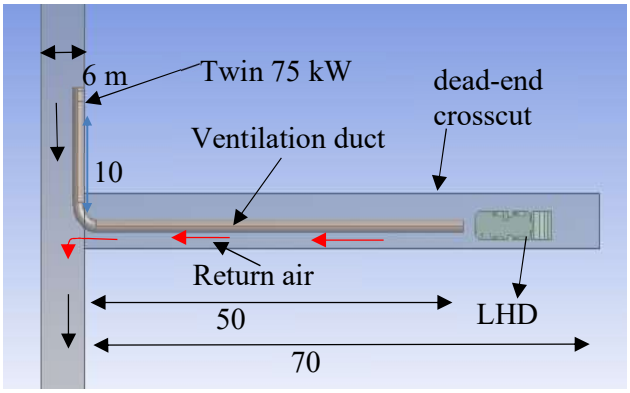

a. Experimental drive, top view

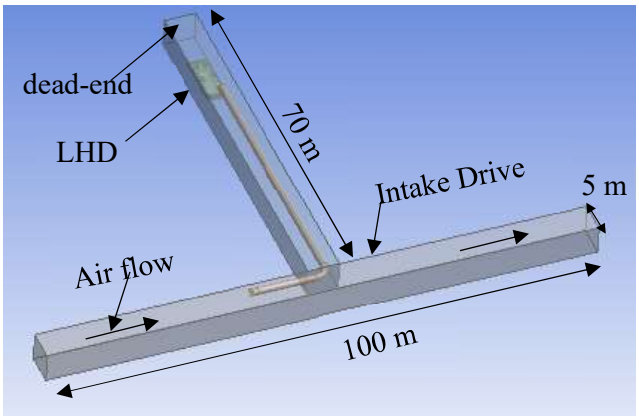

b. Experimental drive, Isometric view

Fig. 7.1 Computational domain with fan, ventilation duct, experimental drive and crosscut

7.1.2 Construction of computational mesh

Fig. 7.2 shows the meshed LHD, ventilation duct with fan, intake air drive and dead-end crosscut. The diameter of the auxiliary fan and the ventilation duct are 1.22 m. To achieve accurate results, a finer mesh with about one million computational cells was used. The minimum size of the cells was 5 x 10^{-3} m, the minimum edge length of the cells was 0.03 m and the size function was 'proximity and curvature'. Program-controlled inflation with ten layers was specified for the solid surfaces in the mesh (channel walls, LHD surfaces and ventilation duct surfaces) to simulate the boundary layer effects. The residual RMS

error value is 10^{-5} and the domain has imbalances of less than 0.01.

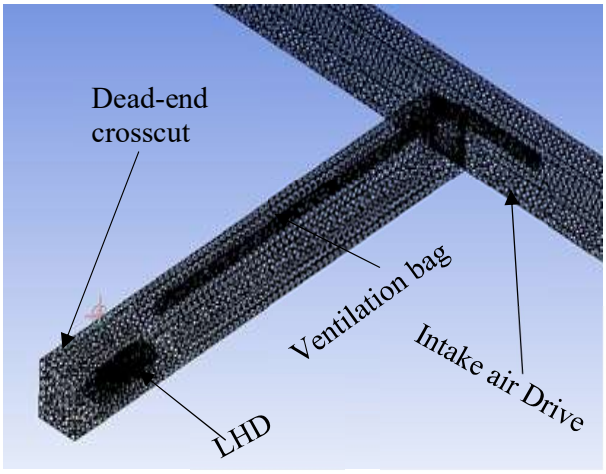

Fig. 7.2 Meshed model of fan, ventilation bag and experimental drive and crosscut

7.1.3 Setting up flow conditions

The boundary conditions of the model were considered: intake air volume flow rates of 30 m^3/s, 45 m^3/s and 60 m^3/s, and intake air temperature of 300 K. The boundary conditions for the fan are a twin 75 kW auxiliary fan with an inlet air pressure of –1000 Pa. This pressure reading was derived from matching the air quantity of 30 m^3/s. To deliver air quantity on the entire cross-section of the gallery face, the ventilation duct was installed in the middle of the gallery.

Discrete-phase modelling was used to model the DPM flow patterns. For this modelling, DPM particle injection is from the LHD exhaust pipe. The diameters of the DPM particles ranged between $1e^{-9}$ m to $1e^{-7}$ m, with a mean diameter of $1e^{-8}$ m. DPM particles were treated as inert materials and the Rosin–Rammler diameter distribution was used. For physical models, the spherical drag law was used as a drag parameter. The intake air and DPM are considered as two different phases. The Eulerian–Lagrangian approach is used whereby the gas phase (air) was solved using the Eulerian approach and the particle-phase

(DPM) was tracked using the Lagrangian approach. Particle-to-particle interactions in the DPM were not considered because the particulate volume fraction was 0.5% (dilute).

7.1.4 Field experiment and model validation

The CFD model was validated against field measurements. **Fig. 7.3** shows the intake drive, fan, ventilation bag and dead-end crosscut. The average air velocity of the intake and return air side of the drive and crosscut was measured with a vane anemometer using the traverse method. **Fig. 7.3** and **Fig. 7.3**b show the field data and CFD simulation results. The very small differences between the simulated and measured results can be attributed to unevenness in the drive or crosscut wall surfaces that were not considered in the modelling. Overall, the difference varies from –3% to +3%.

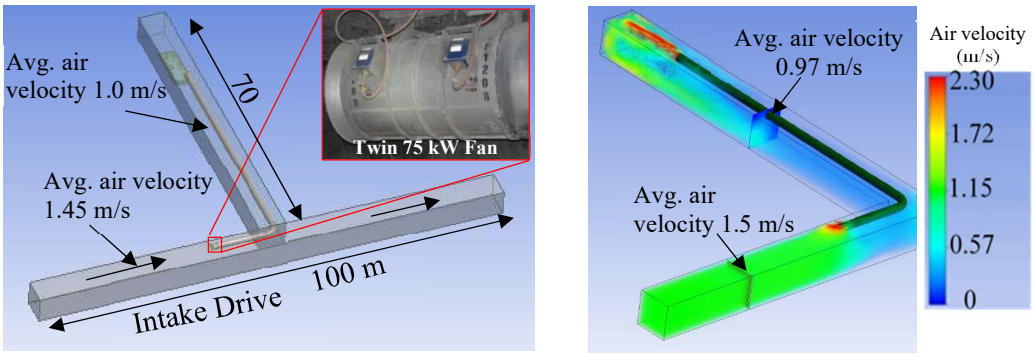

a. Measured air velocity b. Simulated air velocity

Fig. 7.3 Comparison of simulated results with experimental results

7.1.5 Effect of auxiliary fan location (intake airflow = fan capacity)

The initial studies were carried out with 30 m^3/s airflow (same as the capacity of the fan) in the main intake drive and fan locations of 0 m, 1 m, 2 m, 3 m, 4 m, 5 m and 10 m from the crosscut. **Fig. 7.4** shows the results of the simulation studies in terms of 3D streamline fields. The results show that in all cases, the air was recirculating; when the fan was in

line with the crosscut (0 m), most of the secondary fan air was recirculating. The amount of recirculating air was decreasing as the fan was located further away from the crosscut, but recirculation also occurred even when the fan was located 10 m away from the crosscut.

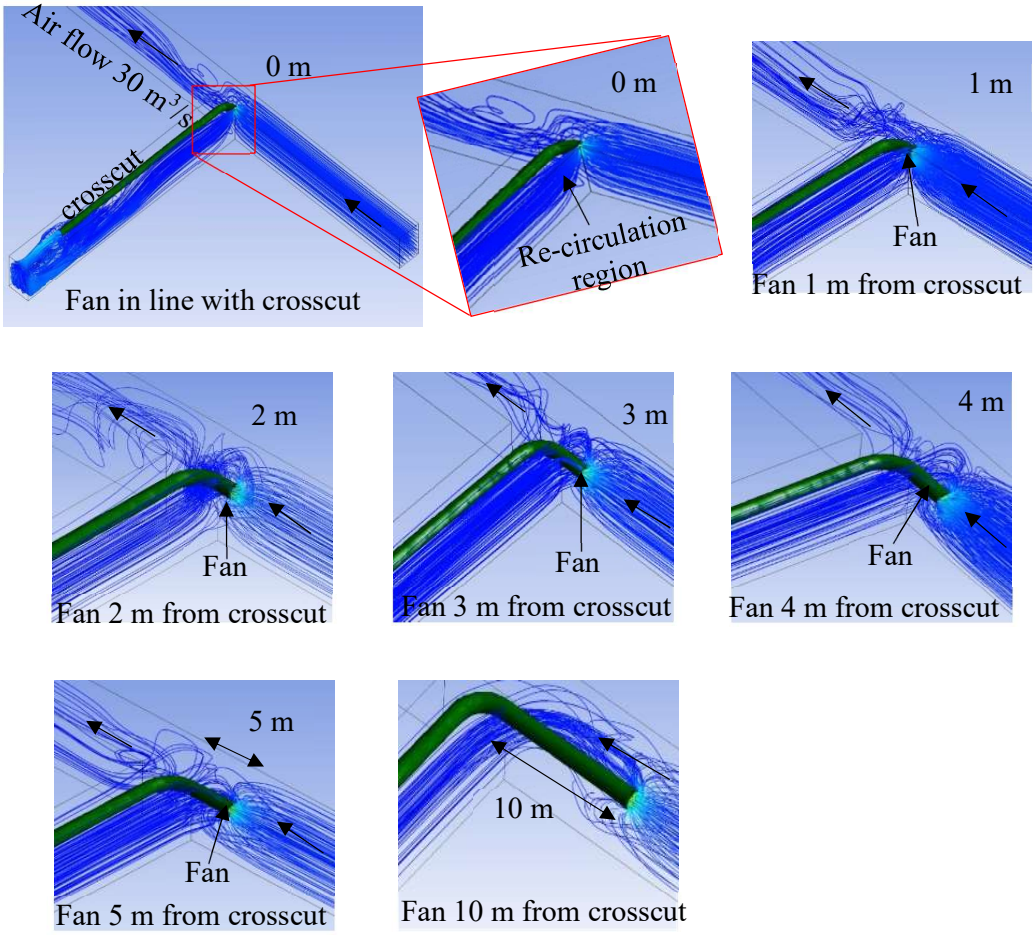

Fig. 7.4 Results of CFD simulations with a secondary fan located at different distances from the crosscut entrance with an intake drive airflow rate of 30 m^3/s

7.1.6 Effect of auxiliary fan location (intake airflow = 1.5 x fan capacity)

The next set of CFD studies were carried out with an intake airflow rate of 45 m^3/s (150% of the fan capacity). In this case maximum recirculation occurred when the fan was in line with the crosscut (offset 0 m). Recirculation gradually decreased when the fan was located from 1 m to 4 m away from the crosscut, but if the fan was 5 m and 10 m away from the crosscut there was no recirculation. **Fig. 7.5** shows the results of simulation studies when the intake air drive airflow rate was 45 m^3/s.

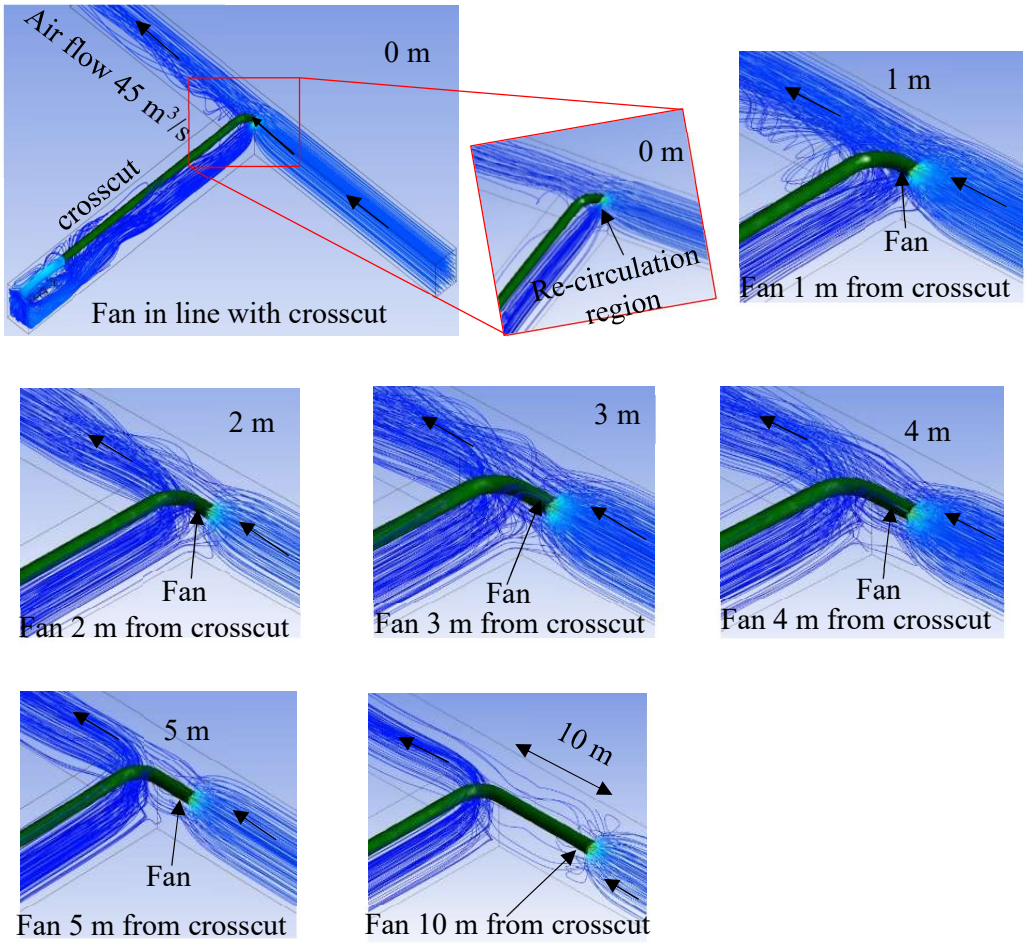

Fig. 7.5 Results of CFD simulations with secondary fans located away from the crosscut entrance at an intake drive airflow rate of 45 m^3/s

7.1.7 Effect of auxiliary fan location (intake airflow = 2 x fan capacity)

Further simulation studies were carried out with an intake air quantity of 60 m^3/s (twice the fan capacity). **Fig. 7.6** shows the results of these simulation studies. The figure shows that recirculation occurred when the fan was located from 0 m to 4 m from the crosscut entry but there was no recirculation when the fan was located 5 m and 10 m away from the crosscut.

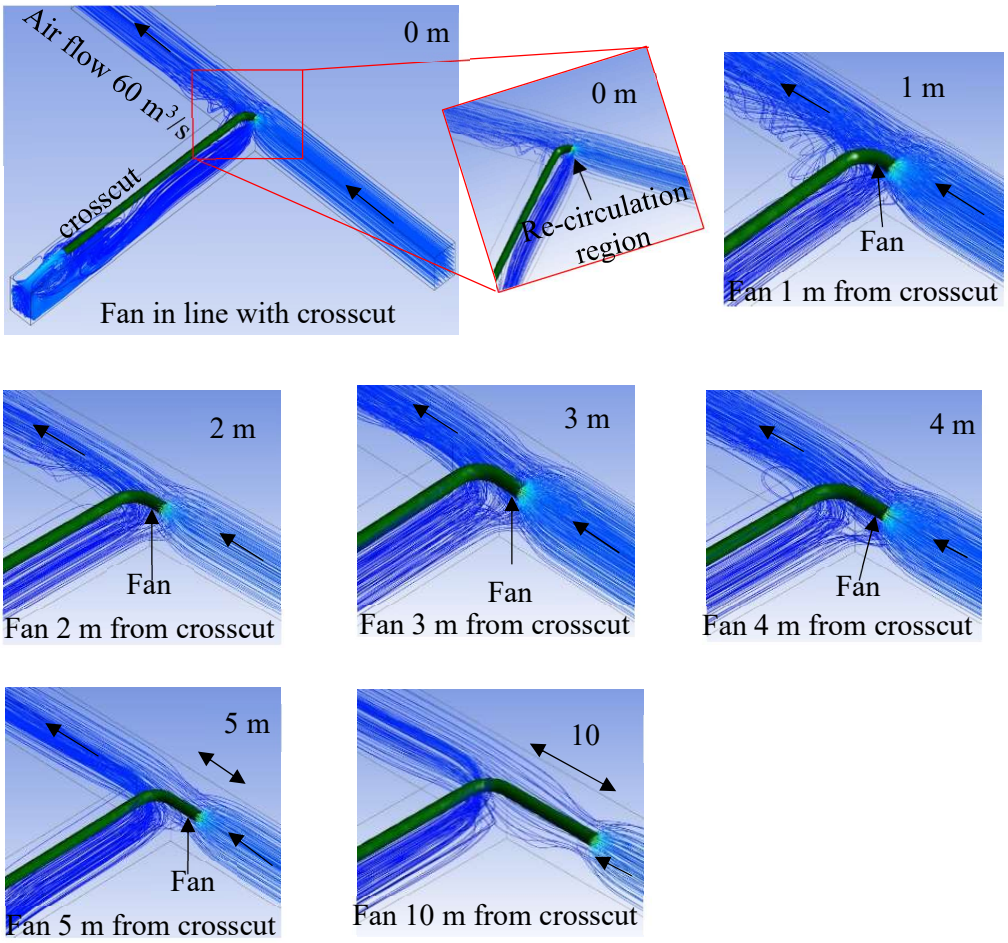

Fig. 7.6 Results of CFD simulations with different secondary fan locations from the crosscut entrance with an intake drive airflow rate of 60 m^3/s

Table 7.1 and **Fig. 7.7** shows the percentage of recirculated air with respect to where the secondary fan is located from the crosscut entry with different quantities of the intake air. The table shows that:

- If the quantity of intake air is 30 m^3/s or the same as the fan capacity, air recirculates.
- If the quantity of intake air is 45 m^3/s or 150% of fan capacity, there is no recirculation when the fan is at least 5 m or more from the crosscut entry.
- Similarly, if the intake air quantity is 60 m^3/s or 200% of the fan quantity, no recirculation occurred when the fan was at least 5 m or more from the crosscut entry.

Table 7.1 Percentage of air recirculation with respect to fan location from the crosscut entry

Air quantity in intake drive	Percentage of recirculation air in the secondary fan						
	Location of the secondary fan from the crosscut entry						
	0 m	1 m	2 m	3 m	4 m	5 m	10 m
30 m^3/s	54%	46 %	41%	37%	31%	24%	15%
45 m^3/s	36%	29%	22%	18%	10%	0	0
60 m^3/s	27%	20%	16%	9%	3%	0	0

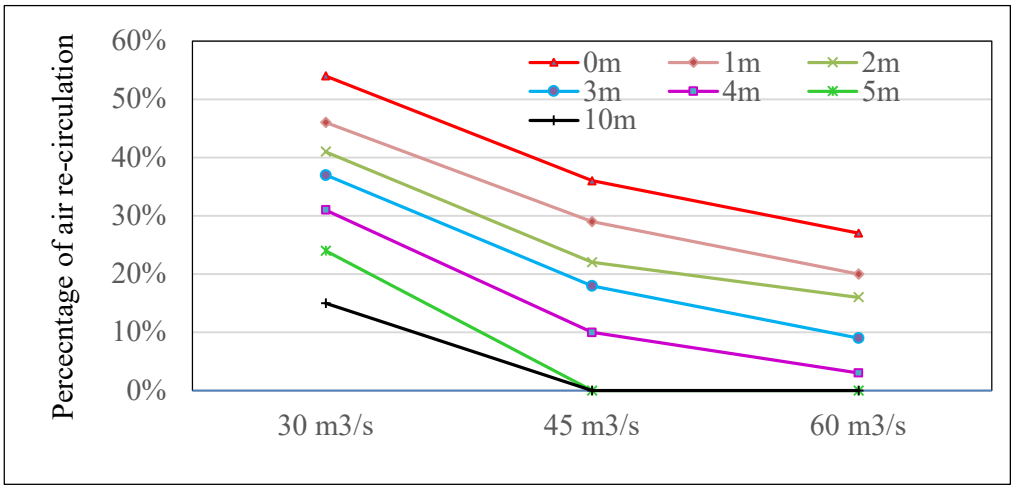

Fig. 7.7 Air recirculation percentage with intake air quantity and secondary fan location

Fig. 7.8a shows the concentration of DPM generated by an LHD in a dead-end crosscut. This heading is ventilated by a twin 75 kW fan located in the intake drive and in line with the crosscut. The average concentration of DPM at 5 m away from the face is 70 µg/m^3. Similarly, **Fig. 7.8**b shows the concentration of DPM generated by the LHD in a dead-end crosscut. This heading is ventilated by a twin 75 kW fan and the average concertation of DPM at 5 m away from the face is 61.5 µg/m^3. In both cases the intake air quantity is 60 m^3/s and the fan capacity is 30 m^3/s. These results indicate that if the fan is in line with the crosscut, the concentration of DPM is 13.8% more than if the fan was 10 m away from the crosscut due to air recirculation.

It is therefore recommended that the recirculating airflow near an auxiliary fan be avoided by placing a fan at least 5 m away from the upstream side of the dead-end entrance and the airflow in the intake air gallery should be at least 150% of the fan capacity. If the replacement/installation of the existing fan is not possible, rigid ducting can also be installed at the intake side of the fan.

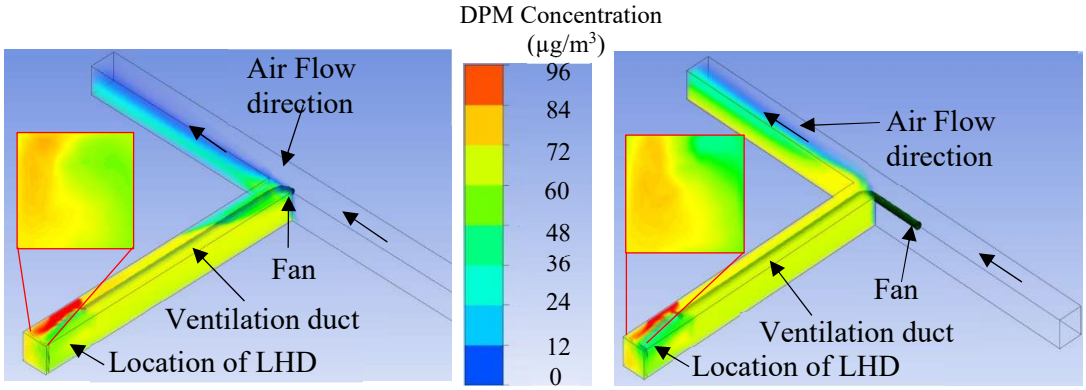

a. Fan is in line with the crosscut

b. Fan is 10 m from the crosscut

Fig. 7.8 DPM concentration field when the fan is 0 m and 10 m from the crosscut

7.2 Controlling of DPM using efficient filters

Diesel particulate filters (DPF) are commonly fitted on underground diesel-powered vehicles to control DPM (Cutler and Hickman, 2002, Koltsakis and Stamatelos, 1997). Some of these DPFs are ceramic filters (Adler, 2005), wall-flow filters (Konstandopoulos and Johnson, 1989) and catalytic filters (Koltsakis and Stamatelos, 1997, Van Setten et al., 2001) etc. The efficiency of DPF depends mainly on the amount of soot deposited in the filter (Tandon et al., 2010). None of the existing filters can control 100% of DPM throughout their usage period. Initially, they are very efficient, but as the soot builds up they become clogged and are less efficient. Soot deposition depends mainly on the number of working hours and the type of filter, but heavy vehicle filters are usually serviced every 4000 to 5000 working hours.

Fig. 7.9 shows DPFs fitted on a 307 kW LHD (**Fig. 7.9**a) and a 567 kW truck (**Fig. 7.9**b). In heavy vehicles, these DPFs contain a combination of four filters (**Fig. 7.9**c and **Fig. 7.9**d), which are generally changed and/or cleaned every 4000 working hours, depending on the manufacturer's specifications.

a. 305 kW LHD DPF

b. 567 kW Truck DPF

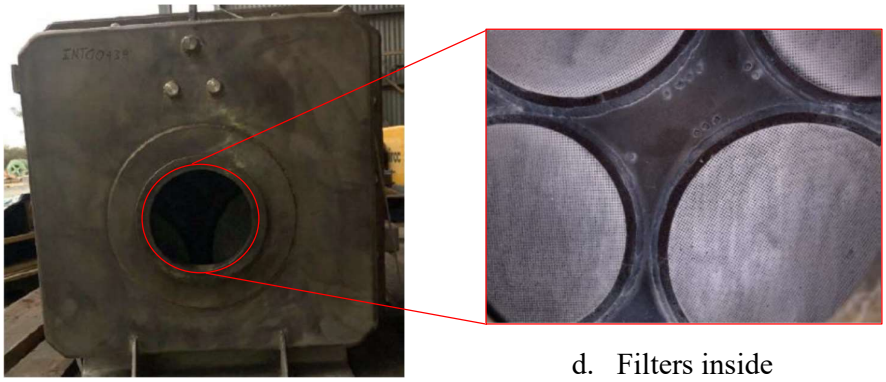

c. LHD DPF side view

d. Filters inside

Fig. 7.9 Diesel particulate filters of truck and LHD

CFD modelling studies were carried out to gauge the concentration of DPM with different filters. In these simulations, a 306 kW capacity LHD filter with 0%, 25%, 50% and 75% efficiency, an air intake velocity of 3 m/s and an air temperature of 303 K were assumed. For these simulations, computational domain, computational mesh, flow and boundary conditions are considered from the base case LHD counter-flow model of section 4.9 of Chapter 4.

Fig. 7.10 shows the results of CFD simulations with different filter efficiencies 50 m downstream of the vehicle, along with spot concentration values in the middle of the roadway 1.2 m above floor level. The figure shows that for filter efficiencies of 0%, 25%, 50% and 75%, the DPM concentration spot value was 65 µg/m^3, 41 µg/m^3, 28 µg/m^3 and

13 µg/m^3, respectively. These results indicate that for every 10% reduction in DPF efficiency, the DPM concentration will increase by 6.5%. To control DPM in underground mines, filters should be cleaned regularly.

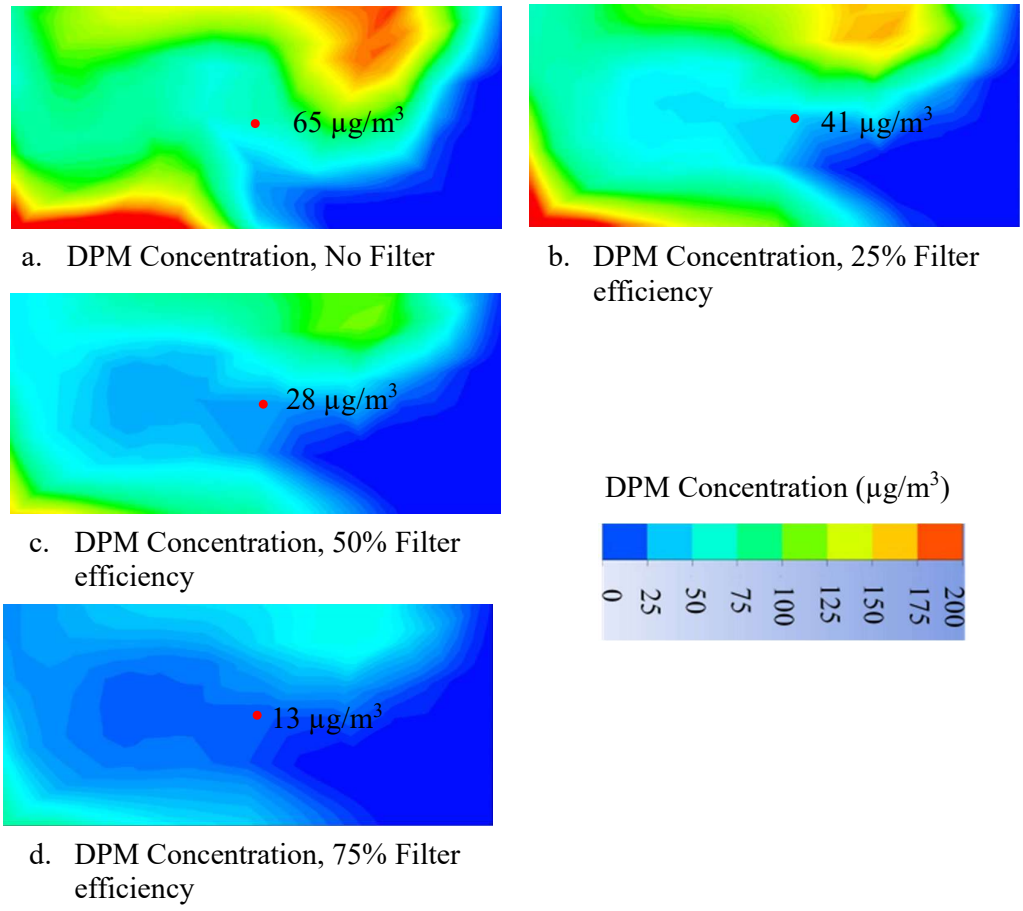

a. DPM Concentration, No Filter

b. DPM Concentration, 25% Filter efficiency

c. DPM Concentration, 50% Filter efficiency

d. DPM Concentration, 75% Filter efficiency

Fig. 7.10 Concentration of DPM with different filter efficiencies 10 m from the downstream side of the vehicle

7.3 Controlling DPM by removing fresh airway resistance in deep mines

The ventilation system for most deep mines (depth over 1000 m) depends mainly on secondary fans (Vutukuri and Lama, 1986), some of which are installed in the fresh air raise (FAR) and some are in the decline. If the fans are in a FAR system, fresh air comes directly from the surface to the fans. **Fig. 7.11** shows a FAR system connected with

various levels and the locations of the secondary fans.

Fig. 7.11 Secondary fans in a FAR system (Ventsim model)

The resistance of a fresh air drive might increase due to squeezing/collapsing as a result of stope-induced wall pressure. In the experimental mine with a FAR system at the 8790 level drive, some of the walls were squeezed due to sidewall pressure created by the 8790 level stopes. **Fig. 7.12** shows the collapsed drive location at the 8790 level and **Fig. 7.13** shows the area where the wall collapsed. Before it collapsed this drive area was 6 m wide by 5 m high, but after it collapsed the area was reduced to 3 m wide by 3.5 m high. In normal working conditions, the average air velocity in this section is 11 m/s and the airflow rate is 325 m^3/s, but after the collapse the average air velocity increased to 31 m/s with the same airflow rate. **Fig. 7.14** shows that the collapse caused a constriction in the

air passage that, corresponds to the air velocity and fall in air pressure. The resistance of the drive increased from 0.00067 Ns^2/m^8 to 0.01154 Ns^2/m^8. This increase in drive resistance caused the increased pressure to drop by 70 Pa to 1080 Pa and the average pressure created by each secondary fan below this level increased by 500 Pa (**Table 7.2)** and air quantity reduced from 35 m^3/s to 32 m^3/s.

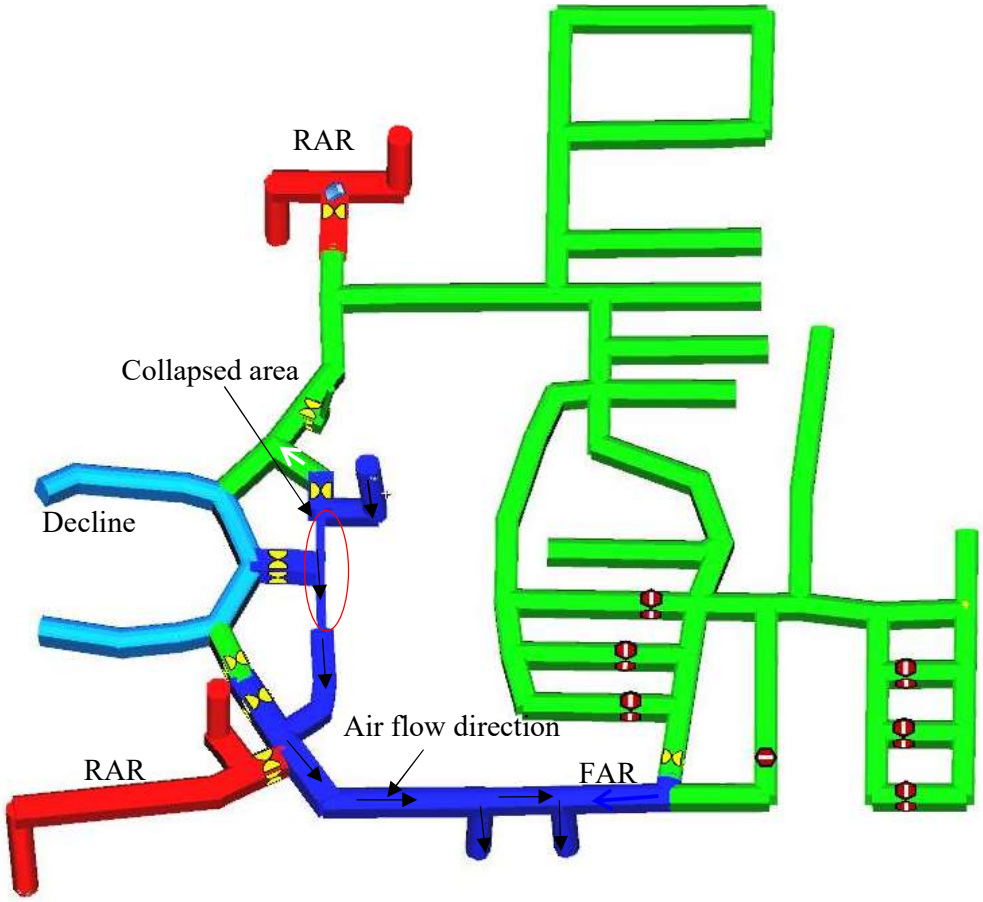

Fig. 7.12 Collapsed fresh air drive

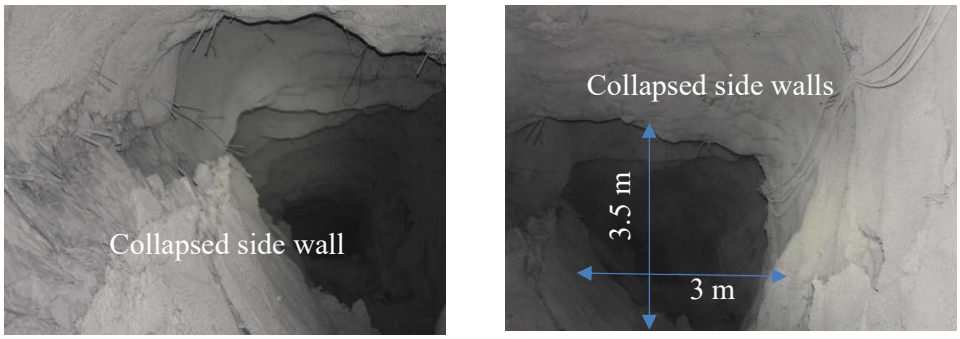

a. Foot wall side collapse wall b. Hanging wall side collapsed wall

Fig. 7.13 Collapsed drive wall at 8790 level

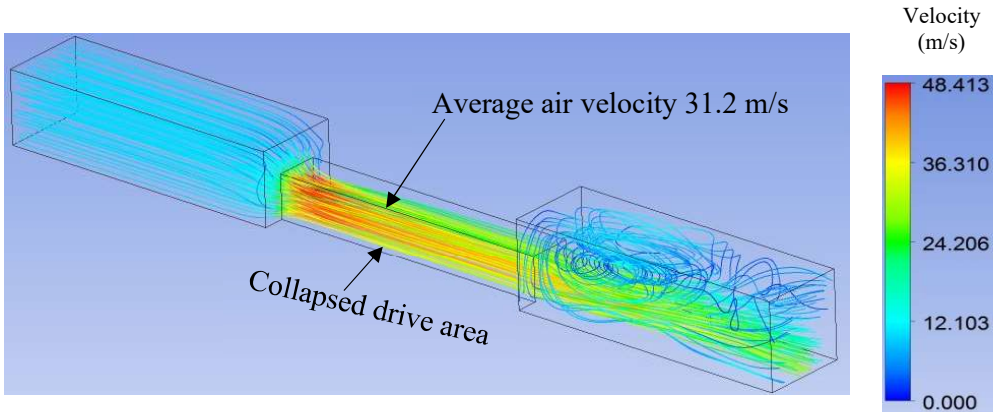

Fig. 7.14 Air velocity in the collapsed area

The temperature of the airflow delivered by the secondary fan depends on the pressure and quantity of air the fan can deliver. The following equations show how dry bulb and wet bulb temperatures change in a fan:

$$Change\ in\ dry\ bulb\ temperature\ \Delta T_{DB} = \frac{P\ Q}{1000\ \eta}\ \frac{1}{(\rho\ Q\ C_p)} \quad \textbf{(7-1)}$$

$$\text{Change in wet bulb temperature } \Delta T_{WB} = \frac{\left(\frac{P\ Q}{1000\ \eta}\right)}{40}\ \frac{10}{Q} \quad \textbf{(7-2)}$$

Where: ΔT is the rise in temperature (AIOH), P is the total pressure (Pa) of the fan, Q is the flow rate of the fan (m^3/s), η is total efficiency of the fan (%), ρ is air density (kg/m^3) and C_p is specific heat capacity of air (KJ/kg).

For example: At the 8520 level, fan pressure (P) is 3400 Pa, fan air quantity is 35 m^3/s, η is 80%, the air density ρ is 1.3 kg/m^3 C_p is 0.7 kJ/kg°C; this means the dry bulb temperature of fan air will increase by 4.6°C and the wet bulb temperature will increase by 1.0°C (**Table 7.2**). This increased air temperature in the workplace increases the increased dispersion of DPM and makes the miners feel sick.

After the collapsed drive at the 8790 level, the average airpower on each secondary fan decreased by 17.5 kW (p x q) and air quantity on each fan increased between 2 m^3/s to 7 m^3/s after rehabilitation. Due to increased air quantities for each fan and reduced air temperatures, DPM concentration at each level of the working area was reduced (**Table 7.3**).

Table 7.2 Secondary fan pressure and temperature before and after the 8790 level collapsed drive rehab

Fan location	With 8790 level collapsed drive		After removal of 8790 level collapsed rock	
	Secondary fan pressure (Pa)	Fan air temperature (Wet bulb °C / Dry bulb °C)	Secondary fan pressure (Pa)	Fan air temperature (Wet bulb °C / Dry bulb °C)
8750	–2750 Pa	26.0°C/39.0 °C	–2175 Pa	24.5°C/36.7 °C
8640	–3050 Pa	26.1°C/39.5 °C	–2560 Pa	25.0°C/37.0 °C
8610A	–3250 Pa	26.5°C/39.8°C	–2750 Pa	25.0°C/37.0 °C
8610B	–3250 Pa	26.5°C/39.8°C	–2760 Pa	25.0°C/37.0 °C
8580A	–3300 Pa	26.5°C/40.0 °C	–2810 Pa	25.2°C/37.2 °C

8580B	–3300 Pa	26.5ºC/40.2 ºC	–2820 Pa	25.2ºC/37.2 ºC
8540A	–3350 Pa	27.0ºC/41.0ºC	–2850 Pa	25.5ºC/37.5 ºC
8540B	–3350 Pa	27.1ºC/41.2ºC	–2860 Pa	25.5ºC/37.5 ºC
8520	–3400 Pa	27.4ºC/41.5ºC	–2910 Pa	25.5ºC/38.0 ºC

Table 7.3 Secondary fan pressure and temperature reduction with FAR collapsed drive removal and rehab

Fan location	After removal of 8790 level collapsed rock			
	Reduction of secondary fan pressure (Pa)	Reduction of fan air wet bulb temperature (ºC)	Reduction of fan air dry bulb temperature (ºC)	Percentage of reduction in DPM concentration
8750	–575	1.5	2.3	–32%
8640	–490	1.1	2.5	–19%
8610A	–500	1.5	2.8	–27%
8610B	–490	1.5	2.8	–21%
8580A	–490	1.3	2.8	–14%
8580B	–480	1.3	3.0	–12%
8540A	–500	1.5	3.5	–28%
8540B	–490	1.6	3.7	–14%
8520	–490	1.9	3.5	–25%
Average	–500	1.46	3.0	–27%

Table 7.3 shows that after removing the collapsed FAR drive, the pressure and discharge air temperatures due to the secondary fans had decreased. The table shows that an average of 500 Pa pressure decreased on each secondary fan and an average of 1.46^{o}C wet bulb temperature and 3^{o}C dry bulb temperature of fan discharge air also decreased. Moreover, it saved 157.5 kW of power, the cost of cooling and the DPM concentration reduced by 27%.

7.4 Pull–push ventilation strategy to control DPM in mine declines

In some deep mines the decline is the only source of transport and tramming, so there is a distinct possibility of high concentrations of DPM, which need enough air to dilute. For example, if a 65 tonne truck with a 567 kW engine capacity is moving upwards with a load, at least 34 m^3/s of airflow is needed to dilute the DPM (airflow at 0.06 m^3/s/kW). If more than one truck or a vehicle is moving at the same time, there will be more significant DPM accumulation and more airflow will be needed. If the area of the decline is 30 m^2, at least 2 m/s air velocity is required to dilute the DPM.

To carry out controlled investigations of DPM in decline, a part of the decline 500 m in vertical depth was chosen out of the total 1.8 km vertical depth. The bottom part of a mine generally has active working areas with high vehicle traffic so the DPM monitoring field experiments were carried out in this region. **Fig. 7.15** shows the total decline and the region where the experimental data was measured. The decline between 9000L and 8500L levels is 5349 m long and the vertical depth deference is 500 m.

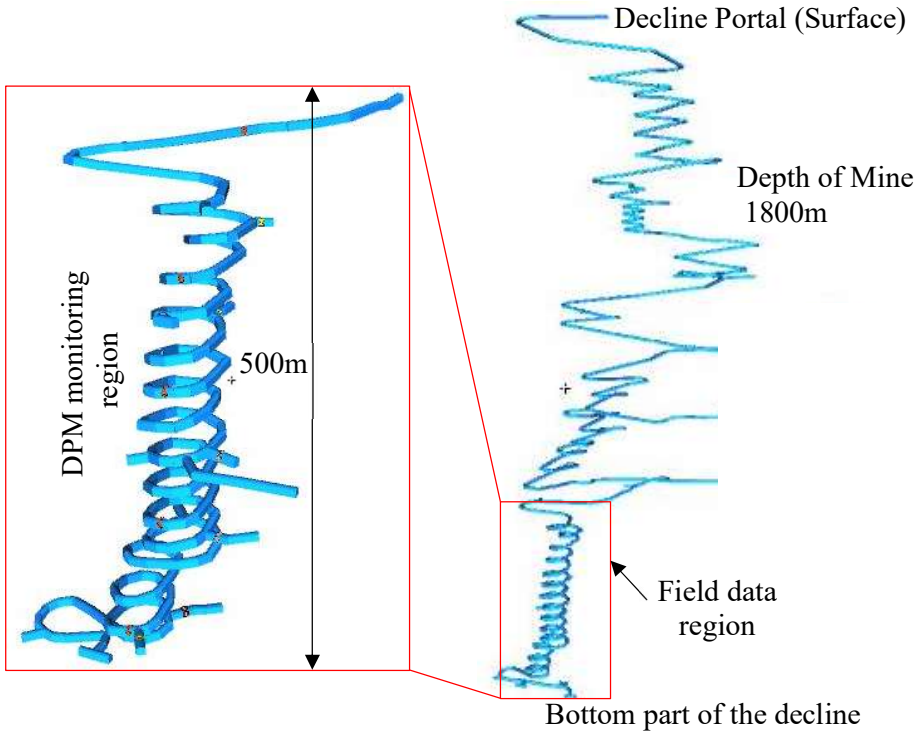

Fig. 7.15 Mine decline and field data region

To model the concentration of DPM in this decline the Ventsim program was used. This is based on the model validated against experimental field data between 9000L to 8500L. For these simulations, computational domain, flow and boundary conditions are considered from the base case decline DPM model of section 4.11 of Chapter 4.The air quantity at 9000L to 8750 was 80 m^3/s. At 8750L, the DPM in decline decreased to 45 $\mu g/m^3$ due to 60 m^3/s fresh air being added to the decline. In 8640L, 30 m^3/s air was added to the decline air reducing the DPM to 32 $\mu g/m^3$ in decline.

7.4.1 Pull–push ventilation system

At every level the declines are generally connected to the fresh air raise (FAR) system, the return air raise (RAR) system and level access. The RAR system with the decline is separated by a ventilation wall fitted with a regulator (Gillies et al., 2002), as shown in

Fig. 7.16a. Two regulators are generally used in deep mines (Mutton, 2010): a drop board regulator (DBR) shown in **Fig. 7.16**b and louvre airflow regulators (LAR) (Mutton, 2008) shown in **Fig. 7.16**c. DBRs contain manually controlled wooden boards and the LAR is mechanically operated by a wheel. **Fig. 7.17** shows the typical level layout with airflow regulators in a RAR system.

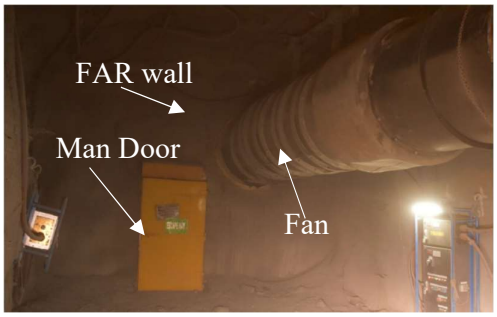

a. FAR wall with Fan

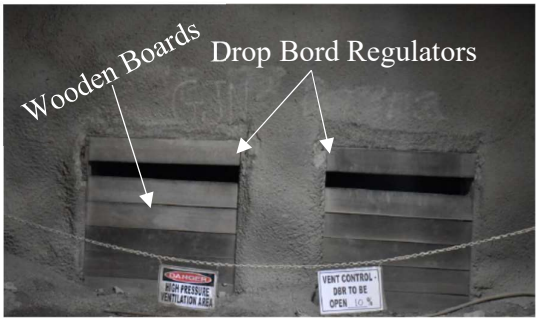

b. RAR wall with DBR

c. Mechanically operated regulator

Fig. 7.16 FAR wall with fan and RAR wall with a regulator

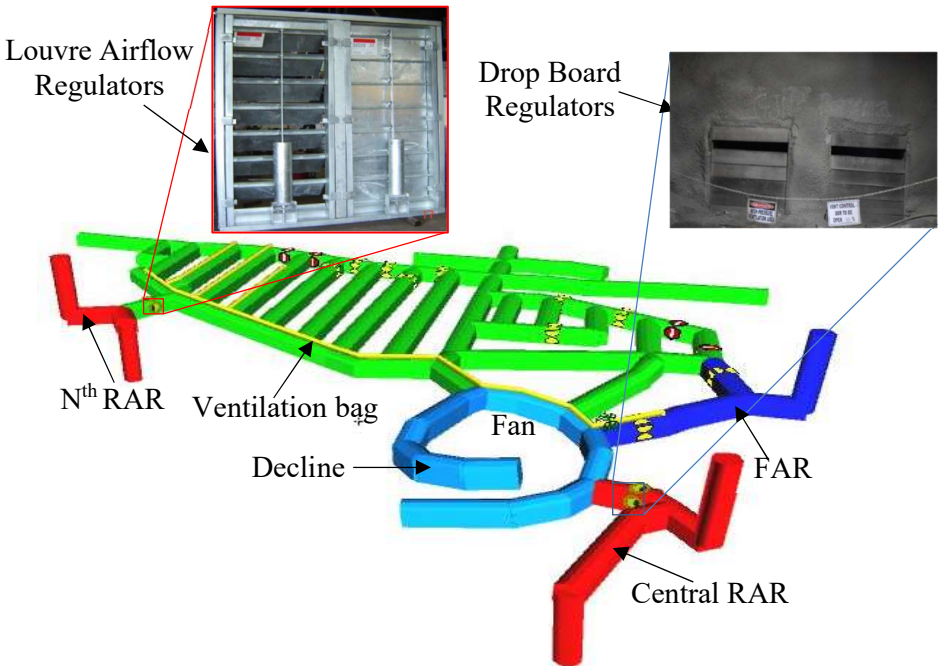

Fig. 7.17 Decline with FAR and RAR and regulators

In a pull–push ventilation system, some of the polluted air in decline will be sent to the return air system using return air regulators and some of the fresh air will be pumped to the decline from fresh airways by auxiliary fans. DPM control modelling studies in decline were carried out using Ventsim. In this modelling, at every 100 m of vertical distance or 1000 m in length, some of the air in the decline (about 20 m^3/s) was sent to the return air system and 20 m^3/s of the air fresh air was pushed to the decline.

Fig. 7.18 shows the results of Ventsim modelling after the control measures were put in place. The figure shows that a pull–push ventilation system reduced the concentration of DPM in decline. This technique was successfully implemented in the mine and achieved outstanding results. With this strategy, the quality of air in decline also improved. This pull–push ventilation system also helps to reduce dust, humidity, wet bulb and dry bulb temperatures and gaseous exhausts from diesel engines.

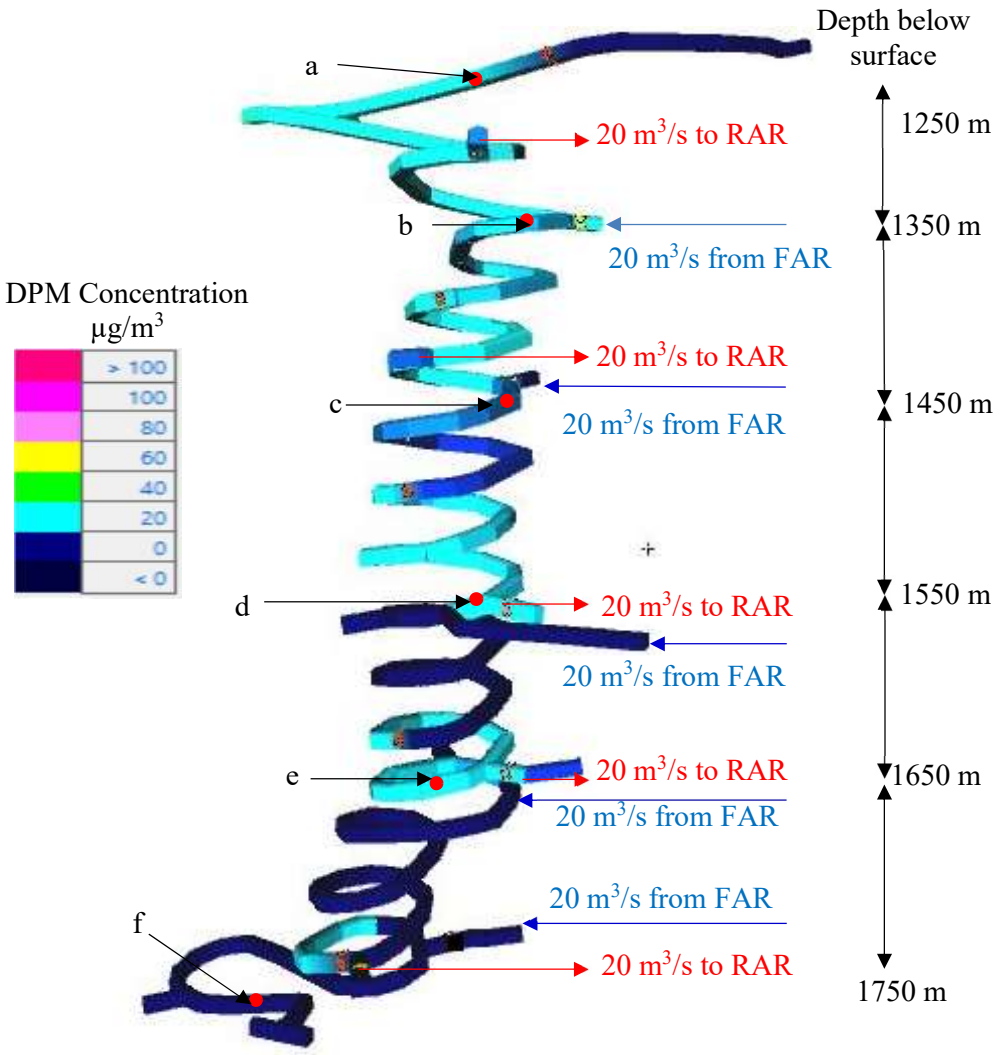

Fig. 7.18 Concentration of DPM in decline after control measures

Table 7.4 Comparison of decline measured DPM data with simulated data using the pull–push method of ventilation

Sampling station	Depth of decline below the surface (m)	DPM concentration without pull–push method ($\mu g/m^3$)	DPM concentration with pull–push method ($\mu g/m^3$)	DPM reduction percentage
a	1250	51	18	–65%
b	1350	58	37	–36%
c	1450	65	19	–71%
d	1550	85	31	–63%
e	1650	45	27	–40%
f	1750	35	12	–66%
Average DPM reduction percentage in decline				–56%

Note: DPM reduction % is the difference between simulation results and field measured results and was calculated as (Simulated value with pull–push method – Experimental value)/ experimental value) × 100.

Table 7.4 shows the reduction in DPM compared to the experimental results with the pull–push system of simulated results. The pull–push ventilation method of ventilating a decline and DPM concentration in decline decreased between 36% to 72%. The overall average reduction in DPM in decline was 56%.

7.5 Controlling DPM dispersion in dead-end crosscut with curtains

If a diesel-powered vehicle operates in a dead-end crosscut and if there is no secondary fan, it takes a long time for the DPM to dilute (section 6.2 of Chapter 6). To help control the DPM in such areas, CFD simulation studies were carried out using curtains at the edge of the crosscut and the main ventilation drive. Curtains are normally used in underground

mines to divert ventilation air and to dilute gas and dust (Zhou et al., 2015b, Babbitt and Ruggieri, 1990, Burgess Jr, 1979).

In this simulation the dead-end crosscut was 15 m away from the main drive and at 90° from the main gallery. The width and height of the crosscut and the main gallery were 6 m and 2.7 m, respectively. The air velocity in the main gallery was 2 m/s. Computational domain, grid structure, boundary and initial conditions are the same as section 4.10. A curtain measuring 2.7 m long × 1 m wide was incorporated into the model. Two orientations were tested (**Fig. 7.20**): (1) Curtain at 90° (**Fig. 7.19**a) to the main gallery and (2) Curtain at 45° to the main gallery (**Fig. 7.19**b). **Fig. 7.21** shows the dead-end crosscuts' meshed models without curtains, with curtains at 90° and 45°. The initial concentration of DPM in the dead-end was set as 820 μg/m^3 and transient flow modelling was carried out to simulate the flow evolving over 15 minutes.

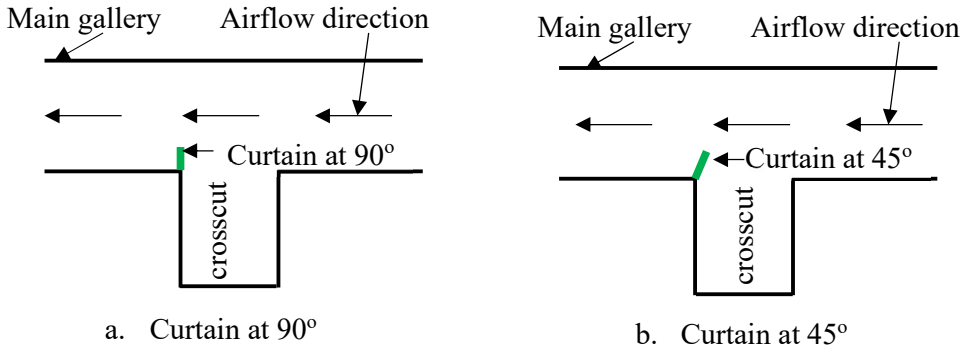

a. Curtain at 90°

b. Curtain at 45°

Fig. 7.19 location of dead-end crosscut with curtain at 90° and with curtain at 45°

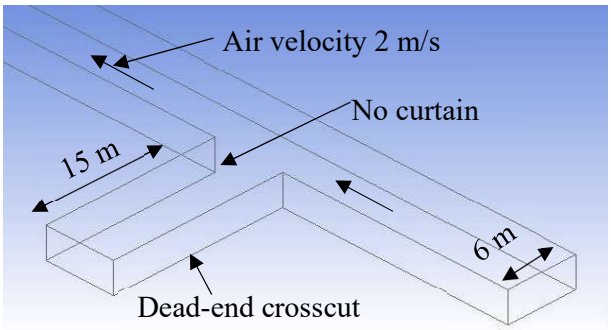

a. Dead-end crosscut with no curtain

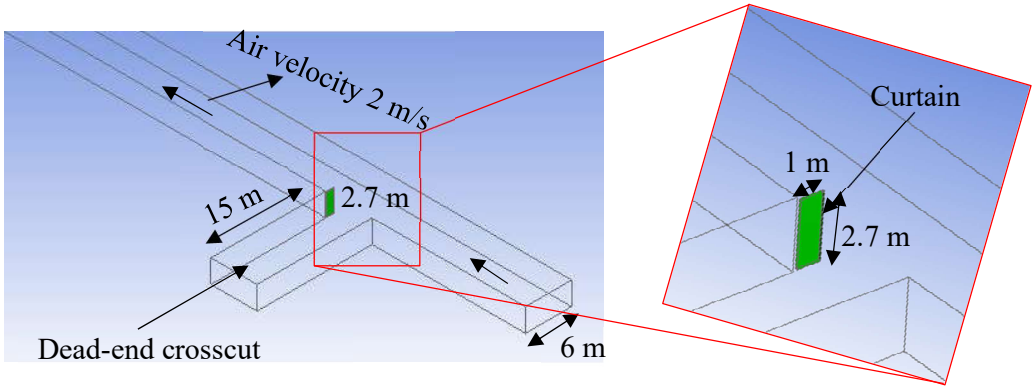

b. Dead-end crosscut with 90° angle curtain

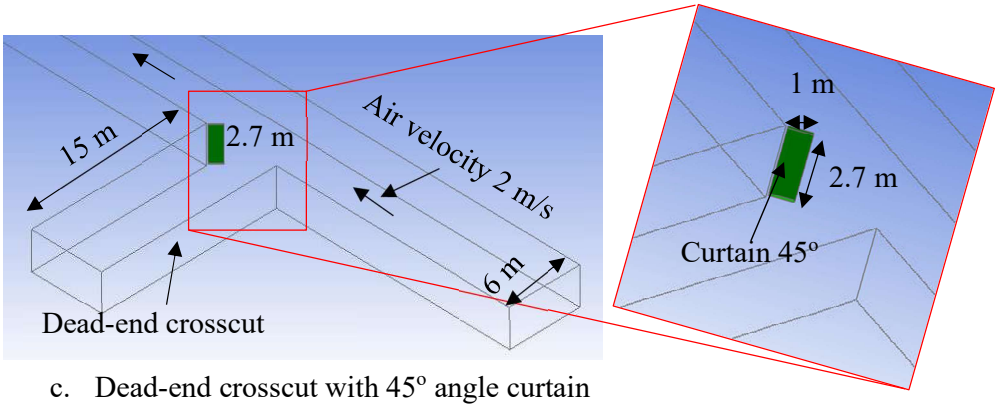

c. Dead-end crosscut with 45° angle curtain

Fig. 7.20 Geometry of dead-end crosscut without curtain, curtain at 90° and curtain at 45°

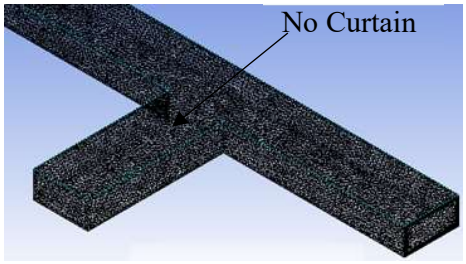

a. Dead-end crosscut with no curtain

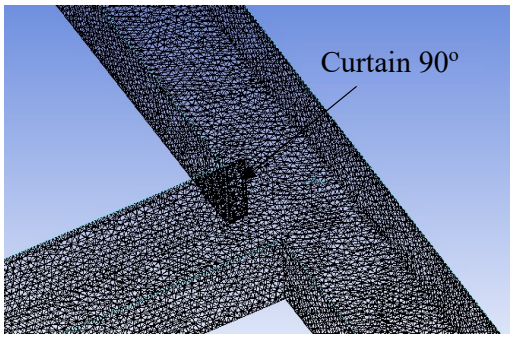

b. Dead-end crosscut with 90° curtain

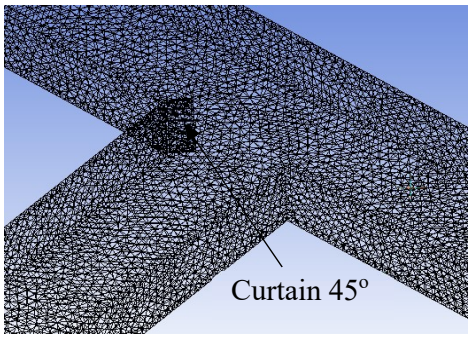

c. Dead-end crosscut with 45° curtain

Fig. 7.21 Meshed models of dead-end crosscut with no curtain and curtains at 90° and 45°

Fig. 7.22 shows the concentration of DPM without and with curtains. **Fig. 7.22**a shows that after 15 min and without a curtain, the concentration of DPM decreased from 820 µg/m^3 to 165 µg/m^3. With a curtain at 90° to the main gallery or in line with the dead-end crosscut wall, **Fig. 7.22**b shows that after 15 min the DPM concentration decreased from 820 µg/m^3 to 111 µg/m^3. With a curtain at 45° to the main gallery, **Fig. 7.22**c shows that after 15 min the DPM concentration decreased from 820 µg/m^3 to 75 µg/m^3. **Fig. 7.23** shows the changes in the concentration of DPM in the dead-end with no curtain, with a curtain at 90° and with a curtain at 45°. However, curtains have a limitation to dilute DPM particles in dead-end crosscuts of up to 50 m in length. For dead-end crosscuts of over 50 m in length, auxiliary fans are useful.

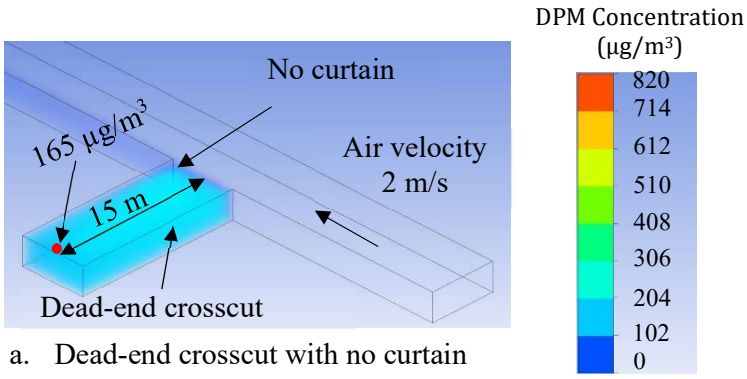

a. Dead-end crosscut with no curtain

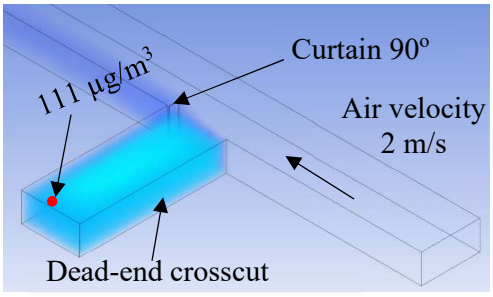

b. Dead-end crosscut with curtain 90° angle

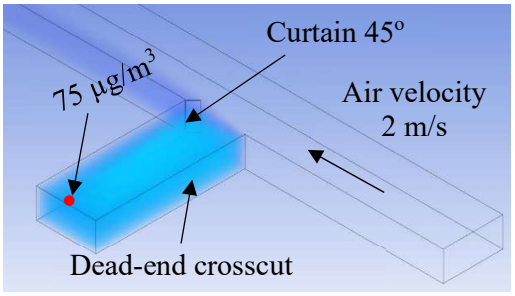

c. Dead-end crosscut with curtain 45° angle

Fig. 7.22 Meshed models of dead-end crosscut with no curtain and curtains at 90° and 45°

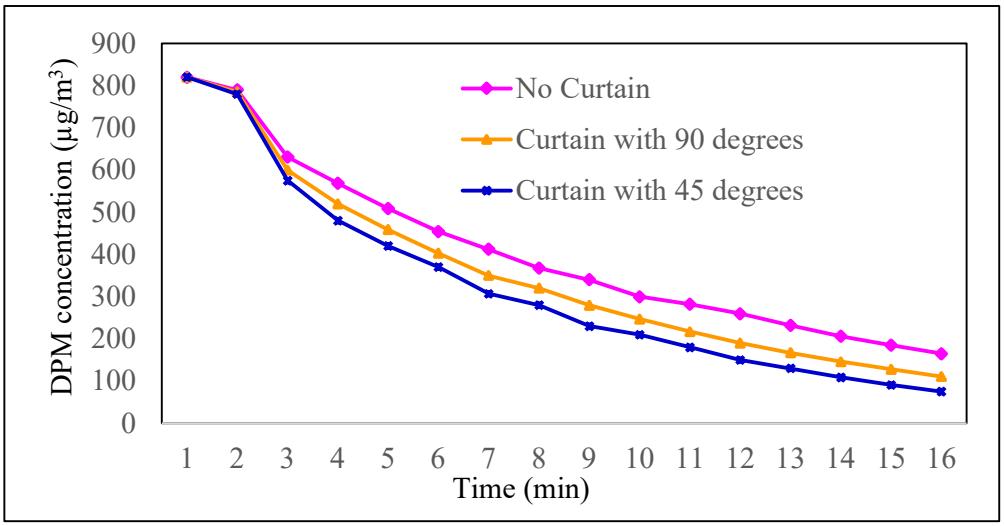

Fig. 7.23 Dead-end DPM dispersion without curtain, curtain at 90° and curtain at 45°

7.6 Summary

DPM controlled strategies were investigated and simulated in this chapter. The best location for an auxiliary fan and the minimum amount of air needed in the intake drive to control the DPM concentration where diesel-powered vehicles operate were also investigated using twin a 75 kW secondary fan of 30 m^3/s air quantity. For this modelling, intake drive air quantities of 100%, 150% and 200% more than the volume of airflow of the auxiliary fan and locations of auxiliary fans of 1 m, 2 m, 3 m, 4 m, 5 m and 10 m away from the dead-end crosscut were considered. A loader (306 kW) working in the dead-end crosscut was also considered. Field-monitoring data was used to validate the model. Results showed that if the quantity of intake drive air was the same as the fan, the air was always recirculated. However, the amount of recirculated air decreased as the distance between the fan and the crosscut increased. Studies also showed that if the intake drive capacity is greater than or equal to 150% of the fan capacity, there was no recirculation if the fan was at least 5 m away from the dead-end crosscut. These results also indicated that if the fan is in line with the crosscut, the concentration of DPM was 13.8% more than if the fan was 10 m away from the crosscut due to air recirculation. This strategy was successfully implemented in a mine.

A DPM control strategy was investigated with different filter efficiencies. The concentration of DPM increases as the efficiency of a diesel particulate filter decreases. For this study, modelling studies were conducted with 25%, 50% and 75% filter efficiencies. Modelling studies were conducted with LHD (306 kW) co-flow model of 3 m/s air velocity and intake air temperature of 303 K. Results indicate that if the DPF efficiency increased from 0% to 25%, 50% and 75%, there would be 36%, 56% and 80% reduction in DPM, respectively. The results showed that if the efficiency of the filter is reduced by 50%, the concentration of DPM will be increased by 56%. Regular

maintenance of DPF was therefore recommended.

DPM control strategy was investigated through the removal of extra resistance in the fresh air raise system. This strategy is applicable for a mine working with secondary fans and that are connected with a fresh air raise system. Fresh air raise systems with nine twin 90 kW fans, a total air quantity of 325 m^3/s, an initial drive area of 30 m^2 and a reduced area of 10.5 m^2 were considered for this modelling. The results showed that when the fresh air raise system collapses or is squeezed, roadway resistance will increase. There was an increase in the fresh air fan pressure, a reduction in the air quantity, fan discharge air temperature and an increase in DPM concentration. After removing the collapsed rock from the FAR drive, the average pressure on each secondary fan decreased by 500 Pa. Each fan's air quantity increased by 4.5 m^3/s and the average 1.46ºC wet bulb temperature and 3ºC dry bulb temperature of the 'fans' discharge air decreased. Moreover, the average DPM concentration decreased by 27%.

DPM control strategy was investigated and modelled with a pull–push ventilation system. This strategy is applicable for a mine having a decline as the primary source of vehicle movement. In this investigation, a decline of 500 m in vertical height and a truck (567 kW), grader (101 kW), Agitator (170 kW), light vehicle (110 kW) and LHD (306 kW) operating in decline were considered. In this model, at every 100 m, 20 m^3/s air was pulled from the decline and 20 m^3/s fresh air was pushed into the decline. The results of this simulations showed that the pull–push method of decline ventilation reduced the concentration of DPM between 36% to 72% and the overall average reduction of DPM in the decline decreased by 56%.

To dilute DPM in unventilated dead-end crosscuts, curtains at the entrance produced good results. Simulation studies were carried out with no-curtain and curtains at 90º and 45º.

A dead-end crosscut 15 m long and an air velocity in the adjacent gallery of 2 m/s were considered for this modelling. The results showed that after 15 min with no curtain, the concentration of DPM decreased from 820 $\mu g/m^3$ to 165 $\mu g/m^3$. If the curtain at 90^o was used at the crosscut, the concentration of DPM after 15 min decreased from 820 $\mu g/m^3$ to 111 $\mu g/m^3$. When a curtain at 45^o was used, the DPM concentration decreased from 820 $\mu g/m^3$ to 75 $\mu g/m^3$. These results proved that installing curtains will help to a certain extent at the dead-end crosscuts and a curtain at 45^o is better than a curtain at 90^o.

Chapter 8

Conclusions and Recommendations

8.1 Introduction

This chapter presents a summary of the main findings relevant to DPM dispersion in underground mines, including DPM literature, field experiments, CFD modelling and DPM control strategies. Recommendations for future work on the underground DPM dispersion are also discussed in this chapter.

In this thesis, field experiments and Computational Fluid Dynamics (CFD) modelling were used to study the dispersion of DPM in an underground mine environment and to develop control strategies. Field experiments were carried out at the Jhanjra Coal Mine in India and a copper mine in Australia. 3D CAD models of underground roadways and diesel-powered vehicles were developed and imported into the CFD software ANSYS Fluent. For CFD simulations, both discrete-phase modelling and species transport modelling with turbulent flow were used. Buoyancy effects and ventilation air and DPM temperature variations were considered. Transient flow modelling was used to model unventilated dead-end crosscuts for DPM dispersion studies. In a few cases, Ventsim modelling was used to simulate DPM patterns in a mine with a long decline. The results of these studies were validated against experimental field data with sufficient accuracy. Steady-state parametric studies were also carried out for different ventilation airflow velocities and temperatures, different exhaust temperatures and exhaust release locations. Transient parametric studies were carried out for different lengths and angles of dead-end crosscuts for different airflow velocities in the main airway. This thesis also suggested DPM control strategies using efficient filters, optimum secondary fan location, pull–push

ventilation system and curtains. The conclusions of this study are as follows:

8.2 Conclusions from the DPM literature

DPM is a Group-1 human carcinogen and is made up of carbon and other abrasive metallic particles, sulphates and silicates. DPM particles are very small in size and range from 1 nm to 100 nm and the density varies from 0.3 g/cm^3 to 1.2 g/cm^3. As per Australian standards, the 8-hour TWA exposure limit of EC is 100 µg/m^3. To dilute DPM within the regulatory limit, the minimum ventilation air quantity requirement is 0.06 m^3/s/kW.

Limited DPM field-monitoring and modelling data are available in the literature. Through field experiments have been conducted in NIOSH, DEEP and S&T, the available data is not enough to validate the CFD models. Also, limited DPM modelling studies and studies on DPM control strategies are available. The NIOSH, DEEP, ACARP and all other DPM control investigations have focused mainly on controlling DPM within the vehicles.

8.3 Conclusions from the field investigations

DPM field-monitoring investigations were conducted in both coal and metal mines. The coal mine DPM monitoring studies were conducted in six stages using a man-riding vehicle (150 kW), an LHD (150 kW) and a shuttle car (200 kW). The metal mine field-monitoring studies were conducted in two stages in a decline and with different occupational groups. Observations include:

a) During DPM field-monitoring with a man-riding vehicle (150 kW), the vehicle was stationary and the velocity of ventilation air in the roadway was 1.26 m/s. The results showed a high concentration of DPM on the exhaust pipe side of the roadway. At 10 m downstream of the vehicle, the DPM particles were spread over

the entire cross-section of the roadway.

b) DPM concentration was measured over a period of 30 minutes while the 150 kW man-riding vehicle was in motion. Over this period the vehicle travelled at speeds between 5 km/h to 18 km/h and the ventilation air velocity was between 1 m/s and 2.5 m/s. The results showed that personnel might be exposed to high concentrations of DPM during travel, up to 226.8 $\mu g/m^3$. This concentration varies with the relative velocity between the vehicle and the air.

c) DPM concentration was measured with a 150 kW capacity LHD. During this monitoring, the air velocity in the gallery was 1.26 m/s and the airflow and exhaust fume flow were in the same direction (co-flow). Similarly, with the same LHD and airflow, DPM concentration was measured when the airflow and exhaust fume flow were in opposite directions (counter-flow). The results indicated that the LHD operator would be exposed to a higher concentration of DPM in counter-flow than in co-flow. In co-flow, most of the DPM particle flow is confined to the middle of the roadway and in counter-flow the particles spread across the entire roadway cross-section.

d) DPM dispersion in an unventilated dead-end cut-through was monitored. During the experiment, the initial DPM concentration was 820 $\mu g/m^3$ in a 10 m long cut-through and the air velocity in the gallery adjacent to the dead-end cut-through was 2.52 m/s. The measured results showed that after 5 minutes the DPM concentration reduced from 820 $\mu g/m^3$ to 232 $\mu g/m^3$.

e) DPM concentration was monitored in a diesel-operated shuttle car (200 kW) working area. During the experiment, the air velocity in the panel was 2.63 m/s. DPM concentration was monitored during two complete shuttle car cycles. In each cycle, the shuttle car was loaded with coal at the loading point, unloaded at the

feeder and returned to the loading point. The average DPM concentration during two shuttle car cycles in the panel's return airway is 254.66 μg/m^3. It was concluded that personnel should not occupy the return side of the shuttle car's panel due to the high DPM concentration levels.

f) DPM concentration was monitored in a metal mine decline at five sampling points. The sampling points were spaced 100 m apart vertically in the decline. During the measurements, vehicles like a truck (567 kW), a grader (101 kW), an agitator (170 kW), a light vehicle (110 kW) and an LHD (306 kW) were moving in the decline and the airflow in the decline varied from 45 m^3/s to 100 m^3/s. At each sample station, DPM and airflow were measured for 15 min. The monitoring results concluded that the DPM concentration in the decline depends mainly on the number of vehicles and the available air quantity. The maximum 15-minute time-weighted average of DPM in the decline was 85 μg/m^3 and the average concentration of DPM in the decline was 56 μg/m^3.

g) In this research the time-weighted average exposure of different occupational personnel to DPM was measured over a 12-hour shift. The results showed that the levels of exposure to DPM for underground personnel measured over a 12-hour shift are within the statutory limit of 100 μg/m^3 of elemental carbon.

8.4 Conclusions from the model validation

CFD was used to address many typical underground mining problems such as ventilation, gases, dust and the spontaneous combustion of coal, mine fires and DPM. After DPM field-monitoring investigations, base case CFD models were developed using ANSYS Fluent and a few case models were developed using Ventsim. These models were created for an underground environment, incorporating diesel-powered vehicles, dead-end

crosscuts and declines etc. To achieve accurate results, fine meshes were used. The minimum size of the cell used to construct the mesh was 7.3×10^{-3} m, the minimum edge length of each cell was 0.025 m and 'size function' activated was 'proximity and curvature'. Program controlled inflation with seven to ten layers were used for the mesh.

After meshing, discrete-phase modelling was used to model the DPM flow. The DPM particle diameter was considered as varying from $1e^{-9}$ m to $1e^{-7}$ m, with a mean diameter of $1e^{-8}$ m. DPM particles were treated as an inert material and the Rosin–Rammler diameter distribution was used. For a few cases like DPM dispersion in unventilated dead-ends, transient flow modelling with species transport modelling was used. The simulated models were in reasonable agreement with the field experimental data, although there were some differences between the simulated and measured results due to uneven gallery walls and uneven machine surfaces that were not modelled in detail.

8.5 Conclusions from the parametric studies with different ventilation and operational conditions

After the development and validation of base case models, parametric studies were conducted by varying ventilation and operational conditions. The results can be summarised as follows:

a) DPM concentration changes with air velocities in the roadway. For this investigation, a man-riding vehicle model and air velocities in the roadway of 0.5 m/s, 1 m/s, 2 m/s and 3 m/s were considered. The concentration of DPM at 40 m downstream in the middle of the roadway and 1.2 m above the floor was monitored. The modelling results showed that if the air velocity was reduced by 40% and 60% of the base case value (1.26 m/s), the average concentration of DPM increased to 48% and 125%, but if the intake air velocity increased by 58% and

98% of the base case value, the average concentration of DPM decreased to 42% and 50%.

b) DPM concentration near the vehicle changes with the exhaust pipe location. DPM modelling was carried out with different exhaust pipe locations such as at the rear, bottom and top of the vehicle. For this modelling, the 150 kW LHD model was used with an air velocity of 2 m/s. The concentration of DPM 50 m downstream in the middle of the roadway and 1.2 m above the floor was monitored. If the exhaust pipe is at the back, bottom and top, the DPM concentrations were 48 $\mu g/m^3$, 52 $\mu g/m^3$ and 23 $\mu g/m^3$, respectively. It is better for the operator to have the exhaust pipe at the bottom of the vehicle.

c) DPM concentration variations were investigated by changing intake air temperature (20°C, 30°C and 40°C) and exhaust fume temperature (50°C, 60°C, 70°C and 80°C). The results showed that the temperature of diesel-powered vehicle exhausts had a slight influence on the concentration of DPM on the downstream side of the vehicle. Increasing the temperature of the intake air increased the concentration of DPM at the downstream side of the vehicle.

d) DPM concentration at the downstream side of the vehicle is influenced by the vehicle morphology (shape). Simulation studies were carried out with a man-riding vehicle and a box of man-riding vehicle size. For this modelling, an air velocity of 1 m/s was considered. The results showed that the 'box' morphology contains less DPM concentration at the downstream than using the actual vehicle. At 40 m downstream side of the vehicle, DPM concentration for the man-riding vehicle and the box were 123 $\mu g/m^3$ and 100 $\mu g/m^3$, respectively.

e) Studies showed a high concentration of DPM on the downstream side of the truck loading bay, so personnel should not remain in this area for a long time.

Simulation studies were carried out with a truck (567 kW), a loader (306 kW) and an air velocity of 1.5 m/s. The results showed that 50 m downstream to the loading bay, with the truck and loader operating at full capacity there was a high DPM concentration of over 200 μg/m^3, so personnel should not remain in this area for a long time. To control exposure to high DPM concentration at the truck loading bay, the loading bay should be located on the return side of the level if possible. Adequate air must also be supplied to reduce the DPM within the statutory limit.

8.6 Conclusions from the unventilated dead-end crosscut modelling

DPM dispersion in an unventilated dead-end crosscut was investigated using transient flow modelling. These investigations revealed that the dispersion and dilution of DPM in the dead-end crosscuts were influenced by the airflow in the adjacent gallery and the length and angle of the unventilated dead-end. In this simulation, an initial DPM concentration in the dead-end crosscut of 820 μg/m^3 was considered. The key conclusions from the simulations are:

a) Increasing the velocity of air in the adjacent gallery reduced the dispersion/dilution of DPM. In this investigation a 20 m long dead-end crosscut with an adjacent footwall drive air velocity of 0.5 m/s, 1 m/s, 2 m/s, 3 m/s and 4 m/s was considered. The initial DPM concentration in the dead-end crosscut was 820 μg/m^3. After 15 minutes, for 0.5 m/s, 1 m/s, 2 m/s, 3 m/s and 4 m/s air velocities the DPM concentration decreased to 820 μg/m^3 (no change), 425 μg/m^3, 220 μg/m^3, 115 μg/m^3 and 95 μg/m^3, respectively. It was also concluded that if the air velocity was 0.5 m/s or less, its influence in an adjacent gallery on dilution in a dead-end crosscut 20 m or longer was negligible.

b) The longer the dead-end, the longer it takes for DPM to dilute. In this modelling,

an air velocity in the adjacent gallery of 2 m/s and dead-end crosscut lengths of 10 m, 15 m, 20 m and 25 m were considered. To reduce the DPM concentration by 50% for 10 m, 15 m, 20 m and 25 m length dead-end crosscuts, it took 4 min, 6.5 min, 7.5 min and 13.5 min, respectively.

c) Investigations were also conducted with a 50 m long dead-end crosscut. For a 50 m long unventilated dead-end crosscut with an air velocity in the adjacent gallery of 2 m/s, it took 5 hours to reduce the DPM from 820 $\mu g/m^3$ to 100 $\mu g/m^3$.

d) The reduction of DPM as the angle of the dead-end crosscut increased was relatively low. The DPM concentration increased as the angle between the cut-through and main gallery decreased. In these simulations, a 20 m long dead-end crosscut with 45°, 90° and 135° angles to the adjacent footwall drive and an adjacent gallery air velocity of 2 m/s was used. After 10 min the DPM concentrations for the 45°, 90° and 135° angled dead-end crosscuts were 239 $\mu g/m^3$, 347 $\mu g/m^3$ and 508 $\mu g/m^3$, respectively.

e) A vortex airflow formed near the dead-end crosscut entrance and revolved in a curved form, while the air velocity and pressure decreased towards the centre of the vortex. DPM concentration increased towards the centre of the vortex. The centre of the vortex depends on the length of the dead-end crosscut and the maximum length was 10 m from the entrance.

8.7 Conclusions from the DPM control strategies

The DPM modelling studies conducted in this research provided a better understanding of the DPM flow distribution. These modelling studies enabled practical and innovative DPM control strategies to be developed in this research. The following are the key conclusions:

a) A study was conducted to find the optimum location for an auxiliary fan to eliminate DPM in mixed air recirculation and to reduce DPM concentration in dead-end workings. This investigation included both CFD modelling and field experiments. A twin 75 kW fan of 30 m^3/s air capacity, a dead-end crosscut length of 70 m, ventilation ducting of 50 m and an LHD (306 kW) were considered. Studies were carried out with intake drive air quantities of 100%, 150% and 200% of the volume of airflow from the auxiliary fan and with the auxiliary fan 1 m, 2 m, 3 m, 4 m, 5 m and 10 m away from the dead-end crosscut. Studies found that the auxiliary fan's intake drive air quantity must be greater than or equal to 150% of the gallery airflow and the auxiliary fan must be located at least 5 m from the dead-end crosscut entry. This study also concluded that if the quantity of intake drive air is the same as the fan, then (1) the air was always recirculated and (2) the amount of recirculated air decreased as the distance between the fan and the crosscut increased. Moreover, if the fan is in line with the crosscut, the concentration of DPM was 13.8% more than if the fan was 10 m away from the crosscut, due to air recirculation. This control strategy was successfully implemented in the field.

b) Studies were carried out to control DPM by using efficient filters. An LHD (306 kW) and co-flow model with 3 m/s air velocity and intake air temperature of 303 K were considered. Modelling was carried out with 25%, 50% and 75% filter efficiencies. The results showed that the concentration of DPM increased as the efficiency of a diesel particulate filter decreased and if the DPF efficiency increased from 0% to 25%, 50% and 75%, there would be 36%, 56% and 80% reduction in DPM concentration. Moreover, if the efficiency of the filter was reduced by 50%, the concentration of DPM would increase by 56%. Regular

maintenance of DPF was therefore recommended.

c) DPM control strategy involving the removal/reduction of intake airway resistance was investigated via CFD modelling and field experiments. This control strategy used a secondary fan ventilation system connected to a common intake airway. Blockages in the fresh airway system due to collapsed rock or squeezed ground increased the pressure of the secondary fans and their air temperatures. The reduced airflow also caused higher DPM concentrations in the working areas. Modelling studies were carried out with a fresh air drive of 6 m x 5 m size; this was then reduced to 3 m x 3.5 m, the quantity of air 325 m^3/s and nine twin 90 kW fans were connected in the FAR system. The results showed that after the blockage had been removed, the average DPM concentration in the working levels decreased by 27% due to an increase in the air quantity and a reduction in the fans' off-air temperatures. This control strategy was successfully implemented in the field.

d) An innovative DPM control strategy in a mine decline with diesel-powered vehicles was investigated using a pull–push ventilation system. In this system and at various intervals, some of the decline's air was pulled out into the return airway and some of the fresh air was pumped into the decline from the FAR system. This investigation considered a decline of 1200 m long and a 500 m vertical height. It was assumed that a truck (567 kW), a grader (101 kW), an agitator (170 kW), a light vehicle (110 kW) and an LHD (306 kW) were operating in the decline. At 100 m intervals, 20 m^3/s air was pulled from the decline and 20 m^3/s fresh air was pushed in; this pull–push method of decline ventilation reduced the concentration of DPM between 36% to 72% and the average amount of DPM in the decline decreased by 56%.

e) A creative DPM control strategy using curtains in the unventilated dead-end crosscuts with no source of secondary ventilation system was investigated. If auxiliary ventilation in a dead-end crosscut is not possible, the DPM can be diluted with a curtain at the dead-end crosscut entrance. This study considered a 15 m long dead-end crosscut with an air velocity of 2 m/s in an adjacent gallery and an initial DPM concentration in the dead-end crosscut of 820 $\mu g/m^3$. In this modelling, transient flow modelling studies were carried out in three scenarios: (1) no curtain, (2) curtain at 90^o and (3) curtain at 45^o angle to the dead-end crosscut. Studies found that over a 15-min duration, the DPM concentration reduced to 165 $\mu g/m^3$, 111 $\mu g/m^3$ and 75 $\mu g/m^3$, respectively for the no curtain, curtain at 90^o and curtain at 45^o models.

The control strategies described in this thesis will effectively control DPM dispersion in an underground mine environment and minimise DPM exposure to underground personnel.

8.8 Recommendations

It is recommended that further research be undertaken in the following areas:

- Effect of inter-particle collisions between DPM, dust and moisture particles;
- Transient DPM flow modelling with multi-vehicle operations in one area with no load and a full load;
- Controlling DPM with water sprays and scrubbers;
- Effect of vehicle movement on the dispersion of DPM using moving mesh in a drive longer than 1 km.

List of References

ADLER, J. 2005. Ceramic diesel particulate filters. *International Journal of Applied Ceramic Technology,* 2, 429-439.

AIOH 2013. Diesel particulate matter Occupational Health Issues. (The Australian Institute of Occupational Hygienists, Inc).

AIRTEC 2019. AIRTEC ™ Wearable, Real Time DPM / EC Monitor. Flir.

AMINOSSADATI, S. M. & HOOMAN, K. Numerical simulation of ventilation air flow in underground mine workings. Proceeding of 12th US/North American Mine Ventilation Symposium, 2008. 253-259.

ANDERSON, J. D. & WENDT, J. 1995. *Computational fluid dynamics*, Springer.

ANSYS 2013. Fluent theory guide.

ARYA, S. & NOVAK, T. 2020. Numerical Investigation of the Effect of a Novel Wet Scrubber on Dust Reduction in an Underground Coal Mine. *Mining, Metallurgy & Exploration,* 37, 129-139.

BABBITT, C. & RUGGIERI, S. 1990. Evaluate fundamental approaches to longwall dust control: Subprogram E, Longwall application of ventilation curtains. Foster-Miller, Inc., Waltham, MA (USA).

BAER, S. C. 1997. Passive ventilation system and method. Google Patents.

BAINES, P. 1988. Auxiliary ventilation utilising recirculation. *Colliery Guardian,* 236:2, 55-58.

BALARAJU, J., GOVINDA RAJ, M. & MURTHY, C. 2018. Estimation of reliability-based maintenance time intervals of Load-Haul-Dumper in an underground coal mine. *Journal of Mining and Environment,* 9, 761-770.

BELLE, B. 2010. Use of baseline personal DPM exposure data for mine ventilation planning-A South African Journey. *J. Mine Vent. Soc. S. Afr.*, 9,12-16.

BENBRAHIM-TALLAA, L., BAAN, R. A., GROSSE, Y., LAUBY-SECRETAN, B., EL GHISSASSI, F., BOUVARD, V., GUHA, N., LOOMIS, D. & STRAIF, K. 2012. Carcinogenicity of diesel-engine and gasoline-engine exhausts and some nitroarenes. Elsevier.

BICKEL, K. L., MCDONALD, J., FRUIN, J. E. & TIFFANY, D. G. 1997. Economic Comparison of Biodiesel Blends to Commercially Available Exhaust Emission Reduction Technologies for Underground Mines, Final Report to the National BiodieselBoard. *University of Minnesota*.

BIRCH, E. Diesel particulate matter (as Elemental Carbon): Method 5040. NIOSH Manual for Occupational Safety and Health, 2003. 1-5.

BLUHM, S., MARX, W., VON GLEHN, F. & BIFFI, M. 2001. VUMA mine ventilation software. *Journal of the Mine Ventilation Society of South Africa,* 54, 27-36.

BRAKE, D. Fire modelling in underground mines using Ventsim Visual VentFIRE Software. Australian Mine Ventilation Conference/Adelaide. SA, Australia, 2013.

BRILL, B. 1989. Deformation and recrystallization microstructures in deformed ores from the CSA mine, Cobar, NSW, Australia. *Journal of structural geology,* 11, 591-601.

BUGARSKI, A., JANISKO, S., CAUDA, E., NOLL, J. & MISCHLER, S. 2012a. Controlling Exposure to Diesel Emissions in Underground Mines. 16-45, *SME*.

BUGARSKI, A., SCHNAKENBERG, G., NOLL, J., MISCHLER, S., PATTS, L., HUMMER, J., VANDERSLICE, S., CRUM, M. & ANDERSON, R. The Effectiveness of Selected Technologies in Controlling Diesel Emissions in an Underground Mine-Isolated Zone Study at Stillwater Mining Company's Nye Mine. 2004. 1-86, *NIOSH.*

BUGARSKI, A., SCHNAKENBERG JR, G. & PATTS, L. Implementation of diesel particulate filter technology in underground metal and nonmetal mines. Proc. 11th

US/North American Mine Ventilation Symp, 2006. 127-133.

BUGARSKI, A. D. 1999. Characterization of particulate matter and hydrocarbon emissions from in-use heavy-duty diesel engines.*BHILC.*

BUGARSKI, A. D., CAUDA, E. G., JANISKO, S. J., HUMMER, J. A. & PATTS, L. D. 2010. Aerosols emitted in underground mine air by diesel engine fueled with biodiesel. *Journal of the Air & Waste Management Association,* 60, 237-244.

BUGARSKI, A. D., CAUDA, E. G., JANISKO, S. J., MISCHLER, S. E. & NOLL, J. D. Diesel Aerosols and Gases in Underground Mines: Guide to Exposure Assessment and Control. National Institute for Occupational Safety and Health, 2011. 1-150.

BUGARSKI, A. D., JANISKO, S. J., CAUDA, E. G., MISCHLER, S. E. & NOLL, J. D. 2012b. *Controlling exposure to diesel emissions in underground mines*, *SME*.

BURGESS-LIMERICK, R., ZUPANC, C. & WALLIS, G. 2013. Effect of control order on steering a simulated underground coal shuttle car. *Applied Ergonomics,* 44, 225-229.

BURGESS-LIMERICK, R., ZUPANC, C. M. & WALLIS, G. 2012. Directional control–response compatibility of joystick steered shuttle cars. *Ergonomics,* 55, 1278-1283.

BURGESS JR, J. V. 1979. Mine ventilation system and elements thereof. Google Patents.

CHANG, P., XU, G., MULLINS, B., ABISHEK, S. & SHARIFZADEH, M. 2020. Numerical investigation of diesel particulate matter dispersion in an underground development face during key mining activities. *Advanced Powder Technology,* 31, 3882-3896.

CHANG, P., XU, G., ZHOU, F., MULLINS, B. & ABISHEK, S. 2019a. Comparison of underground mine DPM simulation using discrete phase and continuous phase models. *Process Safety and Environmental Protection,* 127, 45-55.

CHANG, P., XU, G., ZHOU, F., MULLINS, B., ABISHEK, S. & CHALMERS, D. 2019b. Minimizing DPM pollution in an underground mine by optimizing auxiliary ventilation systems using CFD. *Tunnelling and Underground Space*

Technology, 87, 112-121.

CHENG, J., LI, S., ZHANG, F., ZHAO, C., YANG, S. & GHOSH, A. 2016. CFD modelling of ventilation optimization for improving mine safety in longwall working faces. *Journal of Loss Prevention in the Process Industries,* 40, 285-297.

CMHSR 2006. Coal Mine Health and Safety Regulation.

CROSS, H. 1936. Analysis of flow in networks of conduits or conductors. University of Illinois at Urbana Champaign, College of Engineering.

CUTLER, W. A. & HICKMAN, D. L. 2002. Diesel particulate filters. Google Patents.

DANIEL, J. 1984. Diesels in Underground Mining: *A Review and Evaluation of an Air Quality Monitoring Methodology.* US Department of the Interior, Bureau of Mines.

DAVIES, B. 2002. Diesel particulate control strategies at some Australian underground coal mines. *AIHA Journal,* 63, 554.

DAVIES, B. 2003. The control of diesel particulates in underground coal mines. *Victoria University.UOW*.

DAVIES, B. 2004. The Control of Diesel Particulate in Underground Coal Mines.

DESOUZA, E. 2004. Auxiliary ventilation operation practices. *Ganguli, Rajive; Bandopadhyay, Sukumar, Mine Ventilation, Taylor & Francis Routledge*, 341-349.

DOMESLE, R., VOLKER, H., KOBERSTEIN, E. & PLETKA, H.-D. 1984. Catalyst for reducing the ignition temperature of diesel soot. Google Patents.

DRWIĘGA, A., SZELKA, M. & TUREWICZ, A. Improvement of auxiliary ventilation efficiency in underground workings. IOP Conference Series: Earth and Environmental Science, 2019. IOP Publishing, 012007.

FENG, Y., CHEN, Y., GUO, H., ZHI, G., XIONG, S., LI, J., SHENG, G. & FU, J. 2009. Characteristics of organic and elemental carbon in PM2. 5 samples in Shanghai, China. *Atmospheric Research,* 92, 434-442.

GENG, F., LUO, G., ZHOU, F., ZHAO, P., MA, L., CHAI, H. & ZHANG, T. 2017. Numerical investigation of dust dispersion in a coal roadway with hybrid ventilation system. *Powder Technology,* 313, 260-271.

GEORGARAS, S. 1999. Ventilation system. Google Patents.

GILLIES, A. D. S., WU, H. W., MAYES, T. & HALIM, A. Measurement of airflow through regulators and real time integrated monitoring. *Proceedings 9th Northern American Ninth US Mine Ventilation Symposium,* 2002. 301-308.

GLYNN, P., BATES, D. & CLARKE, M. 2009. Diesel Particulate Agglomeration & Removal Using Ultrasonic Transducers With Electrostatic Precipitation Filter. ACARP: ACARP.

GRAU, R., KROG, R. & ROBERTSON, S. Maximizing the ventilation of large-opening mines. *Proceedings of the 11th US/North American Mine Ventilation Symp*. University Park, PA, 2006. 53-59.

GRAY, H., CASS, G., HUNTZICKER, J., HEYERDAHL, E. & RAU, J. 1984. Elemental and organic carbon particle concentrations: A long-term perspective. *Science of the Total Environment,* 36, 17-25.

GREENWOOD, J., HOWARD, D., O'BEIRNE, T., ZORAN, R. & SURAWSKI, N. B., RANKA. Trialling Alternative Diesel Fuels For Reducing DPM & Solving Emission Toxicity, ACARP, C18014. 2011.

GREENWOOD, J., O'BEIRNE, T. & HOWARD, D. 2009. Diesel Engine Management,. ACARP.

GREENWOOD, J., WANG, H., RISTOVSKI, Z. & O'BEIRNE, T. DPM Risk Factors Extension: Effect of Cooled Exhaust and Scrubber on Toxic Particulate Formation, ACARP, C20036. 2013.

GRENIER, M., GANGAL, M., GOYER, N., MCGINN, S., PENNEY, J. & VERGUNST, J. 2001. Sampling for Diesel Particulate Matter in Mines. *Diesel Emissions Evaluation Program (DEEP).* 34,15, 1-33.

GRENIER, M., GANGAL, M., LASTRA, R., MIKHAIL, S., TURCOTTE, A.-M.,

BUTLER, K., EDWARDSON, E. & LAFLAMME, G. Evaluation of Existing Diesel Particulate Matter Sampling and Analysis Methods at a High Sulphide Ore Mine. 1998. 1-59.

GUO, H., QIN, J. & QU, Q. 2012. CFD Investigation of Goaf Flow of Methane Released From unmined adjacent coal seams. *9th International Conference on CFD in the Minerals and Process Industries*, 1-6.

GUSTAFSON, A. 2013. Automation of Load Haul Dump Machines Comparative performance analysis and maintenance modeling. *PhD*, Luleå University of Technology.

HABIBI, A., KRAMER, R. & GILLIES, A. 2015. Investigating the effects of heat changes in an underground mine. *Applied Thermal Engineering,* 90, 1164-1171.

HALIM, A. Ventilation requirements for diesel equipment in underground mines–Are we using the correct values. 16th North American Mine Ventilation Symposium, Golden, Colorado, 2017. 27, 1-7.

HAMRIN, H., HUSTRULID, W. & BULLOCK, R. 2001. Underground mining methods and applications. *Underground mining methods: Engineering fundamentals and international case studies*, 3-14.

HARRINGTON, D. & EAST, J. H. 1947. *Diesel equipment in underground mining*, US Department of the Interior, Bureau of Mines.

HARTMAN, H. L. & MUTMANSKY, J. M. 2002. *Introductory mining engineering*, John Wiley & Sons.

HARTMAN, H. L., MUTMANSKY, J. M., RAMANI, R. V. & WANG, Y. 2012. *Mine ventilation and air conditioning*, John Wiley & Sons.

HEWAGE, S., RAJAPAKSE, R., RATHNAYAKE, R., PRASANNA, E., DISSANAYAKE, D., DHARMARATNE, P., WELIDENIYA, H. & ROHITHA, L. 2014. Ventilation of Underground Workings and Improvement of Comfort Levels. 41-44, Proceedings of ERE.

HOSHINO, S. & SATO, T. 1987. Laser measuring device. Google Patents.

HOWELL, R. H. & SAUER, H. 1990. Field measurements of air velocity: pitot traverse or vane anemometer. *ASHRAE Journal,* 32, 46-52.

HOWELL, S. & WEBER, J. A. 1997. Biodiesel use in underground metal and non-metal mines. *Dieselnet site http://www. dieselnet. com*.

HWANG, C. C. & EDWARDS, J. C. 2005. The critical ventilation velocity in tunnel fires -A computer simulation. *Fire Safety Journal,* 40, 213-244.

JAKKULA, B. & SN, M. C. 2019. Maintenance management of load haul dumper using reliability analysis. *Journal of Quality in Maintenance Engineering,* 26, 290-310.

JANISKO, S. & NOLL, J. 2008. Near real time monitoring of diesel particulate matter in underground mines. *12th North American Mine Ventilation Symposium,* 50-54.

JIN, T., LU, K., LIU, S., ZHAO, S., QU, L. & XU, X. 2016. Chemical characteristics of particulate matter emission from a heavy-duty diesel engine using ETC cycle dynamometer test. *Aerosol and Air Quality Research,* 17, 406-411.

JIN, T., QU, L., LIU, S., GAO, J., WANG, J., WANG, F., ZHANG, P., BAI, Z. & XU, X. 2014. Chemical characteristics of particulate matter emitted from a heavy duty diesel engine and correlation among inorganic and PAH components. *Fuel,* 116, 655-661.

JOJO S, M., LI. 2004. Application of CFD and Numerical Studies on Tunnel Fire Simulation. *International Journal of Engineering Performance-Based Fire Codes,* 6, 215-222.

KELLERMAN, R., KOCHER, A. J., NAUGHTON, M. T., JUCHNO, B., HIDALGO, C. & MCDONNELL, R. 2002. Vane anemometer. Google Patents.

KHAN, M., USMAN. 2017. Real-Time Diesel Particulate Matter Monitoring in Underground Mine Atmospheres, Association With the Standard Method and Related Challenges.*Missouri University of Science and Technology.*

KHATTRI, S. K., LOG, T. & KRAAIJEVELD, A. 2019. Tunnel fire dynamics as a function of longitudinal ventilation air oxygen content. *Sustainability,* 11, 1-13.

KHERA, S. & PRASAD, B. 1991. Jhanjra Project: a large underground coal mine in Raniganj coalfield. An overview. *Journal of mines, metals and fuels,* 39, 273-276.

KIŠA, M. & JELEMENSKÝ, Ľ. 2009. CFD dispersion modelling for emergency preparedness. *Journal of Loss Prevention in the Process Industries,* 22, 97-104.

KITTELSON, D. B. 2001. Recent Measurements of Nanoparticle Emissions from Engines: Current Research on Diesel Exhaust Particles. *Current Research on Diesel Exhaust Particles. Japan Association of Aerosol Science and Technology.*

KOLTSAKIS, G. C. & STAMATELOS, A. M. 1997. Modes of catalytic regeneration in diesel particulate filters. *Industrial & engineering chemistry research,* 36, 4155-4165.

KONSTANDOPOULOS, A. G. & JOHNSON, J. H. 1989. Wall-flow diesel particulate filters-their pressure drop and collection efficiency. *SAE Transactions*, 625-647.

KURNIA, J. C., SASMITO, A. P., WONG, W. Y. & MUJUMDAR, A. S. 2014. Prediction and innovative control strategies for oxygen and hazardous gases from diesel emission in underground mines. *Science of the Total Environment,* 481, 317-334.

LIANG, F., LU, M., KEENER, T. C., LIU, Z. & KHANG, S.-J. 2005. The organic composition of diesel particulate matter, diesel fuel and engine oil of a non-road diesel generator. *Journal of Environmental Monitoring,* 7, 983-988.

LIU, Q., NIE, W., HUA, Y., JIA, L., LI, C., MA, H., WEI, C., LIU, C., ZHOU, W. & PENG, H. 2019. A study on the dust control effect of the dust extraction system in TBM construction tunnels based on CFD computer simulation technology. *Advanced Powder Technology,* 30, 2059-2075.

LOWNDES, I. S., CROSSLEY, A. J. & YANG, Z.-Y. 2004. The ventilation and climate modelling of rapid development tunnel drivages. *Tunnelling and underground space technology,* 19, 139-150.

MAHE, G. 2012. Summary of world wide underground mine diesel regulations. *MDEC Conference Toronto*, 1-12.

MAJEWSKI, W. A. 2001. Diesel particulate filters. *DieselNet Technology Guide*, 4,36-45.

MALEKI, S., SOTOUDEH, F. & SERESHKI, F. 2018. Application of VENTSIM 3D and mathematical programming to optimize underground mine ventilation network: A case study. *Journal of Mining and Environment,* 9, 741-752.

MATSUI, K. 2009. UNDERGROUND MINING TRANSPORTATION SYSTEMS. *Civil Engineering-Volume II,* 5, 285.

MCGINN, A., GRENIER, M., GANGAL, M., RUBELI, B., BUGARKSI, A., SCHUAKEUBERG, G., JOHNSON, R., PETRIE, D., CROWTHER, G. & PENNEY, J. Diesel Emissions Evaluation Program (DEEP). Norandra Inc.-Brunswick Mine DPF field study. 2004. 4-33.

MCPHERSON, M. J. 1993. Subsurface ventilation systems. *Subsurface Ventilation and Environmental Engineering.* Springer.

MCPHERSON, M. J. 2012. *Subsurface ventilation and environmental engineering*, Springer Science & Business Media.

MCQUEEN, K. 2006. Hidden copper: The early history of the Cornish, Scottish and Australian (CSA) Mine, Cobar, NSW. *Journal of Australasian Mining History,* 4, 20.

MDG 2008. Guideline for the management of diesel engine pollutants in underground environments. *MDG-29, NSW*.

MISCHLER, S. E. & COLINET, J. F. 2009. Controlling and monitoring diesel emissions in underground mines in the United States. *Oxford & IBH Publishing Co. Pvt.Ltd*, 2, 879-888.

MOREBY, R. 2019. Application of Ventsim to low pressure gas drainage and high pressure nitrogen reticulation systems.*Coal Operators Conference,* UOW*,* 223-235

MORLA, R. 2013. Optimum Inertisation Techniques for Blasting Gallery Method. *3rd International Workshop on Mine Hazard Prevention and Control.* Brisbane:

CSIRO.

MORLA, R., BALUSU, R., TANGUTURI, K. & KHANAL, M. 2013. Prediction and control of spontaneous combustion in thick coal seams. *Coal Operators conference.* Wollongong: University of Wollongong.

MORLA, R., BALUSU, R., TANGUTURI, K. & TING, R. 2015. Inertisation options for BG method and optimisation using CFD modelling. *International Journal of Mining Science and Technology,* 25, 401-405.

MORLA, R., KAREKAL, S. & GODBOLE, A. 2019. Analysis of Diesel Particulate Matter Flow Patterns in Different Ventilation and Operational Conditions of Underground Mines. *Diesel Emissions.* IntechOpen.

MSHA. Diesel Particulate Matter Exposure of Underground Metal and Nonmetal Miners. Federal Register, 2001a. 35521-35523.

MSHA. Federal Register/Vol.66, No.13/Friday, January 19, 2001/Rules and Regulations. Federal Register, 2001b. 5536-5538.

MSHA 2008. Air quality-surface and underground. *Mine Safety and Health Administration*.

MUTTON, V. 2008. Airflow Regulator. Google Patents.

MUTTON, V. 2010. Airflow regulator. Google Patents.

NAUSS, K. Diesel exhaust: A critical analysis of emissions, exposure and health effects. Special Report HEI Diesel Working Group, 1995. 1-75.

NDENGUMA, D. D., DIRKER, J. & BURGER, N. D. L. 2014. A computational fluid dynamics model for investigating air flow patterns in underground coal mine sections. *Journal of the Southern African Institute of Mining and Metallurgy,* 114, 419-4226.

NIEKERK, W. C. A. V., SIMPSON, D., FOURIE, H. M. & MOUTON, G. Diesel particulate emissions in the south African mining industry. *Safety in Mine Research Advisory Committee*, SIM 020602, 2002. 1-49.

NIOSH. Carcinogenic Effects of Exposure to Diesel Exhaust. 1988 *Current Intelligence Bulletin* 50, 88-116.

NOLL, J., BUGARSKI, A., PATTS, L., MISCHLER, S. & MCWILLIAMS, L. 2007. Relationship between elemental carbon, total carbon and diesel particulate matter in several underground metal/non-metal mines. *Environmental Science & Technology,* 41, 710-716.

NOLL, J., CECALA, A., ORGANISCAK, J. & RIDER, J. 2014. Effects of MERV 16 filters and routine work practices on enclosed cabs for reducing respirable dust and DPM exposures in an underground limestone mine. *Mining Engineering,* 66, 45.

NOLL, J., MISCHLER, S., CAUDA, E., PATTS, L., JANISKO, S. & GRAU, R. The effects of passive diesel particulate filters on diesel particulate matter concentrations in two underground metal/non metal mines. *Proceedings of the 13th US/North American Mine Ventilation Symposium*, Sudbury, Ontario, Canada, June, 2010. 13-16.

NOLL, J., PATTS, L. & GRAU, R. The effects of ventilation controls and environmental cabs on diesel particulate matter concentrations in some limestone mines. *Proceedings of the 12th US/North American Mine Ventilation Symposium*, 2008. 9-11.

NUNDLALL, A. R. 2014. Development of a regulatory mechanism for the control of exposure to diesel particulate matter (DPM) in the South African mining industry.*MVSSA*, 15-19.

NUSZKOWSKI, J., FLAIM, K. & THOMPSON, G. 2011. The effect of cetane improvers and biodiesel on diesel particulate matter size. *SAE International Journal of Fuels and Lubricants,* 4, 23-33.

O'BEIRNE, T., O'MALLEY, A., JENSEN, B., MULLER, S. & CHRZANOWSKI, D. Improve the Productivity of U/G Diesel Vehicles by Optimising the Engine, Exhaust System and Exhaust Gas Monitoring Process, ACARP, C3033. 1997.

O'BEIRNE, T., WALTON, P., MORRELL, A., BELL, M. & O'MALLEY, A.

Underground Vehicle Design Standards and Statutory Implications, ACARP, C3063. 1996.

PATEL, H., EO, S. & KWON, S. 2011. Effects of diesel particulate matters on inflammatory responses in static and dynamic culture of human alveolar epithelial cells. *Toxicology Letters,* 200, 124-131.

PIVNYAK, G., BONDARENKO, V., KOVALEVS' KA, I. & ILLIASHOV, M. 2013. *Mining of mineral deposits*, CRC Press.

RAMOS, J., CARLOS., BEIZA, M., GASTELURRUTIA, J., RIVAS, A., ANTÓN, R., LARRAONA, G., S. & DE MIGUEL, I. 2013. Numerical modelling of the natural ventilation of underground transformer substations. *Applied Thermal Engineering,* 51, 852-863.

RAWLINS, C. Underground mine ventilation planning, heat loads and diesel equipment. 11th United States/North American Mine Ventilation Symposium. Taylor & Francis Group, Penn State University, College Park. USA, 2006. 75-81.

REN, T. X. & BALUSU, R. 2005. CFD modelling of goaf gas migration for control of spontaneous combustion in longwalls. *Coal Operators Conference.* UOW, 259-264.

RIDLEY, P. & CORKE, P. 2003. Load haul dump vehicle kinematics and control. *J. Dyn. Sys., Meas., Control,* 125, 54-59.

RIS, C. 2007. US EPA health assessment for diesel engine exhaust: a review. *Inhalation Toxicology,* 19, 229-239.

RISTIM, J. 2006. Sampling and Measurement Methods for Diesel Exhaust Aerosol Sampling and Measurement Methods for Diesel Exhaust Aerosol. *Tampere University of Technology*, 638

RISTOVSKI, Z. D., MILJEVIC, B., SURAWSKI, N. C., MORAWSKA, L., FONG, K. M., GOH, F. & YANG, I. A. 2012. Respiratory health effects of diesel particulate matter. *Respirology,* 17, 201-212.

ROBERT, M. A., KLEEMAN, M. J. & JAKOBER, C. A. 2007. Size and composition

distributions of particulate matter emissions: Part 2-Heavy-duty diesel vehicles. *Journal of the Air & Waste Management Association,* 57, 1429-1438.

ROGHANCHI, P. & KOCSIS, K. C. 2017. Improving the climatic conditions in development and production workings of hot underground mines by re-designing the auxiliary ventilation system: a case study. *International Journal of Mining and Mineral Engineering,* 8, 280-293.

RUDOW, M. & KLAWANS, W. 1974. Vane anemometers. Google Patents.

SAKTHI, S., NIRESH, J. & NEELAKRISHNAN, S. 2019. Adaptive Admittance Control for Autonomous Loading of Load Haul Dumper in Underground Coal Mining. *The 5th International Conference on Mechatronics and Robotics Engineering.* New York: Association for Computing Machinery.

SASAKI, K. & DINDIWE, C. An integrated mine ventilation simulator "MIVENA Ver. 6" with applications. 9th *North American/Ninth US Mine Ventilation Symposium, 2002*. Swets & Zeitlinger The Netherlands, 243-251.

SASMITO, A. P., BIRGERSSON, E., LY, H. C. & MUJUMDAR, A. S. 2013. Some approaches to improve ventilation system in underground coal mines environment-A computational fluid dynamic study. *Tunnelling and Underground Space Technology,* 34, 82-95.

SERESHKI, F., SAFFARI, A. & ELAHI, E. 2016. Comparison of Mathematical Approximation Methods for Mine Ventilation Network Analysis. *International Journal of Mining Science,* 2, 1-14.

SHARMA, M., AGARWAL, A. K. & BHARATHI, K. 2005. Characterization of exhaust particulates from diesel engine. *Atmospheric Environment,* 39, 3023-3028.

SHI, J. P., HARRISON, R. M. & BREAR, F. 1999. Particle size distribution from a modern heavy duty diesel engine. *Science of the Total Environment,* 235, 305-317.

SIDORENKO, A. A. & IVANOV, V. V. 2016. Underground mining of multiple seams of coal. *ARPN Journal of Engineering and Applied Sciences,* 11, 4448-4454.

SILVERMAN, D., T., SAMANIC, C., M., LUBIN, J., H., BLAIR, A., E., STEWART, P., A., VERMEULEN, R., COBLE, J., B., ROTHMAN, N., SCHLEIFF, P., L., TRAVIS, W., D., ZIEGLER, R., G., WACHOLDER, S. & ATTFIELD, M., D. 2012. The diesel exhaust in miners study: A nested case-control study of lung cancer and diesel exhaust. *Journal of the National Cancer Institute,* 104 (11), 855–868.

SIVAKUGAN, N., RANKINE, R., RANKINE, K. & RANKINE, K. 2006. Geotechnical considerations in mine backfilling in Australia. *Journal of Cleaner Production,* 14, 1168-1175.

SMOORENBURG, E., OGUNOMEDEDE, O., NICHOLS, S., NEWMAN, A. & BOGIN, G. 2021. Incorporating ventilation and heat in an underground mine production scheduling model. *Mine Ventilation.* CRC Press.

STANTON, D. W., KIELBLOCK, J., SCHOEMAN, J. J. & JOHNSTON, J. 2007. Handbook on mine occupational hygiene measurements. *Mine Health and Safety Council.* Johannesburg, 391.

SWA 2019. Carcinogens. *Safe Work Australia*.

TAATJES, C., A., ZADOR, J., MELONI, G., GEORGIEVSKI, Y., MILLER, J., A., FERNANDES, R. & XAVIER, F. 2007. Theoretical study and modeling of low temperature and high pressure ethanol oxidation. Sandia National Lab. (SNL-CA), Livermore, CA (United States).

TAN, P.-Q., WANG, D.-Y., YAO, C.-J., ZHU, L., WANG, Y.-H., WANG, M.-H., HU, Z.-Y. & LOU, D.-M. 2020. Extended filtration model for diesel particulate filter based on diesel particulate matter morphology characteristics. *Fuel,* 277, 118150.

TANDON, P., HEIBEL, A., WHITMORE, J., KEKRE, N. & CHITHAPRAGADA, K. 2010. Measurement and prediction of filtration efficiency evolution of soot loaded diesel particulate filters. *Chemical Engineering Science,* 65, 4751-4760.

TANGUTURI, K. & BALUSU, R. 2014. CFD Modeling of Methane Gas Distribution and Control Strategies in a Gassy Coal Mine. *Journal of Computational Multiphase Flows,* 6, 65-78.

TANGUTURI, K. M. & BALUSU, R. S. 2018. Computational fluid dynamics simulations for investigation of parameters affecting goaf gas distribution. *Journal of Mining and Environment,* 9, 547-557.

THIRUVENGADAM, M., ZHENG, Y., LAN, H. & TIEN, J. C. 2016a. A diesel particulate matter dispersion study inside a single dead end entry using dynamic mesh model. *International Journal of Mining and Mineral Engineering,* 7, 210.

THIRUVENGADAM, M., ZHENG, Y. & TIEN, J. C. 2016b. DPM simulation in an underground entry: Comparison between particle and species models. *International Journal of Mining Science and Technology,* 26, 487-494.

TORAÑO, J., RODRÍGUEZ, R. & DIEGO, I. 2006. Computational Fluid Dynamics (CFD) use in the simulation of the dead end ventilation in tunnels and galleries. *WIT Transactions on Engineering Sciences,* 52, 113-121.

TORAÑO, J., TORNO, S., MENÉNDEZ, M. & GENT, M. 2011. Auxiliary ventilation in mining roadways driven with roadheaders: Validated CFD modelling of dust behaviour. *Tunnelling and Underground Space Technology incorporating Trenchless Technology Research,* 26, 201-210.

USEPA, 2002. Health assessment document for diesel engine exhaust. Washington, DC: U.S. Environmental Protection Agency.

VAN SETTEN, B. A., MAKKEE, M. & MOULIJN, J. A. 2001. Science and technology of catalytic diesel particulate filters. *Catalysis Reviews,* 43, 489-564.

VENTSIM. Ventsim Visual ™ User Guide. 2019. 1-296.

VIRTANEN, A., RÖNKKÖ, T., KANNOSTO, J., RISTIMÄKI, J., MÄKELÄ, J. M., KESKINEN, J., PAKKANEN, T., HILLAMO, R., PIRJOLA, L. & HÄMERI, K. 2006. Winter and summer time size distributions and densities of traffic-related aerosol particles at a busy highway in Helsinki. *Atmospheric Chemistry and Physics,* 6, 2411-2421.

VUTUKURI, V. & LAMA, R. 1986. *Environmental engineering in mines.* Cambridge University Press.

WANG, G., XU, H., WU, M., WANG, Y., WANG, R. & ZHANG, X. 2018. Porosity model and air leakage flow field simulation of goaf based on DEM-CFD. *Arabian Journal of Geosciences,* 11, 1-17.

WATTS JR, W. F. Industrial Hygiene Issues Arising from the Use of Diesel Equipment in Underground Mines. *Proc. BuMines Technology Transfer Seminar: Diesels in Underground Mines*, BuMines IC, 1987. 4-8.

WHSA 2013. Work Health and Safety (Mines) Act.

WHSR 2014. Work Health and Safety (Mines) Regulations.

WICHMANN, H.-E. 2007. Diesel exhaust particles. *Inhalation Toxicology,* 19, 241-244.

WIDIATMOJO, A., SASAKI, K., WIDODO, N. P., SUGAI, Y., SINAGA, J. & YUSUF, H. 2013. Numerical simulation to evaluate gas diffusion of turbulent flow in mine ventilation system. *International Journal of Mining Science and Technology,* 23, 349-355.

WIDZYK-CAPEHART, E. & FAWCETT, C. Life of mine ventilation requirements for Bronzewing mine using VentSim. Proceeding of 7th International Mine Ventilation Congress, 2001. Citeseer.

WIDZYK-CAPEHART, E. & WATSON, B. Agnew gold mine expansion mine ventilation evaluation using VentSim. *Proc. of the 7th International Mine Ventilation Congress*, 2001.

WOODRUFF, S. D. 2016. *Methods of Working Coal and Metal Mines: Planning and Operations*. Elsevier.

XU, G., CHANG, P., MULLINS, B., ZHOU, F. & HU, S. 2018. Numerical study of diesel particulate matter distribution in an underground mine isolated zone. *Powder Technology,* 339, 947-957.

YERGEY, J. A., RISBY, T. H. & LESTZ, S. S. 1982. Chemical characterization of organic adsorbates on diesel particulate matter. *Analytical Chemistry,* 54, 354-357.

YUAN, L. 2010. Computational fluid dynamics study on the ventilation flow paths in longwall gobs. *11th US/North American Mine Ventilation Symposium 2006*, 591-598.

ZHANG, Z.-H. & BALASUBRAMANIAN, R. 2016. Investigation of particulate emission characteristics of a diesel engine fueled with higher alcohols/biodiesel blends. *Applied Energy,* 163, 71-80.

ZHENG, Y. 2011. Diesel particulate matter dispersion analysis in underground metal/nonmetal mines using computational fluid dynamics. *PhD*, Missouri University of Science and Technology.

ZHENG, Y., LAN, H., THIRUVENGADAM, M., TIEN, J. C. & LI, Y. 2017. Effect of single dead end entry inclination on DPM plume dispersion. *International Journal of Mining Science and Technology,* 27, 401-406.

ZHENG, Y., THIRUVENGADAM, M., LAN, H. & TIEN, C. 2015a. Effect of auxiliary ventilation on diesel particulate matter dispersion inside a dead-end entry. *International Journal of Mining Science and Technology,* 25, 927-932.

ZHENG, Y., THIRUVENGADAM, M., LAN, H. & TIEN, J. 2015b. Simulation of DPM distribution in a long single entry with buoyancy effect. *International Journal of Mining Science and Technology,* 25, 47-52.

ZHENG, Y., THIRUVENGADAM, M., LAN, H. & TIEN, J. C. 2015c. Design of push-pull system to control diesel particulate matter inside a dead-end entry. *International Journal of Coal Science and Technology,* 2, 237-244.

ZHOU, G., ZHANG, Q., BAI, R., FAN, T. & WANG, G. 2017. The diffusion behaviour law of respirable dust at fully mechanized caving face in coal mine: CFD numerical simulation and engineering application. *Process Safety and Environmental Protection,* 106, 117-128.

ZHOU, L., PRITCHARD, C. & ZHENG, Y. 2015a. CFD modeling of methane distribution at a continuous miner face with various curtain setback distances. *International Journal of Mining Science and Technology,* 25, 635-640.

ZHOU, L., PRITCHARD, C. & ZHENG, Y. 2015b. CFD modeling of methane distribution at a continuous miner face with various curtain setback distances. *International Journal of Mining Science and Technology,* 25, 635-640.